Theory of Charge Transfer in Solar Energy Materials

The University Of Sheffield.

Mr Peter N O Gillespie
University of Sheffield, UK
Supervisor: Dr Natalia Martsinovich

A thesis submitted in partial fulfilment of the requirements for the degree of Doctor of Philosophy

January 25, 2019

You can't change the wind, but you can adjust your sails
-Ancient Greek proverb

Abstract

Developing materials for applications in renewable energy is one of the greatest challenges of the 21st century. The work in this thesis explores the electronic structure of several materials for use in solar energy conversion, utilising computational chemical techniques to better understand the mechanisms responsible for these materials' properties. First the graphene/titanium dioxide (TiO_2) photocatalytic composite is studied. This material is known from experimental studies to be much more effective for UV and visible-light photocatalysis than TiO_2 alone, but the mechanism of its photocatalytic activity enhancement is under debate. Out hybrid HF/DFT calculations show that there is ground-state charge transfer from graphene to TiO_2, which provides a rationale for the observed increases in both UV and visible-light photocatalytic rates and rapid charge transfer within the system. In experimental examples of this composite, the graphene is typically derived from graphene oxide (GO) and contains oxygen functional groups in addition to the graphene structure. We therefore develop the model of graphene/TiO_2 further by studying the role of oxygen functional groups in the electronic structure of the composite, which leads to a model for composites of GO and reduced graphene oxide (RGO) with TiO_2. It is found that the interaction of these oxygen functional groups with TiO_2 produces electronic states that can act as electron traps which inhibit undesirable electron-hole recombination. This is proposed to be the reason for the experimentally observed improvements in photocatalytic performance of the composite compared to TiO_2. Finally, a series of dye-sensitised solar cells (DSSCs) based on TiO_2 are studied to understand the source of their unexpectedly low light-harvesting performances seen in experiment. Here variations in the design of the dyes' ligands are presented as a means to improve the performance of these dyes.

Acknowledgements

My thanks go out to all of the people I've worked with, talked with, and even walked with, for all their help, love, and support throughout the years which it took to finish this PhD. I would like to thank my parents and siblings for all their advice and support, all the way from day one. I wish to thank the friends I've made for helping to make my time at Sheffield the great experience that it was; and especially to the UoS theory cluster for the many opportunities to learn how this all works. And I am, of course, hugely indebted to Dr Natalia Martsinovich for being the best supervisor I could have ever asked for.

Contents

Glossary

conduction band A band of energies in an electronic band structure which is not occupied by electrons. 7

graphene oxide A highly oxidised form of graphene, which is typically formed from the oxidation, followed by solvent exfoliation, of graphite. It is a solid material, with no defined crystal structure. 56, 57

heterojunction The interface between two solids with different electronic properties. 9, 46

highest-occupied molecular orbital The highest-energy molecular orbital in a given chemical system that is occupied by two electrons. 7

lowest-unoccupied molecular orbital The lowest-energy molecular orbital in a given chemical system that is not occupied by any electrons. 7

natural hydrogen electrode A platinum/hydrogen gas electrochemical cell, often used as a measurement standard when determining the electrochemical potentials of other electrochemical reactions. 6

parallel scaling A term used when describing the computation speed of a program relative to the number of parallel processors used (using either open-multiprocessing or message-passing interface methods). A program with ideal parallel scaling will increase the rate of computation equal to the increase in processor usage, while a program with "good" parallel scaling will increase computation speed by less than the increase in processor usage.. 58

reduced graphene oxide The product of reducing graphene oxide (GO), through chemical, thermal, or other means. The name is used to distinguish the material from graphene, as reduced graphene oxide contains defects (such as oxygen functional groups and carbon atom vacancies) not present in graphene samples formed through non-chemical means.. 56

Schottky barrier An electronic structure which forms at the interface between a solid semiconductor and a metal. The difference in energy between the work function of the metal and the conduction band of the semiconductor can lead to the separation of a photoexcited electron from its hole, and also allow the material, thus formed, to function as a diode.. 52

unit cell The smallest repeating unit which replicates the physical structure of a particular crystal. 61

valence band A band of energies in an electronic band structure which is occupied by electrons. 7

Chapter 1

Introduction

Whether or not one looks at the consumption of fossil fuels, rising total energy demands,[1] or the effect of CO_2 production on global climate change, one point remains clear: there is a great need for clean, renewable energy sources. Solar energy conversion has progressed consistently in the last few decades,[2,3] and techniques for solar energy conversion (such as photovoltaics and photocatalysis) are certainly a very attractive prospect for solving the energy problem. In particular, since the discovery of the photocatalytic electrolysis of H_2O in 1972 by Fujishima and Honda[4] there has been a steady stream of research aimed at the photocatalytic production of hydrogen, as shown by recent reviews.[5–7]

1.1 The Water Splitting Reaction

The production of hydrogen as an energy source is often seen as the most important application of this developing technology (as seen in the themes of various reviews of the subject area[5–7]). A second, but no less significant, application is the production of hydrogen for use in the chemical industries

— namely the industrial production of ammonia in the Haber-Bosch process.[1] Currently, hydrogen is mainly produced for industrial use through the steam reforming method:

$$\begin{aligned} \mathrm{CH_4 + H_2O} &\longrightarrow \mathrm{CO + 3\,H_2} \\ \mathrm{CO + H_2O} &\longrightarrow \mathrm{CO_2 + H_2} \end{aligned} \tag{1.1}$$

This process effectively utilises fossil fuels such as natural gas and produces CO (followed by CO_2 from the water-gas shift reaction) as a byproduct. Replacing steam reformation with photocatalytic water splitting would therefore significantly reduce the CO_2 emissions associated with the industrial production of hydrogen. The water splitting reaction is an electrochemical redox reaction consisting of an oxygen evolution reaction (OER) (H_2O/O_2) and a hydrogen evolution reaction (HER) (H^+/H_2). These two reactions are shown below, with their electrochemical potentials vs the natural hydrogen electrode (NHE):

$$\begin{aligned} \mathrm{(OER) H_2O + 4\,h^+} &\longrightarrow \mathrm{4\,H^+ + O_2} \qquad 1.23\,\mathrm{V\ vs\ NHE} \\ \mathrm{(HER) 4\,H^+ + 4\,e^-} &\longrightarrow \mathrm{2\,H_2} \qquad 0\,\mathrm{V\ vs\ NHE} \end{aligned} \tag{1.2}$$

This electrochemical reaction can be done with an anode/cathode pair and an input of energy *via* an external source of electricity. A photocatalytic material can also provide these, where the energy input is directly converted from solar energy.

1.2 Principles of Photocatalysis

The generation of usable energy directly from solar radiation is done by two main methods: photovoltaics and photocatalysis. These two methods work using the same fundamental principles: photons are absorbed from radiation

sources and are used to promote an electron from its ground state to an excited state; this energetic electron/hole pair is then used to complete some form of thermodynamic work. In photovoltaics, this work takes the form of generating direct electrical current (for powering electrical devices), or as energy storage in some form of battery. In photocatalysis, this work is instead the activation of electrochemical reactions directly at the photocatalyst's reactive site(s), which can be used to produce simple compounds that store energy in their chemical bonds. These compounds may also be generated in a photovoltaic setup by directly powering an electrolysis cell (referred to as photo-electrocatalysis), while photocatalysts would both absorb photons and generate compounds at their own reactive sites. Despite the similarities of these two main branches of solar energy conversion, different materials are often utilised in their constructions due to the different operating environments. As such the discussion in this introduction will concern only photocatalysis. However, dye-sensitised solar cells (DSSCs) (a form of photovoltaic system) will be discussed in a later chapter (chapter 5). The photophysics and recent advances in photovoltaics have been covered extensively in the wider literature.[8–10]

In a single-component photocatalyst, photons of energies equal to or more than that of the optical gap in Figure 1.2 are absorbed by the material to generate a photoexcited electron-hole pair, which can then be used in electron transfer processes (as shown in Figure 1.1). In the example of water splitting, water is oxidised when electrons from oxygen in the water are transferred to the holes in the photocatalyst's VB/HOMO; the protons from this reaction are then reduced to hydrogen gas when the photoexcited electrons in the photocatalyst's CB/LUMO are transferred to the protons. For the device to function effectively, the energy gap (Eg) between photocatalyst's VB/HOMO and CB/LUMO must be greater than the potential difference of the redox re-

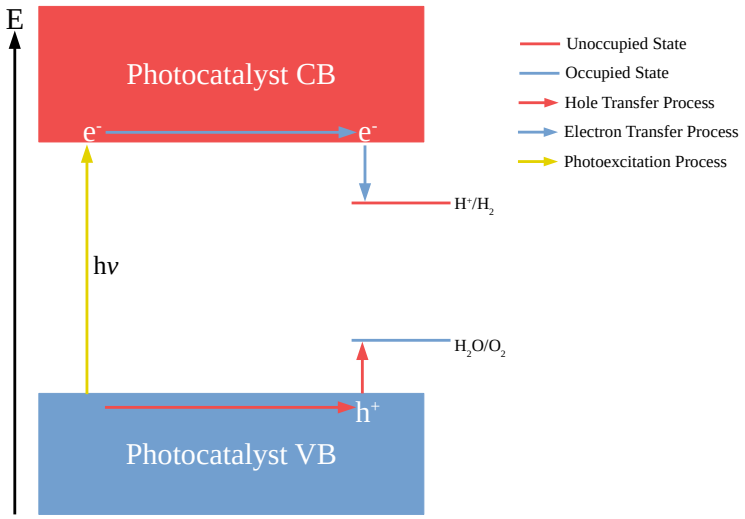

Figure 1.1: Mechanism depicting the photon-assisted excitation of an electron from the valence band (VB) to the conduction band (CB) of a material and the photocatalytic oxidation and reduction of water to yield hydrogen and oxygen. $h\nu$ represents the energy of the photon absorbed by the material.

action; specifically the VB/HOMO will need to correspond to a more positive electrical potential than the OER, and the CB/LUMO will need to correspond to a more negative electrical potential than the HER.[11,12] This reaction may be used in practice as a means of chemical energy storage, as the energy stored in the chemical bonding of hydrogen can be released by oxidising it back to H_2O. Many other photocatalysed processes exist, some are suitable for chemical energy storage and chemical feedstock generation (such as the production of SynGas by CO_2 reduction[13]), while others can be used directly for the breakdown of chemical[14–17] or biological[18] contaminants in water.

A photocatalyst requires three fundamental properties: It must be light-absorbing, it must have the ability to interact chemically with potential substrates, and it must be able to provide the thermodynamic driving force for the desired reaction. As shown in Figure 1.1, the photocatalyst first absorbs an incident photon whose wavelength matches or exceeds the energy of the

gap between the occupied and unoccupied bands/orbitals of the system. For electronic excitations, this energy will be at least equal to the "fundamental" band gap (ΔE_{fund} in Figure 1.2). The photogenerated electron-hole pair will have a binding energy between them, also known as the exciton binding energy (E_{EB}), which represents the energy required to physically separate the two photogenerated charge carriers, and is necessary to overcome in order for charge transport and redox processes to be possible.[19] If photogenerated electrons and holes are left to bind together to form an exciton then the two can rapidly recombine. Depending on the electronic structure of the material, this will lead to one of two outcomes. If there is a significant energy gap between the valence and conduction bands, then a photon of energy equal to the "optical" band gap (ΔE_{opt}) is emitted, and the system will return to its ground electronic state. If there is no significant energy gap between the valence and conduction bands, then the system will return to its ground state and no photon is emitted. As exciting the ΔE_{fund} gap generates separated electron-hole pairs, and exciting the ΔE_{opt} gap does not, these two energy gaps must be differentiated between. "electron-hole recombination" (or more simply as "recombination"), where the electron-hole pair recombine, is the main source of inefficiency in any photocatalytic system, as no useful work is done in the process.

A single photocatalyst can theoretically catalyse both oxidation and reduction processes, assuming its VB/HOMO and CB/LUMO energies are suitably placed (such as those in Figure 1.1. Photoexcited electrons from the photocatalyst's conduction band can be transferred to the species to be reduced, while electrons can be transferred from the species to be oxidised to fill any photogenerated holes in the photocatalyst's valence band. For this to function, the energy of the photocatalyst's LUMO must be higher (closer to the

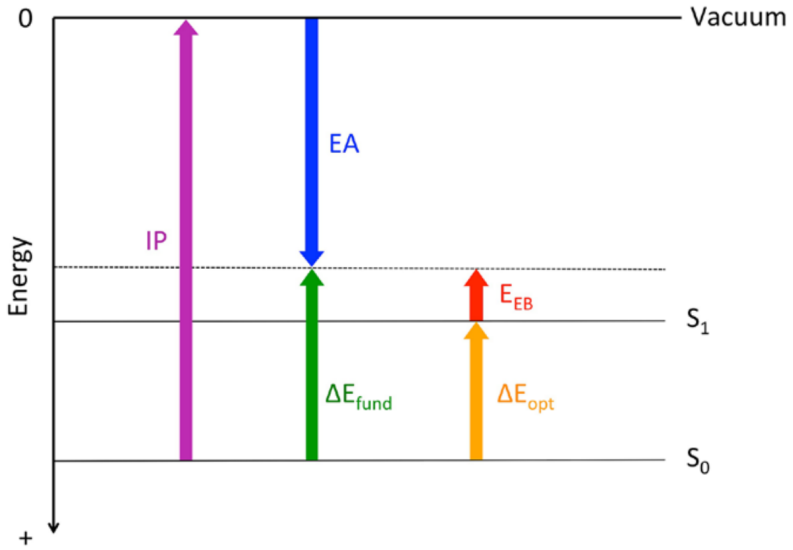

Figure 1.2: A schematic to outline the different energies associated with electronic excitations, originally from ref.[19] The energies represented are: ionisation potential (IP); electron affinity (EA); fundamental band gap (ΔE_{fund}); optical band gap (ΔE_{opt}); and exciton binding energy (E_{EB}). S_0 and S_1 refer to the lowest energy of the ground and excited states, respectively. Reproduced from doi:10.1088/0953-8984/28/7/074001, copyright IOP Publishing 2016. Reproduced under a Creative Commons (CC) license. All rights reserved

vacuum energy in Figure 1.2) than that of the targeted reduction species, and for the HOMO to be lower in energy (farther from the vacuum energy in Figure 1.2) than that of the targeted oxidation species.[20–22] Therefore, for any given photocatalytic process the ΔE_{fund} gap of the photocatalyst needs to be at least greater than the difference in potential difference between the reduction and oxidation processes. In the case of the water splitting reaction in Equation 1.2 this is 1.23 eV, for which a good number of photocatalysts fit this criterion.[11,12] It should be noted, though, that an energy difference between the valence/conduction band energy and that of the species to be oxidised/reduced is often needed in order to attain a reasonable rate of reaction (referred to as an "overpotential"). Effective photocatalysts for water splitting, for example, must have a ΔE_{opt} greater than 1.23 eV.[11,12]

While a single-component photocatalyst is the simplest photocatalytic sys-

tem, photocatalysts are found to be much more efficient for solar energy conversion when used in a pair, or "heterojunction", (or with a counter electrode) as this enables separation of the photoexcited electron from its corresponding hole more effectively. This helps to circumvent the recurring issue of electron-hole recombination, where the photogenerated charge carriers recombine and the system decays to the ground state with the emission of a photon equal in energy to ΔE_{opt}. Electron-hole recombination can be avoided by physically separating the charge carriers and thus not allowing them to recombine.

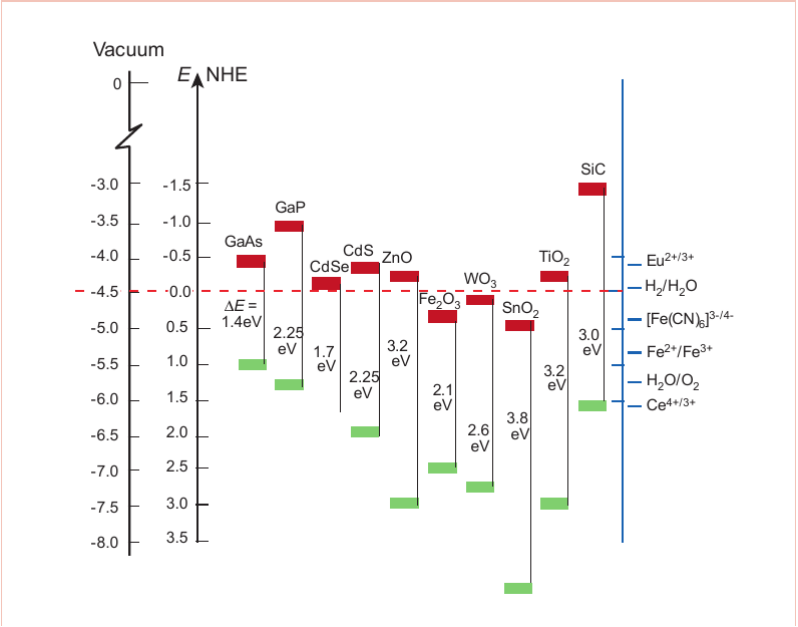

Figure 1.3: Bands gap energies and band positions for a selection of inorganic photocatalysts with the electrochemical potentials for hydrogen generation from water included. Reprinted with permission from Springer Nature Customer Service Center GmbH: [*Nature* M. Grätzel, *Photoelectrochemical Cells*, 2001, **414**, 338–344][11] Copyright 2001.

As with any branch of catalysis, the catalyst may either be hetero- or homogeneous. As this research focusses on heterogeneous systems, photocatalysis will be discussed in the context of heterogeneous photocatalysis. Numerous examples of heterogeneous photocatalysts exist in the wider literature, as shown in Figure 1.3. Transition metal oxides are a common choice for heteroge-

neous photocatalysts, typically those with wholly filled or unfilled d-electron states.[23] Titanium dioxide (TiO_2) is a highly popular choice amongst the transition metal oxides, whose properties will be discussed in chapter 3. Transition metal cations with a partially-filled d-subshell (such as Cr^{3+}, Ni^{2+}, Fe^{3+}, and Rh^{3+})[24–32] and some non-metals (such as nitrogen[33–36] and carbon[37–39]) can be used as impurity species, where they may act as interstitial dopants or substitute metal cations, to introduce impurity states into the electronic structure and thus improve light absorption. Noble metals (such as Pt[40], Rh[41], Au[42]) and some transition metal oxides (such as NiO[43] and RuO_2[44]) can be employed as co-catalysts which can function in two different ways. Noble metals can be used to catalyse either of the two redox reactions (such as platinum for H_2 evolution) while some metal oxides can be introduced to inhibit the likelihood of the reactants (e.g. water) to be reformed from the gaseous products.

1.3 Current Issues in Photocatalysis

There are three main aspects which may inhibit the photoactivity of a potential photocatalyst: electron-hole recombination; photon-absorption efficiency; and surface reactivity. Electron-hole recombination is a common problem encountered in the field of photovoltaics as well as photocatalysis. The process of recombination is where, once promoted to the CB, the high energy electron generated will re-combine with an available hole in the valence band and release its absorbed energy in the form of a photon — this can be thought of as the opposite of the light absorption process and will reduce the efficiency of the catalyst greatly as the energy of the excited state isn't being used for photocatalysis. The photon absorption process is reversible *via* recombination, provided the excited electron and hole are in physical proximity

to each other, and therefore methods aimed at impeding this process typically revolve around separating the electron and hole from each other in space by some means after photon absorption has occurred. One method typically employed in photovoltaics is to create a heterojunction. This is where two materials with different band positions are combined. The difference in the band energies causes the electrons to settle on the acceptor side of the junction while the holes settle on the donor side of the junction thus preventing them from recombining. One interesting application of this concept is found in the performance characteristics of mixed-phase TiO_2 (e.g. a system comprising rutile and anatase phases). One of the proposed explanations of the higher efficiency of this hybrid structure is that heterojunction is formed at the phase boundary.[45]

Photon absorption efficiency has been studied for longer than the recombination problem in photovoltaics and photocatalysis. As mentioned earlier (Principles of Photocatalysis), the minimum band gap required to catalyse water splitting is 1.23 eV. This energy requirement matches the visible part of the solar spectrum very well. However, many of potential photocatalysts (often those with other desirable properties) have band gaps which only allow absorption in the ultra-violet region instead (as seen from Figure 1.3). Although the efficiency in how the photoexcited electrons are used is a major topic research, band gap tuning to improve the absorption of photons overall is equally important where practical applications are involved. For instance, including dopants (as mentioned earlier) can introduce new electronic bands into the system that are higher in energy than the non-doped VB. This can result in a lower energy gap between the VB and CB and thus allow the photocatalyst to absorb photons which correspond to visible-spectrum energies. Alternatively, as will be discussed in detail later on (chapter 3), a second pho-

tocatalyst with an energy gap that allows it to absorb visible-region photons (e.g. CdS) may be physically combined with the wide energy gap photocatalyst (e.g. TiO_2). This will both physically separate the electron-hole pair and allow the "narrow-gap" semiconductor to provide photogenerated holes/electrons for the wider gap semiconductor using visible light.

It is the aim of this thesis to use computational methods to investigate the electronic properties of photocatalytic materials. As such, an in depth description of the theoretical methods used, both in this report and some related works, will be presented in the following chapter.

Chapter 2

Theoretical Models

2.1 Theoretical Background

2.1.1 The Schrödinger Equation

To describe the properties (such as position or momentum) of a particle in classical mechanics, the trajectory, in terms of direction of movement and velocity, is used to calculate these properties. For a sufficiently light particle, such as an electron, this trajectory has wave-like characteristics. This relationship between a particle's mass and its wave-like properties is expressed in the form of the de Broglie equation:

$$\lambda = \frac{h}{p} \tag{2.1}$$

where h is the Planck constant, p is the momentum, and λ is the resulting wavelength of the object. For an electron this wavelength is quite large and therefore its trajectory is described in the form of a wavefunction (Ψ). Instead of classical-mechanical calculations of motion, the calculation of the properties of an electron uses the Schrödinger equation, which relies on the particle's

wavefunction. For a one-dimensional system this is:

$$\begin{aligned} -\frac{\hbar^2}{2m}\frac{d^2\Psi}{dx^2} + \hat{V}(x)\Psi(x) =& E\Psi(x), \\ \hbar =& \frac{h}{2\pi}, \end{aligned} \tag{2.2}$$

where $\hat{V}$ is the potential energy operator for the particle, $\vec{x}$ is the positional vector for the one-dimensional system denoting the particle's position, and m is the mass of the particle. For a three-dimensional case this expands further:

$$\begin{aligned} -\frac{\hbar^2}{2m}\hat{\nabla}^2\Psi + \hat{V}(\vec{r})\Psi(\vec{r}) &= E\Psi(\vec{r}), \\ \frac{\partial^2}{\partial x} + \frac{\partial^2}{\partial y} + \frac{\partial^2}{\partial z} &= \hat{\nabla}^2, \end{aligned} \tag{2.3}$$

where $\hat{\nabla}^2$ is the (in this instance, Cartesian) vector differential operator, and $\vec{r}$ is the positional vector of the electron in the three-dimensional coordinate system. The equation has two separate terms: the kinetic energy operator (the first term in Equation 2.3), and the potential energy (the second term "$\hat{V}$" in Equation 2.3). This eigenvalue equation, where the wavefunction is the eigenfunction, can then be used to calculate the total energy of the electrons in the system. The equations are also more conveniently written in terms of the Hamiltonian operator ($\hat{H}$):

$$\begin{aligned} \hat{H}(\vec{r},\vec{R})\Psi(\vec{r},\vec{R}) &= E\Psi(\vec{r},\vec{R}), \\ \hat{H} &= -\frac{\hbar^2}{2m}\hat{\nabla}^2 + \hat{V}, \end{aligned} \tag{2.4}$$

where $\vec{R}$ is the position vector for the nuclei. This, as described thus far, is the time-independent Schrödinger equation; the time-dependent equation is instead formulated with respect to changes of the wavefunction and the

Hamiltonian in time:

$$\hat{H}(\vec{r},\vec{R},t)\Psi(\vec{r},\vec{R},t) = i\hbar\frac{\partial\Psi}{\partial t}. \tag{2.5}$$

The Hamiltonian operator includes the expressions for both kinetic and potential energies for the whole system, and the total energy arises from a sum of different interactions (in atomic units):

$$\begin{aligned}
\hat{H}(\vec{r},\vec{R})\Psi(\vec{r},\vec{R}) &= E\Psi(\vec{r},\vec{R}) \\
\hat{H} &= T_e + T_n + V_{nn} + V_{ne} + V_{ee} \\
T_n &= -\frac{\hbar^2}{2m}\hat{\nabla}^2 \\
T_e &= -\sum_i^{N_e}\frac{1}{2}\hat{\nabla}_i^2 \\
V_{nn} &= \sum_a^{N_n}\sum_{b>a}^{N_n}\frac{Z_a Z_b}{|R_a - R_b|} \\
V_{ne} &= -\sum_a^{N_n}\sum_i^{N_e}\frac{Z_a}{|R_a - r_i|} \\
V_{ee} &= \sum_i^{N_e}\sum_{j>i}^{N_e}\frac{1}{|r_i - r_j|},
\end{aligned} \tag{2.6}$$

where subscript e refers to electron, and n nuclear, components, nn refers to nuclear-nuclear interactions, en to electron-nuclear interactions, and ee for electron-electron interactions. a and b refer to different nuclei, i and j refer to different electrons, $\vec{R}$ is the position vector of the nucleus, and $\vec{r}$ is the position vector of the electron. This calculation can be simplified, as the nuclei can be assumed to be stationary with respect to the electrons. This "clamped nuclei approximation" is a direct result of the Born-Oppenheimer approximation: the electron mass is insignificant relative to that of the nucleus, thus the kinetic energy ($-\frac{\hbar^2}{2m}\hat{\nabla}^2$) of the electron is much greater than that of the nucleus, and so

any motion of the nuclei will be negligible on the timescale of electron motion. This effectively removes nuclear motion from the calculation, as nuclear motion is now treated as being zero, and leaves only the electron-containing terms to calculate.

2.1.2 Multiple-Electron Systems

While the Schrödinger equation can be used to calculate the properties of a system containing a single electron, a system with multiple electrons quickly becomes impossible to solve analytically due to the rapidly increasing complexity of electron-electron interactions. This is an example of a many-body problem, and therefore requires various approximations to be made in order to keep the calculation solvable for a system with a relatively large number of electrons. The approximations used in this work are based on independent-electron models of the multi-electron system, thus they will be discussed in this context. The major approximation of any independent-electron model is that the electrons do not interact explicitly with each other electron, but instead in an averaged fashion using a single coulombic interaction to represent the other electrons — referred to as the "mean field" approximation to electron-electron interaction. The behaviour of these independent electrons is then described by use of the orbital approximation.

The Orbital Approximation

The solution to the wavefunction of a single-electron system yield a set of electronic "orbitals" (also referred to as the "hydrogenic orbitals"). In the single-electron approximation, these orbitals are used as the basis for the wavefunction of the system. Whereas a true multi-electron wavefunction would depend on the coordinates ($\vec{r}$) of all n electrons within the system, the single-

electron approximation to this depends instead on the wavefunctions of each individual electron's orbitals:

$$\Psi(\vec{r}_1, \vec{r}_2, \vec{r}_3, ..., \vec{r}_n) = \Psi_1(\vec{r}_1)\Psi_2(\vec{r}_2)...\Psi_n(\vec{r}_n), \tag{2.7}$$

These orbitals are represented in calculations using a set of mathematical basis functions (collectively referred to as a basis set), that define the spatial proportions of the orbitals themselves. Each atom will therefore be defined by a set of atomic orbitals (AOs) described by the set of basis functions used. For the interactions between different atoms, the concept of linear combination of atomic orbitals (LCAO) is used. In this, the atomic orbitals are combined spatially to produce a set of molecular orbitals (MOs). The MOs (ϕ) of a system of n electrons can therefore be defined by a set of m AOs, represented as basis functions (χ):

$$\phi_i = \sum_{n=1}^{m} c_{ni}\chi_n, \tag{2.8}$$

where c_n are the molecular orbital coefficients.

Basis Sets

Basis Sets should correctly represent the known properties of atomic orbitals. Two important characteristics are tending to zero at sufficient distance from the nucleus and having a cusp (or singularity) at the nucleus (where $\vec{r} = 0$), as this represents the fact that electrons do not physically penetrate the core of the nucleus itself. Two varieties of basis functions are typically used: Slater-type orbitals (STOs) and Gaussian-type orbitals (GTOs). While STOs provide the best description of an AO's properties, they are much more computationally demanding to integrate than GTOs. Gaussian functions, though they do not individually describe an orbitals properties, are far easier to inte-

grate (as products of integrals of two Gaussian functions are Gaussian themselves) and so combinations of Gaussian functions can be used to represent AOs. Both STOs and GTOs can be represented on a spherical coordinate system, but GTOs are often represented on a Cartesian coordinate system in practice:

$$\begin{aligned}\chi_{\zeta,n,l,m}(r,\theta,\varphi) =& NY_{l,m}(\theta,\varphi)r^{n-1}e^{-\zeta r}\\ \chi_{\zeta,n,l,m}(r,\theta,\varphi) =& NY_{l,m}(\theta,\varphi)r^{2n-2-l}e^{-\zeta r^2}\\ \chi_{\zeta,n,l,m}(x,y,z) =& Nx^{l_x}y^{l_y}z^{l_z}e^{-\zeta r^2},\end{aligned} \tag{2.9}$$

where n, l (l_x, l_y, and l_z on the Cartesian system), and m are the principal, angular momentum, and magnetic quantum numbers respectively, $Y_{l,m}$ represents the spherical harmonic functions, N is the normalisation constant, ζ is the exponent of the given function. While Gaussian-type orbitals (GTOs) decay too rapidly away from the nucleus, and give a derivative of zero near the nucleus, it is generally the case that multiple GTOs can be combined in a linear fashion to model the behaviour of a single Slater-type orbital (STO). A basis set which contains only enough functions to represent the number of electronic orbitals in the system is referred to as "minimal". A single s-orbital function would be acceptable for a single s-electron. For the more directional orbitals (e.g. p and d orbitals) the bonding anisotropy of most heteroatomic species means that representing such states with copies of the same-type orbitals which contain different exponents allows the system to better represent different bonding strengths at the same atomic centers, as well as the electron density distribution in bonds.

Simply representing each orbital with two basis functions, and thus double the number of basis functions, creates a "double-zeta" basis set (due to the two different values of ζ on each pair of functions). Further sizes (e.g. triple-zeta, quadruple-zeta) also exist, however the gains in calculation accuracy

often increase less rapidly with the increase in basis set size. Furthermore, as important chemical changes usually only affect the valence orbitals of a system, many basis sets only increase the number of valence basis functions to save on computational cost. A further cost saving is also achievable by contracting the basis set size for a calculation, where the number of basis functions to be used is reduced for certain orbitals by summing subset of basis functions together into a smaller set of functions. This is typically done for only the core region (e.g. the 1s orbital of a carbon atom) as the core electrons have little effect on the chemistry of the molecule.

This will lead to an increase in total energy, as the contracted set of functions will be less effective at describing these electrons. The degree of contraction therefore becomes a trade between overall accuracy and computational cost, but this is typically less noticeable than changing the number of valence basis functions. To better represent the interactions of species where angular momentum differs between the orbitals on each species (e.g. the hydrogen-carbon bond), additional "polarisation" functions can be included. Such functions will introduce a charge polarisation of the valence orbitals by including basis functions for orbitals of higher angular momentum in addition to those filled by the electrons in the current system. For example an added p-orbital can introduce polarisation in the hydrogen s-orbital, which is found to improve the description of bonding where hydrogen interacts with a p-block element. Finally, 'diffuse' functions (with very small exponents) can be included to model the behaviour of loosely bound electrons (such as in the case of anionic species). A commonly used notation for GTO basis sets, devised by Pople *et al*,[46] uses the general form *a-bcdG*, where a is the number of Gaussian functions used to represent core orbitals, and b, c, and d are the number of Gaussian functions used to represent valence orbitals. The values of b, c, and d indicate

the number of functions with particular values of ζ: a basis set with only b is "single-zeta", one with b and c are "double-zeta", and those with b, c, and d are "triple-zeta". Additional signs, such as either d and p (or * and **) can be placed after the G to indicate the presence of polarisation and diffuse functions respectively. For example, 6-311G** would indicate a triple-zeta basis set with 6 Gaussians representing core orbitals, separate sets of 3, 1, and 1 Gaussians with separate values of ζ representing valence electrons, and that the basis set contains diffuse and polarisation functions.

A further approach to improve computational efficiency can be taken, where, instead of describing the core electrons of a species explicitly using basis functions, a pseudopotential (PP, or effective core potential, ECP) can be used as a substitute. In this case the specified core electrons are removed from the system entirely, and a potential is put in to simulate the electrostatic potential of these core electrons. This will give very small computational time improvements to lighter atoms, but will be much more prominent for heavier elements. In addition, the method of construction allows for the inclusion of relativistic corrections, which is important in describing the behaviour of heavy transition elements correctly (such as Au, Pt, etc).[47] A well-constructed ECP can often achieve similar accuracies as an all-electron basis set, but with a much smaller computational cost to the user. While larger basis sets are preferred to achieve a reliably high level of accuracy, the computational cost increases with the size of the basis set used.

Basis Set Superposition Error

As Gaussian-type basis sets are nucleus-centered, it is possible that basis functions centered around one nucleus may end up being used to expand the electronic wavefunction of a neighbouring atom whose basis set does not ad-

equately describe the electrons centered around it. The error in energy from this is referred to as the basis set superposition error (BSSE).[48,49] This becomes smaller as the basis set is increased in size, as a larger set of basis functions will more accurately describe the electronic structure of the atom. Thus basis functions from a neighbouring atom will have less of an impact on the calculated electronic structure. The magnitude of the error means that typically this presents an issue for calculating the energy of interaction where weak forces dominate, such as hydrogen bonding interactions. Correcting this energy requires firstly optimising the geometry of the entire combined system, then determining the energies of the two or more separate physical components of the system in the positions they adopt in the combined system. Then the energies of these components are calculated again by additionally including the basis sets, but not the nuclei and electrons themselves, of the other components present (referred to as 'ghost functions' or 'ghost atoms'). The inital, uncorrected energy of interaction is determined by calculating the difference between the total optimised energies of the total and the components in the system and the total combined system:

$$E_{int} = E_{tot} - E_A - E_B. \tag{2.10}$$

The correction to this energy, known as the Counterpoise (CP) correction,[49] is determined by calculating the difference in energy between each component in the presence of the ghost species and the isolated components separately, using the geometries adopted in the combined system for each:

$$E_{cp} = (E_{AB^*} - E_A) + (E_{A^*B} - E_B), \tag{2.11}$$

where * represents a ghost species. This, when used to correct the total energy, cancels out the BSSE contribution and thus reduces the total interaction energy:

$$E_{int} = E_{tot} - E_A - E_B - E_{cp}, \tag{2.12}$$

The Pauli Principle

Observations of atomic spectra, as well as patterns in the first ionisation potentials (IPs), for all elements shows show that there is no simple change in electronic structure as electrons in a system increase in quantum number.[50] Particularly the IPs increase across groups in the periodic table, decrease slightly between different groups, and more greatly decrease between periods. This phenomenon is explained through the Pauli principle, which states that, for fermion particles (particles with half-spin, such as electrons), the sign of the total wavefunction must change upon the exchange of two identical fermions. While the n, l, and m quantum numbers define which orbital the electron occupies, the spin quantum number (s) is intrinsic to the electron itself and is not dependent on the orbital which it occupies. The only way that the total wavefunction can change sign therefore is for there to be a difference in spin quantum number; in the context of electronic structure, this leads to the Pauli Exclusion principle: two electrons cannot occupy the same orbital with the same quantum numbers, and thus must have opposing spin quantum numbers (one $+\frac{1}{2}$ and the other $-\frac{1}{2}$). If this were not the case, then orbitals would be fully occupied sooner because the electrons could not "pair together". IPs would therefore decrease rapidly as electrons are forced into orbitals more distant from the nucleus.

To follow the Pauli principle completely, both the wavefunction of each two-electron orbital and the total wavefunction must change sign when two

electrons exchange. Two electrons could have four different arrangements of spin:

$$\alpha(1)\alpha(2), \quad \alpha(1)\beta(2), \quad \beta(1)\alpha(2), \quad \beta(1)\beta(2), \tag{2.13}$$

where α and β are two different spin states (conventionally, α is "spin-up" and β is "spin-down") for electrons 1 and 2. The first and fourth arrangements do not satisfy the Pauli principle, so only the second and third arrangements are allowed. As electrons are indistinguishable, but have different spin states, the second and third arrangements are typically expressed as linear combinations:

$$\begin{aligned} \sigma_+(1,2) &= (1/2^{0.5})[\alpha(1)\beta(2) + \beta(1)\alpha(2)] \\ \sigma_-(1,2) &= (1/2^{0.5})[\alpha(1)\beta(2) - \beta(1)\alpha(2)], \end{aligned} \tag{2.14}$$

where $1/2^{0.5}$ is a normalisation factor. As the product $\sigma_+(1,2) = \sigma_+(2,1)$, this also does not satisfy the Pauli principle and cannot be used. The other product $\sigma_-(1,2)$ *does* change sign upon exchanging the electrons, and so is allowed. The total wavefunction ($\Psi(1,2)$) is the product of $\sigma_-(1,2)$ and the orbitals of each electron ($\phi(1)$ and $\phi(2)$), which can be expressed as a determinant:

$$\begin{aligned} \Psi(1,2) =& \sigma_-(1,2)\phi(1)\phi(2) = 1/2^{0.5}[\phi(1)\alpha(1)\phi(2)\beta(2) - \phi(2)\alpha(2)\phi(1)\beta(1)] \\ =& \begin{vmatrix} \phi(1)\alpha(1) & \phi(1)\beta(1) \\ \phi(2)\alpha(2) & \phi(2)\beta(2) \end{vmatrix}. \end{aligned} \tag{2.15}$$

An important property of determinants, such as $\Psi(1,2)$, is that interchanging any two rows/columns only changes the sign of the result, so this formulation obeys the exclusion principle. In the general case of N electrons and n orbitals, the total wavefunction is conventionally represented by a "Slater Determinant"

(Ψ_{SD}):

$$\Psi_{SD}(1,2,3,...,N) = \frac{1}{\sqrt{N!}} \begin{vmatrix} \phi_1(1)\alpha(1) & \phi_1(2)\alpha(2) & \cdots & \phi_1(N)\alpha(N) \\ \phi_1(1)\beta(1) & \phi_1(2)\beta(2) & \cdots & \phi_1(N)\beta(N) \\ \phi_2(1)\alpha(1) & \phi_2(2)\alpha(2) & \cdots & \phi_2(N)\alpha(N) \\ \phi_2(1)\beta(1) & \phi_2(2)\beta(2) & \cdots & \phi_2(N)\beta(N) \\ \vdots & \vdots & \ddots & \vdots \\ \phi_n(1)\beta(1) & \phi_n(2)\beta(2) & \cdots & \phi_n(N)\beta(N) \end{vmatrix} \quad (2.16)$$

The Aufbau Principle and Hund's Rule

A further consideration for the analysis of electronic structure is the exact way in which it is built when the electrons are added to the system. The previously-mentioned observations of electronic structure lead to the conclusion that, as the electron count increases, electrons are added to the lowest-energy orbital first (without disobeying the Pauli principle). This "building-up" (or Aufbau) principle also combines with another observation: for any electron configuration, electrons will occupy empty orbitals before "pairing-up" with an electron already occupying an orbital (providing that this does not break the Aufbau principle). This is known as Hund's rule of maximum multiplicity, which more generally states that electron configurations are most energetically stable with a maximum possible number of unpaired electrons. For instance, there are 3 energy-degenerate p-orbitals for each principal quantum number; the first 3 electrons will occupy the 3 orbitals separately first, and the last 3 electrons will then occupy the three orbitals in the opposite spin state to those already occupying them.

2.1.3 Hartree-Fock Theory

The approximations and principles presented so far can be generally applied to a number of different quantum-mechanical models. One of the simplest independent-electron wavefunction-based method used for the calculation of many-electron systems is the Hartree-Fock (HF) method. The separation of the different terms of the Hamiltonian operator (as mentioned briefly in Equation 2.6) is formalised in HF theory (in atomic units) as:

$$\begin{aligned}
\hat{H} =& T_e + V_{nn} + V_{ne} + V_{ee} \\
T_e =& -\sum_{i}^{N_e} \frac{1}{2}\hat{\nabla}^2 \\
V_{nn} =& \sum_{a}^{N_n}\sum_{b>a}^{N_n} \frac{Z_a Z_b}{\vec{R}_a - \vec{R}_b|} \\
V_{ne} =& -\sum_{a}^{N_n}\sum_{i}^{N_e} \frac{Z_a}{|\vec{R}_a - \vec{r}_i|} \\
V_{ee} =& \sum_{i}^{N_e}\sum_{j>i}^{N_e} \frac{1}{|\vec{r}_i - \vec{r}_j|},
\end{aligned} \tag{2.17}$$

where a and b refer to different nuclei, i and j refer to different electrons, $\vec{R}$ is the position vector of the nucleus, and $\vec{r}$ is the position vector of the electron. As exact solutions to the Schrödinger equation are not possible for multi-electronic wavefunctions, an approximate wavefunction needs to be used instead. The terms T_e and V_{ne} depend only on one electron coordinates, while V_{ee} depends on two electron coordinates, thus in HF theory these terms are

grouped to give the one ($\hat{h}_i$) and two ($\hat{g}_{ij}$) electron operators respectively:

$$\begin{aligned}
\hat{H} =& \hat{H}_e \\
\hat{H}_e =& T_e + V_{nn} + V_{ne} + V_{ee} \\
\hat{H}_e =& \sum_i^N \hat{h}_i + \sum_{j>i}^N \hat{g}_{ij} + V_{nn} \\
\hat{h}_i =& -\frac{1}{2}\hat{\nabla}^2 - \sum_a^N \frac{Z_a}{|\vec{R}_a - \vec{r}_i|} \\
\hat{g}_{ij} =& \frac{1}{|\vec{r}_i - \vec{r}_j|},
\end{aligned} \tag{2.18}$$

where N is the number of electrons. By substituting the Slater determinant in the Schrödinger equation, it can be derived that the two electron operator $\hat{g}_{ij}$ gives rise to the coulomb (J) and exchange (K) integrals:

$$\begin{aligned}
J_i(1) =& \langle \phi_i(1)\phi_j(2)|\hat{g}_{12}|\phi_i(1)\phi_j(2)\rangle \\
=& \int\int \phi_i^*(1)\phi_j^*(2)\hat{g}_{12}\phi_i(1)\phi_j(2)d\vec{r}_1 d\vec{r}_2 \\
K_i(1) =& \langle \phi_i(1)\phi_j(2)|\hat{g}_{12}|\phi_j(1)\phi_i(2)\rangle \\
=& \int \phi_i^*(1)\phi_j^*(2)\hat{g}_{12}\phi_j(1)\phi_i(2)d\vec{r}
\end{aligned} \tag{2.19}$$

using the commonly-employed "bra-ket" notation. The Coulomb term describes the interactions between the formal charges on each electron with each other electron; the exchange interaction does not have a simple classical definition, but is a result of the wavefunction of two indistinguishable particles changing sign upon the exchange of the two particles. The total energy of an N-electron system is the sum of the one and two electron terms, and the nuclear interaction energy:

$$E = \sum_{i=1}^N \hat{h}_i + \frac{1}{2}\sum_{i=1}^N \sum_{j>i}^N (J_{ij} - K_{ij}) + V_{nn}, \tag{2.20}$$

where the factor of 1/2 prevents the double-counting of electrons. The form of the second term ensures the sign change due to the exchange of terms in K relative to J, and conveniently cancels the so-called "self-interaction" error (where the sum of J would include interactions of electron i with electron i). Conventionally, the two integrals are written in terms of the coulomb and exchange *operators* ($\hat{J}_i$ and $\hat{K}_i$, respectively):

$$\begin{aligned} E =& \sum_{i=1}^{N} \langle \phi_i | \hat{h}_i | \phi_i \rangle + \frac{1}{2} \sum_{i=1}^{N} \sum_{j>i}^{N} (\langle \phi_j | \hat{J}_i | \phi_j \rangle - \langle \phi_j | \hat{K}_i | \phi_j \rangle) + V_{nn} \\ \hat{J}_i | \phi_j(2) \rangle =& \langle \phi_i(1) | \hat{g}_{ij} | \phi_i(1) \rangle | \phi_j(2) \rangle \\ \hat{K}_i | \phi_j(2) \rangle =& \langle \phi_i(1) | \hat{g}_{ij} | \phi_j(1) \rangle | \phi_i(2) \rangle. \end{aligned} \tag{2.21}$$

This gives a way to calculate the total energy of the system (for a given geometry of atoms); to calculate the *minimum* energy of a system with a given set of atomic positions (and thus its electronic ground state), an optimisation of the total energy with respect to the orbitals must be done subject to the constraint that the orbitals remain orthogonal and normalised ($\langle \phi_i | \phi_j \rangle = 0$ and $\langle \phi_i | \phi_i \rangle = 1$). According to the variational principle, any approximation to the "true" wavefunction of a system will yield a total energy which is either equal to or greater than that of the true wavefunction. Thus, constrained optimisation proceeds through the use of Lagrange multipliers (λ), where the variation in total energy is expressed as part of a Lagrange function (L):

$$\begin{aligned} \delta L =& \delta E - \sum_{ij}^{N} \lambda_{ij} (\langle \delta \phi_i | \phi_j \rangle - \langle \phi_i | \delta \phi_j \rangle = 0 \\ \delta E =& \sum_{i}^{N} (\langle \delta \phi_i | \hat{F}_i | \phi_i \rangle + \langle \phi_i | \hat{F}_i | \delta \phi_i \rangle) \\ \hat{F}_i =& \hat{h}_i + \sum_{j}^{N} (\hat{J}_j - \hat{K}_j), \end{aligned} \tag{2.22}$$

where $\hat{F}_i$ is known as the Fock operator and is a commonly-used shorthand. The final Hartree-Fock equations are commonly written in shorthand from Equation 2.22 as:

$$\hat{F}_i\phi_i = \sum_j^N \lambda_{ij}\phi_j. \tag{2.23}$$

The eigenvalues in Equation 2.23 depend on the calculation of $\hat{J}$ and $\hat{K}$ (equation 2.21), which themselves depend on the wavefunctions (the MO coefficients in this case) of all of the orbitals in the system. Solutions to this eigenvalue problem are found through the use of iterative numerical methods, known collectively as the self-consistent field (SCF) method.

Overall, Hartree-Fock theory yields surprisingly accurate predictions for a range of different model systems, given the assumptions used, regarding their physical and electronic properties. The major shortcoming is the assumption that electrons only interact with one another in the form of an averaged potential. By ignoring the dynamic interaction between electrons, such properties which depend on them (such as electronic transitions and electron dispersion interactions) cannot be calculated from this method alone — instead, methods such as time-dependent HF (TDHF) must be used. In addition, the absolute energy values of states within the systems will clearly not be calculated accurately. Compared to experimental data, errors will occur in the calculation of chemical properties from HF theory for most systems. However, these errors are relatively small and systematic. Thus, while exact values (e.g. for bond and MO energies) will differ from experiment, some qualitative results and trends can still be accurately predicted using HF theory.

2.1.4 The SCF Procedure

The objective of HF theory is to calculate the total energy of a system from its wavefunction. Calculating the minimum total energy of the system requires a solution to the coulomb and exchange terms in equation 2.22, which both require the MO coefficients corresponding to this minimum energy. However, in order to determine the correct MO coefficients, the correct wavefunction must also be known. A numerical solution to this problem proceeds by firstly generating the matrix of one- and two-electron integrals (equation 2.21) from an initial guess, based on the structure and chemical composition of the system. This is used to form the matrix for the Fock operator (referred to as the Fock matrix) for the calculation, which is diagonalised to derive a sufficiently correct set of MO coefficients (and thus wavefunction) for the system. These new coefficients are then used in a new calculation of the updated Fock matrix to produce another new set of coefficients. This iterative method, referred to as the Self-Consistent Field (SCF) method, continues until the system is essentially unchanged by a new iteration, based on a set criterion (or criteria) such as a change in total energy or change in MO coefficients (i.e. such that the Lagrange function in equation 2.22 is satisfied). While the SCF method will gradually converge to a minimum total energy, the process can be sped-up considerably by the use of certain convergence tools. This includes using various energy gradient minimisation algorithms, such as the direct inversion in the iterative subspace (DIIS)[51] and conjugate gradients (CG) methods.

2.1.5 Density Functional Theory

Following from the HF method, numerous "post-HF" methods (such as coupled-cluster and MP2) have been developed to improve the accuracy of the

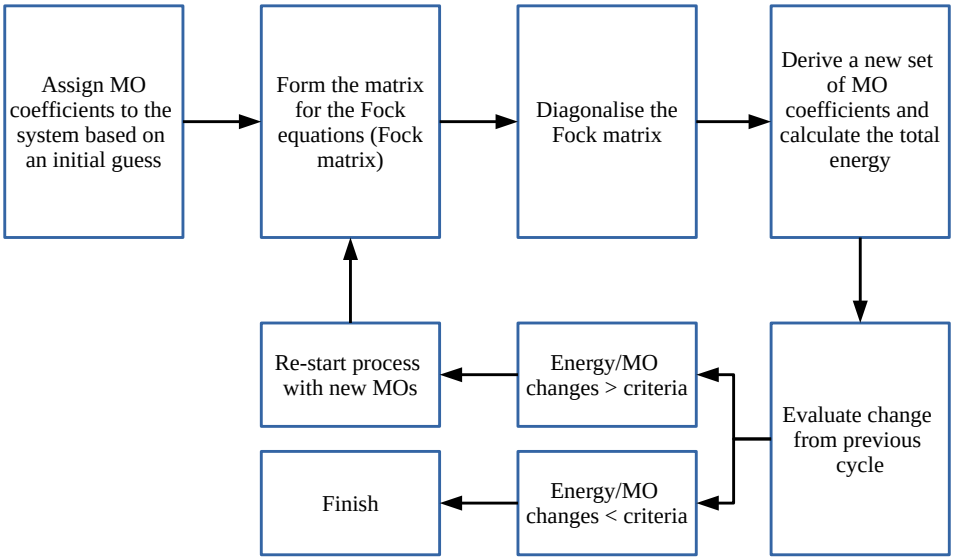

Figure 2.1: Diagram showing the workflow of a typical SCF optimisation procedure

simulation model, often by advancing on the approximations used in HF theory. At the same time as these purely wavefunction-based post-HF methods were being developed and used, an alternative methodology was developed by Walter Kohn and Pierre Hohenberg[52] based on the electron density rather than the wavefunction itself. These Hohenberg-Kohn (H-K) theorems demonstrate two points. Firstly, that the ground-state electronic properties of a multi-electron system are uniquely determined by the ground state electron density. Secondly, that there exists an energy functional (or function of a function) for the system and that the correct ground state minimises this energy functional. The use of "functional" here refers to the fact that the electron density and energy are both functions which depend on variables, and the function which acts upon these functions in order to connect the two is a functional of electron density. Functions are conventionally represented with round brackets

($f(x)$) while functionals are represented with square braces ($f[x]$). Although the existence of this relationship between energy and electron density can be demonstrated, the form of the functional which relates the two functions is not known. This density functional-based method is typically referred to as Density Functional Theory (DFT). The further development of DFT by Kohn and Lu Jeu Sham,[53] known as Kohn-Sham DFT (KS DFT), formalised it such that it may be practically applied to any generic system, as outlined below.

The Hamiltonian in DFT is separated into three separate operators: kinetic energy ($\hat{T}$), external potential ($\hat{V}$), and electron-electron interaction energy ($\hat{U}$):

$$\begin{aligned}
\hat{H}\Psi =& E\Psi \\
\hat{H}\Psi =& \left[\hat{T} + \hat{V} + \hat{U}\right]\Psi \\
\hat{T} =& -\sum_{i}^{n} \frac{\hbar^2}{2m_i}\vec{\nabla}^2 \\
\hat{V} =& -\sum_{i}^{n} \frac{Z_a}{|\vec{r_i} - \vec{R}_a|} \\
\hat{U} =& \frac{1}{2}\sum_{i<j}^{n} \frac{1}{|\vec{r_i} - \vec{r_j}|},
\end{aligned} \tag{2.24}$$

where i and j are different electrons, a refers to specific nuclei, $\vec{r}$ is the position vector of the electron, and $\vec{R}$ is the position vector of the nucleus. The electron density ($\rho(\vec{r})$) is given by:

$$\rho(r) = \sum_{i=1}^{n} |\Psi_i(\vec{r})|^2 \tag{2.25}$$

which is also often referred to as the electron probablity density. As each operator represents a function of the electron density (which is itself a function of the wavefunction), they can be written in shorthand as a functional of the density (e.g. $\hat{V}(\rho) = V[\rho]$). The "external potential" in $\hat{V}$ refers to the energy

of interaction of the electrons with the nuclei, and is thus given by the classical Coulombic term. In the same way as HF theory, the total energy of a system is calculated in KS DFT using an independent-electron approximation to the many-electron system. In the case of DFT, this also extends to the calculation of kinetic energy, which is calculated under the assumption of non-interacting electrons. The total energy of an n-electron system is typically defined as:

$$E_{DFT}[\rho] = T_S[\rho] + V[\rho] + J[\rho] + E_{xc}[\rho] \tag{2.26}$$

where $T_S[\rho]$ is the kinetic energy calculated from a single Slater determinant (and thus using the independent-electron approximation), $J[\rho]$ is the electron-electron repulsion term, and E_{xc} is the exchange-correlation energy. E_{xc} essentially exists as a correction to the rest of the equation, and contains the difference between the approximated terms and their true values:

$$E_{xc}[\rho] = (T[\rho] - T_S[\rho]) + (E_{ee}[\rho] - J[\rho]) \tag{2.27}$$

where E_{ee} is the correct electron-electron interaction energy. One of the challenges in DFT therefore is to find a good approximation to $E_{xc}[\rho]$. There are a number of theoretical criteria which an accurate functional should meet, such as correcting for the self-interaction error. However, it may also be desirable for the chosen functional to match known experimental data in order to reliably study a given system. Such a difference in approach is reflected in the wide range of different functionals that have been developed.

Local Density Approximation (LDA) (LDA) The simplest form of DFT functional is the local density approximation (LDA). In this form, the exchange-correlation energy is dependent only on the electron density at any given point:

$$E_{xc}^{LDA}[\rho] = \int \rho(\vec{r})\varepsilon_{xc}(\rho)d\vec{r}, \tag{2.28}$$

where ε_{xc} is the exchange-corellation energy per electron, and the exchange energy (E_x^{LDA}) is based on a simple analytic form for the homogeneous electron gas(HEG) model (an orbital-free form of DFT itself):

$$\begin{aligned} E_X^{LDA}[\rho] =& - C_X \int \rho^{\frac{4}{3}}(\vec{r})d\vec{r} \\ \varepsilon_X^{LDA} =& - C_X\rho^{\frac{1}{3}} \\ C_X =& \frac{3}{4}(\frac{3}{\pi})^{\frac{1}{3}}. \end{aligned} \tag{2.29}$$

This expression can be used on any system, even if it does not have a homogeneous electron density, as the calculation is done at numerous spatial points. This takes the assumption, however, that the electron density does not vary greatly over small distances in the system. For this form, the overall electron spin is presumed to be zero. If this is not the case then the Local Spin Density Approximation (LSDA) is used instead.

$$\begin{aligned} E_X^{LSDA}[\rho] =& - 2^{\frac{1}{3}}C_X \int (\rho_\alpha^{\frac{4}{3}} + \rho_\beta^{\frac{4}{3}})d\vec{r} \\ \varepsilon_{LSDA} =& - C_X f_1(\zeta)\rho^{\frac{1}{3}} \\ f_1(\zeta) =& \frac{1}{2}[(1+\varsigma)^{\frac{4}{3}} + (1-\varsigma)^{\frac{4}{3}}], \end{aligned} \tag{2.30}$$

where $f(\zeta)$ is the spin-polarisation function of parameter ς. L(S)DA is useful for the accurate description of periodic systems, especially metallic systems where electron density is roughly uniform in distribution. The accuracy of most results obtained is improved over HF theory, however bond strengths are overestimated relative to experimental observations and thus simulated systems will be more strongly bound than in reality.[54]

Generalised Gradient Approximation (GGA) An improvement over the LDA is to include the first derivative (gradient) of the density in calculations. Unlike the LDA, there are a number of different forms of this type of functional. For instance the Becke (B or B88) functional[55] works as a correction for the exchange energy to LSDA.

$$\begin{aligned} \varepsilon_X^{B88} =& \varepsilon_X^{LDA} + \delta\varepsilon_X^{B88} \\ \delta\varepsilon =& -\beta\rho^{\frac{1}{3}} \frac{x^2}{1 + 6\beta x \sinh^{-1} x} \\ x =& \frac{|\nabla\rho|}{\rho^{\frac{4}{3}}}, \end{aligned} \tag{2.31}$$

where β and x are parameters derived from fitting to experimental data from the rare gas species. This functional is also combined with the Lee-Yang-Parr (LYP)[56] correlation functional to create a new functional (entitled BLYP). In addition to these examples of functionals fitted to some experimental data, there are also non-empirical functionals such as that by Perdew, Burke, and Ernzerhof (PBE)[57]. This functional is, again, denoted as an enhancement to LSDA:

$$\begin{aligned} \varepsilon_X^{PBE} =& \varepsilon_X^{LDA} F(x) \\ F(x) =& 1 + a - \frac{a}{1 + bx^2}. \end{aligned} \tag{2.32}$$

Correlation is also, similarly, an enhancement to LSDA:

$$\varepsilon_C^{PBE} = \varepsilon_C^{LDA} + H(t), \tag{2.33}$$

where $H(t)$ itself contains parameters a, and b in addition to a number of others, and is included to ensure that the correlation energy conforms to the expected theoretical behaviour of the "exact" density functional.[47,57,58] The performance of GGA functionals in general is in good agreement with exper-

imental data for molecule/crystal geometries, however many electronic properties of systems of interest (such as electron transfer between species and electronic band gaps) are poorly described by the GGA alone.[54,58?]

Hybrid HF/DFT Functionals One of the issues with GGA methods for electronic structure is that the DFT exchange-correlation potential does not correct for the unphysical self-interaction error.[54,58?] Solving this problem requires calculating the exchange potential, such that the self-interaction error is cancelled out of the correlation potential. While HF handles this easily, Kohn-Sham DFT alone does not contain any self-interaction cancellation. Methods combining the two run into issues regarding the differences in the definition of exchange and correlation between HF and DFT, as the HF $E_{elec-elec}$ term operates at both long and short ranges, while the DFT E_X and E_C terms (due to its dependence on density) interact at only short range.

In order to include HF exchange in a DFT calculation, the Adiabatic Connection Formula (ACF) is used:

$$E_{XC} = \int_0^1 \langle \Psi_\lambda | V_{XC}^{Hole}(\lambda) | \Psi_\lambda \rangle d\lambda. \tag{2.34}$$

Here, λ indicates the degree of interaction in the system, from 0 (no interaction) to 1 (full interaction). The V_{XC}^{Hole} term refers to the exchange-correlation energy arising from the reduced probability of an electron being near the chosen reference electron (also known as the exchange-correlation "hole"). Assuming that the V_{XC}^{Hole} is linear in response to λ, gives the approximate relationship:

$$E_{XC} = \frac{1}{2}(\langle \Psi_0 | V_{XC}^{Hole}(0) | \Psi_0 \rangle + \langle \Psi_1 | V_{XC}^{Hole}(1) | \Psi_1 \rangle). \tag{2.35}$$

While the second term in Equation 2.35 is not known, for the $\lambda = 0$ case

different electrons do not interact and thus only the exchange energy is present, which can be calculated exactly. A simple implementation is the use of LSDA in place of the correlation term, giving what is known as the Half and Half (H+H) method:

$$E_{XC}^{H+H} = \frac{1}{2}E_X^{exact} + \frac{1}{2}(E_X^{LSDA} + E_C^{LSDA}). \tag{2.36}$$

Here, E_X^{exact} is the exact exchange calculated from the first term in Equation 2.35. Taking this further with GGA functionals yields what are commonly referred to as 'Hybrid' HF/DFT functionals, which contain a combination of 'exact' exchange, some LSDA exchange and correlation, and a gradient corrected terms. The popular Becke 3-parameter/Lee-Yang-Parr (B3LYP)[59] functional takes the form:

$$E_{XC}^{B3LYP} = (1-a)E_X^{LSDA} + aE_X^{exact} + b\Delta E_X^{B88} + (1-c)E_C^{LSDA} + cE_C^{LYP}, \tag{2.37}$$

where the parameters a, b, and c are derived to fit the functional to known experimental results.[59] Another treatment has been applied to the PBE functional to create the PBE0 hybrid functional[60]:

$$E_{XC}^{PBE0} = aE_X^{HF} + (1-a)E_X^{PBE} + E_C^{PBE}, \tag{2.38}$$

where the parameter a sets the fraction of HF exchange to include in the calculation. The fraction of exact exchange to include can differ between functionals, but generally ranges between 10–33%.[47] Varying the amount of exact exchange used directly affects the accuracy of calculated electronic properties *differently*,[47] and as such the chosen amount of exact exchange is dependent on a variety of rationales.[59–62]

Generally speaking the inclusion of some exact exchange corrects most of the self-interaction error present in 'pure' DFT methods, resulting in both a more localised depiction of the electron density within a given system and a wider gap in energy between the highest occupied and lowest unoccupied molecular orbitals (HOMO and LUMO respectively).[47,54,58] Due to the fact that pure DFT methods notably underestimate the HOMO–LUMO gap, the hybrid methods are generally considered to be an improvement to the description of insulating and semiconducting systems.[47,54,58] For a solid state system it is known that the exchange interaction decays very rapidly in intensity through space. Attempts have therefore been made to improve the efficiency of calculating HF exchange in extended solids (such as semiconductor supercells) by either truncating the exchange interaction or separating the interaction out according to long and short-range terms. The range-separated HSE06 functional[62] is based on the PBE0 functional[60] (equation 2.38), but where each component of the exchange part are separated according to long (LR) and short-range (SR) contributions:

$$E_X^{PBE0} = aE_X^{HF,SR}(\omega) + (1-a)E_X^{PBE,SR}(\omega) + E_X^{PBE,LR}(\omega), \tag{2.39}$$

where the term ω is a parameter derived from theoretical arguments to be 0.33. Here it is found that for most systems the long range exchange contributions are small, and subsequently cancel to leave only the PBE-LR, PBE-SR, and HF-SR exchange terms. This cancellation gives the justification that only the short range component of the exchange energy needs to be calculated. Efficiency is typically further increased by the application of integral screening, whereby only exchange integrals of a sufficiently high magnitude are used in the calculation, all others are discarded.

Hubbard U Correction for DFT For solid-state systems containing strongly correlated electrons (e.g. transition metal compounds, such as oxides) the deficiencies of DFT can pose big problems, as there is tendency for pure DFT functionals to delocalise electrons yielding a very poor picture of localised-electron systems in particular. While the improvement in the description of insulating systems afforded by hybrid HF/DFT functionals is essential for the accurate study of electronic properties of such systems, inclusion of HF exchange also increases computational cost as a direct result (i.e. the computational cost increases as N^4 for systems with N electrons). An often-used alternative is to include a correction to the energy functional which forces the electronic states in the metal's d-orbitals to be either fully filled or unfilled:

$$E = E^{LDA} + \frac{1}{2}\sum_{m,m',\sigma} U(n_{im\sigma} - n^0)(n_{im'-\sigma} - n^0)$$
$$+\frac{1}{2}\sum_{m,m',\sigma,(m\neq m')} (U-J)(n_{im\sigma} - n^0)(n_{im'-\sigma} - n^0)$$

where n^0 is the average occupancy of a single d-orbital, $n_{im\sigma}$ is the orbital (m) and spin (σ) dependent occupation of d-orbital i. The parameters U and J are, respectively, the Hubbard and Stoner parameters.[63] These are entirely system-dependent and must be chosen by the researcher to correct the electronic structure of the system according to that of experimental results. This approach is commonly referred to as the "DFT + U" method,[64] due to the addition of the additional parameters U and J. As there are no two-electron integrals to compute, the typical computational cost of a calculation using DFT + U is similar to a simple DFT calculation, while the quality of electronic structure improves dramatically. While there is a theoretical rationale for calculating the correct value of U for a given material,[64] the values of U and J are often chosen arbitrarily to fit known experimental datasets. Unlike

the case for hybrid HF/DFT functionals there is therefore a greater variation in the U and J values applied for the same system,[65–67] and there is more variation in the electronic properties calculated with DFT + U methods compared to the more standardised DFT and HF/DFT methods.

Dispersion Correction for DFT One of the fundamental issues with DFT (and similar single-electron methods) is that there is no accounting for the dispersion interaction within its basic formulation. As such, systems with considerable dispersion interactions (e.g. graphite, non-polar molecules) are poorly described by DFT or HF alone. An approach that became popular over the last 10 years is to apply, empirical corrections to simulate the weak attractive intermolecular forces which result from the dispersion interaction. The commonly-used method for calculating this interaction is the "pairwise" interaction, as formalised by Stefan Grimme.[68] In this method, the dispersion-corrected DFT (DFT-D) total energy is equal to the sum of the total energy calculated by the chosen density functional (E_{DFT}) and the energy of the dispersion interaction (E_{disp}):

$$E_{DFTD} = E_{DFT} + E_{disp} \tag{2.41}$$

where the E_{disp}, for a system of N atoms and interacting atoms i and j, is given by:[68]

$$\begin{aligned} E_{disp} &= -s_6 \sum_{i=1}^{N-1} \sum_{j>i}^{N} \frac{C_{6,ij}}{R_{ij}^6} f_{dmp}(R_{ij}) \\ f_{dmp}(R_{ij}) &= \frac{1}{1 + e^{-d(R_{ij}/R_r - 1)}} \end{aligned} \tag{2.42}$$

where s_6 is a scaling factor specific for each particular density functional, $C_{6,ij}$ is the dispersion coefficient, R_{ij} is the interatomic distance of atom pair i and j, R_r is the sum of van der Waals radii, $f_{dmp}(R_{ij})$ is a dampening function to avoid

singularities associated with small values of R, and d is a fitting parameter. The dispersion correction can be applied to most density functionals, where the approach is denoted as DFT-D. As an alternative approach, some density functionals are also being developed where dispersion interactions are incorporated within the functional itself *via* a non-local interaction term, rather than being a separate empirical correction.[68]

2.1.6 Solid-State Electronic Structure

The concepts reviewed so far can be applied relatively easily to molecular systems, as the physical system in this case is very clearly defined. Calculations of an individual molecule with no accounting for interactions between the molecule and its surroundings are thus commonly referred to as "gas-phase" calculations. In the solid state, matter packs together to form larger structures. Experimental work using X-ray diffraction (XRD) techniques demonstrates that the atoms in a solid are often arranged in defined, periodically-repeating patterns. Bragg's law is used to determine the spacing between planes of atoms or other formula units (otherwise known as unit cells) that make up the repeating structure:

$$n\lambda = 2d\sin\theta, \tag{2.43}$$

where n is an integer, λ is the X-ray wavelength used, d is the spacing between atomic planes, and θ is the measured scattering angle of the X-rays. It is assumed that the X-rays in these experiments are simply scattered off the atoms within the solid, and that the interaction between the electrons and the X-rays, and subsequent constructive and destructive interference between these X-rays, leads to the diffraction patterns observed in experiment.[69] As is conventional, systems whose structures follow a periodically-repeating

pattern are referred to as "crystals", while those which do not are referred to as "amorphous solids" (or, simply, "amorphous"). Each atom in a crystal will interact with each atom surrounding it; each of these atoms will interact with each other surrounding them, and so on throughout the crystal. The same fundamental inter-atomic interactions commonly seen in chemistry (such as covalent, coulombic, dispersion and others) are present in both solid and molecular systems. The interactions *between* molecules are often too weak to do more than shift the energies of its electronic states, while the strong interactions between atoms leads to the unique electronic an physical properties present in large crystals. While molecular properties can be calculated to a reasonable degree of accuracy from a single molecule, the properties of a crystal cannot be calculated from only a few atoms using the techniques mentioned so far.

Experimentally-measured energies for different electronic orbitals of a solid, determined by X-ray photoelectron spectroscopy (XPS), show that the core orbitals have a very narrow range of energies, while the valence orbitals typically have a wide range of energies.[69] This difference between the discrete orbital energies seen in small molecules and atoms and the bands of energies seen in solids show that, in order to accurately simulate the electronic structure of a solid-state system, the many interactions between each atom in the solid-state system must be accounted for by the simulation model. Simulating the entirety of even small crystals, and their many billions of atoms, is completely unfeasible for even the simplest DFT or HF method. As such, different approaches are needed in order to calculate the electronic properties of crystals and other matter in the solid state.

The Free Electron Model

One of the earliest models of electronic structure in solids is the "free electron model" (or "free electron theory"). In this model, the electrons are proposed to move freely (without the spatial confinement of orbitals) throughout the solid system (though, in reality this is only applicable for the valence electrons to a certain extent), while the solid system is represented as a potential energy well that extends to the complete physical size of the solid itself. Electrons then occupy energy levels within this well according to the solutions to the 'particle in a box' description of electrons, which, though formally discrete, are effectively continuous due to the very small spacing between the energy levels themselves. In a neutral particle in a box system, the potential energy inside the solid is taken to be *zero*, and so the energies of the electrons are defined only by their kinetic energy:

$$\begin{aligned} T =& \frac{mv^2}{2} \\ =& \frac{p^2}{2m}, \end{aligned} \tag{2.44}$$

where p is momentum ($p = mv$). The electrons are described as standing waves (or plane waves) which have wavelengths related to the length of the potential well (l,$\lambda = 2l/n$, where n is a positive integer) and thus, according to the de Broglie equation (equation 2.1) their momentum is also related to the well's length ($p = hn/2l$). Combining these relationships together gives

the energy of any electron in the well:

$$\begin{aligned} E =& \frac{h^2 n^2}{8ml^2} \\ E =& \frac{h^2 k^2}{8\pi^2 m} \\ k =& \frac{2\pi}{\lambda} \\ =& \frac{n\pi}{l}, \end{aligned} \tag{2.45}$$

where k is a commonly-used shorthand to represent the wavenumber of a plane wave (or, number of cycles per unit of distance). A plot of E against k produces a simple parabolic function, which shows that electron energies are continuous, as is the case of a free electron. This theory works (to a limited degree) in predicting the behaviour of metallic systems,[69] but not for any other kind of solid. On the other hand, it can be used as a starting point for more elaborate theories of solid-state electronic structure.

The Nearly-Free Electron Model

A major shortcoming of the free electron model is that it doesn't account for the potential felt by the electrons from the atoms *within* the solid. In a real crystalline solid, the system has a periodic arrangement of atoms, and so the potential energy of the electrons varies in the same periodic fashion (as this interaction only varies according to distance between the electrons and nuclei in this instance). The solution to the Schrödinger equation in a periodic background potential shows that the potential energy reaches a minimum at the nuclei positions, and a maximum at the farthest distance from the nuclei, and as such there cannot be a completely continuous range of energies that the electrons may possess.

It can be argued that the behaviour of electrons in solids is given by the

scattering of X-rays in diffraction experiments, due to the similar behaviour of free electrons and X-rays with mutual energies, where Bragg's law (equation 2.43) relates the wavelength of diffracted X-rays to the distance between periodically-repeating structures (also known as "unit cells"), in particular the solution where $\theta = 90°$:

$$n\lambda = 2d, \tag{2.46}$$

directly gives a direct relationship between the diffracted X-ray (or electron) wavelength and the box length in the 1-dimensional particle-in-a-box problem (equivalent to the spacing between identical atoms in adjacent unit cells). Wavelengths that satisfy (or almost satisfy) Bragg's law do not correspond to propagation through the crystal system. Such wavelengths are, therefore, forbidden to the electrons in the system, and this results in discontinuities in the range of energies available to the electron; discontinuities which relate directly to the physical structure of the crystal system. By relating the physical structure of the solid to the energies of the electrons within it, this approach improves on the free electron model and is referred to as the "nearly free-electron model". This model depicts the electronic structure of a solid as being made up of "bands" of allowed energies for the electrons (as opposed to the discrete levels seen in non-periodic molecular systems) and falls under the "band theory" of electronic structure. The existence of energy bands is supported by experimental evidence from X-ray emission spectroscopy (capable of showing electronic transfers between core and valence orbitals), which show that core orbitals have discrete energies and valence orbitals have "bands" of energies.[69]

Band Theory and the Reciprocal Lattice

The electronic "band structures" of solids can lead to different types of systems as a result of the widths of electronic energy bands and forbidden regions. If there is a large energy gap between the highest energy occupied band (or valence band (VB)) and the lowest-energy unoccupied band (or conduction band (CB)), then the system is defined as an insulator. An insulator with a low optical band gap (e.g. within the visible or infrared regions of the electromagnetic spectrum) is also called a semiconductor. If there is no energy gap between the VB and CB, or the VB is only partially occupied, then the system is defined as a conductor. Other, more specific, definitions also exist. For instance, a system where there is partial overlap of a fully-occupied VB and unoccupied CB is defined as a semimetal (or, less often, a gapless semiconductor) and it typically possesses electronic properties of both an insulator and a conductor.

In a periodic system, the dependence of energy on the value of k is periodic and has an inverse relationship to the physical lattice vector (by combining Equation 2.45 and Equation 2.46). The wavenumber is a vector quantity in this case (known as the "wave vector" $\vec{k}$) which is composited of up to three basis vectors, equal to the number of periodic dimensions in the physical system. The basis vectors are often denoted as $\vec{b}_1$, $\vec{b}_2$, $\vec{b}_3$ in solid state physics literature, but (for the sake of consistency) will be denoted here as $\vec{k}_x$, $\vec{k}_y$, and $\vec{k}_z$. The vector space of $\vec{k}$ is, due to the inverse relationship of $\vec{k}$ with lattice vector, often referred to as "inverse space" (or reciprocal space). The unit cell of this reciprocal lattice is called a "Brillouin zone", and is sufficient to fully describe the dependence of energy with $\vec{k}$, thus giving the full range of allowed and forbidden energies for the electron.

All the aspects of this theory, together, leads to a description of the elec-

tronic structure of any given solid with continuous allowed energy ranges for the electrons, and gaps or ranges of forbidden energies. This agrees with the experimental evidence mentioned previously for bands of electron energies. Importantly, the concept of the Brillouin zone provides a basis to perform electronic structure calculations of a large solid using only its unit cell as a reasonable approximation. Due to the model producing electronic structures which consist of "bands" of allowed and forbidden energies, this is referred to as "band theory".

The Periodic Wavefunction

The periodically-repeating electronic structure will therefore have a periodically-repeating wavefunction to describe it. The solution to the Schrödinger equation for a particle in a periodically-repeating background potential is given by the Bloch wavefunction:

$$\Psi_{\vec{k}}(\vec{r}) = e^{i\vec{k}\vec{r}} u_{\vec{k}}(\vec{r}) \tag{2.47}$$

where $\vec{r}$ is the position vector of the electron, and $u_{\vec{k}}(\vec{r})$ is a function which is periodic with the background potential. The periodicity of $u_{\vec{k}}(\vec{r})$ corresponds to the translation of the function by the unit cell vector ($\vec{a}$, such that $u_{\vec{k}}(\vec{r}) = u_{\vec{k}}(\vec{r}+\vec{a})$, and thus Equation 2.47 can be re-written in terms of the wavefuncion which is defined by crystalline orbitals (COs, ϕ):

$$\Psi_{\vec{k}}(\vec{r}+\vec{a}) = e^{i\vec{k}\vec{a}} \phi_{\vec{k}}(\vec{r}) \tag{2.48}$$

Variants of Equation 2.48 exist also for 2-dimensional and 3-dimensional systems with different cell parameters. Using the orbital approximation, $\Psi(\vec{r})$ is described by a set of COs and, analogous to the case of MOs, are represented by a set of m basis functions (χ). Plane-wave functions (χ^{PW}) can

easily be used as basis functions, as they easily conform to the requirement of periodicity:

$$\phi_n(\vec{r}) = e^{i\vec{k}\vec{r}} \sum_{n=1}^{m} c_{nj} \chi_n^{PW}(\vec{r}), \tag{2.49}$$

where j is the jth electron that this basis function applies to. While this approach is simple to implement, in some situtations it can be advantageous to use a localised basis set, such as an atom-centred Gaussian-type orbital (GTO) set instead. A system with a large number of electrons per unit volume may be handled more efficiently using a PW basis set, as the basis set size (for a given planewave cutoff) only increases with the size of the physical system. However, if the physical system has a low number of electrons relative to its size (for instance, a simulation of a 2D surface), then a localised basis set is the more efficient choice. For a localised basis set (such as Gaussian-type orbtials, χ^{GTO}), the $e^{i\vec{k}\vec{a}}$ term ensures that the functions conform to the requirement of periodicity:

$$\phi_n(\vec{r}) = e^{i\vec{k}\vec{a}} \sum_{n=1}^{m} c_{nj} \chi^{GTO}(\vec{r} + \vec{a}) \tag{2.50}$$

Using these COs in a calculation which represents the physical system as infinitely-repeating, based on the structure of its unit cell, therefore allows for the calculation of electronic structures that are representative of a large solid. In reality, the solid is of finite size with an immense number of atoms and electrons, but the use of a theoretically infinite system works acceptably well when analysing the properties of a specific region of it. For example, a computational cell can be used to be representative of either the surface or central bulk regions of the real structure, and not both simultaneously.

K-Point Sampling

Though band theory reduces the size of the calculation greatly by using a unit cell to simulate an entire crystal, the wavefunction now varies as a function of the wave vector ($\vec{k}$). This variation cannot be calculated analytically, so the only solution is to numerically integrate the Bloch wavefunction as a function of $\vec{k}$. This is done by solving the eigenvalue equation (within a chosen electronic structure method) at a set of points in reciprocal space (referred to as $\vec{k}$-points). This is commonly referred to as $\vec{k}$-point sampling, and a number of methods exist to choose this grid (e.g. the Monkhorst-Pack method[70]). The number, and positioning, of the $\vec{k}$-points used for sampling must be sufficient to capture the correct variation of the band energies through the reciprocal space, but increasing the number of $\vec{k}$-points in a calculation will clearly increase the computational cost of the calculation. For an insulator/semiconductor this variation of band energy is often very low, and a small number of $\vec{k}$-points can be used to obtain reasonable accuracy. For more complex systems, such as classical conductors or semimetals, the variation is typically much greater, and requires a larger number of $\vec{k}$-points to sample. The use of a minimal number of $\vec{k}$-points is usually sufficient for the optimisation of geometries, however a much larger number of points will be required in any system if an accurate calculation of the band structure is sought after.

The Γ-Point Approximation A special case regarding the use of minimal-size $\vec{k}$-point sampling is the Γ-point approximation. As the reciprocal space vector $\vec{k}$ is inversely proportional in magnitude to that of its correspondent real-space vector ($\vec{a}$, $\vec{b}$, or $\vec{c}$), its magnitude will decrease as the real-space vector increase. For a very large physical system (such as the large supercell for a unit cell), the reciprocal-space vector can be sufficiently small that even an

eigenvalue equation of a single value of $\vec{k}$ will acceptably describe the electronic band structure. This is known as the Γ-point approximation, as typically only the $\vec{k}$-point which lies at the centre of the Brillouin zone, conventionally referred to as Γ, is used in the calculation.

Chapter 3

The Graphene/TiO_2 Photocatalytic Interface

The original research in this chapter has been published in *The Journal of Physical Chemistry C*.[71]

3.1 Chemical and Physical properties of TiO_2

TiO_2 was the first photocatalyst and still the most widely researched[5,6]. The structure of TiO_2 takes the form of one of three polymorphs (or phases): rutile, anatase and brookite. Each possess differences in electronic structure, physical properties, and chemical properties from one another. For instance, the electronic band gap of the rutile polymorph is 0.2 eV less than that of the anatase polymorph. Electronic properties are key to the description of photocatalytic properties, and physical properties will of course provide the basis for electronic structure. Chemical properties are also important where photochemistry is concerned as the ability for the photocatalyst to interact with its substrate will be just as important in the catalytic cycle as generating

the photoexcited electron-hole pair in the first place.

3.1.1 Rutile

Known to be the most thermodynamically stable phase of the three, with the lowest total free energy, it is the most common form of TiO_2 found naturally. The structure is noted to be the most compact of the three forms and upon heating of any other TiO_2 structure to around 600 °C to 800 °C, will be the predominant crystal structure formed[72]. Its bulk crystal structure is tetragonal, with A and C lattice vectors of: 4.593 Å and 2.958 Å respectively, the long-range repeating structure consists of multiple octahedra of Ti^{4+} surrounded by 6 Oxygen atoms (see Figure 3.1). Within this bulk structure the (110) plane forms the most thermodynamically stable surface, believed to be due to the fact that the surface leaves an equal number of broken oxygen and titanium bonds — each of which were formerly long bonds between repeating layers of the crystal. The (110) surface exposes lines of 5-coordinated Ti atoms, with the unoccupied bonds protruding perpendicular to the surface, which provide chemical binding sites for catalysis. The "bridging" oxygen atoms are believed to be overall negatively charged and provide the main contribution to physisorbtion interactions.

3.1.2 Anatase

Anatase TiO_2 also possesses a tetragonal crystal system, with A and C lattice vectors of 3.782 Å and 9.502 Å respectively, in addition to the repeating TiO_6 octahedra as seen in Rutile (Figure 3.1). The crystal structure of anatase is more diffuse than rutile, firstly this results in anatase having a lower density than rutile (c.a. 3.78 and 4.23 g cm^{-3} respectively), and also affects the elec-

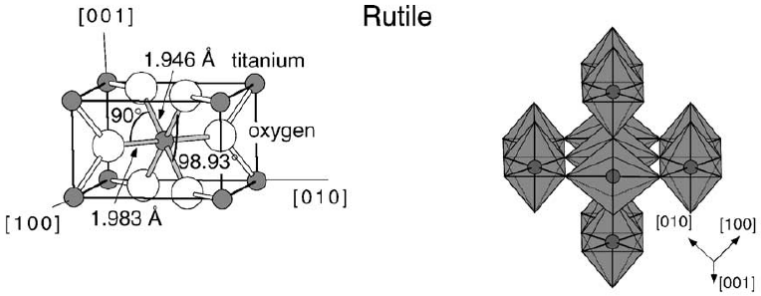

Figure 3.1: Crystal structure of the rutile polymorph of TiO_2 with Miller Indices, bond lengths, and bond angles shown (left); and the stacking arrangement of TiO_6 octahedra in the bulk material (right). Large white spheres represent oxygen atoms and smaller black spheres titanium. Reprinted from [*Surf. Sci. Rep.*, **48**, U. Diebold, *The Surface Science of Titanium dioxide*] copyright 2003, with permission from Elsevier

tronic structure. In this crystal system the (101) surface is the most stable as, in the same way for the (110) face of rutile, there is a clean break in the long-range order of the system. Here the surface termination gives, as for rutile, 5-coordinated titania and 2-coordinated oxygen. However the crystal system produced for this face is triclinic (no matching cell vectors or orthogonality) and is parallelepiped (A cuboid produced from 6 parallelogram faces). This shape is needed to create the "stepped" unit cell and, interestingly, creates two effects: Firstly there are "step edges" where one will find 4-coordinated titania; and secondly it causes a considerable challenge for simulating co-continuous solid interfaces as the top surface will not tessellate with many other surface shapes (see later for an example using the graphene-anatase hybrid). Theoretical studies have shown that both rutile and brookite possess direct ($\Gamma \rightarrow \Gamma$) electronic band gaps (where there is no electron momentum difference between the CBM and VBM), while anatase has an indirect ($M \rightarrow \Gamma$) band gap (where there is a difference in electron momentum between the CBM and VBM) (band structures shown in Figure 3.5).[73] This implies that anatase TiO_2 should in practice show longer-lived excited states. Indeed, it is seen from experiment

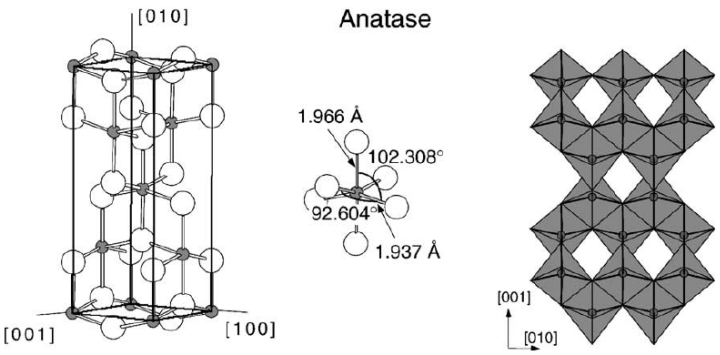

Figure 3.2: Crystal structure of the anatase polymorph of TiO_2 with Miller Inidces, bond lengths, and bond angles shown (left); and the stacking arrangement of TiO_6 octahedra in the bulk material (right). Large white spheres represent oxygen atoms and smaller black spheres titanium. Reprinted from [*Surf. Sci. Rep.*, **48**, U. Diebold, *The Surface Science of Titanium dioxide*] copyright 2003, with permission from Elsevier.

that the charge recombination rate for anatase is lower than for rutile — thus making anatase preferred for photocatalytic systems over rutile. As mentioned previously (page 54) anatase TiO_2 is less dense than rutile. This is found to be due to a less-efficient stacking of the TiO_6 octahedra. DoS plots of anatase and rutile Figure 3.3 show that there is a sharp spike in the Ti 3d band density near its CBM, which is not present in rutile. The z-axis distortion of the anatase TiO_6 octahedron (as shown in Figure 3.2) leads to crystal field splitting of the Ti t_{2g} states. This leads to the formation of a narrow energy band based on the more spatially-localised d_{xy} orbital in the MO-bonding diagram of anatase. It has been proposed by these theoretical arguements that the more spatially-separated CBM of anatase is the cause behind the indirect band gap, and subsequently the reduced recombination rate.

Band gaps can be experimentally derived by most optical spectroscopic methods, and the positions of the band edges in terms of energy can be derived from x-ray photoelectron spectroscopy (XPS). The exact structure of the bands however can, so far, only be determined through the use of computational

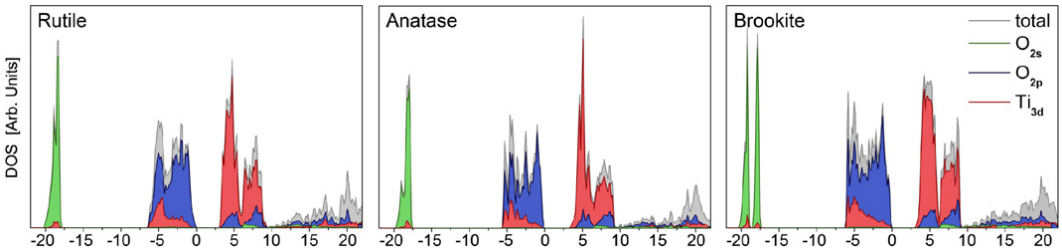

Figure 3.3: DOS spectra for the three main polymorphs of TiO_2, divided up according to the contributions of O 2s, O 2p and Ti 3d states to the total density, calculated with the HSE06 DFT functional[73]. Reprinted from `doi:10.1088/0953-8984/24/19/195503`, copyright IOP Publishing. Reproduced with permission. All rights reserved.

modelling. Pure DFT functionals will underestimate the magnitude of the band gap, primarily resulting from the incorrect positioning of the CBM at lower energy than its true value. Hybrid functionals, those which combine the DFT and Hartree-Fock (HF) descriptions of electron interaction, are known to give a better description of the band gap energy than pure DFT. It has been found also that the shape of the valence and conduction band edges are very well described by hybrid DFT methods[73]. The experimental band gaps of rutile and anatase have been determined to be 3.0 eV and 3.2 eV respectively. DFT calculations using the PBE[57] (pure DFT) functional give fundamental band gaps of 1.88 eV and 1.94 eV for rutile and anatase, while the same calculations using the hybrid HF/DFT HSE06[62] functional give gaps of 3.39 eV and 3.60 eV for the same systems respectively.[73]

3.2 Composite Titania Photocatalysts

Combination of TiO_2 with another semiconducting material in a hetero-junction arrangement has been a long-studied concept in both photovoltaics and photocatalysis,[6,74–76] and has been quite successful as a means of tackling both the charge recombination problem (through interfacial charge carrier

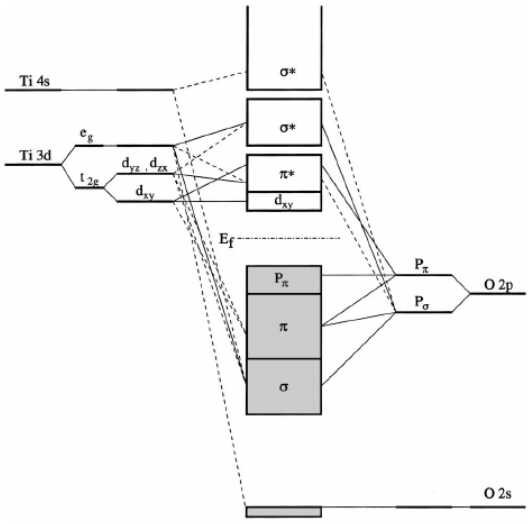

Figure 3.4: An MO bonding diagram for the Ti−O bonding in anatase TiO_2. Solid and dashed lines represent strong and weak contributions to different bands, respectively. Reprinted with permission from [R. Asahi *et al*, *Phys. Rev. B*,**61**, 1117–1119, 2000] Copyright 2000 by the American Physical Society.

separation) and, by using a narrow-gap semiconductor, extending photon absorption into the visible region. A popular approach from previous decades has been to combine TiO_2 with cadmium sulphide (CdS).[6,7] Anchoring CdS to the surface of TiO_2 has been shown to increase photocatalytic activity notably and longevity to some extent, however issues with photocorrosion in particular raise issues for potential industrial applications.[5,77]

3.2.1 Metal Oxides/Chalconides

The concept of utilising a heterojunction design for photocatalytic applications was initially investigated by Serphone *et al*,[78] and updated further a decade later,[79] which showed that combining TiO_2 with either other metal oxide solids or cadmium sulphides improved the photocatalytic degradation of hydrogen sulphide (H_2S) when compared to intrinsic TiO_2. Experiments by Kamat and Vinodgopal[80] in the same year, using an SnO_2/TiO_2 working electrode with an applied external bias (schematic in Figure 3.6), showed a notable

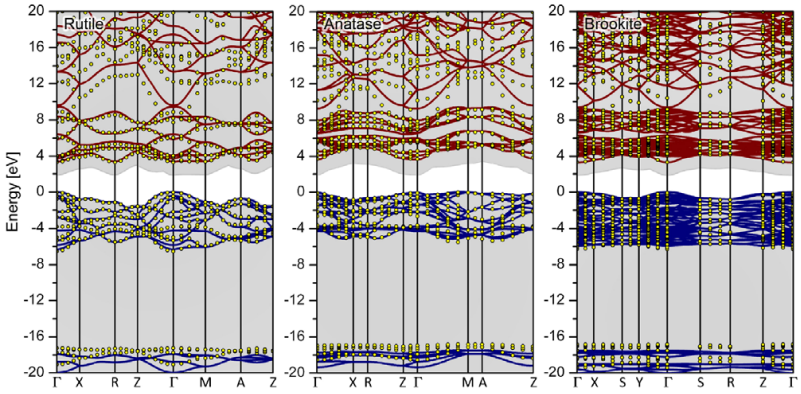

Figure 3.5: Band Structures of the three main polymorphs of TiO_2 calculated using the HSE06 HF/DFT Functional with the GW approximation (dots) and without (lines). Reprinted from `doi:10.1088/0953-8984/24/19/195503`, copyright IOP Publishing. Reproduced with permission. All rights reserved.[73]

improvement in photocatalytic performance against the azo dye Acid Orange 7 (AO7) compared to the separate components on their own. In this case neither subcomponent provides any improvement in the absorption profile of the material (as SnO_2 and TiO_2 possess comparable band gaps of over 3.0 eV, as shown in Figure 1.3) and any improvements in photocatalytic rate should be down to the charge separation afforded by the formation of the heterojunction (depicted in Figure 3.6). Additionally the catalytic activity as a function of the ratio of TiO_2 to SnO_2 in the system relative to pure TiO_2, and vice-versa, was evaluated (see Figure 3.7) where it was deduced that high photocatalytic activity is achieved when the composition of the composite is at least 1:1 for both parts and peak rate is reached at a 2:1 Sn to Ti ratio.[80]

Despite poor results reported initially,[81] composites of TiO_2 and ZnO have shown some potential improvement in photocatalytic rate over intrinsic TiO_2.[82] ZnO/TiO_2 composites initially displayed worse photocatalytic activity than their constituent parts. This was believed to be down to the fact that the conduction band edges of both semiconductors (specifically for anatase TiO_2) are very similar (as shown in Figure 1.3) which, combined with similar band

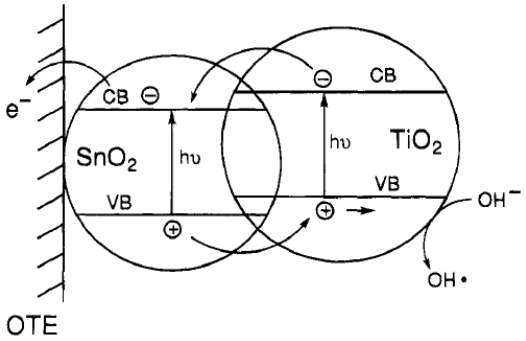

Figure 3.6: Schematic of the band structure of an SnO_2/TiO_2 composite system, where OTE refers to the Optically Transparent (Bias) Electrode. Here the staggering in the band structure between the tin and titanium sections is shown, where photoexcited electrons settle on the tin side of the interface (where they are collected by the OTE) and holes on the titanium side (where they can oxidise AO7). Reprinted with permission from [*Environ. Sci. & Tech.* 1995, **29**, 841–845]. Copyright 1995 American Chemical Society.

gaps producing comparable photon absorption rates at the same wavelength, results in a poor separation of charge carriers.[81] Conversely, it was found that reproducing this interface with a mixed-phase (anatase/rutile) TiO_2 component (schematic shown in Figure 3.8) results in an improvement in the photocatalytic rate over the unmodified hybrid phase TiO_2 (Degussa P25).[82] Though referred to as surface doping in this instance, the deposited ZnO forms a heterojunction with the surface of the TiO_2 crystals. The observation here is that the addition of ZnO to the surface improves the photocatalytic breakdown of nitric oxide (NO, a common atmospheric pollutant) as the concentration (in percentage of Zinc atoms) of ZnO is increased. Crucially though there is maximum in performance at around 0.5% zinc content, after which the rate drops off to *below* intrinsic P25 levels. This is due to the fact that ZnO has a propensity to act as a recombination centre, so beyond a certain point any photocatalytic enhancements are outweighed by the increased recombination rate.

With the properties of the heterojunction in a photocatalytic system es-

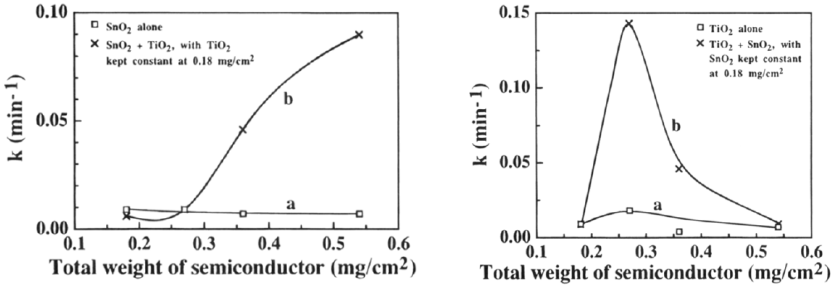

(a) Photocatalytic rate with varying Sn concentration

(b) Photocatalytic rate with varying Ti concentration

Figure 3.7: Comparison of the rate of photocatalytic degradation of azo dye Acid Orange 7 (AO7) using a composite SnO_2/TiO_2 photocatalyst at varying Tin (a) and Titanium (b) dioxide compositions. Reprinted with permission from [*Environ. Sci. & Tech.* 1995, **29**, 841–845]. Copyright 1995 American Chemical Society.

tablished, a further logical step from this point would be therefore to produce a heterostructured system where one component can be focussed on visible-spectrum photon absorption and the other on catalysis. As before the conduction band edge of the absorber should be greater than the CBM of the catalyst material, and for the instance of photocatalytic water splitting the absorber should have either a VBM which can drive the oxidation process or be coupled to a suitable component which can catalyse that reaction instead. Semiconductors based on cadmium, such as CdSe and CdS, are quite popular for because the bulk band gap lies within the visible region, the band edges (particularly CdS) sit offset from TiO_2 such that a suitable heterojunction can be formed at the interface between the two, and the relative ease of synthesising size-controlled Quantum Dots (QDs) allows for band gap tuning of the sensitizer.

As the quantum size effect does alter the band gap of any nanosized material, it therefore bears importance to understand the limits to which particle sizes can be modified before the beneficial effects of the heterojunction break down. In a study by Kamat and Sant[83] the effect of size control was looked at

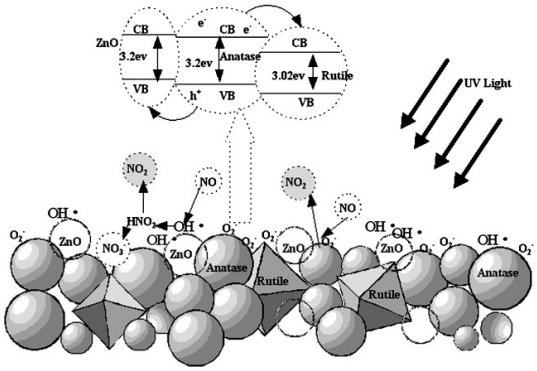

Figure 3.8: Schematic detailing the generalised structure of the composite ZnO/Degussa P25 TiO_2 system, including the NO oxidation mechanism and band structure diagram. Reprinted from [*J. Mol. Catal. A Chem.* **287**, H. Wang *et al*, The characterization of ZnOanataserutile three-component semiconductor and enhanced photocatalytic activity of nitrogen oxides, 176–181]. Copyright 2008, with permission from Elsevier.[82]

in nanoclusters of TiO_2 and CdS, where it was found that the efficient electron transfer process seen for CdS nanoparticles on bulk TiO_2 does not occur at all when the smaller sizes of TiO_2 were synthesised. This shows that although production of photocatalytic nanoparticles is desirable for increases in surface area, care must be taken with size control as the negative effects of quantum confinement are realisable without much difficulty. A further study by Wu *et al*[84] also raised concerns about the applicability of the system to photocatalysis, as it is found that despite being bound with TiO_2 it is possible for the photogenerated holes which will collect on the CdS component to take part in a photocorrosion process. This is due to the fact that the VBM potential of CdS is not able to oxidise OH^- to $OH^\bullet$ and so will precipitate Cd^{2+} from the structure.[84]

On the basis that CdS is highly effective for photon absorption and TiO_2 is better suited to electrochemistry, Lee *et al*[85] investigated methods to determine the best structural arrangement for the two semiconductors. Comparisons of pure CdS (calcined at either 673 or 873 K[85]) against CdS/TiO_2

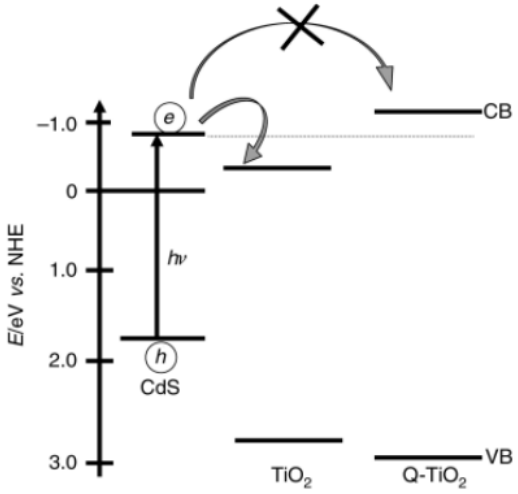

Figure 3.9: Band gap schematic describing the effect of quantum confinement on the electron transfer between CdS and TiO_2[83]. Here we see that once sufficiently small TiO_2 nanoparticles are used in the system the TiO_2 band gap widens to the point where electron transfer to the TiO_2 component is unfavourable and therefore doesn't occur. Republished from [P. A. Sant and P. V. Kamat, *Phys. Chem. Chem. Phys.*, 2002, **4**, 198–203], Copyright 2002 The Royal Society of Chemistry.

composites where one of two components in each constituted the bulk of the material were made, using the photocatalytic production of hydrogen from aqueous H_2S. As one may expect, the samples comprising of bulk CdS with TiO_2 nanoparticles on the surface demonstrated far more photocatalytic activity than any of the other samples. In addition to the improvement in photocatalytic activity there were no significant signs of photocorrosion (determined from XPS data), showing that the TiO_2 surface cover does guard against this. It should be noted however that the long term stability of the system is still an issue because (as mentioned in the introductory section) cadmium can still be leached into solution.

The hazards (and costs) associated with cadmium-chalconide systems have prompted efforts to produce effective alternatives with lower toxicity and cost than cadmium. Lead sulphide PbS has been thought of as an alternative due to its much narrower band gap of around 0.43 eV and low toxicity (due to how

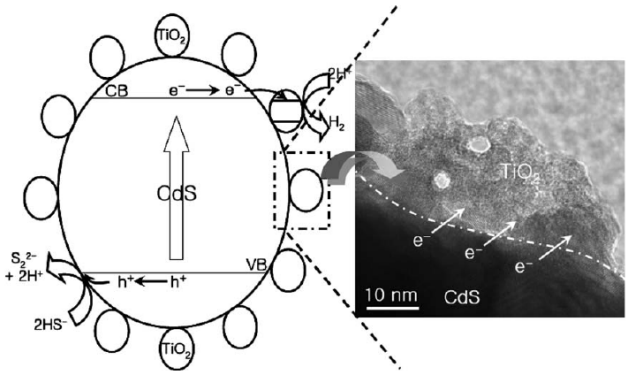

Figure 3.10: Schematic depicting the composite of bulk CdS with TiO_2 nanoparticles synthesised by Jang *et al*[85]. Shown here is the generalised flow of electrons to TiO_2 for hydrogen reduction, the oxidation of HS^- by photo-generated holes, and a Transmission Electron Microscope (TEM) image inset showing the surface structure. Reprinted from [*Chem. Phys. Lett.*, Fabrication of CdS/TiO2 nano-bulk composite photocatalysts for hydrogen production from aqueous H2S solution under visible light, **425**, J. S. Jang *et al*, 278–282]. Copyright 2002 Elsevier.

insoluble PbS is). Efforts to produce systems based upon PbS have shown decent progress relatively recently[86–88] however the positioning of the VB edge at such a high potential prevents direct use in photocatalytic water splitting as it cannot drive the oxidation reaction by itself, and thus would require a third component to function. Furthermore efforts have been made to utilise tin sulphide (SnS) in a heterojunction system with TiO_2.[89,90] SnS has a very well placed direct band gap of 1.3 eV but intrinsically suffers from poor photoactivity, combination with TiO_2 has been shown to only increase photon efficiency to around 2.8%[90] relative to the measured efficiency of unmodified TiO_2 of around 2.1%.[91]The main advantage to SnS systems is the low production cost and very low toxicity, however the lack of detailed analysis (particularly with regards to photocatalytic applications) leaves this avenue open to further investigation.

3.3 Carbon Nanostructures

3.3.1 Carbon Nanotube/TiO_2 Structures

An early major breakthrough in carbon nanotechnology came in 1991 by Iijima[92] with the production of Carbon Nanotubes (NTs). The exceptional electronic properties of these carbon nanostructures, along with a greater work function (of 4.95 eV to 5.05 eV[93]) than TiO_2, then started a new effort to produce composites based on NTs and other carbon nanostructures. Combining the solid matrices of carbon NTs and TiO_2 was achieved not long after the analysis of its electronic properties.[94–96] Initial photocatalytic experiments were focussed on wastewater treatment (particularly of azo dyes),[97,98] but further studies into the photocatalytic production of hydrogen has shown that composite carbon NT/TiO_2 can give comparable or better results compared to noble metals such as Pt and Pd.[99–102]

Carbon NTs are believed to enhance the photocatalytic properties of the system in a number of ways. Firstly the effect of charge carrier separation, in a similar manner to that of noble metals, by the formation of a semiconductor-metal Schottky barrier (for metallic nanotubes only).[103] Secondly, the addition of a carbon NT has been shown to extend the absorption spectrum into the visible region.[98,104–107] Thirdly, Carbon-Oxygen-Titanium bonds can be formed at the interface between TiO_2 and the carbon NT, which have been proposed to introduce a carbon impurity energy level within the TiO_2 band structure, thus adding similar effects to that observed for mild carbon doping.[103] Lastly, it has been noted that the formation of the composite structure will stabilise smaller particle sizes of TiO_2 nanoparticles in the system and also markedly increase the effective surface area of the system for photocatalysis.[104,108]

Carbon NT/TiO_2 composites show a much greater synergy than other het-

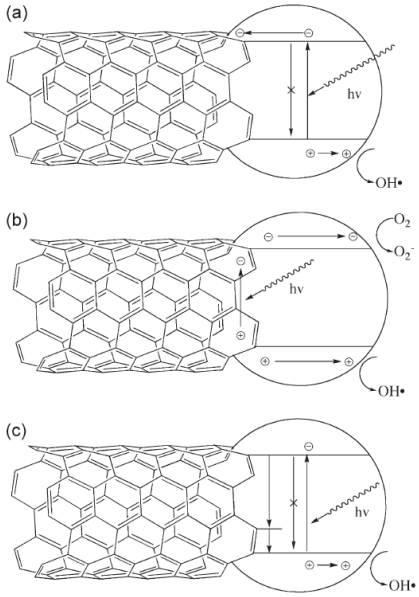

Figure 3.11: Potential mechanisms to explain the photoactivity of carbon NT/TiO_2 composite systems.[103] (a) the NT acts as an electron sink, analogously to a noble metal system, with TiO_2 absorbing UV light. (b) the NT acts as a photosensetiser, injecting photoexcited electrons and holes to TiO_2 (proposed by Faria *et al*[104]). (c) the NT forms impurity electronic states through Ti–O–C bonding, which alters the band structure of TiO_2. Reprinted from [Sigmund *et al, Adv. Mater.* 2009, **21**, 2233–2239] with permission. Copyright 2009 WILEY-VCH Verlag GmbH & Co.

erostructures, with optimal loadings of roughly 5–10% by weight for NTs.[98,99,101,102] There is however a less clear picture of the generic properties of composite carbon NT/TiO_2 systems as much of the beneficial properties observed can vary significantly depending on the morphology of the composite. Studies by Faria *et al*,[104] Kusumoto *et al*[99] and Gray *et al*[98] have shown such differences between superficially analogous systems (see also Figure 3.12 for different surface structures). The large surface area of the carbon NT also allows for a great deal of surface functionalisation to be done to improve the composite's photocatalytic properties further. This has been attempted with noble metals[100,109–111] which give a moderate synergistic improvement to photocatalytic properties. Other studies have also used this potential to create quite effec-

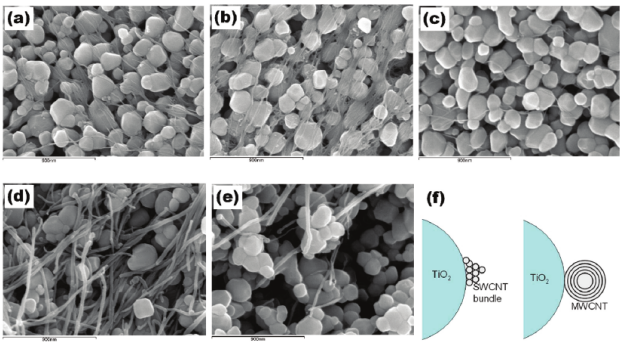

(a) SEM imagery of carbon NT/TiO_2 composites[98]. Shown here are single walled NTs at TiO_2/NT mass ratios of (a) 20:1 (b) 10:1 (c) 100:1, and multi-walled NTs with mass ratios of (d) 20:1 and (e) 100:1. (f) represents a schematic of the difference between bundles of single-walled NTs vs a single multi-walled NT.

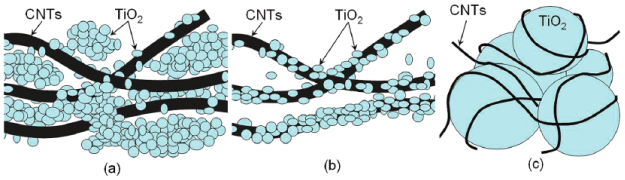

(b) Varieties of different carbon NT/TiO_2 structures based on SEM imagery from Figure 3.12a

Figure 3.12: Comparison of potential carbon NT/TiO_2 structural arrangements in (a) SEM imagery and (b) schematic drawings.[98] The authors in particular note the proposed advantage of single- over multi-walled carbon NTs due to the increased surface contact between the SWNT bundle and TiO_2 nanoparticles compared to the MWNT case. Reprinted with permission from [*Environ. Sci. & Tech.* 2008, **42**, 4952–4957]. Copyright 2008 American Chemical Society.

tive Dye-Sensitized Solar Cells (DSSCs) by addition of other sensitizers to the existing composite.[105,112]

In addition to the construction of the composite itself, the type of carbon NT used in the system is critical to the potential properties as they can be either metallic or semiconducting depending upon their construction.[113] Due to the hollow cylindrical structure of carbon NTs they will conduct in only one dimension: the tube axis. The tube axis can be related to the surface structure of a graphene sheet, where one imagines the NT being formed by rolling-up

the graphene sheet into a tube. The chosen vector along the graphene sheet thus determines its electronic properties, this vector (C_h) is described by the unit cell vector (a) of hexagonal graphene with the following equation:

$$C_h = na_1 + ma_2 \tag{3.1}$$

At infinite length the nanotube will be metallic if $n = m$ (forming an "arm-chair" nanotube), and semiconducting if $n = 0$, $m = 0$ (referred to as a "zig-zag" nanotube) or $n \neq m$ (referred to as a "chiral" nanotube). The nanotube can switch from semiconducting to metallic if $\frac{n-m}{3}$ is an integer value, in addition the band gap of semiconducting nanotubes will vary *inversely* according to the tube diameter.[113]

3.3.2 Graphene and Graphene Oxide/TiO_2 Structures

Graphene, a 2-dimensional carbon nanostructure based on a repeating hexagonal unit cell, possesses electronic properties similar to that of metallic carbon NTs.[114] Graphene is a semimetal. At most points in the Brillouin zone it is a semiconductor, but at a specific point (referred to as the Dirac point) the valence and conduction bands intersect and the system behaves as a conductor (see Figure 3.13). This combination of conducting and semiconducting elements in the band structure grants graphene the electronic properties of both conductors and semiconductors.

Following the first successful isolation of graphene from graphite in 2004 by Geim *et al*,[114] reports of its exceptional electronic properties[116,117] yielded a new possibility for graphene/TiO_2 composites to be trialled relative to existing carbon nanotube composites. Graphene shows a comparable work function compared to carbon NTs (recorded between 4.89 eV and 5.16 eV[118,119]) and an

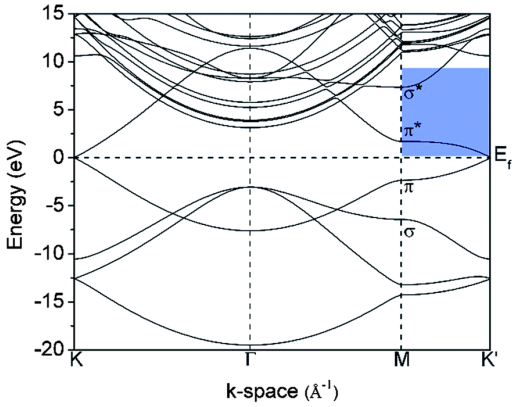

Figure 3.13: Band structure of the valence region of graphene, calculated from NEXAFS spectroscopy data. The Dirac point is visible at the edges of the plot, centered at k-point "K". Republished with permission from [X-ray absorption spectroscopy studies of electronic structure recovery and nitrogen local structure upon thermal reduction of graphene oxide in an ammonia environment, *RSC Adv.*, B. J. Schultz *et al*, **4**, 2014][115] with permission of The Royal Society of Chemistry.

incredible surface area of around 2600 m^2 g^{-1},[120] which will provide a much more extensive surface interaction between the two systems. Initial attempts to synthesise this composite used graphene oxide (GO) as a precursor material, produced from the oxidation and solvent exfoliation of graphite.[121,122] Graphene is then produced from the photocatalytic reduction of graphene oxide using a TiO_2 photocatalyst, yielding reduced graphene oxide (RGO).[123] Following from this synthesis method further improvements have been made to the production of the composite[15–17,124–128] and characterisation of the photocatalytic properties have given either similar or improved photocatalytic activities compared to carbon NT composites.[15,107,129–133]

Graphene oxide has also been investigated as a component in a composite with TiO_2.[134–137] Graphene oxide differs from other carbon nanostructures as the high oxygen content breaks the long-range π-conjugation, changing elec-

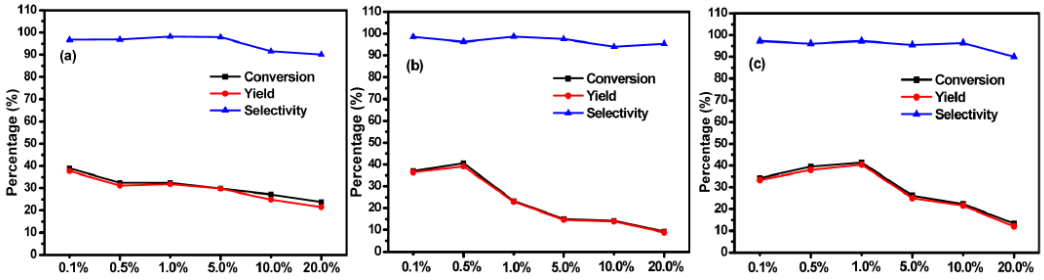

Figure 3.14: Graphical comparison of composites of carbon NTs (a), Reduced Graphene Oxide (b) and Buckminsterfullerene (c) composites with TiO_2 from a comparative study by Xu *et al*[106] at differing weight percentages of carbon nanostructure. Results here are for the selective oxidation of Benzyl Alcohol to Benzaldehyde, showing overall rate and selectivity measures after 4 hours of reaction time. Reprinted with permission from [*ACS Appl. Mater. & Interfaces*, 2013, **5**, 1156–1164]. Copyright 2013 American Chemical Society.

tronic behaviour from semimetallic to semiconducting. The band gap of GO is reported to be around 2.1 eV,[138] and it has been demonstrated that this can be blue-shifted through the partial removal of oxygen from the system.[138,139] This modification of GO has been shown to allow it to be used directly as a photocatalyst,[139] due to the shift in its conduction and valence band energies (see Figure 3.15). The formation of a GO/TiO_2 composite leads to the formation of a heterojunction, which enables charge carriers to be separated between the two phases — made possible by the differences in CB edges: -0.08 eV and -0.24 eV vs a Standard Hydrogen Electrode (SHE) for GO and anatase respectively.[140] While this system has been reported to be and effective photocatalyst,[127] the fact that TiO_2 can photocatalyse the reduction of GO to RGO[123] means that the GO will gradually photocorrode over multiple life-cycles. For this reason, GO is generally used only as a precursor. Finally it should be noted that the method used to reduce GO to RGO will directly affect the oxygen content and electronic properties of the end product,[127,130,141] which is covered in more detail in a later chapter.

As it was mentioned earlier in this section, while there are generally ac-

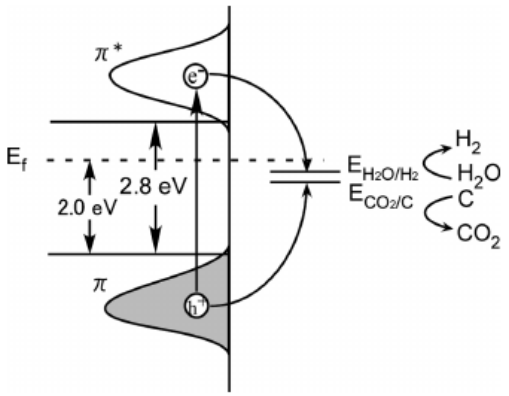

Figure 3.15: Figure showing the density of electronic states in the band edges of graphene oxide (GO) relative to the hydrogen reduction and Carbon oxidation potentials. Reprinted with permission from [*J Phys. Chem. C*, 2011, **115**, 19280–19286]. Copyright 2011 American Chemical Society.

cepted theories about the benefits of carbon nanostructures to photocatalysis (such as the Schottky Barrier formation) some more clarity is needed to deconvolute the proposed mechanisms of electronic behaviour in carbon NT and graphene-TiO_2 composites (see Figure 3.11). Almost as much attention has been aimed at studying the electronic behaviour of this composite system using theroetical modelling as there has been in synthesising the systems themselves.[65–67,142–146] In particular the nature of photon absorption in graphene is important to discuss as the likelihood of charge carrier recombination in the graphene band structure (at its Dirac Point) vs charge injection to the TiO_2 phase, as graphene absorbs visible light but does not show emission alone yet can still enhance photoactivity. An essential study by Prezhdo *et al*[66] on the graphene-TiO_2 interface demonstrated, using a combined Time-Dependent Density Functional Theory (TD-DFT)/non-adiabatic molecular dynamics theoretical method, that charge transfer across the interface is sufficiently fast to beat recombination of the charge carriers in the graphene phase and thus efficiently separate the charge carriers post-absorption. The effect of undulations in the graphene component is also shown to actively increase the electronic

coupling in the transition (see Figure 3.16)

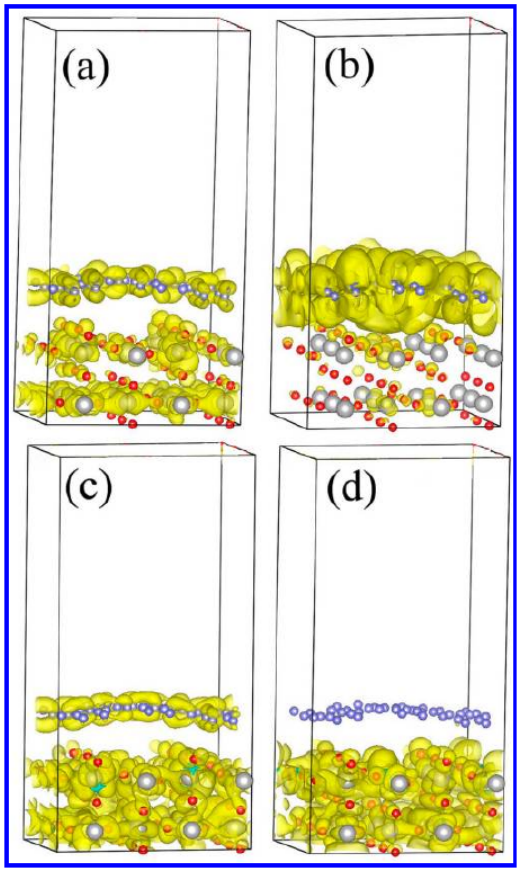

(a) Diagram depicting the electron densities in 3 separate donor and the acceptor states in the graphene/TiO_2 interface.[66]

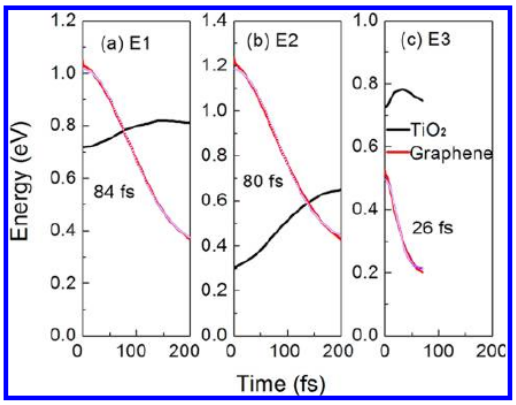

(b) Graphical plot of the change in energies in the graphene/TiO_2 system from graphene to TiO_2 followed by relaxation,[66] where E1 2 and 3 are (in order) the donor states shown in Figure 3.16a.

Figure 3.16: Data showing the change in electron density (a) and energy (b) across the graphene/TiO_2 interface. Reprinted with permission from [*J Am. Chem. Soc.*, 2012, **134**, 14238–14248]. Copyright 2012 American Chemical Society.

Studying the interface itself is, from a purely computational perspective, very challenging, as the crystal structures of TiO_2 polymorphs and graphene differ in size and also shape. To generate the composite unit cell (UC) each component system is extended such that the resulting supercells of each component are roughly equal to each other in dimension (see Figure 3.17). The main problem with this approach is that the resulting "composite" unit cell is typically very large (in the range of 100-300 atoms) and computationally

expensive to simulate without parallel scaling software. Secondly, a known shortcoming with pure DFT functionals is the underestimation of semiconductor band gaps.[73] To better represent the electronic properties of TiO_2 a hybrid Hartree-Fock(HF)/DFT functional can be used in the simulation, but with a large system such as those represented here the cost (depending typically n^4 with a calculation of n basis functions) is often difficult to manage. On top of this, the system also contains semi-metallic graphene which can make hybrid HF/DFT simulations more susceptible to problems with numerical stability. As a result of the high computational expense of studying this interface, there are limits to the methods available for use. In particular for this system it has been more common for studies to employ pure DFT with a Hubbard 'U' correction, which can correctly reproduce the band gaps and band positions of TiO_2, but where the value of the empirical parameter U can be quite ambiguous.[65–67,144,147]

3.4 Aims

The primary aim of this study is to characterise the geometric and electronic properties of the TiO_2/graphene interface. As an improvement over past research into the topic, this study will attempt, for the first time on the chosen model system, to conduct all electronic structure analysis using the hybrid HF/DFT HSE06 functional as opposed to the DFT+U method used previously. The effect of fitting the graphene and rutile (110) crystal systems together is assessed, along with the binding energy and ground-state charge transfer across the interface and finally the electronic structure of the system as a whole. By assessing the electronic properties with hybrid HF/DFT functionals it is hoped that more light could be shed on the mechanism governing

charge transfer across this interface.

3.5 Computational Methodology

3.5.1 Computational Methods

All geometry optimisations and binding energy analyses were carried out using the QUICKSTEP program,[148] within the CP2K sofware package. All pure DFT calculations used the PBE[57] exchange-correlation functional, with empirical Grimme D2[68] dispersion correction included. The calculations utilised Goedecker-Teter-Hutter pseudopotentials[149] and double-zeta basis sets with diffuse and polarisation functions, which have been optimised for use in CP2K.[150] The plane-wave cutoff used for the auxiliary plane wave basis set used in CP2K was 250 Rydberg for calculations of the graphene supercell, and 600 Rydberg for calculations of the rutile and rutile/graphene supercells. Basis set superposition error (BSSE) in calculations of binding energies was corrected using the counterpoise method.[48] For all hybrid DFT calculations the HSE06[62,151] range-separated exchange-correlation functional was used, in addition to the Auxiliary Density Matrix Method (ADMM)[152], featured in the CP2K software package. In such calculations Hartree-Fock exchange is computed with a much smaller auxiliary basis set, while the primary basis set (carried over from PBE-level calculations in this instance) is used in the non-HF exchange part of the functional. The auxiliary basis set cpFIT3 (contracted, 3 gaussian exponents per valence orbital, includes polarisation d-functions) was used for carbon and oxygen, while FIT11 (4 s, 3 p, and 3 d shells and 1 f shell in total) was used for titanium.

As k-point sampling methods were not implemented in CP2K at the time of this work, the optimised coordinates obtained in CP2K HSE06 calculations

were then used as input for calculations with a fine k-point grid using the CRYSTAL14 software package[153]. All density of states, band structure, and graphene strain test calculations were carried out using CRYSTAL14. For calculations of properties of the rutile (110)/graphene interface a Monkhorst-Pack k-point mesh of 12×12×1 was used. For the graphene strain tests a denser k-point mesh of $16 \times 16 \times 1$ was used. Band structures were calculated with 300 points along the path. The DFT functional used for graphene strain tests was PBE, and the hybrid DFT functional used for TiO_2-graphene calculations was HSE06. Empirical Grimme D2 dispersion corrections were added in all CRYSTAL14 calculations. All these calculations used all-electron triple-zeta basis sets with polarisation functions from the work of M. Peintinger *et al.*.[154] In order to obtain band energies relative to the vacuum level, the electrostatic potential of the vacuum region above the unit cell was calculated and was then subtracted from each band energy.

3.5.2 Unit Cell Construction

To construct the unit cell of the rutile (110)/graphene composite, the lowest common multiples of the cell parameters of rutile (110) compared to graphene need to be found. The rutile (110) unit cell has a rectangular shape (see Figure 3.17), with cell parameters $a = 6.529$ Å and $a = 2.995$ Å (obtained from our CP2K PBE calculations of bulk rutile). Graphene was represented with an orthorhombic unit cell for ease of fitting with rutile (110) (see Figure 3.17), with the lattice parameters defined from the experimental value of the graphene carbon-carbon bond length (1.42 Å).

It was found that the best compromise of system size with commensurability was to fit a 3×6 (armchair × zigzag) supercell of graphene with a 2×5 supercell of rutile (110), where the armchair line of graphene runs parallel to

the **a** lattice vector of rutile (110) (Figure 3.17). This composite results in an applied strain to graphene of +2.27% and +1.44% in the armchair and zigzag lines, respectively. This is the same size of the composite unit cell as was used in a previous DFT+U study of the rutile (110)/graphene interface using DFT+U.[65] This smallest commensurate unit cell, if used with a thin 6 atomic layer rutile (110) slab (two unit-cell layers), has a total of 192 atoms (40 TiO_2 units and 72 carbon atoms); the 9 atomic layer (three unit-cell layers) rutile (110) slab results in a 252-atom cell; both were used in this work.

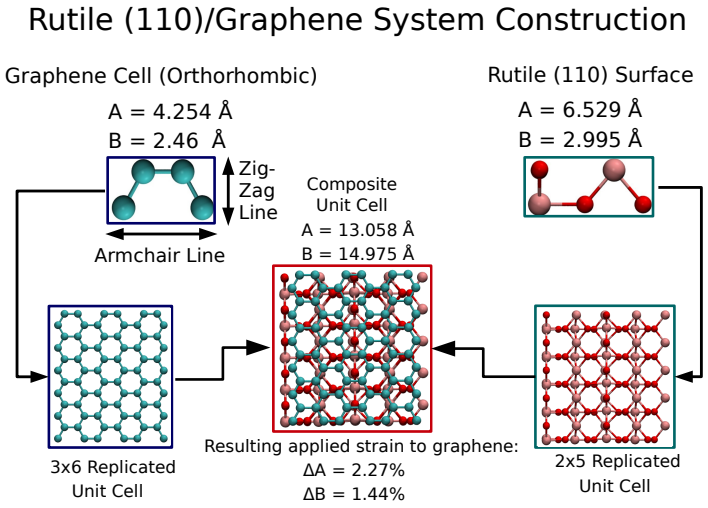

Figure 3.17: Construction of the composite rutile (110)/graphene unit cell used in this research

An alternative UC of the composite was also considered, where the zigzag line of graphene runs parallel to the **a** cell vector of rutile (110). Here the smallest identified commensurate unit cell ("commensurate" defined here as having mismatch under 5%) comprised of an 8×5 supercell of graphene with a 3×7 supercell of rutile (110). This resulted in an applied compressive strain of -1.43% and -0.47% to the armchair and zigzag graphene directions, respectively. This composite UC, containing a total of 412 atoms with a 6 atomic layer slab of rutile (110), was constructed to investigate the effect of orientation of

graphene relative to rutile (110) on the physical properties of the interface. The structure (interfacial C-O distances) and interfacial interaction energies (described in the next section) were very similar to the smaller cell described above and in Figure 3.17, therefore this larger cell was not investigated further.

Larger composite unit cells with smaller lattice mismatch can be constructed but their cell sizes have been found to be too large for practical use, and improvements in quality are expected to be minimal.

3.6 Results and Discussion

3.6.1 Effects of Lattice Strain on Graphene

The fact that the two crystal systems are non-commensurate leads to lattice mismatch and applied compressive or tensile strain at the interface. This issue is encountered *e.g.* in epitaxial films and interfaces[155,156], which often have strong chemical bonding at the interfaces, and also in computational studies of any periodic composite system because of the need to construct finite-size cells.[157] Due to the greater geometric flexibility of graphene relative to rutile, the final lattice parameters are chosen to fit the rutile (110) component, forcing graphene to be deformed. This may change the electronic properties of graphene in such interfaces, compared to isolated graphene. Thus far, computational studies of the TiO_2-graphene interfaces have not explored the structural and electronic effects that this applied strain may have on the graphene component of the system.

The effect of strain was, however, explored in fundamental studies of pristine graphene. While some studies indicated that an applied tensile deformation of 1% to the graphene lattice was sufficient to introduce a band gap[158,159], further investigations[160–164] instead showed that the observed band gap open-

ing in graphene was due to the migration of the Dirac point (where the band structure of graphene moves from insulating to metallic) from its original position at the high symmetry k-point 'K', as a direct consequence of the change in lattice symmetry. It was found that the applied deformation required to introduce a band gap in graphene is at least 26.5% for uniaxial tensile strain (only in the zigzag direction)[160,161]; the gap can also be opened by anisotropic biaxial strain combining tension (11% in the zigzag direction) and compression (-20% in the armchair direction)[164]. Notably, these levels of strain are quite close to the predicted[165,166] and measured[167] failure strain of graphene, $20-25\%$. While these levels of strain are much higher than those encountered in our composite cell, we will set out to explore the effect of low levels of strain on the electronic properties of graphene.

In this work lattice deformation was applied to the orthorhombic graphene cell in the zigzag and armchair directions, up to ±6 % strain in steps of 1% relative to the fully optimised cell. In addition, much larger strain values of up to ±30% (*i.e.* up to the predicted strains for gap opening[160,161] and for graphene's mechanical failure[165–167]) in steps of 5% were also tested to determine the strain required to open a band gap in graphene. The fundamental band gaps (Figure 3.18) were obtained based on the band structures produced for each of the unstrained and strained cells (see examples in Figure 3.19 and Figure 3.20).

The band gap values show that the structure remains a conductor through most of the low values of strain tested. There is no significant change observed in the band structure for graphene under applied tensile or compressive uniaxial strain. The Dirac point remains observable up to ±6% applied strain (the amount of strain that we have assumed acceptable for commensurate cells) and as far as $-20\% - +25\%$ strain. Consequently, the observed fundamental

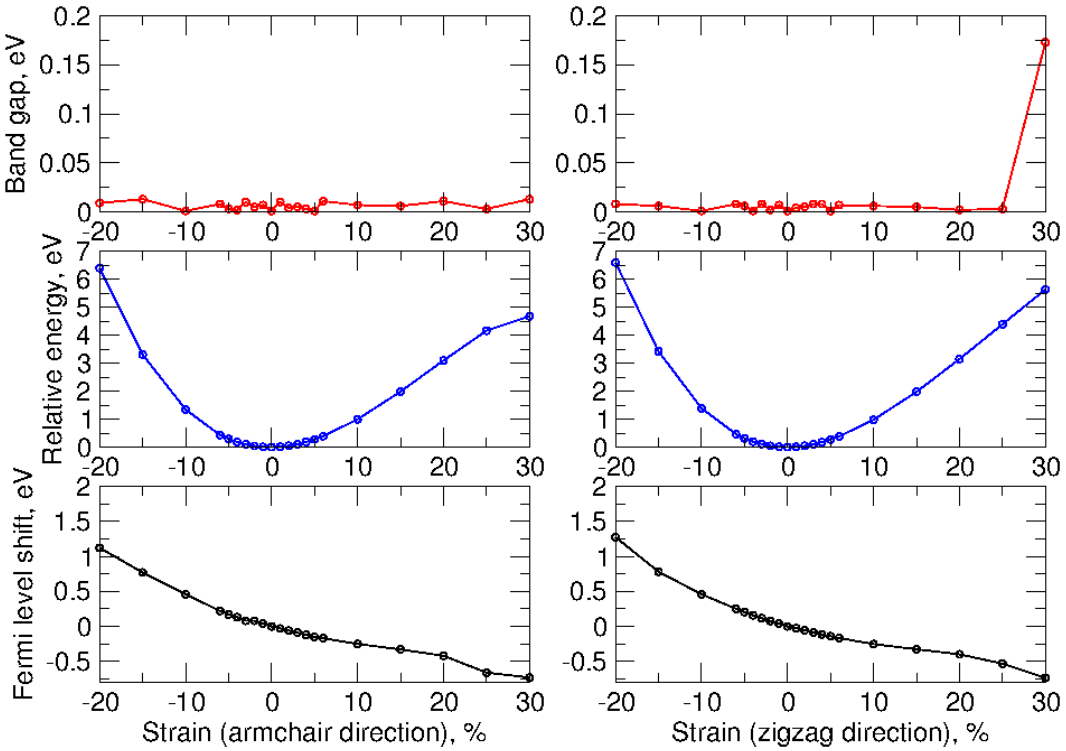

Figure 3.18: Effect of strain on the physical properties of graphene. Top row: change in the calculated band gap; middle row: total energy relative to the fully optimised orthorhombic graphene, bottom row: shift of the Fermi level compared to the unstrained graphene. Left column: strain is applied along the armchair direction: right column: strain is applied along the zigzag direction.

band gaps show very little variation from zero (nor any discernible pattern) for all applied strains between -20% and $+25\%$ in both uniaxial directions. Only at the highest tested level of strain, 30% stretching in the zigzag direction, the Dirac point disappears and a band gap can be observed, which agrees with literature observations[160,161,164].

While there is no band gap opening in graphene observed at low levels of strain, there is however an increase in the total energy, which follows a roughly parabolic trend (Figure 3.18): very small changes (below 0.1 eV) for the first $\pm 2\%$ of applied strain and is relatively minor changes (below 0.5 eV) for the first $\pm 6\%$, followed by a rapid increase. These changes in the total energy result in a shift of the energy levels and thus will result in a change

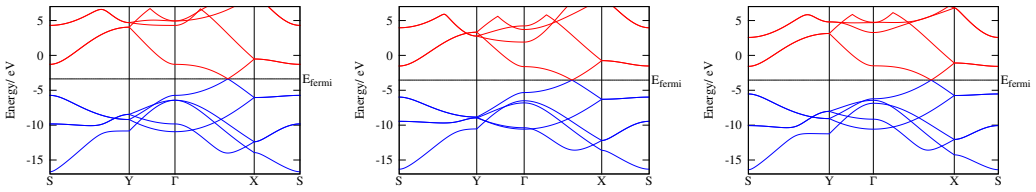

(a) Optimised Graphene (b) 6% ZigZag strain (c) 6% Armchair Strain

Figure 3.19: Band structures of orthorhombic graphene cells: optimised (a), 6% zigzag tensile strain (b), and 6% armchair tensile strain (c). Occupied bands are represented in blue, unoccupied bands are in red, and the dashed line represents the Fermi level. Slight changes in the band shapes and a migration of the Dirac point along the Γ-X line can be seen.

in the work function of graphene in the composite: the change in the work function is small (within ±0.2 eV) for the first ±6% of applied strain, but becomes larger for hypothetical large applied strain (Figure 3.18). Any shift in band energies will therefore have a direct impact on where the valence band of graphene lies in relation to rutile (110), and at large strains it may affect the predicted transfer of charge across the interface.

In conclusion, we have demonstrated that the small applied strain on the graphene component in our composite system will not disrupt the semimetallic properties of graphene in the system, nor will it have a significant effect on its band positions.

3.6.2 Binding Properties of the TiO_2/Graphene Interface

To investigate the physical properties of the TiO_2/graphene composite system, the interlayer spacing, and interface interaction energies and binding energies were calculated using CP2K with the PBE+D method. For this work the interlayer spacing is determined as the vertical (z-axis) distance, in Ångströms, between the uppermost atomic layer of two-coordinated oxygen atoms of rutile

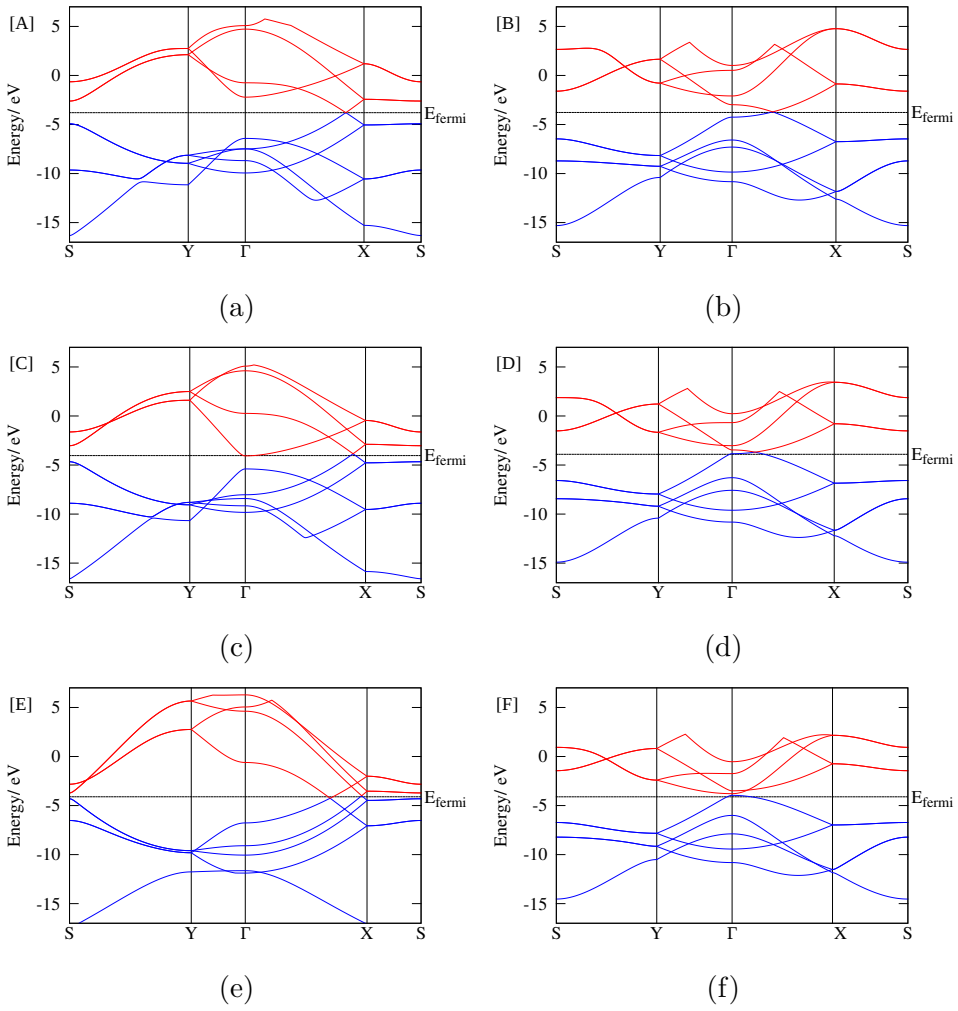

Figure 3.20: Band structures of orthorhombic graphene unit cells with differing amounts of uniaxial strain: 20% armchair (a) and zigzag (b), 25% armchair (c) and zigzag (d), and 30% armchair (e) and zigzag (f).

(110) and the graphene layer. The interface interaction energy is defined as:

$$E_{int} = E_{tot} - E_{ru-opt} - E_{gr-opt} + E_{BSSE} \tag{3.2}$$

where E_{int} is the interaction energy, E_{tot} is the computed total energy of the system, E_{ru-opt} is the total energy of the optimised rutile (110) slab, E_{gr-opt} is the total energy of the optimised graphene sheet, and E_{BSSE} is the basis set superposition error correction. The interaction energy can be decomposed

into the *deformation* energy E_{def} (the energy change when deforming the TiO_2 and graphene components upon formation of the composite structure) and the *binding* energy E_{bind} (the energy gain due to the binding of these deformed components, or, the interaction energy excluding the change due to deformation) defined as:

$$E_{bind} = E_{int} - E_{def} \tag{3.3}$$

$$E_{def} = (E_{ru-def} - E_{ru-opt}) + (E_{gr-def} - E_{gr-opt}) \tag{3.4}$$

where E_{ru-def} and E_{gr-def} are, respectively, the energies of the rutile (110) and graphene components in the geometry of the composite system. Interaction and binding energies and interlayer spacing for our system and a few reference systems are provided in Figure 3.21. BSSE energies calculated for the 6 and 9-atomic layer composites are 0.029 eV and 0.049 eV for each, respectively. The interaction energies calculated in this work (-0.019 to -0.023 eV per carbon atom and -1.35 to -1.67 eV per cell, Table 3.1) are very similar to the literature values for the same rutile (110)-graphene interface obtained using a different method (LDA+U)[65]. These weak interaction energies indicate physisorption. The alternative orientation of graphene above rutile, where the zigzag line of graphene is parallel to the a cell vector of rutile (110), results in very similar energies per carbon atom, confirming that interaction energies are very weakly dependent on the interfacial orientation, as expected for physisorption. Therefore the selected orientation of graphene above TiO_2 is representative of the properties of the many possible random orientations which may occur in experimental TiO_2/graphene composites.

Comparing our interface interaction energies (scaled per carbon atom) to the literature values for the anatase (101)-graphene interface (-0.032 to

-0.050 eV per carbon atom),[67,168] the rutile (110)-based system is less strongly bound, probably because fewer atoms in the rutile (110) surface are close enough to graphene (only 2-coordinated surface oxygens). Comparing the rutile (110)/graphene composite to graphite, the composite's interaction energies per carbon atom are half as small as computational and experimental values for the interlayer binding in graphite and multilayer graphene[169,170] — this can be expected, since the TiO_2-graphene interface does not offer π-stacking such as found in graphite.

The deformation energies are 1.03 and 1.56 eV for the 6- and 9-atomic-layer TiO_2 slabs, respectively. A large part of this is the deformation of graphene resulting mainly from the lattice mismatch (see the computational methods section). This gives an energy change due to deformation of 0.68 and 0.83 eV/cell for the 3 and 2-layer composite systems respectively. The deformation of rutile (110) costs 0.22 and 0.89 eV in the 6- and 9-atomic-layer TiO_2 slabs, respectively.

The difference between the 6-atomic layer and 9-atomic layer TiO_2 systems is related to the well-known oscillation of physical properties in odd- and even-layer rutile (110) slabs: for example, odd-layer rutile (110) slabs are found to have higher surface energies than even-layer slabs.[171–174] The results of this work are in agreement with this pattern: since the 9-layer slab has a larger surface energy, it displays a larger energy gain due to the formation of the interface with graphene, especially obvious in the binding energies which do not include deformation.

To study the effect of the alignment of graphene above the rutile (110) surface, the potential energy surface (PES) was sampled by moving the graphene sheet in both the A and B directions of the composite unit cell (defined in Figure 3.17), initially in steps of 0.6 Å in both directions and then additionally in

System	Method	Interaction Energy			Interlayer Spacing (Å)
		eV	per C atom (eV)	mJ m^{-2}	
This work (6 atomic layers rutile (110))[a]	PBE+D[c]	-1.35 (-2.40)	-0.019 (-0.033)	-0.11 (-0.20)	2.90
This work (9 atomic layers rutile (110))	PBE+D[c]	-1.67 (-3.24)	-0.023 (-0.045)	-0.14 (-0.26)	2.76
This work (6 atomic layers rutile (110))[b]	PBE+D[c]	-3.67 (-4.55)	-0.023 (-0.028)	-0.14 (-0.18)	2.90
Du *et al*[65] (9 atomic layers rutile (110))	LDA+U[d]	-1.69	-0.023	-0.14	2.75
Li *et al*[67] (7 atomic layers anatase (101))	LDA+U[e]	-1.49	-0.050	-0.29	2.57
Ferrighi *et al*[168] (7 atomic layers anatase (101))	PBE-D2[f]	-1.25	-0.042	-0.24	2.84
	PBE-D2[g]	-1.01	-0.034	-0.19	2.97
	B3LYP-D*[f]	-1.44	-0.048	-0.28	2.84
	HSE06-D2[f]	-1.33	-0.044	-0.26	2.77
	vdw-DF2[f]	-0.95	-0.032	-0.18	3.05
Graphite (this work)	PBE+D[c]	n/a	-0.044	-0.27	3.35
Graphite[169]	PBE+D	n/a	-0.051	-0.31	3.35
Graphite[175]	vdW-DF	n/a	-0.050	-0.31	3.59
Graphite[176]	LDA	n/a	-0.024	-0.15	3.33
Multilayer graphene[f][170]	Experimental	n/a	-0.035	-0.21	n/a

a: using a 2×5 rutile (110) slab; b: using a 3×7 rutile (110) slab; c: using CP2K d: using VASP; e: using CASTEP; f: using CRYSTAL14; g: using Quantum Espesso;

Table 3.1: Interlayer interaction energies (with binding energies in brackets) and interlayer spacings obtained in this work and in several published systems (see references).

steps of 0.2 Å in the A direction. The analysis showed very little variation in energy (0.03 eV) upon displacement along the B direction (graphene moving along the row of 2-coordinated oxygens of TiO_2), while the displacement along the A direction showed noticeable changes in energy. It can be seen in Figure 3.21 that the total energy increases as the carbon atoms in the graphene layer approach the 2-coordinated oxygen atoms in the rutile (110) surface layer, and is the most favourable when C–C bonds in the graphene layer rest over the top of these surface oxygen atoms (see insets in Figure 3.21). The inter-

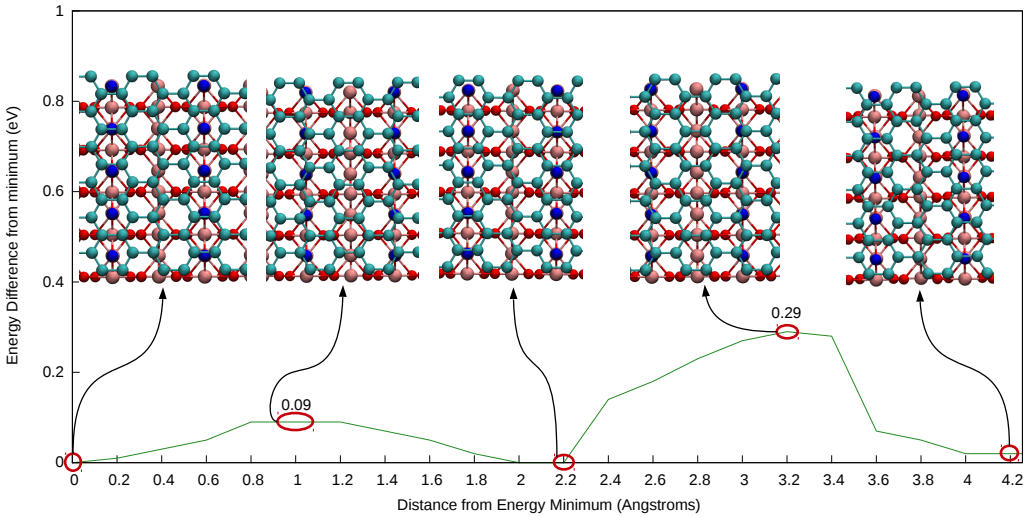

Figure 3.21: One-dimensional potential energy surface (PES) plot of the rutile (110)/graphene composite. Insets show the alignment of graphene carbon atoms (teal) with the surface 2-coordinated oxygen atoms (blue) at several positions (maxima and minima) of the PES.

action energy varies by up to only 0.29 eV/cell – a small variation, suggesting that there is no strongly preferred position of graphene above rutile (110), and a variety of graphene/TiO_2 positions and orientations are likely to exist in experimental systems.

In conclusion, we have demonstrated that the interface between rutile (110) and graphene forms through a physisorption interaction, slightly weaker than the strength of interaction in multilayer graphene. The potential energy surface for this system is largely flat in shape, however, there exists a weak preference for aligning the surface 2-coordinated oxygen atoms with the mid-point of the carbon–carbon bonds in the graphene layer above.

3.6.3 Electronic Properties of the Rutile (110)/Graphene Interface

To analyse the posibility of charge transfer in the rutile (110)/graphene interface, we investigated the alignment of the electronic energy levels of TiO_2

and graphene in the composite system. Projected density of states (PDoS) spectra for the 6- and 9-atomic-layer rutile (110)/graphene composites and their corresponding isolated rutile (110) slabs have been calculated using the HSE06 hybrid functional in CRYSTAL14 (see Figure 3.22, all DoS plots incorporate vacuum level correction, as stated in the Computational Methods section).

The band gaps of isolated TiO_2 slabs are found to be 3.9 eV in the 6-layer system and 2.8 eV in the 9-layer system (band edges are shown with dashed lines in Figure 3.22). This variation in the band gap values reflects the odd-even slabs' oscillation of properties, characteristic of rutile (110): the band gaps are notably larger than the bulk value for even-layer slabs and smaller for odd-layer slabs.[171–174] Overall, the band gaps found in this work are in good agreement with the value of 3.39 eV found for bulk rutile calculated with HSE06.[73] and with the experimental values of 3.0 eV for the optical gap[177] and 3.3 ± 0.5 eV fundamental band gap[178] for rutile.

The graph Figure 3.22 shows that both in isolated TiO_2 and in the composite system the conduction band (CB) is primarily made up of titanium states, and the valence band (VB) of oxygen states, as is known from the literature on TiO_2 bulk and surfaces.[172,173] In the 6 atomic layer rutile (110) systems the conduction band contains both the 5-coordinated Ti (Ti_{5c}) and 6-coordinated Ti (Ti_{6c}) surface states in roughly equal intensities (Figure 3.22). In the composite system containing the 9 atomic layer rutile (110) slab, the states localised on 5-coordinated titanium atoms and subsurface titanium atoms immediately below dominate in the low-energy part of the CB. The most prominent difference between the isolated rutile (110) slab and the composite is the shift of the surface 5-coordinated titanium atoms' states (dark blue line in Figure 3.22) towards the low-energy part of the CB of the composite, which confirms elec-

tronic interaction between the TiO_2 surface and graphene.

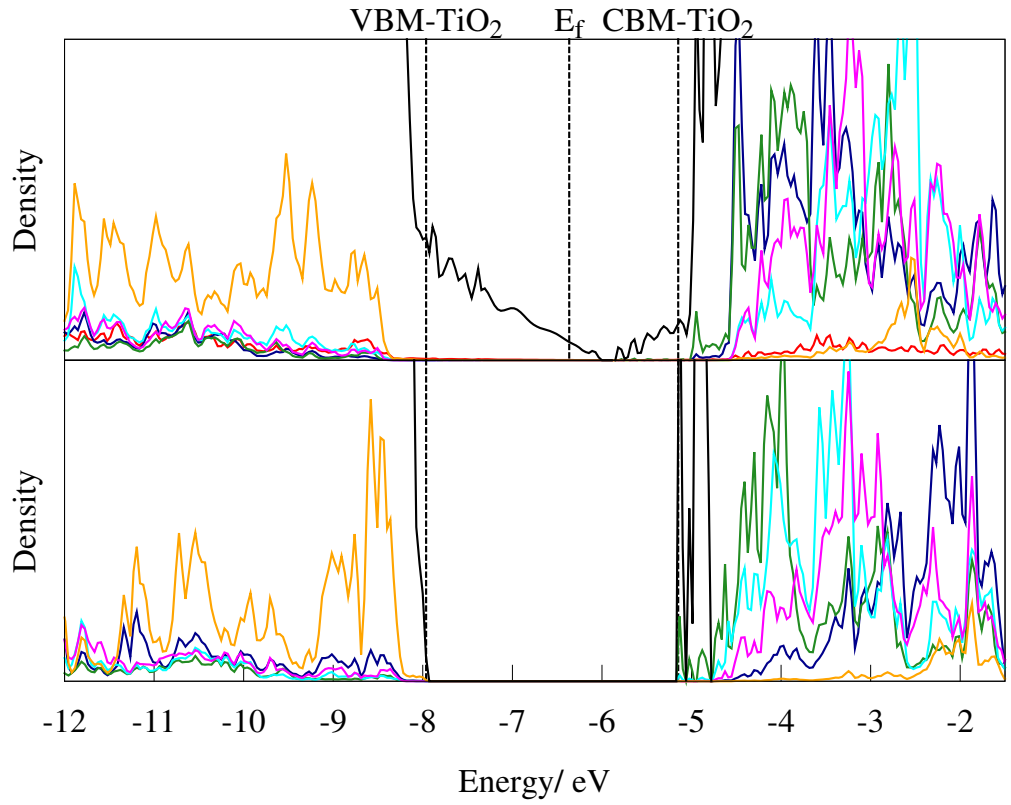

Figure 3.22: PDoS spectra of the 9 atomic layer rutile (110) slab (bottom) and its composite with graphene (top). The projections shown are: carbon (red), surface site 5-coordinated titanium (dark blue), surface site 6-coordinated titanium (cyan), subsurface titanium positions: below surface Ti_{5c} (green); below surface Ti_{6C} (purple), 2-coordinated oxygen (orange). The total DoS is shown in black. The dashed lines represent the valence and conduction bands of the isolated rutile (110) slab and the Fermi-level of the composite.

The high-resolution PDoS plots in Figure 3.23 show that both the upper part of the valence band and the lowest part of the conduction band of the composite system (both located in the TiO_2 band gap region) are made up mostly of graphene states. Notably, the graphene-dominated conduction band edge is ~ 0.8 eV and ~ 1.3 eV, in composites with the 9- and 6-atomic-layer rutile (110) slabs respectively, below the Ti-dominated high-intensity states of the conduction band (which start between -5.0 and -4.5 eV). We observe

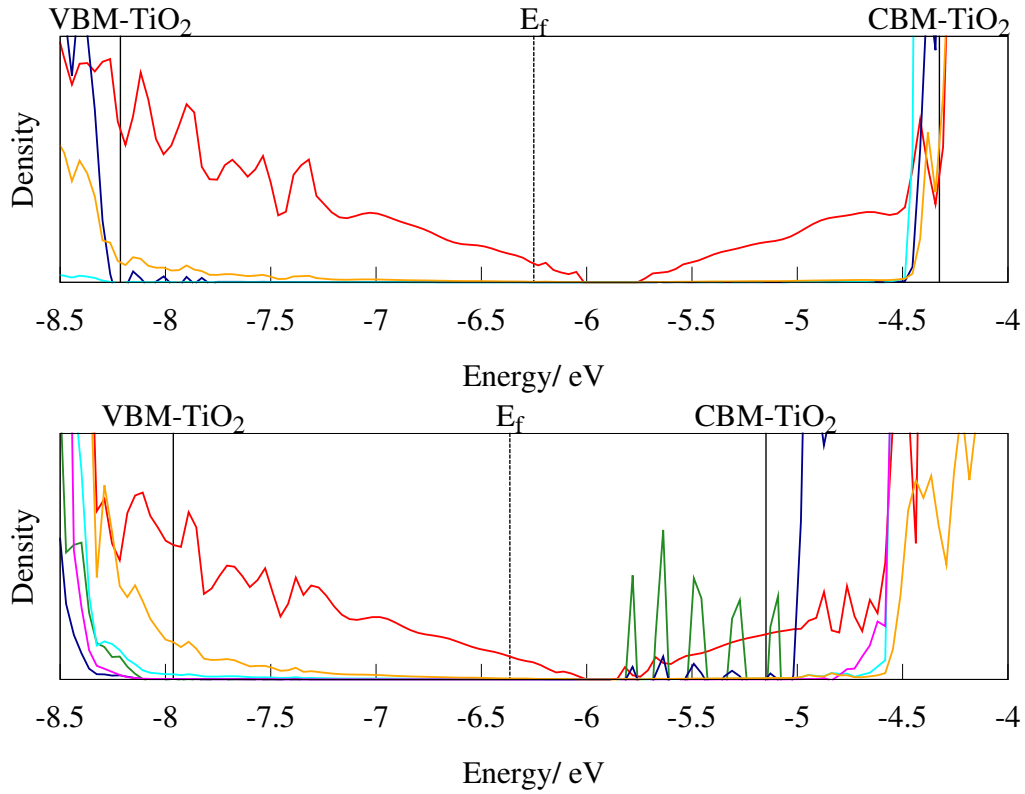

Figure 3.23: PDoS spectra of the 6 (top) and 9 (bottom) atomic layer rutile (110)/graphene composites. The projections shown are: Carbon (red), 5-coordinated titanium (dark blue), 6-coordinated titanium (cyan), subsurface titanium (green: below 5-coordinated surface site, purple: below 6-coordinated surface site), and 2-coordinated oxygen (orange). The dashed line represents the Fermi level, the solid black lines represent the valence and conduction band edges of the isolated rutile (110) slab.

that the unoccupied states of graphene lie well below the unoccupied states of TiO_2 which is in agreement with experimental work function values, which show graphene to have a larger work function (reported as 4.5 eV[179] or between 4.89 and 5.16 eV,[119]) compared to TiO_2 (experimentally reported as -4.2 eV[180] and calculated as -4.3 eV[181] with respect to vacuum).

Note that this alignment of Ti and carbon states is different from several recently published studies of TiO_2-graphene interfaces, where the graphene conduction band edge as usually found to lie near, just below, or just above the TiO_2 band edge.[65,67,168,182,183] There is, however, no agreement on the align-

ment of C- and Ti-based conduction band states in the published studies, and there are examples of C states being lower in energy than Ti states, similar to the results of this work, notably in graphene interfaces with anatase (001)[144,184] and rutile (110).[185] This difference is likely to be caused by differences in the electronic properties of anatase and rutile polymorphs of TiO_2 (indeed, the CB of anatase is believed to be $0.2 - 0.4$ eV below that of rutile[45,181]). It is also likely that the TiO_2 band positions in the DFT+U calculations[65,67,144,184,185] are affected by the choice of the 'U' parameter which is applied to describe the on-site Coulomb interaction of Ti 3d electrons. We believe that hybrid functionals offer a less ambiguous description of band gaps and band positions. In particular, the HSE06 functional used in this work accurately predicts the band gaps, band positions and defect states in TiO_2.[45,73,186] This functional has also been successfully used to describe optical properties of carbon nanotubes,[187] band gaps of carbon nanoribbons[188] and workfunctions of graphene, carbon nanoribbons and nanotubes[189,190]. With this good description of the individual TiO_2 and nanocarbon components, it can be expected that this functional's description of the TiO_2-graphene interface is also reliable.

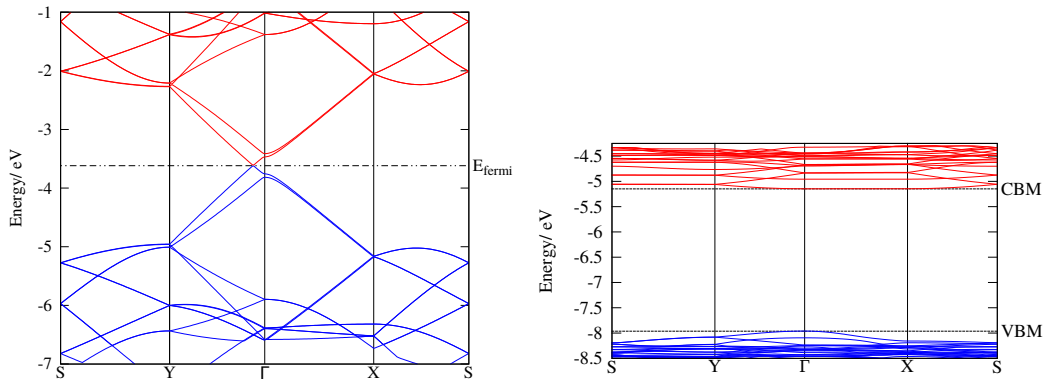

(a) (b)

Figure 3.24: Band structures of the graphene (a) and rutile (b) components of the graphene/rutile (110) composite in isolation from one another, calculated using the HSE06 functional.

This position of graphene-dominated states far below TiO_2 states rather than just below TiO_2 states has important implications for charge transfer in this composite system: it is strongly favourable for photoexcited electrons to decay to the bottom of the conduction band, *i.e.* to these low-lying graphene-dominated states.

The high-resolution PDoS plots (Figure 3.23) show a clear qualitative difference between the composite systems involving 9-atomic-layer and 6-atomic layer TiO_2 slabs. In the 6-layer-based composite, only carbon-based states appear in the band gap of TiO_2, suggesting very little electronic interaction between graphene and TiO_2. By contrast, in the 9-layer-based composite, Ti-based states appear together with the carbon-based states near the bottom of the conduction band, in what would be the TiO_2 band gap. This points to electronic interaction between carbon and TiO_2 components, as these states are not present in the rutile component alone (see Figure 3.22). This mixture of titanium and carbon states in the conduction band is likely to affect the nature of charge transfer in this system. To investigate the origin of these Ti states, we plot the band structure and then explore the atomic orbitals which make up these bands.

The band structure of the 9 atomic layer composite is compared to the corresponding DoS spectrum in Figure 3.25. The band structure clearly shows that the Dirac point of graphene is preserved and can be seen close to the Γ point, along the $\Gamma-Y$ line. The Fermi level lies slightly below the Dirac point, indicating hole doping of graphene; this is confirmed by the electron density difference plot (Figure 3.26), which shows some electron transfer from graphene to TiO_2. The amount of charge transferred has been evaluated as 0.68 electrons per cell (or 0.01 electrons per carbon atom), which is comparable to 0.02 electrons per carbon found for the similar system in Ref.[65] The downshift

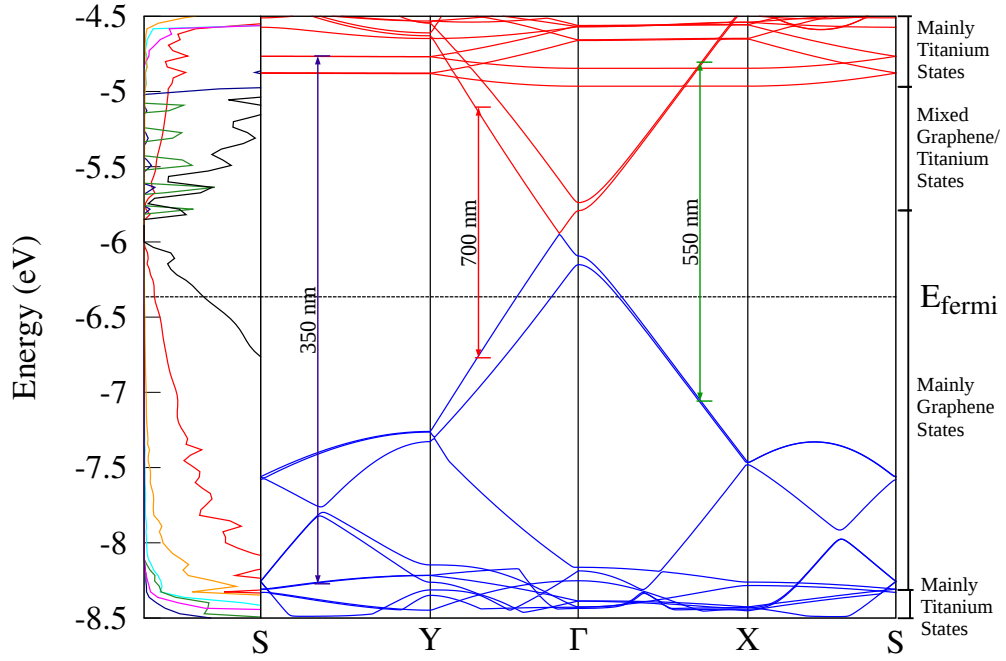

Figure 3.25: Band structure of the 9 atomic layer rutile (110)/graphene composite system, showing 10 occupied bands (shown in blue) and 10 unoccupied bands (in red). The PDoS spectrum of this interface is shown to the left, with the total DoS included in black, and guide-lines relating parts of the DoS spectrum to the band structure. Additional annotations show the energies of possible electronic transitions and the composition of various regions of the band structure (assigned according to the analysis shown in Figure 3.27)

of the Fermi level (0.42 eV) is slightly smaller than in the previously reported study of this interface using the DFT + U method (0.65 eV[65]). Comparing the band structure of the composite system in Figure 3.25 with the band structure of the isolated rutile slab and isolated graphene sheet (Figure 3.24), we can see that the electronic structure of TiO_2 and graphene remain essentially intact in the composite system. Although the Dirac point has not been captured in our DoS plots, it is clearly present in the band structure. The small[67,182,185] or very small[168] band gaps observed in some of the previous studies of similar interfaces have likely been caused by the use of insufficiently dense k-point grids, similar to the early studies of strained isolated graphene alone[158,159].

The absence of a band gap means that electrons can be easily promoted to the unoccupied graphene states. From these spectra it can also be seen that the thermodynamically favoured location of photoexcited electrons will be on graphene.

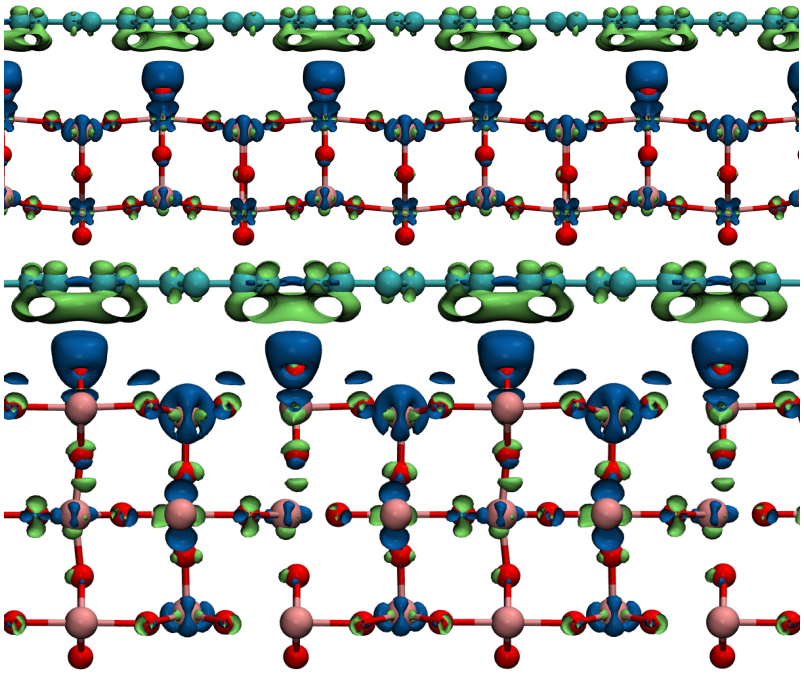

Figure 3.26: Charge density difference plots of the 6-atomic layer (top) and 9 atomic layer (bottom) graphene/rutile (110) composite systems. Charge accumulation is shown in blue and charge depletion is shown in green

The question still remains about the origin of Ti-based states in the region corresponding to the band gap of pure TiO_2. These states do not correspond to any special points in the conduction band (see Figure 3.25). The DoS plots in Figure 3.23 show that these states are localised on subsurface (bulk-like) Ti atoms of the 9 atomic layer rutile slab. The 6 atomic layer slab, which has no bulk-like Ti atoms, has no such gap states. This shows that subsurface Ti atoms are essential for strong electronic interaction between TiO_2 and graphene and that the 6 atomic layer slab, which has no subsurface atoms, is too small to model the rutile-graphene interface. The narrower band

gap of the odd-layer rutile slab also brings the conduction band edge closer to the highest occupied band of graphene, facilitating the electronic interaction between graphene and TiO_2 (in agreement with the larger binding energy of graphene with the 9 atomic layer rutile slab). The localisation on subsurface Ti atoms is in qualitative agreement with the LDA+U study of Du *et al.*[65], which showed that the first two CB states are predominantly based on graphene and subsurface Ti atoms below surface Ti_{5c}. From these results one can see that, in order to correctly model the properties of this composite system, at least one subsurface layer of rutile (110) must be present.

To understand the origin of these Ti-based gap states, eigenvalues (atomic orbital (AO) coefficients) of several highest occupied and lowest unoccupied bands were analysed. Squares (complex conjugates) of AO coefficients $c_{i,j,k}c^*_{i,j,k}$ (where i is the atom number, j is the orbital (eigenstate), k is the k-point) were calculated and summed over all Ti, all O and all C atoms, to give the contributions of Ti, O and C to each eigenstate at each k-point: $\sum cc^*_{Ti,j,k}$, $\sum cc^*_{O,j,k}$ and $\sum cc^*_{C,j,k}$. The analysis of the AO coefficients at the k-points along the band structure path (Figure 3.27) confirms that the highest occupied band (labelled "VBM") as a whole consists mainly of carbon states. Similarly, the 3 highest energy VBs consist entirely of carbon states, and titanium and oxygen states begin to emerge at the VBM-4 and lower (energy -8.3 eV and below in Figure 3.25). The lowest unoccupied band (labelled "CBM") around the Γ-point, and along most of the Γ-X and Γ-Y lines, consists mainly of carbon states, while at and around k-points X, Y, and S it is predominantly titanium. These rutile titanium bands can be identified easily by their characteristically flat profiles – they are essentially the same as lowest-energy unoccupied bands of isolated rutile (also seen as intense peaks in the DoS, starting at ~ -5.0 eV, see Figure 3.22 and Figure 3.23).

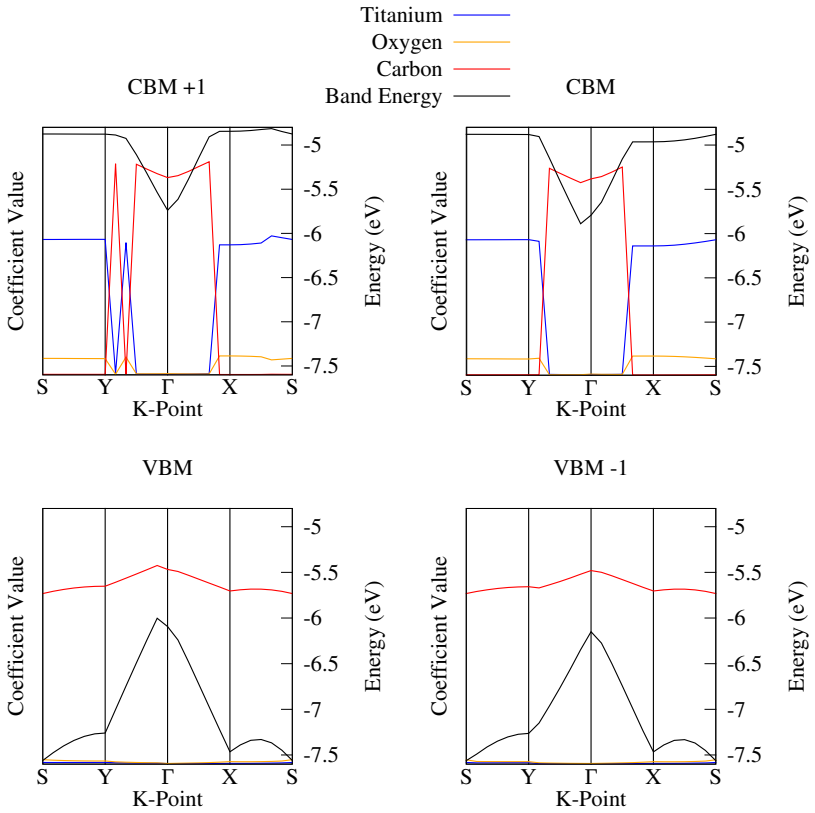

Figure 3.27: Energies of selected bands (VBM-1, VBM, CBM, CBM+1), plotted together with the sums of squared atomic orbital coefficients for all titanium, oxygen, and carbon species in the 9 atomic layer composite system. These data points cover all k-points in the path chosen for the band structure in Figure 3.25

The band lines in Figure 3.25 and Figure 3.27 look smooth and do not reflect the sharp Ti peaks seen near the bottom of the CB in the DoS. However, the band structure is plotted along special high-symmetry lines in the Brillouin zone (BZ), while the DoS is calculated by integrating over the whole BZ. To explain the DoS shape, we analysed atomic orbital coefficients of the highest occupied and two lowest unoccupied states across the full BZ. The contributions by atom type ($\sum c^{c}{*}_{Ti,j,k}$, $\sum cc^{*}_{O,j,k}$ and $\sum cc^{*}_{C,j,k}$) were calculated for VBM, CBM and CBM+1 on the $12 \times 12 \times 1$ grid of k-points covering the whole BZ (the same grid as used in the DOS calculations).

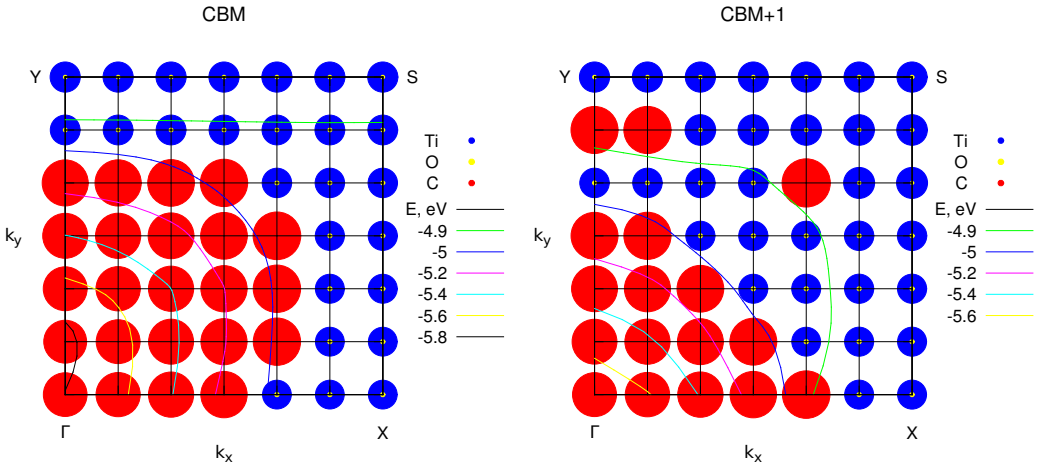

Figure 3.28: Sums of squared atomic orbital coefficients (shown as circles) for all titanium, oxygen, and carbon species in the 9 atomic layer composite system, plotted in the irreducible part of the Brillouin zone of the rutile (110)/graphene composite system. The areas of the circles correlate with the magnitude of each atomic species' contribution to the eigenstate (CBM or CBM+1) at each k-point (blue circles for Ti, yellow for O, red for C). The variation of these bands' energies across the BZ is shown with thin contour lines.

Figure 3.28 shows these AO contributions for the CBM and CBM+1, plotted on a 2D grid covering the irreducible part of the BZ of the composite. The sizes of circles in Figure 3.28 correspond to the magnitude of the species' contribution to each of these bands at each k-point. The VBM (results not shown) is predominantly $(97 - 99\%)$ composed of C states at all considered k-points, as shown by our DoS and band line analysis. The CBM is separated into two regions. Across most of the BZ (from -6.0 to -5.0 eV), this band is entirely localised on carbon atoms with negligible contributions from Ti and O atoms; however, the regions of the BZ immediately next to the X-S and Y-S lines (at > -5.0 eV) are almost entirely localised on Ti atoms with very small contributions of O atoms. The second unoccupied band (labelled "CBM+1") has the most interesting pattern of atomic orbitals' contributions across the BZ: the regions next to the X-S and Y-S lines are again almost entirely lo-

calised on Ti atoms, the region around the Γ point is entirely localised on C atoms, while in the intermediate BZ region, as the electron energies increase, the main contributors change from C to Ti. Thus, Ti contributions appear at lower energies than in pure TiO_2. Therefore, this second unoccupied band is not entirely graphitic and demonstrates electronic interaction between the carbon and TiO_2 components of the composite. Interestingly, there are no "mixed" states equally made up of C and Ti at any of the points in the BZ in this region; there is clear separation between C-dominated and Ti-dominated states.

The spatial charge density difference observed in Figure 3.26 shows that the non-bonding orbitals of the surface 5-coordinated and subsurface 6-coordinated titanium atoms accumulate electron density when interfaced with graphene. This charge accumulation is only observed to be significant for the surface 5-coordinated and subsurface 6-coordinated titanium atoms, and appears to a much lesser extent in the surface 6-coordinated titanium atoms and 6-coordinated titanium atoms directly below. The 5-coordinated and subsurface 6-coordinated titanium states shown in the DoS appear to be very spatially localised, based on the narrow energy width of the states, and thus likely result directly from the transfer of charge from graphene to TiO_2. The interaction between graphene and these particlar subsurface titanium atom orbitals in the conduction band seen in this work has also been demonstrated at the LDA+U level by Du *et al.*[65] While it is therefore clear that these spatially localised titanium atom states arise from ground-state charge transfer from graphene to TiO_2, the reason for their energy placement below the TiO_2 conduction band is less clear.

From this analysis of the electronic structure, and from the evidence in published research,[15,65,107] it is now possible to infer more details about the

mechanism of photosensitisation enhancement upon irradiation of this composite system. The combination of our DoS, band structure, and atomic orbital coefficient analysis enable us to make predictions about the likely nature of photoexcitation transitions in the TiO_2-graphene system. We note that a calculation of transition dipole moments and electronic excitations would be necessary for a full description of photoexcitation processes. This is beyond the scope of the current work, however, a qualitative picture of photoexcitation can be obtained from our DoS and atomic orbital data. Our data suggest that the mechanism of photoexcitation will differ depending on the energy of a given incident photon. For a visible-region photon (2.5–1.5 eV, some possible transitions shown schematically by red and green arrows in Figure 3.25), electronic transitions must originate from a carbon state within graphene. The excited state reached by the transition may then be either carbon- or titanium-based depending upon the photon energy. Very low-energy photons can excite only carbon π to π^* electronic transitions (*i.e.* no charge transfer). Visible-light photons can span the band gap further away from the Γ point and nearer the points X and Y, where titanium states begin to appear in the unoccupied states. Then, these titanium states may accept the photoexcited electron, resulting in graphene $\rightarrow$ TiO_2 transition.

Thus, the experimentally observed broadening of the absorption range of the TiO_2 composites[16,100,101,106,127,129,130,134,136] is attributed to the presence of these mixed graphene and titanium states. Transfer of photoinduced electrons to TiO_2 creates an efficient photoreduction catalyst[191,192]. Note however, that the lowest-energy unoccupied states are all graphene-based (both at the bottom of the conduction band and just above the Fermi level), therefore the thermodynamically favourable process is for the photoexcited electrons will eventually decay to these lowest-energy unoccupied carbon states. Similarly,

if an electron is supplied from elsewhere (e.g. using molecular sensitisers[193]), it will most likely end up in these lowest-occupied carbon states. Both processes make graphene the electron-rich part of the composite, so that it may act as an electron shuttle in complex photocatalyst architectures, as proposed by Kamat.[194] It is also those electrons in the lowest-energy unoccupied carbon states which are then likely to recombine with holes in the valence band.

Photons in the ultraviolet range (> 3.0 eV) are able to excite transitions that originate from deeper levels in the lower VBs, which are localised on TiO_2. The accepting states are likely to be mixed graphene/titanium or purely titanium based, thus the overall direction of the charge transfer in this case is from TiO_2 to graphene, as observed in many UV-Vis experiments.[15,124]

In all cases that we have discussed, the final states reached by photoexcitations are likely to involve both carbon- and titanium-based states. The direct carbon π to π^* electronic excitations are likely to be more intense than charge-transfer carbon$\rightarrow$ TiO_2 excitations, even if the energy of the excitation is the same. These carbon π to π^* excitations, however, can be followed by excited-state charge injection to same-energy titanium-based states, as observed by Manga *et al*[124] and described computationally by Long *et al.*[66] Experimental data showing the visible-region photon absorption enhancement provided by graphene in this system[15,107] support this model of a combination of direct (e.g. carbon $\pi - \pi^*$) and charge-transfer excitations.

Chapter 4

The Reduced Graphene Oxide/TiO_2 Photocatalytic Interface

4.1 Oxygen Defects in Graphene/TiO_2 Composites

A number of theoretical studies (including this work) have so far looked at the graphene/TiO_2 composite using "pristine" (i.e. unmodified) graphene as a model.[65,66] The pristine graphene model serves as a useful first approximation, however the vast majority of experimentally-produced samples of the graphene/TiO_2 composite system are derived from a graphene oxide (GO) precursor (structure described in[6,7,195,196]). The precursor is typically reduced in the synthesis procedure to form what is referred to in the literature as reduced graphene oxide (RGO, or rGO), which differs from idealised pristine graphene due to the presence of oxygen defects. Past theoretical chemistry studies have modelled the composite system using pristine graphene[65–67], though some at-

tempts have been made to probe the properties of oxygen functional groups and their role in the composites.[147,168,182,197] These oxygen defects are, as shall be demonstrated in this chapter, a critical aspect of the mechanism by which this composite material acts as a photocatalyst.

4.1.1 Introduction

Physical Structure of Graphene Oxide and Reduced Graphene Oxide

To understand the properties of the oxygen defects present in RGO, we will start by looking at the GO precursor. A typical GO synthesis begins by forming "graphite oxide" from either a natural or synthesised graphite sample. This is done using a combination of concentrated nitric (HNO_3) and sulphuric (H_2SO_4) acids and a suitably strong oxidising agent. For the next step the synthesis method varies according to which oxidising agent is used: Staudenmeier's method,[198] using $KClO_3$; and Hummers and Offemann's method,[121] using $KMnO_4$. Both methods yield a graphite oxide product. Graphite oxide is highly decorated with oxygen functional groups, which allows for the sample to be ultrasonically exfoliated in a polar solvent to yield a suspension of GO. Graphite oxide differs from GO as the sheets of graphite oxide are still bound together by the interactions of oxygen functional groups between different graphite sheets. The as-synthesised GO can then be reduced, either prior to or after being deposited on a TiO_2 substrate, using a preferred reduction method (see below). The reduction process mostly removes oxygen functional groups from the GO, yielding RGO as the product.

Numerous methods of GO reduction exist in the literature, and the choice of reduction method directly affects the number of remaining oxygen functional groups in the RGO product. Synthesised GO typically has a carbon atom

to oxygen atom ratio of around 2:1.[199–201] Chemical reduction methods, which use reducing agents such as hydrazine and sometimes even vitamin C (ascorbic acid), typically yield a carbon:oxygen ratio of around 6:1 ($\sim$ 15% oxygen).[201] A popular alternative is to use "hydrothermal" reduction, where the samples are autoclaved at high temperatures (150 °C to 200 °C), resulting in carbon:oxygen ratios of roughly 12:1 ($\sim$ 8%).[15,124,128,200] Finally there is the photocatalytic reduction method, where TiO_2 is used to photocatalytically reduce the GO substrate, which is often only used in the synthesis of RGO/TiO_2 composites and yields similar carbon:oxygen ratios as chemical reduction.[124,126]

The oxygen content of a sample can be gleaned from either X-ray photoelectron spectroscopy (XPS)[15,127,128] or resonance Raman spectroscopy.[15,127] In an XPS spectrum the carbon 1s signal can be de-convoluted to show the different components of the observed peak. The separate components correspond to electrons in different chemical environments, and the relative intensities of these components can then be used to give a measure of where the standard binding energies of electrons in particular chemical environments are taken from literature sources. Analysing the area under each separate peak can give a reasonably accurate estimation of oxygen content from the relative abundance of C−C/C=C and C−O bonded carbon atoms. In resonance Raman spectra of RGO and GO samples there are characteristic D and G bands (at 1350 cm^{-1} and 1590 cm^{-1} respectively). The G-Band is caused by the stretching of sp^2 C−C carbon atoms, while the D-band is caused by the effect of defects on the carbon sp^2 network — which can be oxygen defects or sp^3 carbon atoms.[202] The ratio of measured intensities of these two bands can be used to give a rough indication of the oxygen content of the sample. The resonance Raman method gives little indication of the chemical identities of the defects present however, and thus should be used in conjunction with element-specific

data such as XPS and elemental analysis.

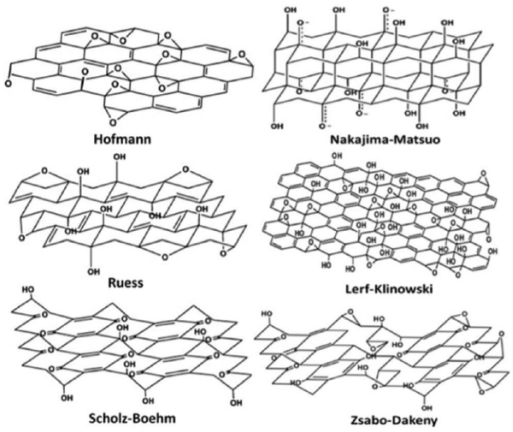

Figure 4.1: Proposed models of the physical structure of graphene oxide. Republished with permission from [Chemical reduction of graphene oxide: a synthetic chemistry viewpoint, *RSC Adv.*, C. K. Chua and P. Martin, **43**, 291–312, 2014]. Copyright 2014 The Royal Society of Chemistry

While the oxygen content of a GO sample can be quantified experimentally, defining the physical structure is much less straightforward. Various models for the physical structure of GO (see Figure 4.1) proposed that the material has some form of patterned arrangement of oxygen functional groups. The currently accepted model, known as the Lerf-Klinowski model,[203] depicts the system as amorphous instead of crystalline. The core regions of a GO "flake" (formerly the flat planes of carbon atoms present in graphite) contain only epoxide and hydroxyl/oxide groups, while the edges also contain lactone and carboxylate groups. Previous experimental characterisation of GO[203–205] have found that epoxide groups do not form 1,3 ether linkages in great abundance. DFT calculations by Boukhvalov and Katsnelson[206] have also shown that these will exclusively form 1,2 ether linkages, as a 1,3 linkage cannot be accommodated without a significant, unfavourable out-of-plane distortion of the graphene sheet. It is also more thermodynamically favourable for the functional groups to be close together and aligned *trans* to each other.[206] From

thermogravimetric (TGA) analysis,[15,205] it is often observed that GO loses a large amount of its mass at around 180 °C to 200 °C, due to the loss of oxygen functional groups. It is believed that epoxide and hydroxyl groups are lost before lactones and carboxylic acids under heating,[203] as only carbon oxides and H_2O are liberated at this point.

Electronic Structure

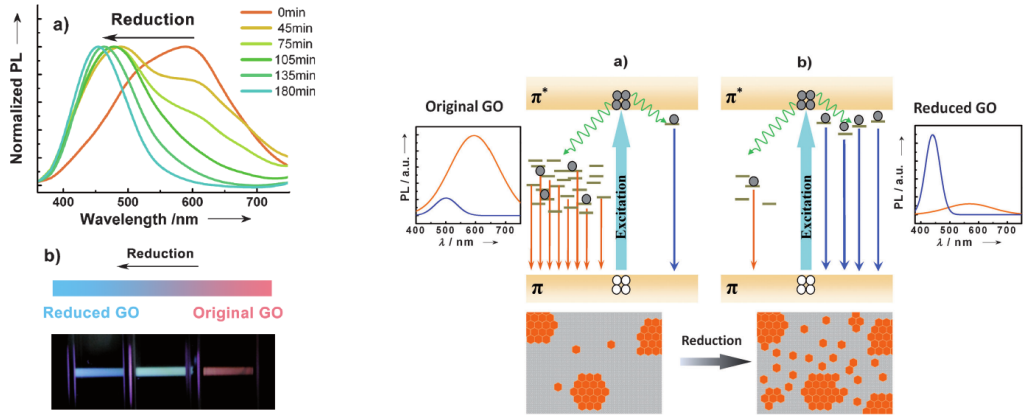

(a) (b)

Figure 4.2: The PL emission spectrum of GO (a) measured before (0 min) and during (40 min to 180 min) chemical reduction, and schematic (b) showing the likely physical changes to GO as the system is converted to reduced GO, and changes in the electronic structure and emission processes in GO and RGO. Reprinted with permission from [*Angew. Chemie Int. Ed.* 2012, **51**, 6662-6666]. Copyright 2012 WILEY-VCH Verlag GmbH

Combining the conclusions from the previously-mentioned studies shows that, while some weak thermodynamic preferences guide the arrangement of different functional groups, the system as a whole is amorphous and there is no long-range ordering of these groups. This is supported by the electronic structure data for a typical GO sample. Measurements of the optical band gap with photoluminescence (PL) spectroscopy (example shown in 4.2a) typically yields a very broad principal emission peak centred at ∼600 nm where the

base spans from 400 to just over 700 nm.[138,207] The accepted theory as to the origin of this broad PL peak is that GO samples have "islands" of sp^2 carbons isolated by oxygen functional groups.[138,208] The physical size of the islands limits their $\pi \rightarrow \pi^*$ transition energies to the visible region of the spectrum due to quantum confinement effects. Observations of the change in PL emission upon reduction of GO show that, initially, there is blue-shift of the emission peak from 600 nm to 450 nm, which corresponds to the formation of new, smaller islands.[138] While increasing numbers of small islands are being formed, the larger islands will increase in size and thus red-shift their emission peaks out of the visible range. The combination of these two effects leads to a change in the PL emission peak, changing from a broad peak centered at 600 nm to a sharper peak at around 450 nm (see Figure 4.2a). Complete reduction of the system is then usually signified by a colour change to a graphite-black.[123,124,128] This signifies the re-establishment of the long range semimetallic sp^2 network which will quench any further PL emission.

The literature data thus far give us a representative picture of the structure of GO and RGO. The basal plane of carbon atoms in the structure is heavily saturated with epoxide and hydroxyl oxygen functional groups, with regions of unsaturated sp^2 carbon atoms which are responsible for the material's optical properties. The preference for oxygen functional groups to be clustered together,[206] means that RGO can be represented as a graphene structure with "islands" of oxygen functional groups surrounded by conjugated sp^2 carbon atoms. While this still means that structures of both GO and RGO are amorphous, representative structures which use the previously mentioned structural features of these materials can be used for theoretical calculations. It should be cautioned however that this means one particular representation of GO or RGO may be insufficient for accurate theoretical analysis, because there are

likely to be different structural domains in the experimental system, therefore a range of possible structures need to be included in the analysis.

4.2 RGO/Titanium Dioxide Composites

As mentioned previously, there are numerous examples of RGO/TiO_2 composites in the literature which demonstrate that the addition of RGO enhances the photocatalytic effectiveness of the TiO_2 catalyst under both UV and visible light irradiation,[14–18,127,130,133,209] some of these studies attempt to tie this effectiveness to specific structural properties of the composite.[127,133] It is often quite difficult to assess and compare the effectiveness of composites formed using different reduction techniques, as there is often a disparity in experimental setups and chosen means of measuring photocatalytic rate between different experimental studies. From the few examples where composites are formed by different reduction methods and tested in the same group's photoreactor, there are small but measurable differences in photocatalytic efficiency between those different reduction methods.[127,130] What is considered even less frequently in the literature is whether reducing GO before or after combination with TiO_2 has a direct effect on the photocatalytic properties of the composite material.[15,127] What has also been a potential shortcoming in this area of research is the lack of experimental studies which investigate the mechanism by which photocatalytic rate enhancement is achieved, and the limited information made available by previous theoretical studies. This section reviews several important studies which attempt to demonstrate the means by which photocatalytic properties and visible light activation of the system is measured.

In two separate studies[15,127] Pastrana-Martínez *et al* demonstrated the differences between carrying out reduction before and after combination of

GO with TiO_2, as well as the role that oxygen atoms have in the photocatalytic enhancement of this type of composite material. In their 2012 study,[15] samples were produced by combining GO and as-synthesised TiO_2 nanoparticles before annealing them at either 200 °C or 350 °C. Photocatalytic activity was quantified by measuring the rates of degradation of either methyl orange (MO) or diphenhydramine (DP) under either UV/Vis (>350 nm) or visible-only (>430 nm) light sources. In this study the measured photocatalytic degradation rates of both dyes were higher than those for the unmodified P25 (a 25% to 75% mixture of rutile and anatase, respectively) control for both composite samples using either light source. In a second study in 2014,[127] samples of RGO/TiO_2 composites were produced by combining RGO with TiO_2 *after* chemically-reducing the GO precursor, in addition to forming unreduced GO/TiO_2 composites for comparison. The photocatalytic rates of the samples were measured by the photocatalytic degradation of DP under UV/Vis (>350 nm) and visible-only (>430 nm) light sources. With the UV/Vis light source, composites of RGO and TiO_2 showed a lessened photocatalytic rate when compared to an unmodified P25 control, while there was a consistent increase in photocatalytic rate with the visible-only light source. Surprisingly the unreduced GO/TiO_2 samples showed *more* photocatalytic rate enhancement in both tests compared to RGO/TiO_2 samples. It is also noted by the authors that aggregation of RGO has been seen to occur in a previous study by Stankovich *et al*,[199] where GO was chemically reduced without the use of a heterogeneous support. Aggregation of RGO to hydrophobic surfaces in the reaction vessel used in this study was attributed to the loss of hydrophilic oxygen functional groups. The improved stability of the GO suspension vs the RGO suspension observed in the study[199] likely allowed more of the GO to deposit on the surface of TiO_2 during synthesis. The observed improvement

in photocatalytic activity of samples reduced before[15] compared to after[127] deposition therefore suggests that the former process must improve interfacial binding and electronic interaction in some manner.

As was mentioned on page 101, different GO reduction methods yield products with different oxygen contents. Thermal reduction methods frequently yield RGO with around 8% oxygen by atom composition[15,126,128,129] (which, by the same analysis, has been found to be close to unmodified graphite samples[128]), while chemical/photochemical reduction methods frequently yield RGO with around 15% oxygen by atom percentage or greater.[124,126,127,129] For example, a previous study by Fan *et al*[130] found that RGO/TiO_2 samples with lower oxygen content perform better as photocatalysts than samples with higher oxygen content when composites with TiO_2 are prepared prior to reduction. Comparing the two studies of Pastrana-Martìnez *et al*[15,127] with that of Fan *et al*[130] gives us an important conclusion: while removal of oxygen defects enhances the photocatalytic properties of the composite material, these defects also play an important role in the mechanism by which RGO enhances the photocatalytic efficiency of TiO_2.

The improvement of photocatalytic rate with decreasing oxygen content supports claims from other studies that the restoration of the sp^2 network during the reduction process should enhance charge carrier separation within the system, as well as charge mobility between different TiO_2 nanoparticles and/or domains.[15,126,129] There is also a second important effect at work: that the oxygen functional groups in GO and RGO are critical for the interaction between RGO and TiO_2. XPS analyses of the oxygen 2p spectrum have found there to be interfacial Ti−O−C bonding present in the RGO/TiO_2 composites.[133,209] While it could be assumed that the formation of interfacial crosslinks would be facilitated by heating the system to high temperatures (120 °C to 200 °C, often

used for thermal reduction of GO[15,128–130]), the formation of such crosslinks has been also observed in experimental studies which use chemical reduction methods at lower temperatures as well.[133] As it has been noted that hydroxyl and epoxide groups are more labile than lactones and carboxylic acids,[15,205] it is quite likely that reduction of the as-formed GO/TiO_2 composite will remove a large number of non-crosslinking oxygen functional groups without removing the crosslinks.

In a previous chapter the rapid charge transfer between TiO_2 and graphene had been reviewed as being a common theme in the academic literature for explaining both the UV and visible light photocatalytic enhancement effect. Another theory which has been proposed as the source of visible-light photocatalytic enhancement is the possibility that these Ti−O−C bonds give the system a second, higher-energy VBM which allows for visible light photons to excite electrons to the TiO_2 CBM. In particular, analysis by Cruz-Ortiz *et al*[18] (see Figure 4.3) in 2017 of reactive oxygen species (ROS) generated by photocatalytically-reduced RGO/TiO_2 samples gives some insight into the electronic band positions within this material.

This study demonstrates that a composite of photocatalytically-reduced GO and P25 is more effective for the photocatalytic disinfection of an E. Coli culture in water than P25 alone, both with UV/Vis and visible-only light (<420 nm light sources). Mechanistic studies were then performed by detecting for various ROS: singlet oxygen ($^1O_2$); oxide radicals ($O_2^{\bullet-}$); hydroxyl radicals ($OH^\bullet$); and hydrogen peroxide (H_2O_2). Each ROS has its own reaction mechanism and particular redox potential required to produce it from H_2O. By monitoring their concentrations, it is possible to measure both how the electronic structure of TiO_2 has changed when combined with RGO and how this composite interacts with light sources. $^1O_2$ was found to be produced by both

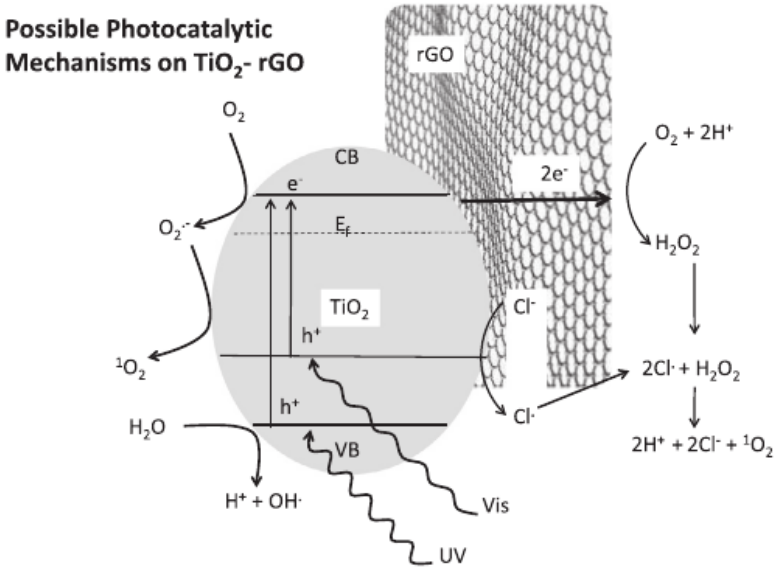

Figure 4.3: Proposed photoreaction mechanisms for the generation of ROS using P25 and RGO/P25 with UV/Vis and visible light sources, from the work of Cruz-Ortiz *et al.*[18] The simplified band structure of the TiO_2 nanoparticle shows the different valence and conduction band edges which can produce different ROSs. The new valence band formed from the interaction of RGO with TiO_2 reduces the effective band gap of TiO_2, allowing visible light to be used for photocatalysis, but does not have a sufficient oxidative potential to generate $OH^\bullet$ from H_2O. Reprinted from [*Chem. Eng. J*, **316**, B. R. Cruz-Ortiz *et al*, Mechanism of photocatalytic disinfection using titania-graphene composites under UV and visible irradiation, 179–186]. Copyright 2012, with permission from Elsevier

P25 and RGO/P25 in both UV/Vis and visible-only tests, with RGO/P25 showing consistent improvement over P25 in each case and RGO alone being inactive. No $O_2^{\bullet-}$ was detected in any test, which has been attributed to rapid conversion to $^1O_2$. Both RGO/P25 and P25 produce $OH^\bullet$ in UV/Vis tests, where RGO/P25 shows a consistent increase in production rate of $OH^\bullet$ over P25, but not in visible-only tests. In each test RGO alone shows no $OH^\bullet$ production. RGO/P25 shows production of H_2O_2 in UV/Vis but not in visible light tests, while P25 is not reported to produce H_2O_2 with either light source.

Production of $^1O_2$ is a single-electron transfer which occurs at the P25 CBM. The enhancement in $^1O_2$ production in UV/Vis and visible-only tests

with RGO/P25 shows that the composite has enhanced visible-light photocatalytic reduction properties and longer excited state lifetime vs bare P25. Production of H_2O_2 is a two-electron process, thus the ability for RGO/P25 to produce H_2O_2 with UV/Vis light, where the rate for P25 alone is negligible, also indicates that the concentration of photoexcited electrons and the lifetime of the excited state is greatly enhanced vs bare P25. The oxidation potential required to generate $OH^{\bullet}$ is achievable by the TiO_2 VBM.[18] The observation that P25 and RGO/P25 both produce $OH^{\bullet}$ in UV/Vis light tests but not visible light tests therefore indicates two important things. Firstly that the mechanism of visible light photocatalytic activity goes via an electronic transition from an occupied state with a less-oxidative potential than the TiO_2 VBM, and is not sufficient to oxidise water to $OH^{\bullet}$. Secondly that the RGO/TiO_2 occupied electronic level which acts as the initial state of the visible light excitation in the system is somehow separated from the VBM of TiO_2 itself (while the TiO_2 VBM is involved in the UV/Vis photoexcitation). Otherwise if the two occupied states were strongly coupled the photogenerated hole created by UV/Vis excitation would move to the higher-energy RGO/TiO_2 state, lose its oxidative potential, and yield an observably reduced $OH^{\bullet}$ production rate. The increase in the rate of $OH^{\bullet}$ production of RGO/P25 vs bare P25 in UV/Vis light tests also shows that the photoexcited hole lifetime has been increased, therefore the electron-hole recombination rate has decreased.[18]

Whilst there are few experimental studies investigating the mechanism of photocatalytic enhancement in the RGO/TiO_2 material or the role of oxygen defects, there are even fewer computational studies which attempt to do the same. The unique difficulty involved in studying this co-continuous solid composite (that the crystal systems of TiO_2 and graphene are quite different from each other) are mentioned in subsection 3.5.2, the main result of these

difficulties (the large simulation sizes) has made comprehensive computational analysis difficult. A computational study by Ferrighi, Fazio, and Di Valentin[168] in 2016 used hybrid HF/DFT calculations to simulate the interface between graphene and anatase (101), and in particular showed the effect of including an oxygen defect in the system. The oxygen defect (in this case an epoxide group bound to graphene) was found to directly bond to a surface 5-coordinate Ti atom, and as a result the binding strength of graphene to anatase (101) increased. Furthermore, new states appeared just below the TiO_2 CBM which corresponded to contributions from graphene's carbon and oxygen atoms (see Figure 4.4b). Closer analysis shows that these states originate directly from the observed Ti−O−C bonding in the system. Spin-unrestricted electronic structure calculations also suggest that graphene is able to easily trap holes in the photoexcited state of the system, and thus spatially separate them from the electrons which are trapped in the anatase (101) CBM.[168] This study shows that the electronic structure of the composite system should change when Ti−O−C crosslinks are included. On the other hand, there are some important aspects of the RGO/TiO_2 system which are left untested. Firstly, only one RGO structure is examined in Ref[168]. The oxygen content of this RGO structure (30 carbons:1 oxygen, 3.33% oxygen) is much lower than the typical oxygen content of experimentally-derived RGO,[15,124,128,200,201] and only one oxygen functional group is used in the simulation. Secondly, the analysis does not delve deep into the electronic structure of the chosen composite system, as only DoS projections and no band structures are analysed in the report. Furthermore, while there is analysis of charge trapping within the system, it is only performed for graphene/TiO_2 and not for RGO/TiO_2.

The main conclusions that can be drawn from these past analyses about this material are twofold. Firstly the oxygen defects present in GO and RGO

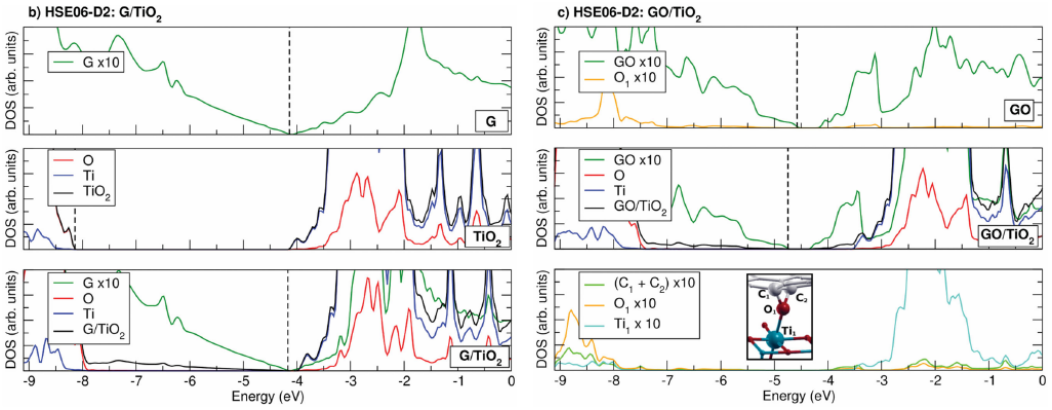

(a) (b)

Figure 4.4: DoS plots of the graphene/anatase (101) (a) and reduced graphene oxide/anatase(101) (b) composites simulated by Ferrighi *et al.*[168] For (a) the top and middle plots are for graphene and anatase separately, and the bottom is for the two combined as a composite. For (b) the top plot is for RGO, the middle for RGO and anatase combined, and the bottom for atoms involved in the Ti−O−C bond specifically (as shown in the inset in that figure). Reprinted with permission from [*Adv. Mater. Interfaces*, 2016, **3**, 1500624]. Copyright 2016 WILEY-VCH Verlag GmbH.

can form Ti−O−C bonds which anchor the graphene part of the composite to the TiO_2 surface, and these groups are typically preserved after GO is reduced to RGO. Secondly the Ti−O−C bonds, thus formed, will yield new electronic states which electronically couple the graphene part to the TiO_2 surface, which could lie within the band gap of TiO_2. These additional states could therefore be the source of the enhanced visible-light photocatalytic properties, as well as allowing for recombination-slowing trap states to form which could account for the extended excited state lifetimes observed for this system.[124,126,128] What is still unknown in the literature is what exactly the atomistic-level origins of these effects are. Experimental analysis can only probe global properties of the composite, and theoretical studies have been mostly limited so far by the high computing cost of using robust and accurate methods (such as hybrid HF/DFT and Post-HF theory) to analyse the system's properties. In this chapter we present an advancement of the model proposed in an earlier chapter, which

focused on the modelling of a defect-free graphene/rutile (110) composite. The updated model will now include oxygen defects — thus changing the graphene/rutile (110) composite of the previous model to a GO/rutile (110) or RGO/rutile (110) composite (depending on oxygen content). The intention therefore is to determine the nature of interfacial binding in the system, as well as the effect that these defects will have on the electronic structure compared to a defect-free system. With a more detailed accounting of the properties of different oxygen defects and potential Ti−O−C crosslinks in the system it is hoped that this analysis will help to rationalise available experimental data for this composite system.

4.3 Computational Methodology

4.3.1 Geometry Optimisations

All geometry optimisations were done with the *QuickStep* program,[148] from the CP2K software package (www.cp2k.org). All pure-DFT calculations used the PBE[57] exchange-correlation functional, and all hybrid HF/DFT calculations used the range-separated HSE06[151] functional. All structures were first optimised using the PBE functional and then re-optimised using the HSE06 functional afterwards. All binding and interaction energy calculations accounted for basis set superposition error (BSSE) using the Counterpoise (CP) method.[49] In all cases calculations included Grimme's D2 dispersion corrections.[68] All calculations utilised double-zeta basis sets with diffuse and polarisation functions, and Goedecker-Teter-Hutter pseudopotentials,[149,150] optimised for use in CP2K (denoted as DZVP-MOLOPT-GTH-qn in the program). The plane-wave cutoff used for the auxiliary plane wave basis set used in CP2K was 250 Rydberg for calculations of the GO and RGO supercells, and 600 Ry-

dberg for calculations of the rutile and rutile/graphene supercells. All hybrid HF/DFT calculations used the Auxiliary Density Matrix Method (ADMM),[152] which is implemented in CP2K. In these calculations Hartree-Fock exchange is computed using a small auxiliary basis set and density matrix, while all non-HF parts of the calculation are computed using the primary basis set and density matrix. Auxiliary basis set cpFIT3 (contracted, 3 gaussian exponents per valence orbital, includes polarisation functions) was used for carbon, oxygen, and hydrogen, while FIT3 (3 gaussian exponents per valence orbital) was used for all titanium atoms. All optimisation calculations were done at the Γ-point only.

4.3.2 Electronic Structure Calculations

After geometry optimisations were completed, an optimised wavefunction was produced in a single-point calculation using the CRYSTAL14 software package.[153] All system properties and one-electron properties were then obtained from subsequent CRYSTAL14 calculations, while crystalline orbital data were obtained from CRYSTAL17 calculations.[210] The range-separated HSE06[151] hybrid HF/DFT functional with Grimme's D2 dispersion correction was used for all calculations. All calculations used all-electron triple-zeta basis sets with diffuse and polarisation functions, as originally devised by M. Peintinger, D. Oliveira, and T. Bredow,[154] and a Monkhorst-Pack k-point mesh of $12 \times 12 \times 1$. In order to present absolute orbital energies, each density of states (DoS) and band structure representation shown is corrected for the energy of the electron in vacuum, which is done simply by offsetting the energies of the plots. The magnitude of the energy shift is determined using the electrostatic energy calculated at a point in the simulation box sufficiently far away in the cell's C-axis (>50 Å) from the atoms in the simulation cell.

4.4 Unit Cell Construction

The structure of the rutile (110) slab used in this study is the same as the 9 atomic layer slab we used in section 3.6. Similarly each RGO structure we investigated was based on the geometry of the graphene supercell that was featured in the same chapter. Each RGO/rutile (110) composite therefore uses a 2 × 5-extended 3-unit cell thick slab of rutile with the (110) surface exposed (60 titanium atoms, 120 oxygen atoms) and a 3 × 6 supercell of an orthorhombic graphene unit cell (72 carbon atoms) as a basis. Graphene sheets functionalised with hydroxyl and epoxide groups were constructed, guided by the literature analysis of the arrangements of oxygen functional groups in GO and RGO by Boukhvalov and Katsnelson.[206] In their analysis it was shown that it is more thermodynamically favourable for the functional groups to be adjacent, and arranged *trans* to one another. Five structures were created, and the carbon:oxygen ratio of each system was based roughly on the reported common oxygen contents reported in experimental GO and RGO samples: the C:O ratio in GO was taken to be 2:1 (50% oxygen coverage)[199–201]; while in RGO it was assumed to be either 12:1 (8% oxygen coverage) or 6:1 (16% oxygen coverage);[15,124,128,200] highly reduced GO with C:O ratios of 18:1 and 36:1 was also modelled for comparison. Each system contained different arrangements of functional groups: 2:1 (30 hydroxyl groups, 10 epoxide groups); 6:1 (6 hydroxyl groups, 6 epoxide groups); 12:1 (4 hydroxyl groups, 2 epoxide groups); 18:1 (2 hydroxyl groups, 2 epoxide groups); and 36:1 (2 hydroxyl groups, 0 epoxide groups). No requirement was made to provide specific ratios of hydroxyl and epoxide functional groups, as we are unaware of any studies which report the relative abundances of these two functional groups. More hydroxyl groups were added than epoxide groups to promote interfacial interactions, while the

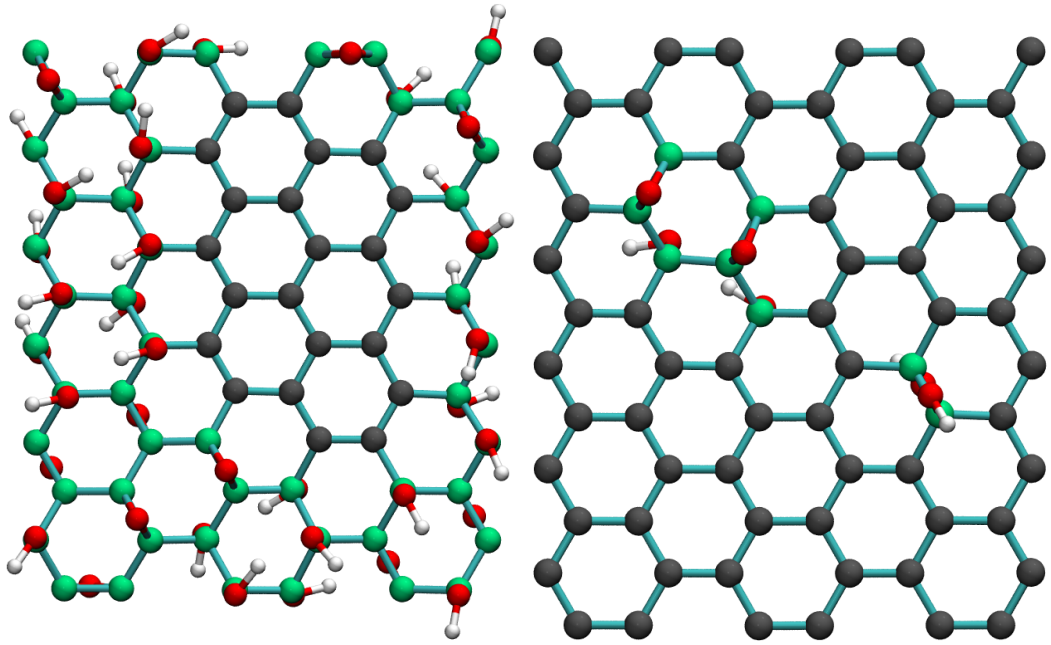

(a) (b)

Figure 4.5: Images showing the basic structures of the 2:1 C:O ratio (GO) (4.5a) and 12:1 C:O ratio (RGO) (4.5b) systems used in this study. Colour coding: oxygen (red); hydrogen (white); sp^2 carbon (dark grey); sp^3 carbon (sea green)

number of hydroxyl groups was kept even to avoid producing a spin-polarised system.

Colour-coded images of the 2:1 and 12:1 C:O ratio structures (henceforth referred to as GO and 12-RGO respectively) are shown in Figure 4.5, and a similar figure for the 6:1 ratio RGO structure (6-RGO) is shown in Figure 4.6. 12-RGO was used as our main RGO structure, as it was found to be difficult to obtain a converged wavefunction of 6-RGO for electronic structure analysis. The 18:1 (18-RGO) and 36:1 (36-RGO) ratio RGO structures were used to assess the effect of removing various functional groups from 12-RGO. The carbon atoms of the sp^2 region in GO were arranged to resemble the poly-aromatic hydrocarbon anthanthrene, as a large singular sp^2 region was expected to be more energetically stable than several smaller isolated regions.

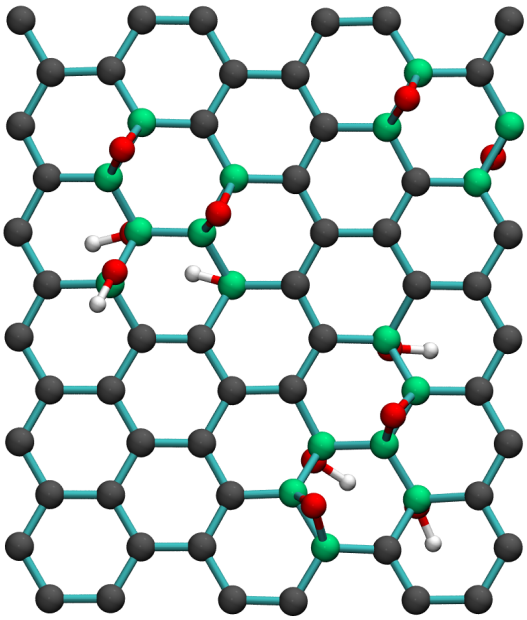

Figure 4.6: Image showing the structure of the 6:1 C:O ratio RGO system used in this study. Colour coding: oxygen (red); hydrogen (white); sp^2 carbon (dark grey); sp^3 carbon (sea green)

4.5 Design of Composite Unit Cells

The structures of RGO and GO used to form various composite systems have been outlined in the Computational Methodology section. For RGO-based composites, hydrogen bonded structures (12H and 6H) and chemisorbed structures (12C and 6C) were considered. Positions of some hydroxyl groups were varied in the cases of 12-RGO (see Figure 4.7b and Figure 4.7c) and 6-RGO composites in order to both ensure some degree of variety in the structure, and to spread out interfacial hydrogen bonding interactions instead of concentrating them in one part of the composite. Chemisorption of the 12-RGO and 6-RGO systems on rutile (110) was done by removing two hydrogen atoms from hydroxyl groups of 12-RGO and 6-RGO, thus creating the 12C-RGO and 6C-RGO composites. One hydrogen atom was removed from a hydroxyl group on the face of RGO closest to that of rutile (110) to facilitate the formation of a Ti-O-C bond, and the other hydrogen was removed

from a hydroxyl group on the other face of RGO (creating an epoxide group) to keep the total number of electrons even — thus avoiding the need for the calculations to be spin-polarised.

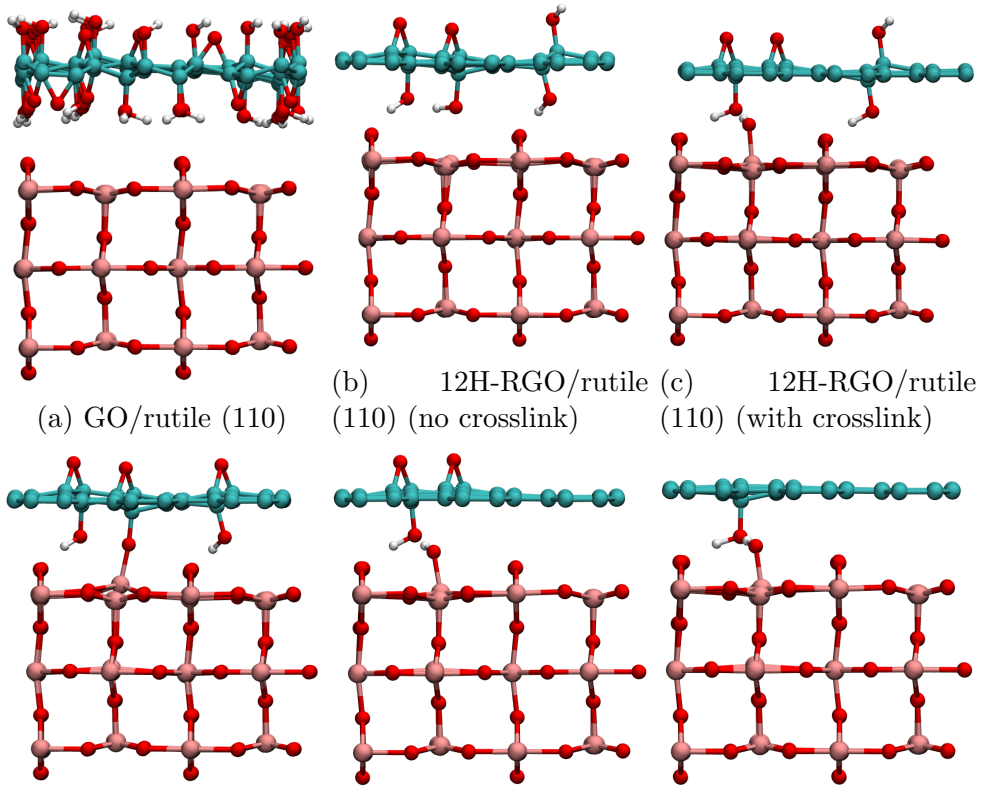

(a) GO/rutile (110) (b) 12H-RGO/rutile (110) (no crosslink) (c) 12H-RGO/rutile (110) (with crosslink)

(d) 12C-RGO/rutile (110) (e) 18H-RGO/rutile (110) (f) 36H-RGO/rutile (110)

Figure 4.7: Images of the GO and RGO/Rutile (110) composites used in this work: GO/Rutile (110) (4.7a); 12:1 RGO/Rutile (110) 4.7b: hydrogen bonded, 4.7c: hydrogen bonded with crosslink, 4.7d: chemisorbed); 18:1 RGO/Rutile (110) (4.7e); and 36:1 RGO/Rutile (110) (4.7f)

Each GO and RGO structure was first optimised alone using the PBE functional, then interfaced with rutile (110), and then the as-formed composite was optimised again using first the PBE and then the HSE06 functionals. The 6H-RGO and 6C-RGO structures were only optimised using the PBE functional as it was found to be too difficult to attain SCF convergence with these systems using the HSE06 functional. The full range of GO and RGO-based composite structures studied in this work are presented in Table 4.1

and Figure 4.7. The crosslinked 12H-RGO/rutile (110) structure specifically features a Ti−O−H$\cdots$O−C bonding arrangement, where $\cdots$ indicates a strong hydrogen bonding interaction between H and O with a bond length of 1.55 Å. The optimisation of the 12H-RGO composite system with PBE (optimised structure Figure 4.7b) resulted in a purely hydrogen-bonded structure. Further optimisation with HSE06 resulted in a re-arrangement where a hydroxyl group from RGO was transferred to the surface of rutile (110) (optimised structure in (Figure 4.7c) and forms an O−H$\cdots$O bond with a hydroxyl group on RGO. This is in direct contrast to 12C-RGO/rutile (110), which forms a Ti−O−C covalent bond between RGO and the surface of rutile (110). This was also attempted with the 6C-RGO/rutile (110) system, however this resulted in no covalent bonding between RGO and the rutile (110) surface and a hydrogen bonding interfacial interaction resulted instead. The structures of 18H- and 36H-RGO/rutile (110) (Figure 4.7e and Figure 4.7f respectively) were then derived from the HSE06-optimised 12H-RGO/rutile (110) system by removing oxygen functional groups not involved in the crosslink.

4.6 Binding Properties of the TiO_2/RGO Interface

To investigate the binding of the RGO structures to the rutile (110) surface, the interfacial binding (E_{bind}) and interaction (E_{int}) energies were calculated using the following relation:

$$E_{int} = E_{tot} - E_{ru(opt)} - E_{gr(opt)} + E_{BSSE} \tag{4.1}$$

Where E_{tot} is the total energy of the composite system, $E_{ru(opt)}$ is the total energy of the optimised rutile (110) slab, $E_{gr(opt)}$ is the total energy of the optimised GO or RGO sheet, and E_{BSSE} is the basis-set superposition error correction. This gives the overall energy difference resulting from bringing the two parts of the composite together. To decompose this overall interaction energy into the energy changes due to binding the two parts together (E_{bind}) and the structural deformation (E_{def}) resulting from the combination of the two parts, the following two relationships can be used:

$$E_{bind} = E_{int} - E_{def} \tag{4.2}$$

$$E_{def} = (E_{ru(def)} - E_{ru(opt)}) + (E_{gr(def)} - E_{gr(opt)}) \tag{4.3}$$

Where $E_{ru(def)}$ and $E_{gr(def)}$ are, respectively, the total energies of the rutile and graphene parts of the composite fixed in the geometries that they adopt in the composite system. These energies, calculated with *Quickstep* using the PBE functional with the D2 correction, are shown in Table 4.1. BSSE energies for each non-chemisorbed system were determined to be around 0.009 eV for each. Comparing the results for the GO, RGO, and previously-calculated graphene systems shows that having a small number of oxygen functional groups (as with the case of RGO) strengthens interfacial binding, while the much greater number present in the GO system appears to have a detrimental effect on interfacial binding strength in this case. It is possible therefore that having greater numbers of functional groups in this case leads to greater intra-GO hydrogen bonding than in RGO, which leaves fewer functional groups to form hydrogen bonds with the surface of rutile (110).

The two 6-RGO systems were found to have very similar binding and in-

System	E_{int} (eV)	E_{bind} (eV)	E_{def} (eV)	$E_{def(ru)}$ (eV)	$E_{def(gr)}$ (eV)
GO/rutile (110)	−1.12	−3.02	1.91	0.76	1.15
6H-RGO/rutile (110) (NCL)	−2.45	−3.06	0.61	0.51	0.10
6C-RGO/rutile (110) (NCL)	−2.23	−3.05	0.82	0.52	0.30
12H-RGO/rutile (110) (NCL)	−1.74	−3.66	1.92	0.77	1.15
12H-RGO/rutile (110) (CL)	−4.21	−5.66	1.45	1.11	0.34
12C-RGO/rutile (110) (CL)	−3.44	−7.39	3.95	2.49	1.46
18H-RGO/rutile (110) (CL)	−3.97	−5.14	1.17	0.95	0.22
36H-RGO/rutile (110) (CL)	−4.10	−5.45	1.35	1.16	0.18
Graphene/rutile (110)	−1.67	−3.24	1.57	0.89	0.69

NCL:No crosslink. CL: with crosslink.

Table 4.1: Binding energies of the RGO/rutile (110) composite systems used in our work, calculated using PBE+D. Each value shown is corrected for the Basis Set Superposition Error (BSSE) using the Counterpoise (CP) method. Values for the graphene/rutile (110) system have been obtained from our previous work. Shorthand system names are defined in Figure 4.7.

teraction energies, due to the fact that no interfacial covalent bonding was achieved for the 6C-RGO system. In contrast, significant differences are seen when comparing the 12H-RGO/rutile (110) composite with the interfacial crosslink (CL) and without (NCL) the interfacial crosslink. Not only is there a large (2 eV) increase in the interfacial binding and interaction energies, but the deformation energy due to the formation of the composite also decreases when the crosslink is formed. We believe this binding energy change is due to the formation of a new Ti−O bond (bond energy $666.5 \pm 5.6\,\mathrm{kJ\,mol^{-1}}$ [211]) in the CL structures, which results in a net decrease in Gibbs free and total energies and outweighs the cost of breaking a single C−O bond ($385 \pm 6.3\,\mathrm{kJ\,mol^{-1}}$ [211]). This binding energy increases significantly (by 2.5 eV) when RGO is chemisorbed onto the rutile (110) surface using a Ti−O−C bond, as seen in the case of 12C-RGO/rutile (110). On the other hand from the data it can be seen that there is significant disruption to both the rutile and the RGO components of the 12C-RGO/rutile composite, with deformation energies for the rutile and RGO parts of 2.49 eV and 1.46 eV respectively, and the majority of the deformation energy originates from the rutile slab due to the displacement of a surface 5-coordinate Ti during bond formation. While the energy barrier to formation

of the Ti−O−C is not calculated in this work, it is clear from the deformation energies reported that this type of bonding will form mainly at elevated temperatures — such as those used in experimental studies which employ thermal GO-reduction methods.[15,128]

When the two hydroxyl groups not involved in crosslinking are removed from 12H-RGO (CL) to form 18H-RGO the interfacial binding energy decreases by around 0.5 eV, which is likely due to the removal of a hydroxyl group which would otherwise be able to form a hydrogen bond with rutile (110). Removing the two epoxide groups to yield 36H-RGO increases the interfacial binding energy in the composite slightly (by 0.13 eV). The epoxide groups facing away from the rutile (110) surface do not participate in the interfacial binding interaction, but they (as noted in the electron density difference plot Figure 4.8) have a notable electron withdrawing effect on the carbon atoms surrounding them. This electron withdrawal will draw some electron density from the atoms involved in the crosslinking bond, which weakens this interfacial interaction in the 12- and 18-RGO composites.

To investigate the interaction in this composite system further, the electron density difference was mapped for the 12H-RGO/rutile (110) system (Figure 4.8). This difference was defined as the difference in electron density between the full composite and the isolated 12H-RGO and rutile (110) parts in their composite geometries. From an initial glance we can see large rearrangements of electron density which highlight the most significant aspects of the interface binding. Hydrogen bonding can be seen clearly from the alternating charge depletion (yellow) and accumulation (blue) areas, while the lower face of RGO (which faces the rutile (110) surface directly) shows a noticeable re-arrangement of charge in response to the surface 2-coordinate oxygen atoms of rutile (110). Some re-arrangement of charge can be seen in the ru-

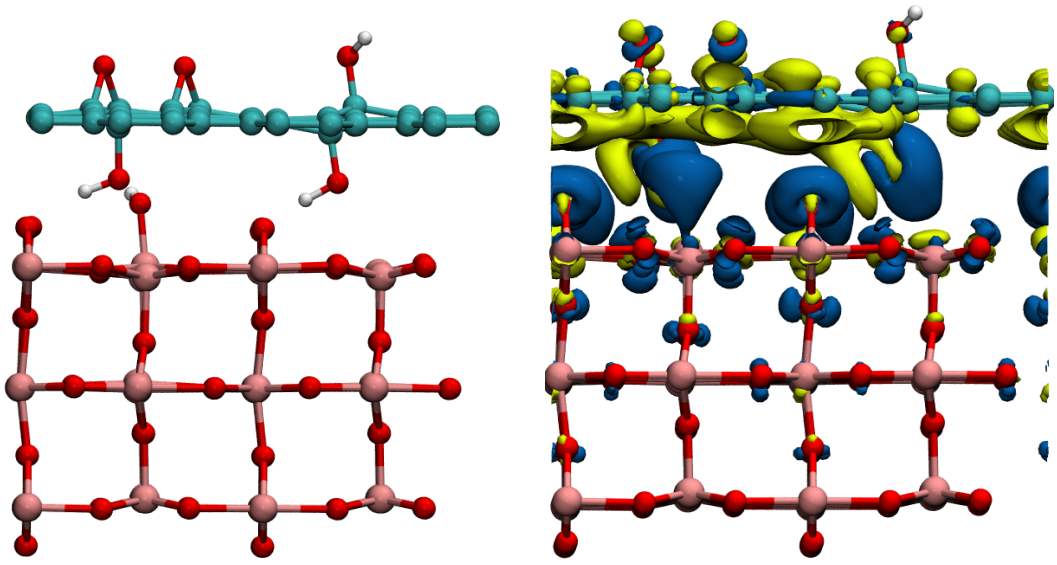

(a) (b)

Figure 4.8: Isosurface of the electron density difference upon combination of 12H-RGO and rutile (110), calculated using the HSE06 functional. The left panel shows the underlying atomic structure, while the right panel shows the charge density difference isosurface (rendered at 0.001 e Å^{-3}). Charge depletion is shown in yellow, while charge accumulation is shown in blue

tile (110) slab itself, as electron density depletion can be seen in the bonding orbitals of some of the subsurface oxygen atoms while non-bonding orbitals show accumulations of density. What is most interesting to note is that there is a widespread depletion of charge in the π orbitals of the sp^2 carbon atoms in RGO, while at the same time there is a slight increase in charge density in the σ orbitals of the same atoms. This indicates that, upon forming the interfacial crosslink structure, there is a shift in electron density from the π system to local σ bonding. Furthermore there are clear differences between the oxygen functional groups on the upper face of the RGO sheet. The charge density accumulation on the hydroxyl group is less than the equivalent accumulation on the epoxide groups. This shows that the epoxide groups have a much greater electron withdrawing effect on the surrounding carbon sp^2 atoms. These charge density differences are also notably different to the density differences observed

in the graphene/rutile (110) system studied in a previous chapter. While, in the graphene/rutile (110) system, there is a similar (though less significant) shift in electron density from the π-network to local carbon σ-bonding, overall there is a clear transfer of charge from graphene to rutile (110) oxygen atoms.

In order to explain the rather weak interfacial bonding in the GO/rutile (110) composite, the optimised structure of GO/rutile (110) was analysed for the presence of hydrogen bonding (shown in Figure 4.9). Hydrogen bonds were visualised for the system using the VMD software package,[212] with a maximum bond distance cutoff of 3 Å and O−H$\cdots$O maximum bond angle deviation from the ideal value of 180° of 20°. This contrasts strongly with the result of the equivalent analysis performed for the crosslinked 12H-RGO/rutile (110) (Figure 4.10), where multiple hydrogen bonds form with deviations from the ideal angle of $\leq$20°. From the images it can be seen that any hydrogen bonds formed with rutile (110) would be very weak in the GO/rutile (110) structure, as the hydrogen bond angles deviate very far (up to 50°) from the ideal value of 180°. Earlier observations in experimental works using chemical reduction methods[127,199] had suggested that oxygen defects may play an important role in the interfacial binding in RGO composite materials. From the results presented in this work it is clear that the formation of crosslinks and interfacial hydrogen bonds are the important means by which strong interfacial binding is achieved. High local concentrations of functional groups (such as is the case with GO) will not necessarily promote interfacial binding, as there will be less chance for those functional groups to form hydrogen bonds and covalent bonds with TiO_2. Further, it can be seen that far more hydrogen bonds are seen between oxygen functional groups in GO than between GO and rutile (110). Lower local concentrations of functional groups will lead to less intra-GO hydrogen bonding and a small improvement in interfacial binding.

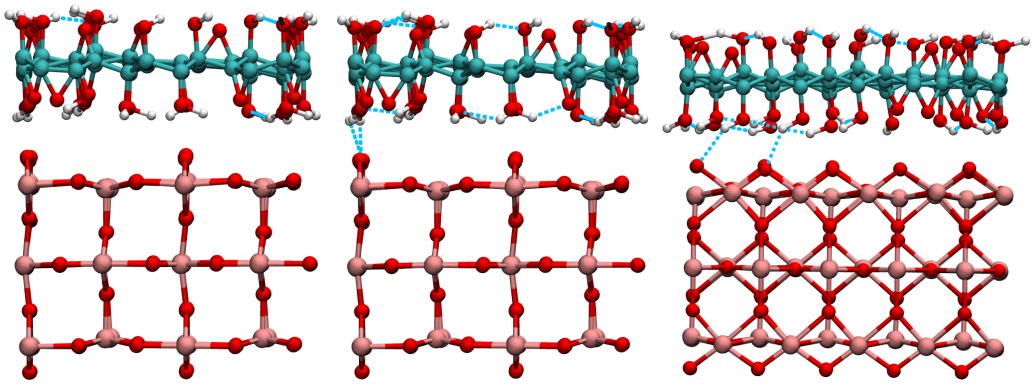

(a) (b) (c)

Figure 4.9: Hydrogen bonding interactions (blue dashed lines) in the GO/rutile (110) composite visualised with a maximum distance cutoff of 3 Å and maximum O−H···O bond angle deviation from the ideal value of 180° of (4.9a) 20° and (4.9b & 4.9c) 50° (front and side respectively)

The formation of Ti−O−C and Ti−O−H···O−C crosslinks (as seen in Figure 4.7d, and Figure 4.7c) significantly improves the interfacial binding compared to hydrogen bonding alone. The removal of electron-withdrawing, non-binding functional groups (such as epoxides) slightly increases this binding strength further, as electron density will then be more drawn to the bonding functional groups — thus strengthening the crosslinks and providing better conditions for the RGO/rutile (110) charge transfer. It can be expected, based on chemical intuition, that the formation of these new crosslinks would require overcoming an energy barrier. It may be the case that high-temperature (150 °C to 200 °C) processes such as hydrothermal reduction or high-temperature annealing would favour the formation of crosslinks during the reduction process. On the other hand a study by Umrao *et al*[133] shows that Ti−O−C and Ti−C bonding can be seen in samples of RGO/TiO_2 chemically reduced using hydrazine prior to combination with TiO_2 and kept at relatively low temperatures (40 °C to 80 °C). The kinetics of the formation of these crosslinks would therefore need to be modelled in order to make con-

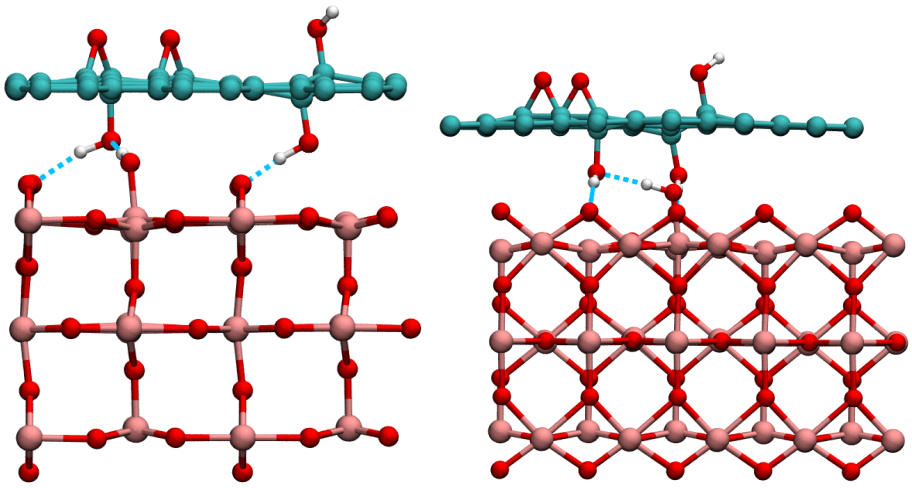

(a) (b)

Figure 4.10: Hydrogen bonding interactions (blue dashed lines) in the crosslinked 12H-RGO/rutile (110) composite, visualised with a maximum distance cutoff of 3 Å and maximum O−H···O bond angle deviation from the ideal value of 180° of 20°

clusions on the favourable experimental conditions for preparation of these cross-links. However, this is beyond the scope of this study.

4.7 Electronic Properties of the TiO_2/RGO Interface

4.7.1 Graphene Oxide/Rutile (110)

To understand the enhanced photocatalytic efficiency of TiO_2 composites with GO and RGO we investigate the electronic properties (density of states and band structure) of these composites. Firstly we analyse the electronic structure of the rutile (110)/GO composite. The density of states (DoS) spectrum (shown in Figure 4.11a) indicates that GO in this composite has an electronic structure similar to that of an isolated organic molecule (e.g. pyrene, anthracene), with discrete band energies and the HOMO of GO situated just

below the rutile (110) CBM. The HOMO is almost entirely composed of π-orbitals of sp^2 carbon atoms, while the corresponding π^* orbital is roughly 2.1 eV higher in energy and is positioned deep within the TiO_2 CB (see Figure 4.11d). No mid-gap states which have mixed TiO_2 and GO character are found in this particular system, indicating there is very little interaction across the interface. Geometry optimisation of this particular composite did not result in any crosslinks being formed with the surface of rutile (110). Without such strong interactions with the surface, it is clear that mixed TiO_2/GO electronic states would therefore not form. It is still possible (based on the position of energy levels) that the visible-light excitation of GO could then lead to electron transfer to the rutile (110) conduction band as a second step, however the weak interactions between GO and rutile (110) would likely lead to slow rates of charge transfer. Therefore it is unlikely that this type of interfacial binding arrangement will show enhanced absorption or strong charge separation compared to pure TiO_2, thus we do not expect enhanced photocatalytic properties in this type of system.

4.7.2 Reduced Graphene Oxide/Rutile (110)

Variations in RGO/Rutile (110) Interfacial Binding

The DoS and band structure of non-crosslinked 12H-RGO/rutile (110) (see Figure 4.12) are analysed first. In this system we can see that the graphene Dirac point is present (between the Y and Γ points), indicating that RGO is still semimetallic in this system. The way that the RGO bands intersect the rutile (110) bands without obvious signs of interaction indicates that there is no strong chemical interaction between the two. Besides the highest-occupied and lowest-unoccupied graphene-like bands, the band structure in this case

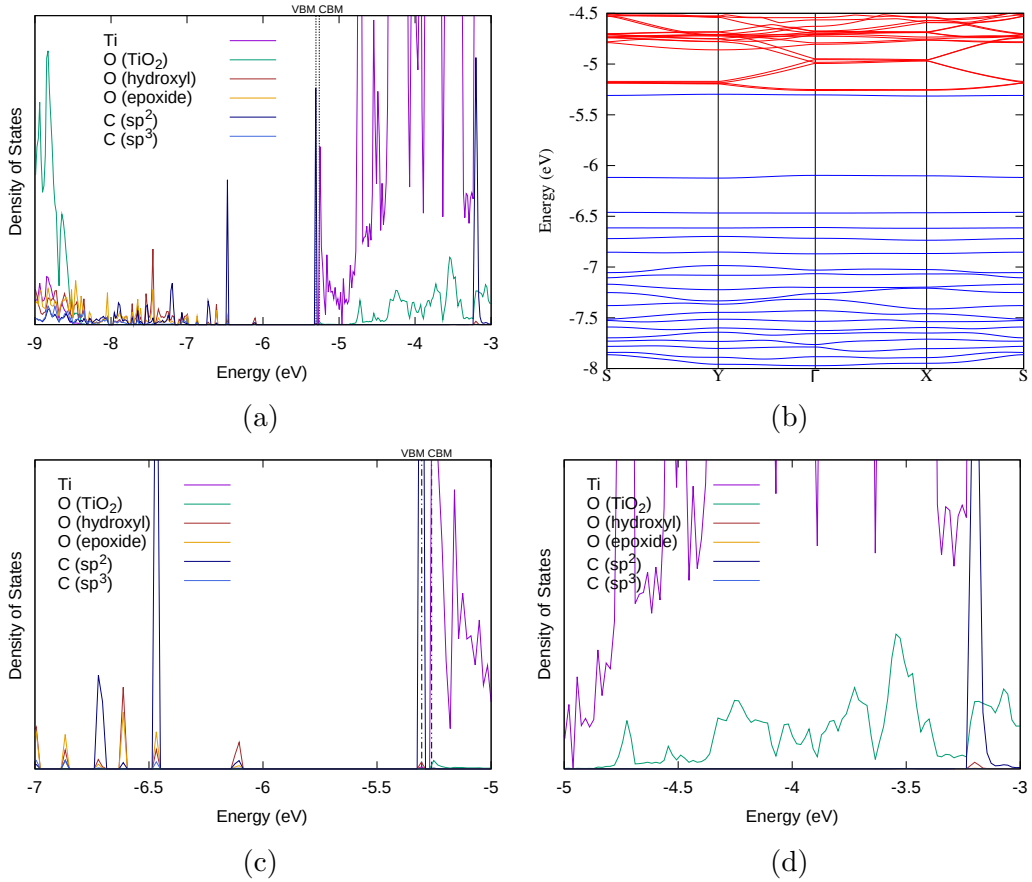

Figure 4.11: Electronic structure data for the GO/rutile (110) composite: Comprehensive DoS (a), band structure (b), DoS of the VBM and CBM (c), DoS of the conduction band region (d). Colour schemes: DoS; see legend, band structures; blue bands are formally occupied, red bands are formally unoccupied

has some less dispersed bands, which, according to the DoS analysis, belong to oxygen functional groups. For example, the sixth highest-occupied band has a very narrow energy dispersion, particularly at around $-8.75\,\mathrm{eV}$, and is derived mainly from the orbitals of the oxygen functional groups. The first and second occupied bands, between $-6.6\,\mathrm{eV}$ to $-7.30\,\mathrm{eV}$ for the first and $-7.5\,\mathrm{eV}$ to $8.0\,\mathrm{eV}$ for the second, have much higher energy dispersions and are characteristic of states belonging to graphene-like sp^2 hybridised carbon atoms, these can be seen throughout the rutile (110) forbidden region. Analogous to the band structure of graphene/rutile (110) shown previously, it is quite

clear from this data that there is, similar to the case for GO/rutile (110), little electronic interaction between RGO and rutile (110) in this particular system. The band structure shows no signs that the RGO electronic bands are interacting with those of rutile (110), while the DoS shows no evidence of any mixing of electronic states between the two materials. It is not expected, therefore, that this type of local chemical environment would be the source of the enhanced visible light photocatalytic properties seen in experimental RGO/TiO_2 composite systems.

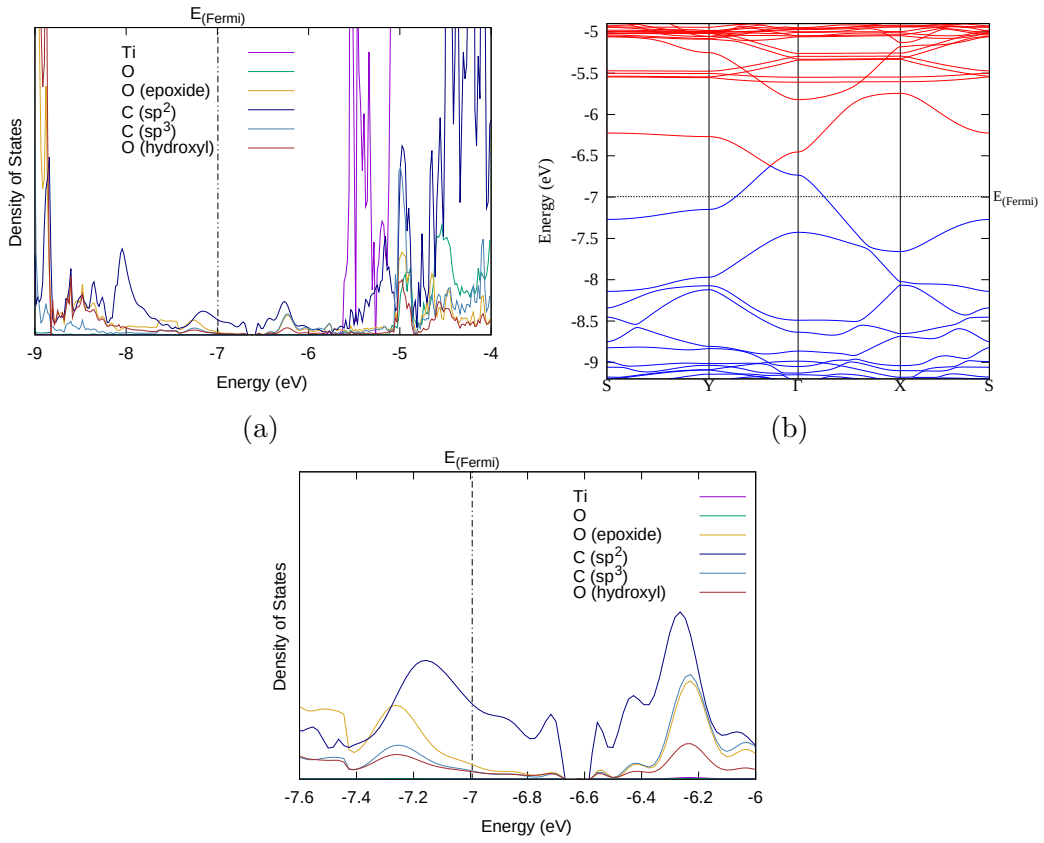

Figure 4.12: Electronic structure data for the 12H-RGO/rutile (110) (NCL) composite: Comprehensive DoS (a), band structure (b), and DoS of the VBM and CBM (c). Colour schemes: DoS; see legend, band structure; blue bands are formally occupied, red bands are formally unoccupied

For the crosslinked 12H-RGO/rutile (110) system the electronic structure

is very different (Figure 4.13). The DoS spectrum and band structure of the crosslinked 12H-RGO/rutile (110) composite (Figure 4.13a) show an unoccupied state forming between the VBM of RGO and the rutile (110) CBM. In this unoccupied state we can see contributions from sp^2 carbon, sp^3 carbon, both types of oxygen functional group (O, hydroxyl and O, epoxide), and the transferred hydroxyl group (OH (Ti−OH)) which make up this rather complex band. This particular band now forms the CB of the system. This band has an unusual dependence on electron momentum: the energy of this band is highest at the Γ-point and lowest much farther away in the Brillouin zone near k-point S. From the shape of this band (Figure 4.13b) it is clear that it may share orbital characteristics with the VBM, which itself is largely based on RGO sp^2 carbon (according to its DoS spectrum Figure 4.13a). The DoS confirms this interpretation: the state density of the CB at Γ corresponds to contributions from the epoxide oxygen and sp^2 carbon atoms, while as it moves away from Γ the density of states of this band acquires greater contributions from sp^3 carbon and oxygen functional groups as well as some contributions from the surface Ti atom bonded to OH and fewer contributions from sp^2 carbon. The decrease in energy from the CB at Γ to the energy minimum of the CB at S, and the presence of the VBM at Γ results in a large electron momentum difference between the CBM and VBM. This difference is expected to greatly slow the recombination of charge carriers and lead to long-lived excited states.

The different chemical environments of sp^2 carbons, and sp^3 carbons and oxygen functional groups can be seen from their band structures: purely sp^2 carbon bands have a wide range of allowed energies, which shows that the states which make up these bands are spatially delocalised (e.g. the band between −6.7 eV and −6.2 eV along the X-Γ-Y path); while bands composed of sp^3 carbon and oxygen functional group have a very narrow range of allowed

energies and are well separated in energy from each other, which shows that these electronic states are localised on particular atoms (e.g. the first and second occupied bands around −6.75 eV and −7.00 eV respectively between k-points Y-S and X-S, localised on the oxygen functional groups of RGO). The band structure and DoS spectrum of the crosslinked 12H-RGO/rutile (110) composite show that the electronic states in this system are moderately more delocalised than those in GO/rutile (110), which is a direct consequence of the partial restoration of the sp^2 network in this particular system. From the DoS data in Figure 4.13 it is clear that these RGO-rutile interactions are weakening the contributions of sp^2 carbon to the bands in the system, which leads to a band structure with more localised electronic states when compared to a defect-free graphene system (see Figure 4.18) and even compared to a weakly adsorbed RGO system (Figure 4.12). Finally it can also be seen from the DoS that there are additional contributions from the Ti atoms in the Ti−OH group at the same energies where oxygen groups' contributions are prominent (between −0.46 eV and −0.48 eV, seen in Figure 4.13d), which indicate that the RGO states directly overlap with states belonging to rutile (110). The overlap between these states could facilitate the transfer of excited-state electrons from RGO to rutile (110) as a one step (direct O to Ti transtition) or two step (O to O* to Ti transition) process.

The nature of the CB was investigated further by visualising the crystalline orbitals (COs) of the composite material at k-points Γ and S (from data calculated using CRYSTAL17[210]). From the visualised orbitals (Figure 4.14) it can be seen that, overall the first CB at S and Γ are quite similar, but there are subtle differences. Both points in this band show a combination of carbon, RGO oxygen, and some titanium atom AOs, but there is a greater contribution of carbon sp^2 AOs at Γ than at S, which is shown by the greater number of sp^2

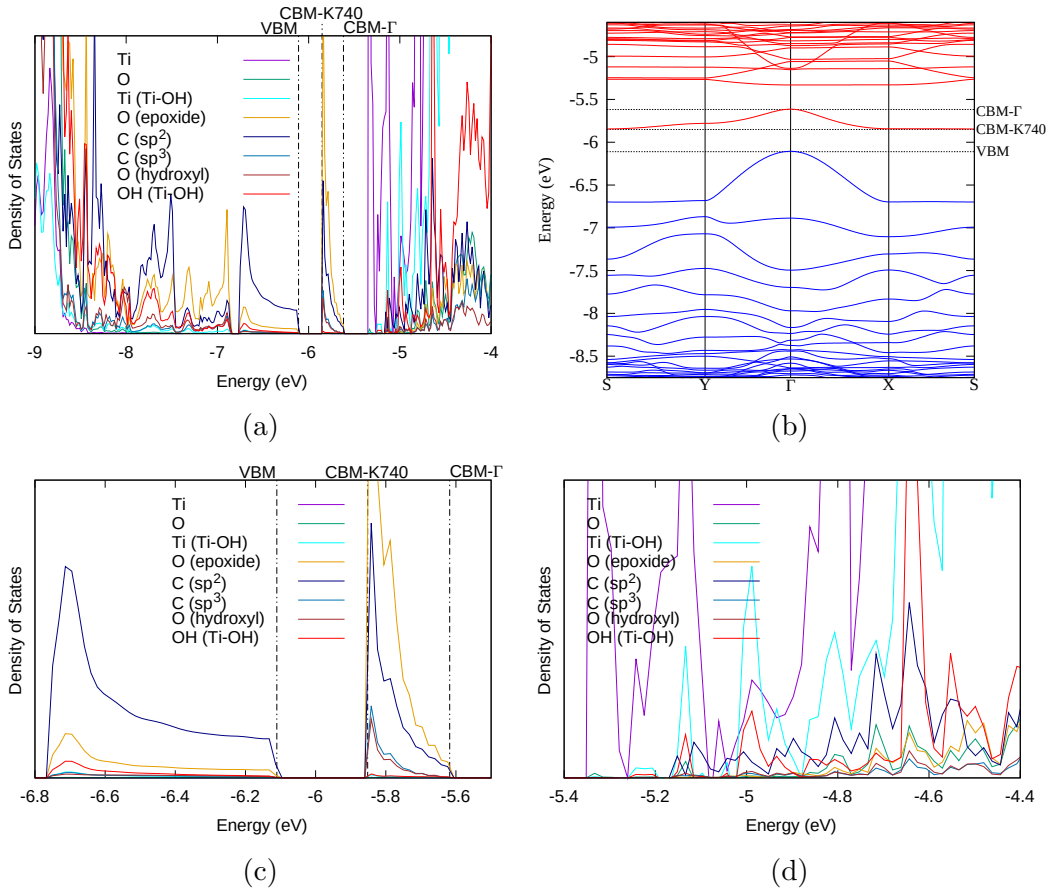

Figure 4.13: Electronic structure data for the 12H-RGO/rutile (110) (CL) composite: Comprehensive DoS (a), band structure (b), DoS of the VBM and CBM (c), DoS of the conduction band region (d). Colour schemes: DoS; see legend, band structure; blue bands are formally occupied, red bands are formally unoccupied. "K740" refers to the k-point (in the $12 \times 12 \times 1$ grid) where the CBM is observed

carbon atoms contributing in the former (Figure 4.14a) relative to the latter (Figure 4.14c). The carbon sp^2 AOs at k-point S are much more localised and mostly belong to carbon atoms nearest to the epoxide oxygen atoms in the structure, are therefore likely to originate from interactions between epoxide oxygen and the surrounding carbon atoms. This explains the DoS and band structure data for this CB in Figure 4.13: although sp^2 carbons contribute to this band at all energies, the band is delocalised over many sp^2 carbon atoms near the Γ point but is localised only on a few sp^2 carbon atoms at the S point.

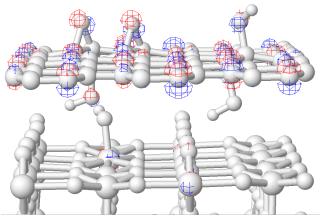

(a) A visualisation of the crystalline orbitals (COs) of the 12H-RGO/rutile (110) composite, for the first conduction band at k-point Γ

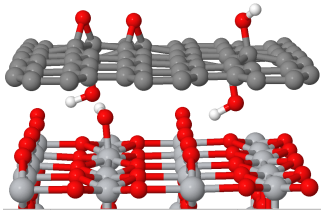

(b) A reference structure of the 12H-RGO/rutile (110) (CL) composite showing the atom colouring scheme, to compare with (a) and (c)

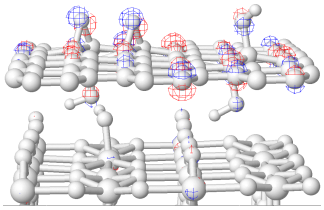

(c) A visualisation of the crystalline orbitals (COs) of the 12H-RGO/rutile (110) composite, for the first conduction band at k-point S

Figure 4.14

The electronic structure of the chemisorbed 12C-RGO/rutile (110) system was also analysed by the same means (see Figure 4.15). Formation of the 12C-RGO composite was done by removing two hydrogen atoms from the RGO structure, one of these was to facilitate the formation of the Ti−O−C bond and the other was to maintain spin-parity and avoid a more costly spin-polarised simulation. The second deprotonated hydroxyl group converted into an epoxide group upon optimisation. Interestingly both crosslinked 12H-RGO and 12C-RGO composites possess, qualitatively, the same type of lowest-unoccupied band. The width of the band is decreased in 12C-RGO, though it contains the same orbital components as in 12H-RGO: carbon sp^2, carbon sp^3, epoxide, and hydroxyl. The width of the RGO-based occupied bands is similarly decreased, which indicates that there is likely more disruption to the carbon sp^2 system than seen in the crosslinked 12H-RGO system. Furthermore there is a significant increase in the intensity of carbon sp^3 states present in the first VB and CB. The conversion of one hydroxyl group to an epoxide group will have converted one sp^2 carbon atom to sp^3, and the presence of an extra epoxide group will (as demonstrated in Figure 4.8) draw more electron density away from the surrounding sp^2 carbon atoms. For the 12C-RGO/rutile

composite this leads to a greater localisation of the sp^2 carbon atom states, and greater interaction between sp^3 and the epoxide groups.

In the crosslinked 12H-RGO system the epoxide groups interact with the π-network of the sp^2 carbon atoms, which is clear from the mixed-composition states between $-6.1\,eV$ and $-8\,eV$ in its DoS spectrum (Figure 4.13a), where carbon sp^2 and epoxide oxygen contributions appear at the same energy range. This will have the effect of drawing electron density away from the π-system to the epoxide groups, which reduces the contribution of sp^2 carbon π-orbitals to the occupied bands in the system. This ultimately leads to greater spatial localisation of carbon-based orbitals and a lower range of allowed energies for these bands. It is possible therefore that the reason why the band structure of 12C-RGO/rutile (110) features bands with more localised orbitals is that this new epoxide group draws more electron density from the carbon atoms in the system than the hydroxyl group which it replaced. In addition more carbons atoms are now sp^3 hybridised because of the change in functional group, thus the size of the sp^2 network will be reduced slightly. Comparing this electronic structure to that of crosslinked 12H-RGO indicates that the unoccupied RGO CBM always contains contributions from atoms that form the interfacial $Ti{-}O{-}H\cdots O$ bond or a stronger $Ti{-}O{-}C$ bond. Based on this it can be concluded that the formation of either variant of crosslink provides the necessary chemical environment to form the new CBM of the system.

Variations in Oxygen Content in RGO

To determine whether the formation of the crosslink or the presence of oxygen defects alone lead to the formation of the new CBM, the crosslinked 12H-RGO/rutile (110) composite was modified by sequentially removing oxygen functional groups. Firstly two hydroxyl groups (of the original total of

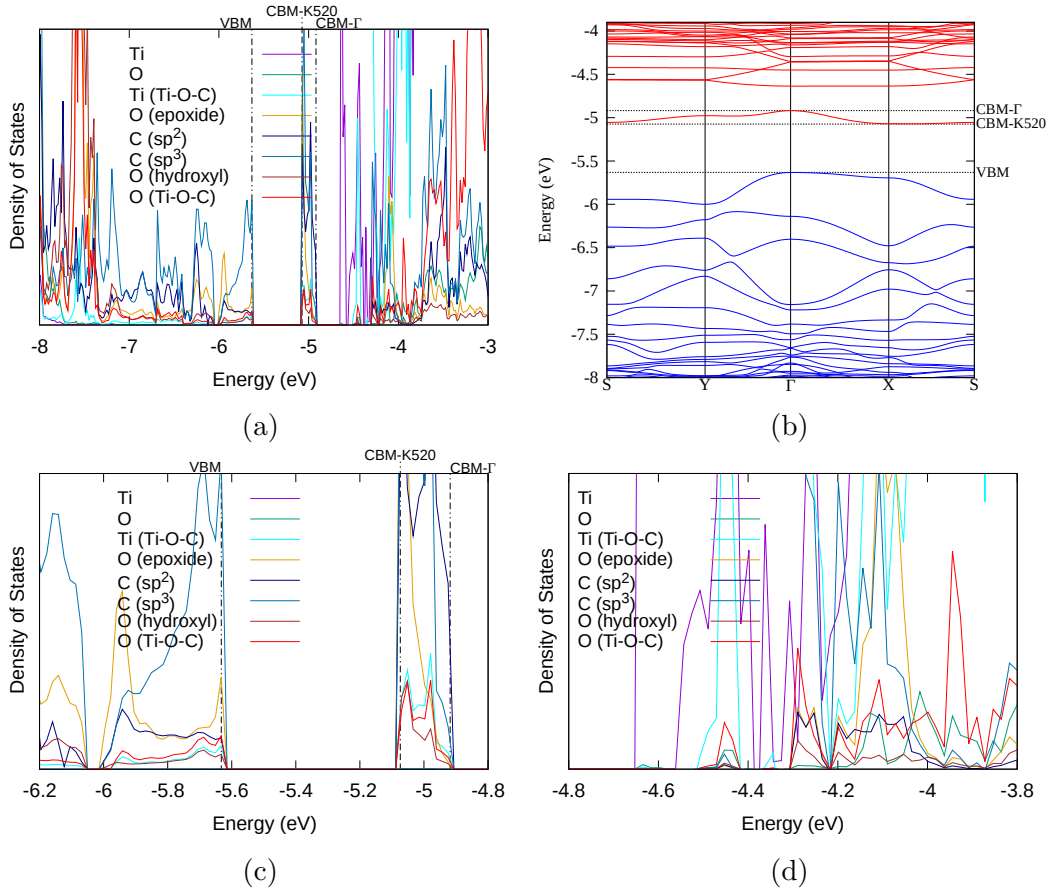

Figure 4.15: Electronic structure data for the 12C-RGO/rutile (110) composite: Comprehensive DoS (a), band structure (b), DoS of the VBM and CBM (c), DoS of the conduction band region (d). Colour schemes: DoS; see legend, band structure; blue bands are formally occupied, red bands are formally unoccupied. "K520" refers to the k-point (in the $12 \times 12 \times 1$ grid) where the CBM is observed

4) were removed (structure shown in Figure 4.7e), leaving the two epoxide groups and the crosslinking hydroxyl groups to form the 18H-RGO composite (electronic structure in Figure 4.16). The previously observed RGO CBM is still present, the width of which does not change significantly. The composition of the band is similar to the 12H-RGO (CL (CL)) composite (Shown in Figure 4.13). The band's maximum energy is still centred at Γ, while the minimum has shifted to be exactly at the S-point. The DoS (Figure 4.16a) shows that there is a majority contribution from sp^2 carbon around maximum

energy, while the lower energy states of the band are again predominantly made from epoxide oxygens.

The functional groups in GO and RGO act to break up the sp^2 network of graphene, which leads to both the semiconducting behaviour of GO and the reduced conductivity of RGO relative to graphene.[198] RGO system can be compared with 1D-periodic graphene nanoribbons where DFT calculations using the HSE06 functional yield calculated band gaps which are inversely proportional to the width of the nanoribbon.[213] In RGO the hydroxyl groups not involved in the crosslink act to spatially localise the sp^2 network in this structure, and thus removing these groups will extend the sp^2 network.

The 2nd and lower occupied bands (VB and VB-1) shows signs of separation of the oxygen functional group and carbon sp^2 states, where the sharp change in epoxide state density (Figure 4.16a) around $-6.6\,\mathrm{eV}$ matches the energy maximum of the 2nd valence band of the band structure (Figure 4.16b). This clear difference in the composition of the VB and VB-1 indicates that there is less mixing of states between the oxygen functional groups and carbon sp^2, this is likely due to the expansion of the sp^2 network following the removal of the two hydroxyl groups. In the CBM this type of change can also be seen, as the epoxide state density drops to zero near the band maximum while the carbon sp^2 state density continues to become dominant at the peak of the band around Γ. Though the differences in electronic structure between 12H and 18H-RGO are small, there is clear evidence of segregation of carbon sp^2-based and oxygen-based states, suggesting that the mixing of different RGO atom states in the electronic bands of the system decreases as the local defect density decreases.

Removing the final two epoxide groups from the 18H-RGO structure, thus yielding the 36H-RGO/rutile (110) composite (Figure 4.7f), leads to a much

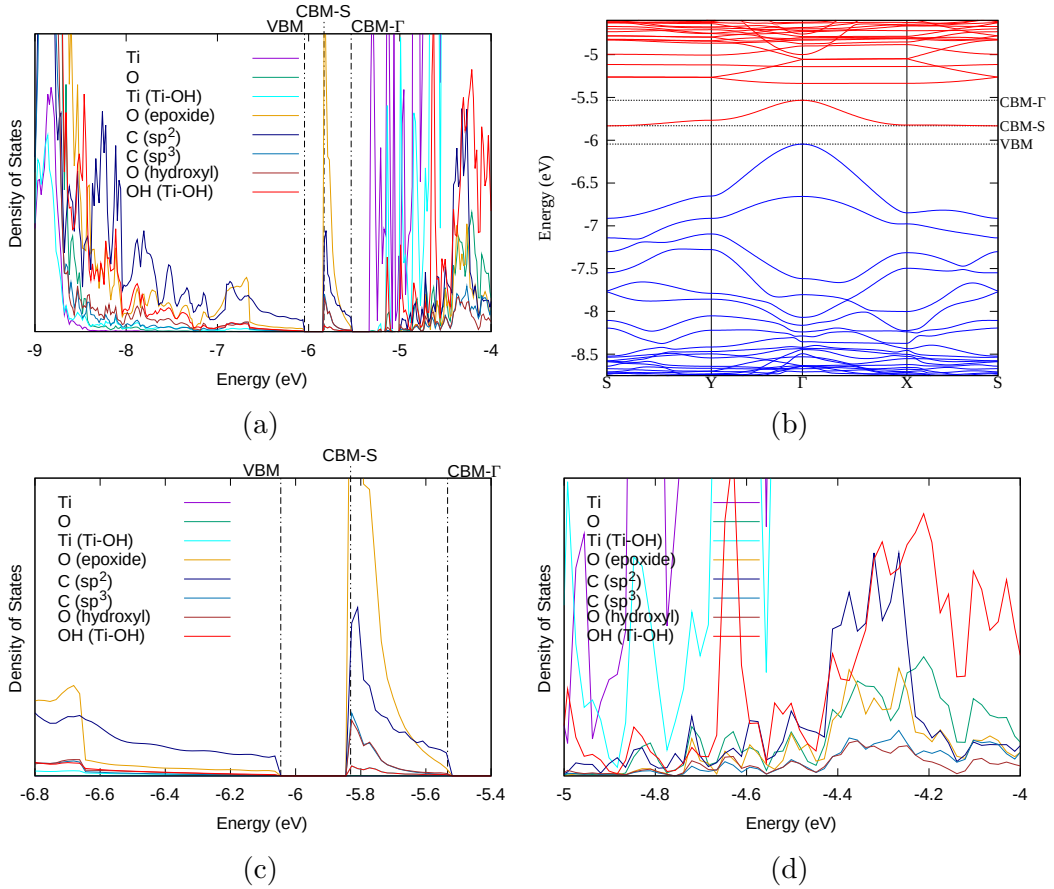

Figure 4.16: Electronic structure data for the 18H-RGO/rutile(110) (CL) composite: Comprehensive DoS (a), band structure (b), DoS of the VBM and CBM (c), DoS of the conduction band region (d). Colour schemes: DoS; see legend, band structures; blue bands are formally occupied, red bands are formally unoccupied

greater change in the electronic structure than was seen in the 18H-RGO composite. From the DoS and band structure (Figure 4.17) we see that there is a distinct graphene-like valence band, and that the direct energy gap between the CBM and VBM has has closed sufficiently to make the system an indirect zero-gap semiconductor. The width of the CBM has also increased slightly, and carbon sp^2 and oxygen functional group states are even more distinct in the DoS than in the previous structures. This shows that the carbon sp^2 network has been expanded further following the removal of both epoxide groups. In addition the energy gap between the carbon π and π^* bands has decreased

significantly to around 0.48 eV, again indicating that the sp^2 network has expanded further. The difference in the effect on the carbon sp^2 network between removing the hydroxyl groups and the epoxide groups indicates that, the epoxide groups have a much stronger effect on the surrounding carbon atoms than the hydroxyl groups. This is attributed to the greater electron-withdrawing ability of the epoxide groups compared to hydroxyl groups (see Figure 4.8).

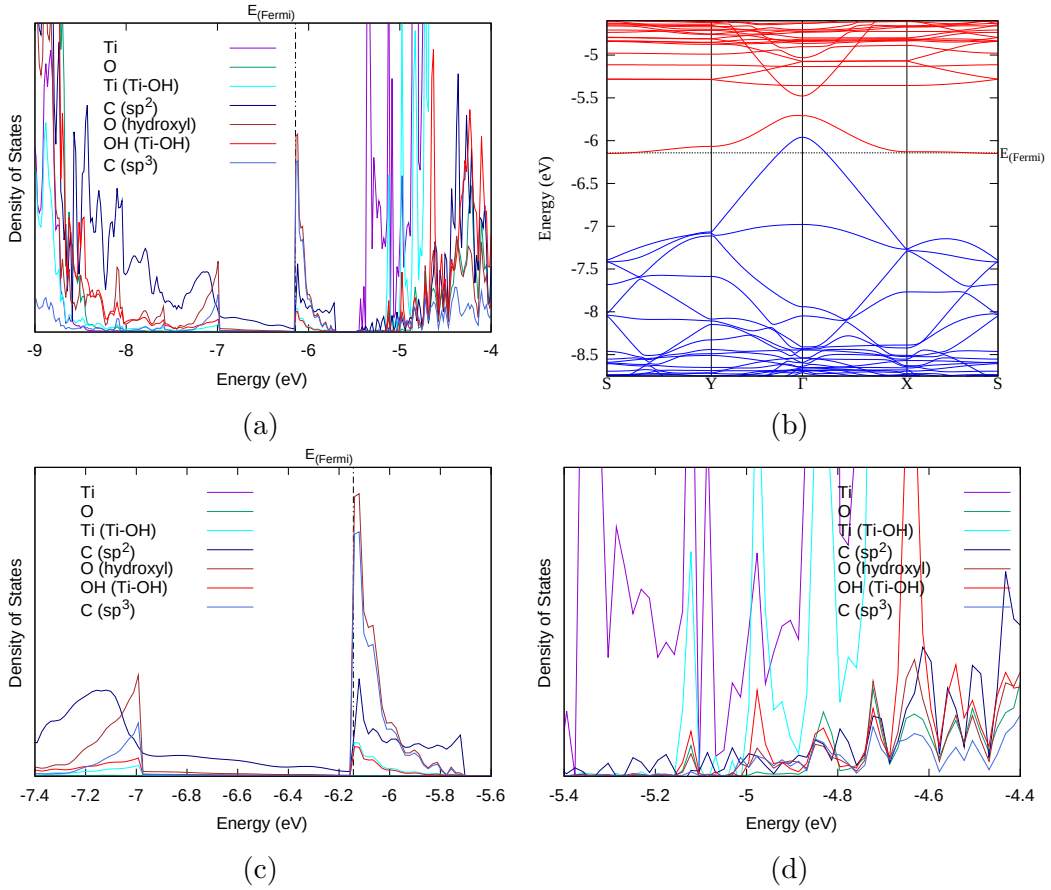

Figure 4.17: Electronic structure data for the 36H-RGO/rutile (110) (CL) composite: Comprehensive DoS (a), band structure (b), DoS of the VBM and CBM (c), and DoS of the conduction band region (d). Colour schemes: DoS; see legend, band structure; blue bands are formally occupied, red bands are formally unoccupied

We compare the band structure for the 36H-RGO/rutile system in Figure 4.17b with the analogous plot for graphene/rutile (110) (analysed in a previous chapter) in Figure 4.18. Besides the obvious difference between the

semimetallic graphene/rutile (110) composite and the zero-gap indirect semiconductor 36H-RGO/rutile (110) composite, there are clear similarities between the valence bands of both systems, as the bands are both composed of delocalised carbon sp^2 states. Clear differences can also be seen in the lower valence bands, where various bands with narrow allowed energy ranges (e.g. at $-7.0\,\text{eV}$ and $-8.1\,\text{eV}$ caused by the presence of oxygen defects) can be seen in the 36H-RGO system but not in the graphene system. It is therefore clear that the presence of crosslinking oxygen defects, even at very low concentrations, has a very strong effect on the electronic structure of RGO/TiO_2 composites. As such it is essential that any computational modelling of RGO-based composites must take into account both the presence of functional groups, and crosslinks formed from them.

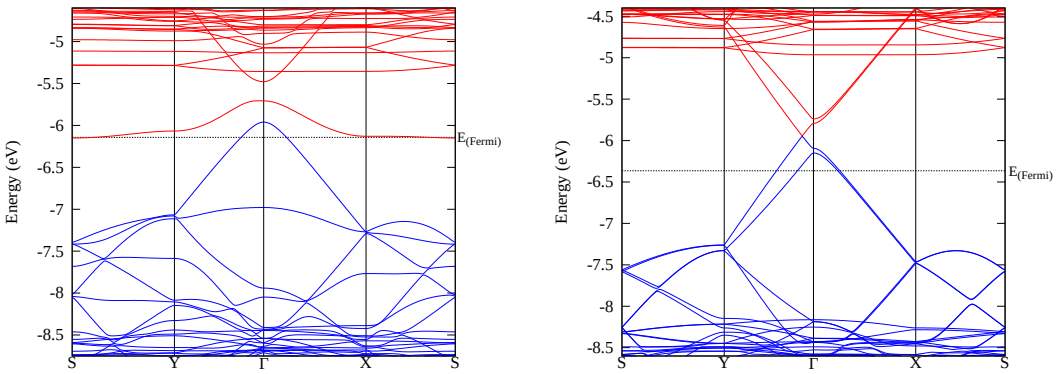

Figure 4.18: Band structures of (4.18a) 36H-RGO/rutile (110), and (4.18b) graphene/rutile (110), calculated with the HSE06 functional. Blue bands are formally occupied, red bands are formally unoccupied

Electronic Structure Analysis of RGO

The electronic structures of the isolated RGO components taken from the crosslinked 12H-RGO and 36H-RGO/rutile (110) composites were analysed, in order to separate the effects of the RGO oxygen groups on the electronic

structure from those caused by the interfacial binding in their composites. Both RGO systems were optimised with the same method as for previous systems. The hydroxyl group that is transferred to the rutile (110) surface was not included in these RGO structures, as this was determined to be part of the rutile (110) component instead of the RGO component, thus creating a spin-polarised RGO system. Band structures for the α and β spin states were produced (Figure 4.19) for each of these RGO structures, where the α spin state contains the unpaired electron. Both spin states of the two band structures are semiconducting, as opposed to semimetallic in the case of pristine graphene, and have a singly-occupied (α spin) or first unoccupied (β spin) band which closely resembles the CB of their respective composite systems (Figure 4.13 and Figure 4.17). In particular, the CB in the β-spin and VB in the α-spin band structure has a similar composition to the CB of the RGO/rutile (110) composites: mainly sp^2 carbon around Γ, and sp^3 and sp^2 carbon, hydroxyl and epoxide oxygen between Y-S-X.

The energy width of the RGO β-spin CB is much narrower than that of the composite CB. There is also a decrease in direct and indirect energy gaps betweeen each β-spin RGO band structure and their respective composites: 0.34 eV and 0.52 eV respectively for direct and indirect gaps of 12H-RGO; and 0.24 eV and 0.54 eV respectively for direct and indirect gaps of 36H-RGO. The indirect energy gap is mostly dependent on the energy position of the RGO oxygen and carbon states which make up the lower part of the CB. These are the atoms that interact with titanium atom states on the surface of rutile (110) (in Figure 4.13). Therefore the β-spin CB can be seen as the precursor to the composite CB. This band is unoccupied in the composite, due to transfer of both electron density and a hydroxyl group from RGO to rutile (110). The width of the band (the energy difference between the band energy

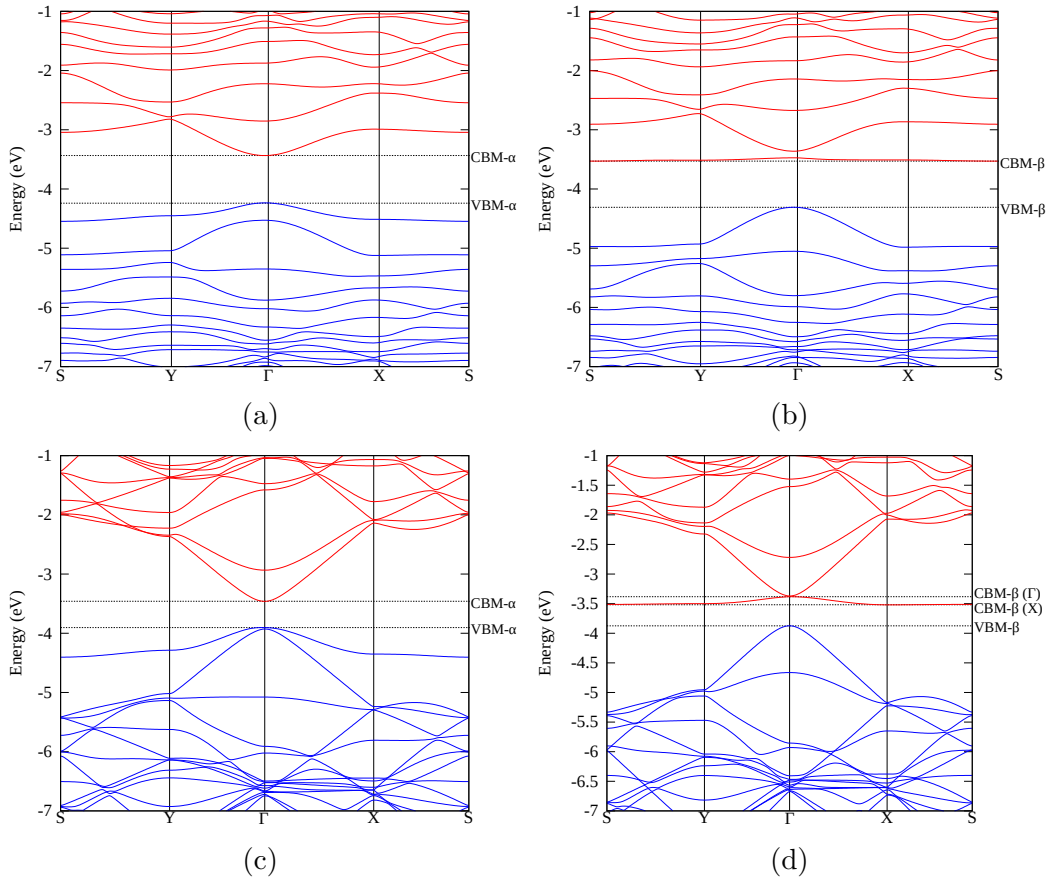

Figure 4.19: α and β-spin band structures of the isolated RGO components of the 12H-RGO (a and b respectively) and 36H-RGO (c and d respectively) composite systems, where the hydroxyl group transferred to rutile (110) is considered not to be a part of the isolated RGO structure

at Γ and S) is then increased in the composite by the stabilising electronic interaction between the RGO oxygen functional groups of the crosslink and the titanium terminus of the crosslink on rutile (110). This comparison of the RGO electronic structure with its composites shows that some of the key features present in the composite's electronic structure, most notably the pronounced "inverted" shape of the first CB in the composite, originate from the change in RGO chemical structure upon formation of the interfacial crosslink. The CB itself is an RGO band that becomes unoccupied when the composite is formed, which arises in the composite as the formation of the Ti−O bond shifts the

electrons in the RGO band to lower energy. The electronic coupling of this unoccupied band with surface Ti states lowers the energy of the RGO oxygen states more than the carbon sp^2 states, which accentuates the inverted curve of the CB and provides a means to trap the photogenerated charge carriers in the system.

Discussion: The Role of Crosslinks in Composite Photocatalysis

It is important to note that, in each crosslinked system studied so far, it is possible to see orbital components in each of these RGO oxygen bands which are derived from the surface titanium atom forming the rutile (110) terminus of the crosslink — labelled as Ti (Ti−OH) in the DoS plots. Some past studies have proposed that the enhanced visible-light photocatalytic properties of this composite system are due to the formation of Ti−O−C and Ti−O−H$\cdots$O−C crosslinks, which provide a direct means of promoting ground-state electrons from RGO to the TiO_2 conduction band with visible light photons.[103,133] The data in this work supports this hypothesis, our results show that the formation of a crosslink changes the electronic behaviour of the RGO component and couples the electronic structures of RGO and rutile (110). From the electronic structure information we can see that oxygen functional group-based bands have very suitable energies and compositions to facilitate this sort of photosensitisation process, as the DoS plots of the conduction band region (-4.8 eV to -4.6 eV in Figure 4.13d, -4.8 eV to -4.6 eV in Figure 4.16d, and -5.2 eV to -4.6 eV in Figure 4.17d) show that there is some electronic coupling between the orbitals of the oxygen functional groups in RGO and the Ti atoms involved in the crosslink. While the methodology used in this study cannot calculate the oscillator strength of transitions (which could be achieved using time-dependent DFT), it would still be reasonable to assume that these oxygen

functional group bands are likely candidates to promote photosensitisation and photoexcitation of TiO_2. This is supported by past experimental observations which show that oxygen-containing RGO/TiO_2 composites have improved photocatalytic activities over unmodified TiO_2,[15,18,126,127,129,130,133,209,214] and that these composites have measurable quantities of interfacial crosslinks.[133,209]

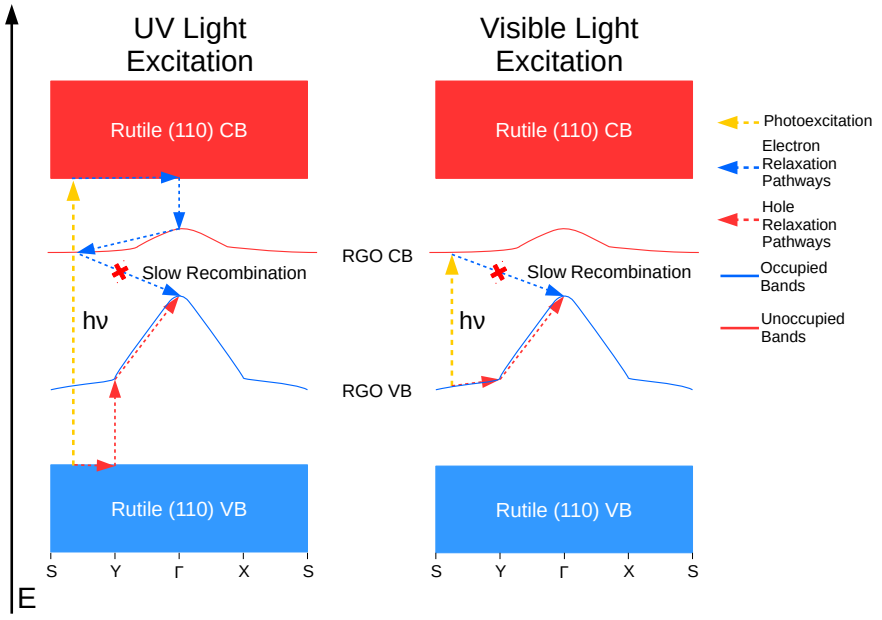

Figure 4.20: A proposed schematic of the charge trapping process in the RGO/TiO_2 composite system (key shown to the right hand side of the schematic). From this it can be seen that the large difference in electron momentum between the two charge carriers is what slows recombination, and results in long excited state lifetimes for this composite

Another important observation of the RGO composite systems in this study is the shape of the RGO CB. The maximum energy of the CB is at the Γ-point and its minimum energy is at around the S-point. As the energy profile of the CB is qualitatively similar to the VB, the band gap of the system is indirect with a very large difference in electron momentum between the top of the VB and bottom of the CB. The RGO CB is also below the rutile (110) CB, and is energetically separated from the TiO_2. It is therefore possible that this

type of conduction band could act to trap photoexcited electrons in such a way that would hinder electron-hole recombination. While there is no direct experimental verification of the shape of the band structure or the energy distribution of the CB of RGO/TiO_2 composites, there is some support from studies which look at photocurrent responses. Some previous studies have shown that the combination of RGO and TiO_2 yields very low ($\sim$1 µA) visible-light photocurrent.[124] At the same time it has also been observed that the UV photocurrent response increases when RGO is added to the system,[125,126,128] and that it increases further as oxygen functional groups are removed from the system.[124] The increase in photocurrent from UV light sources points to reduced charge-carrier recombination, which is ascribed to the trapping of photogenerated electrons in the system. It has been for instance noted that there is a decrease in the decay rate of the initially-recorded UV-photocurrent when RGO is combined with TiO_2, indicating that the lifetime of the excited state is increased.[126] The very low visible-light photocurrent,[124,128] at first seems at odds with the often reported improved visible light photocatalytic rates.[15,17,18,127] Visible light excitations must originate from an RGO VB (as visible-light photons do not have sufficient energy to overcome the TiO_2 band gap), and the RGO CB has the greatest orbital overlap with these bands. The narrow energy range of the RGO CB is likely the cause of the low visible-light photocurrent, as its spatially localised orbitals would reduce charge carrier mobility significantly.

An important caveat must be applied to this conclusion, however. The methodology used in this work models the chosen system as an infinitely-repeating solid, instead of directly simulating the full crystal structure. Because the shape of the RGO CB is a result of the interaction between sp^2 carbon atoms and the non-crystalline oxygen functional groups, its is possible

that this is an artefact of the infinitely-repeating periodic cell used. The presence of oxygen functional groups and the interfacial crosslink may therefore not behave in this manner in a real sample of the composite. This behaviour should thus not be considered to be conclusively proven from this work alone.

4.8 Conclusions

In this chapter, different modes of interfacial binding between GO or RGO and rutile (110), and the effect on local oxygen defect concentration and their relationship with the electronic properties and especially photocatalytic properties of the composite have been investigated using DFT simulations. From the analysis of binding energies it is clear that the formation of crosslinks, such as Ti−O−C and Ti−O−H$\cdots$O−C bonds, between RGO and TiO_2 is a key factor in achieving strong adhesion in the composite. Hydrogen bonding has also been identified as an important aspect of the interfacial binding in this composite. The formation of crosslinking bonds has been shown to strengthen the interfacial binding. It is found that higher concentrations of oxygen functional groups do not always promote the formation of interfacial hydrogen bonding, and that in the extreme case of very high concentrations of oxygen functional groups (such as our GO/rutile (110) system) these groups predomiantly participate in non-interfacial hydrogen bonding within GO itself instead. The trend in binding energy strengths also shows that some oxygen functional groups of RGO which do not participate in interfacial binding, such as epoxide oxygen, slightly weaken the interfacial interaction. By analysing the electron density difference in the 12H-RGO/rutile (110) system, it is concluded that the influence of non-binding epoxide groups on binding energies is due to these groups drawing electron density away from the crosslinking hydroxyl groups and their

associated sp^3 carbon atoms. It can be expected, based on the data shown in this work, that intefacial binding would be strongest in a system containing more hydroxyl oxygen groups rather than epoxide groups. The kinetics of the formation of the interfacial crosslinks are still unknown however, and future work in this field will need to focus on this to explain how the formation of these crosslinks could be more effectively controlled during synthesis of such composites.

The electronic structure data presented here helps to explain numerous experimentally-described unusual behaviours of the RGO/TiO_2 composite; such as increased UV- and visible-light photocatalytic performance, the long recorded lifetime of the excited state, and changes in measured UV- and visible-light photocurrent. It has been demonstrated that covalent bonding between RGO and TiO_2, from both Ti−O−C and Ti−O−H$\cdots$O−C motifs, may associated with the formation of a new conduction band that is predominantly localised on RGO below the conduction band of TiO_2. The energy profile of this band is such that it would promote the trapping of photoexcited electrons in such a way that would hinder charge carrier recombination and extend the lifetime of the excited state. However, as stated previously, the use of a periodically-repeating unit cell on an amorphous material casts doubt on this conclusion, and thus requires further study to prove conclusively. This band is formed by only a few oxygen functional groups, but the local concentration of oxygen defects affects the composition of both this band and other RGO bands in the system. The electron-withdrawing effect of the epoxide groups, which in turn depletes the electron density of their π orbitals, thus weakening the local sp^2 network and yielding more mixing of carbon sp^2 and oxygen states in the RGO bands. The RGO CB has atomic orbital components from atoms of RGO and rutile (110), which indicates that electrons could be photoexcited

to it from occupied RGO bands directly. It is also possible that electrons originating from RGO bands with strong oxygen character may be able to be photoexcited directly to the TiO_2 CB, as the spatial orbital overlap between RGO oxygen and the TiO_2-terminus of the crosslink thus formed forms densities of states higher in energy than the rutile TiO_2 conduction band. This latter possibility would constitute a type II heterojunction (allowing direct transition from photosensitiser VBM to semiconductor CBM), though the orbital overlap will also yield a type I heterojunction (allowing transfer of charge carrier from photosensitiser to semiconductor post-excitation). It is clear from the results in this report that a variety of oxygen functional groups should be included in simulations, and that a pure graphene composite alone is insufficient to describe the full range of possible interactions present in this composite system.

A common feature which appears in the electronic structure data presented in this work is that the band gap of many RGO/rutile (110) composites is very low, at around 0.5 eV. This means that the band gap energy would fall within the infrared region of the spectrum, and would thus be hard to determine using current experimental or spectroscopic techniques. The electronic structure data presented here could be complemented by calculating excitation and emission spectra for each system. This could be done, for example, through the use of time-dependent DFT (TDDFT) methods, however at present such calculations have not been practically achievable with currently-available hardware and software. It should also be reiterated that the RGO and GO structures proposed in this study are a sample of the wide range of potential structures that these amorphous materials could form. Further work would therefore be required to investigate the effect of other important structural domains that exist in this type of composites (e.g. looking at the effects of lactone and

carboxylic acid group interaction with TiO_2), and how domains with different concentrations of functional groups interact with each other (e.g. how these crosslinks interact with nearby non-crosslinked/graphene-like domains in the structure). Modelling the interactions between domains would allow more in-depth explanations of the bulk properties of this system to be made, such as photocatalytic and photocurrent performance.

Chapter 5

Cyclometallated Ru-Based Dyes for DSSC Applications

5.1 Dye-Sensitised Solar Cells

While photocatalytic systems can be used to convert solar energy directly into chemical energy, solar cells can instead convert solar energy into electrical energy. Dye-sensitised solar cells (DSSCs) in particular share some similarities with the photocatalytic systems mentioned previously: both types of system are frequently based on TiO_2 and make use of sensitisers through charge-transfer processes. Similar in function to the semiconductor/semiconductor hybrid systems mentioned in the previous chapter, DSSCs have grown in prominence since the first DSSC system was produced by Grätzel and O'Regan in 1991.[215] Their development has been spurred on by the prospect of them being a cheaper alternative to silicon solar cells,[216] and by their potentially high power conversion efficiencies (PCEs).[216,217]

A typical DSSC system (see schematic in Figure 5.1) contains a semiconducting material, such as titanium dioxide (TiO_2) or zinc oxide (ZnO), and a

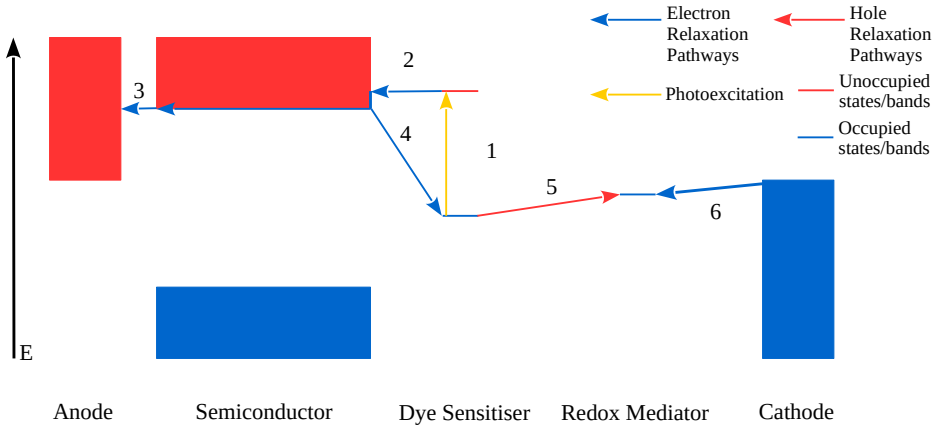

Figure 5.1: Schematic for the overall mechanism of charge-transfer processes in a dye-sensitised solar cell (DSSC) system: (1) Absorption of a photon to generate the dye's excited state, (2) photoexcited electron injection into the semiconductor conduction band (CB), (3) transport of the photoexcited electron through the semiconductor to a conducting anode material, (4) recombination of the photoexcited electron in the semiconductor with the hole in the dye cation, (5) re-generation of the dye by the redox mediator, and (6) re-generation of the redox mediator by a conducting cathode material.

"dye" species which functions as a photosensitiser. The dye itself is usually either metal-organic (a transition metal complex) or organic (often utilising conjugated π-systems). Dyes in this context refer to molecules which are capable of absorbing in the visible region of the solar spectrum. In a DSSC, dyes are covalently bonded to the surface of the semiconductor. The dye then acts as a sensitiser by injecting its photoexcited electron directly into the conduction band (CB) of the semiconductor to which it is bonded. Thus, for a dye to be effective for sensitisation, its lowest-unoccupied molecular orbital (LUMO) must be higher in energy than the conduction band minimum (CBM) of the semiconductor it is bound to. This excited-state electron is then transported through the semiconductor, in order to yield some thermodynamic work elsewhere; either collected at the anode for use in an electrical circuit (in a photovoltaic system) or used directly in a photocatalytic reaction (in a photoelectrocatalytic system). The process of charge injection oxidises the dye sensitiser,

leaving a hole behind (forming a dye cation). This hole is then transferred to the redox mediator (usually I^-/I_3^-), which is then reduced at the cathode. The difference in electrical potential between the anode and cathode directly relates to the efficiency of the device. As a description of TiO_2 properties has already been presented in previous sections (chapter 3), this overview will focus on the dye molecules themselves, and the dye-semiconductor interactions involved in n-type DSSC devices. The relative advantages and disadvantages of both metal-organic and organic dyes will be discussed. In addition both the effects of different calculation parameters (choice of functional and solvation method, for example) and heterogeneous surface interactions will be discussed. Research work on p-type DSSC devices has intensified more recently;[218] however this will not be covered here, as our work is concerned only with n-type DSSCs.

5.1.1 Metal-Organic Dyes

Ruthenium (II) Complexes

The structure of almost all inorganic dyes is fairly consistent: each uses a transition metal centre which forms a complex with suitable organic ligands. Though there are examples of a few other transition metals in the literature (as described later in this section), the vast majority of published DSSC works utilising metal-organic dyes use Ru(II).[216,217,219] Thus we will discuss this topic primarily through examples of Ru(II) complexes. The first published examples of an inorganic dye for DSSC applications were the so-called "N3" dye (*cis*-Ru(4,4'-dicarboxy-2,2'-bipyridineH_2)$_2$(NCS)$_2$) and its doubly-deprotonated variant "N719" (shown in Figure 5.2). Both dyes have achieved PCEs of almost 12%, are among the most sucessful DSSC dyes, and are fre-

quently used as benchmarks for other proposed DSSC dyes in both experimental[216] and computational[217,219] works. As our work that will be presented in this section is computational in nature, particular attention in this section will be paid to computational works.

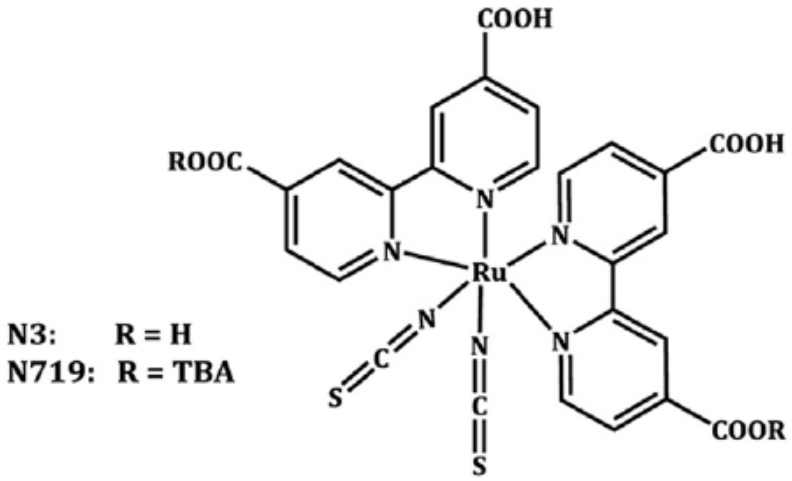

Figure 5.2: The chemical structures of the N3/N719 dye sensitiser, originally from ref.[218] TBA in this structure stands for tributylamine, which is typically used as an inert counter-ion for N719. Reprinted from [*J. of Photochem. Photobiol. C*, **28**, A. Nattestad, P. Ishanie, and S. Leone, Developments in and prospects for photocathodic and tandem dye-sensitized solar cells, 44–71] Copyright 2016 with permission from Elsevier.

From computational analysis of these dyes it is known that several of the highest-occupied molecular orbitals (HOMOs) are localised on the metal centre of the complex and the thiocyanate (NCS^-) ligand, and several of the LUMOs show a strong contribution from the dicarboxy-bipyridine ligands.[219–223] The HOMO-LUMO excitations of these dye molecules therefore represent both metal-to-ligand charge transfer (MLCT) and ligand-to-ligand charge transfer (LLCT) processes, where electron density moves from the metal centre and the NCS^- ligands to the dicarboxy-bipyridine ligands. The bipyridine ligands also aid the overall mechanism of excited-state electron transfer from the dye to the semiconductor to which they are bound, as molecular orbital components

of the carboxylic acid groups attached to the bipyridine ligands also feature prominently in the first few LUMOs of the dye.[221,223] The fact that the acid groups anchor directly to the semiconductor surface provides direct orbital overlap of the first conduction band (CB) and the dye's LUMO and allows fast transfer of photoexcited electrons to the semiconductor. In addition, the photogenerated hole is localised on the metal centre and the thiocyanate ligands, and is spatially separated from the photoexcited electron localised on the bipyridiyl groups, and from electrons injected into TiO_2 the photogenerated hole from the electron transferred to the metal centre.

An important consideration to make when calculating the electronic structure of metal-organic dyes, which has been noted in the literature,[223] is the effect of solvent. For these dye systems it has been generally noted that the HOMO-LUMO gap of the dye increases when polar solvent is included in the system,[219] implicitly by the use of polarisable continuum models[224] (PCMs). An in-depth computational study[223] by Fantacci *et al* showed that there was both an increase in the energy of the LUMO of N3, and a decrease in the HOMO energy. As the HOMO of the dye is localised on both the metal centre and the NCS^- ligands, a polar solvent will interact favourably with the MOs of these polar groups, thus lowering their MO energy.[223] As the LUMO is localised on the π^* system of the bipyridine ligands, a polar solvent will interact unfavourably with the MOs of these non-polar groups, thus increasing their MO energy.[223] Due to the way that these solvent effects affect ligands and the metal centre differently, the energies of MLCT excitations will be much more affected by the local solvent environment than the energies of any non-MLCT (metal-centred (MC) or intra-ligand (IL)) electronic excitations.[225]

Studies have also investigated the effect of modifications to the ligand system. It has been found from DFT analyses[226,227] that increasing the number

of carboxylic acid groups on a ligand where the LUMO is localised extends the absorption spectra of the dye to lower (red wavelength) energies.[226] In addition, a DFT study by Zhang *et al*[228] found that the HOMO-LUMO energy of the system decreases if NCS^- is replaced with cyanide (CN^-), chloride (Cl^-), or di-carboxy bipyridyl (dcbpy). The change in ligand directly affects the absorption spectrum of the resulting complex, however it is noted that this is brought about by lowering the LUMO energy (most significantly for CN^- and dcbpy) and has no noted significant effect on the *composition* of the LUMO itself.[228] Modifications to the dcbpy ligand system have also been shown to directly affect the HOMO-LUMO energies of Ru(II) dyes by altering their HOMO and LUMO energies.[229,230] Shifting the absorption spectra to lower energies is desirable as this will increase the available range of wavelengths in the solar spectrum which can be absorbed. The limitation on these changes of the gap is that the HOMO energies must still be lower than those of the redox mediator in order for the oxidised dye to be regenerated, while LUMO energies must be higher than those of the TiO_2 CBM in order to provide electron injection.

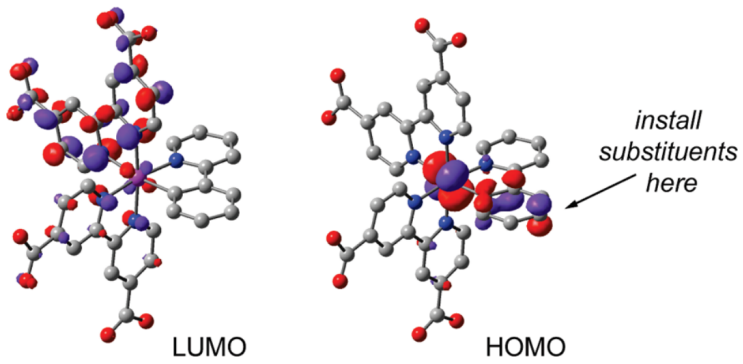

Figure 5.3: Isosurfaces visualising the HOMO and LUMO states of a cyclometalated analogue of the N719 dye system. Colour scheme; Ru: purple, O: red, C: grey, H atoms not shown. Reprinted with permission from [*Inorg. Chem.* 2010, **49**, 4960–4971]. Copyright 2010 American Chemical Society.

Cyclometallated Dyes Much more recently there has been a push to develop the N3/N719-derived dye systems further by replacing the NCS^- ligand, which is known to be quite labile,[231,232] with alternatives. The use of cyclometalating ligands (a chelating ligand which forms a C−Ru bond) had been proposed based on their potentially interesting σ-bonding properties,[233,234] however initial difficulties with the synthesis of such complexes and poor light-harvesting effectiveness lead to slow progress.[235,236] As a result of later developments in synthesis techniques,[237] several works have since demonstrated that cyclometalated complexes could function well as DSSC dyes.[238–240] Computational studies have demonstrated that the electronic states associated with the C−Ru bond yield MOs spread between the metal centre and the ligand (Figure 5.3), filling the role of the NCS^- ligand in the N3/N719 system.[240] The potential to modify the N′C′/N′N′C′ chelating ligands (denoting the elements which bond with the metal centre) also allows for photophysical properties to be tuned by adding substituents near the C−Ru bond.[240–243] The properties of cyclometallated Ru dyes will be studied later in this chapter.

Dyes Based on Other Group 8 Metals

Dyes based on group 8 elements and numerous other transition metals have been tested for DSSC applications.[216] Osmium (II) complexes were initially predicted to have an effectiveness similar to ruthenium complexes, based on their intense MLCT absorption band observed in spectroscopic experiments.[216] A series of dyes, based on the architecture of the previously-reported Ru(II) dyes have been prepared[222,244–247] over the 2000s. Spectroscopic tests of the dye systems have shown that Os(II) analogues of the previously-mentioned Ru (II) dyes (N3 and N719) have a very broad absorption (Figure 5.4), with an observed onset around 1100 nm and reaching around 50% incident photon-to-

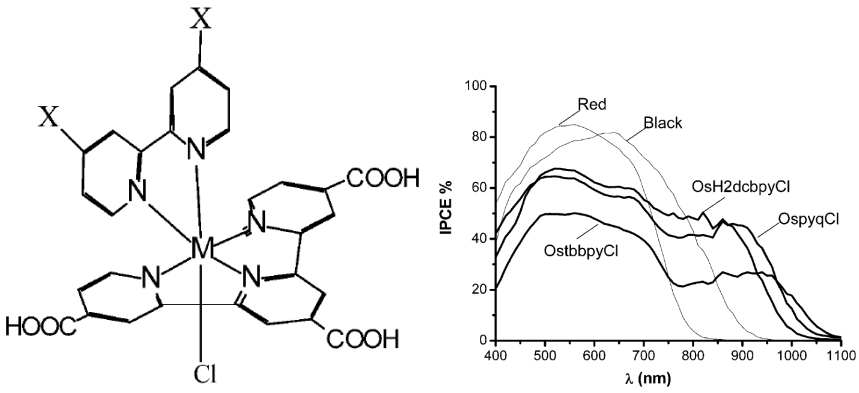

(a) (b)

Figure 5.4: Chemical structure (a) and % incident-photon-to-electron conversion efficiency (IPCE) spectrum for an osmium complex. The "red" and "black" labels used in the IPCE spectrum refer to the N3 and N719 dyes respectively. Reprinted with permission from [*J Am. Chem. Soc.* 2005, **127**, 15342–15343]. Copyright 2005 American Chemical Society.

electron conversion efficiency (IPCE) at 900 nm.[247] However, it was noted that overall performance was hampered by inefficient electron transfer between the Os(II) complexes and the iodide electrolyte used to re-cycle the dye.[247] Computational studies on group 8 metal-based dyes have shown that this observed red-shift in absorption spectrum is due to the destabilisation of the e_g orbitals in the metal centre. This raises the HOMO energy of the system to be greater than that of the iodide redox pair which thus inhibits dye regeneration. This effect becomes more prominent down the group in the order: Fe−Ru−Os.[222,248]

While ruthenium has been used successfully in dyes such as N3 and N719, and modifications thereof,[249–252] it is not very abundant in the Earth's crust (at around 1×10^{-8} kg kg^{-1} [253]). As a result, some studies explored dyes based on more earth-abundant transition metals, such as Fe.[254–256] However, iron complexes were found to be much less effective than ruthenium and osmium for DSSC operation, with maximum IPCEs measured at around 10-11% across a range of complexes compared to maxima of around 80-84% for Ru complexes (Figure 5.4b), as the excited-state lifetime of the dyes were found to be too

short-lived — a known issue with first-row transition element complexes.[254]

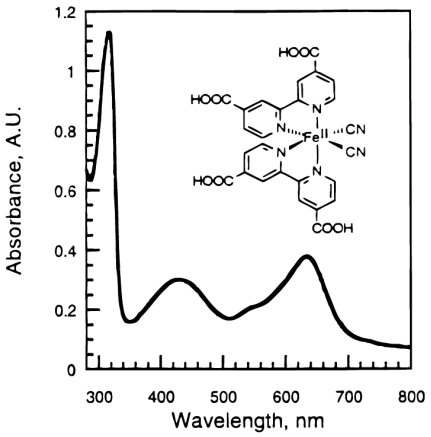

Figure 5.5: The absorption spectrum and chemical structure (inset) of an $Fe(dcbpy)_2(CN)_2$ complex. Reprinted with permission from [*J Am. Chem. Soc.* 1998, **120**, 843–844]. Copyright 1998 American Chemical Society.

Other Metal-Organic Dyes

Beyond the group 8 elements, some early work by Hasselmann and Meyer[257] has been done which looked at dyes based on rhenium (I) complexes. The report showed that the complexes yielded relatively low IPCEs of between 9 and 18%, with a high-energy onset wavelength of around 500 nm,[257] which in both cases is notably lower than that of Ru-based dyes. What was, interestingly, also noted is that the observed recombination rates were roughly equal for different variations of the Re-based sensitiser, as well as being similar to complexes of other Ru-based complexes.[257] This indicates that light-harvesting for Re complexes may be improved by developing effective ligand systems to enhance solar spectrum absorption, and effective Re complexes have been since developed for other light harvesting applications.[13]

Platinum complexes have also been tested for DSSC activity.[258–261] Square-planar complexes of Pt(II) were found to be quite effective at shorter wavelengths, with observed IPCE values of around 47% at 500 nm, and were found

to have some tunable properties based on the choice of ligands.[258] However it was found that light-harvesting performance dropped considerably at wavelengths longer than its 500 nm maximum,[258] which is also found to be the case for N3/N719 (see Figure 5.4). Later modifications of these complexes[259–261] were able to improve the overall device efficiency to a maximum of only 0.64%. Although rates of charge carrier recombination were noticeably reduced in these new dyes, their poor semiconductor surface coverage and still poor overall light absorption properties[216,259–261] resulted in less-than-ideal device performances.

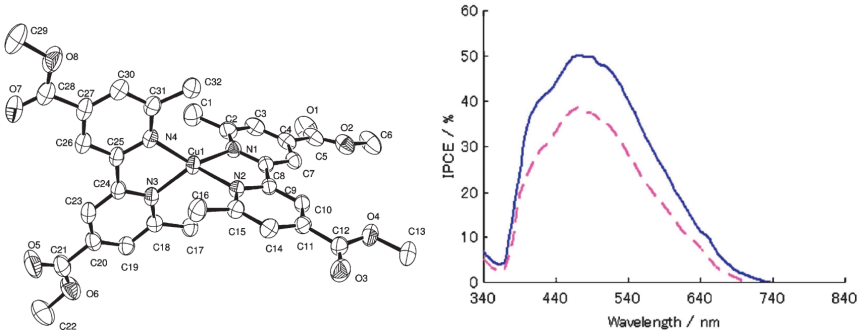

(a) (b)

Figure 5.6: The crystal structure (a) and IPCE spectrum (b) of a Cu(I)(bpyCOOCH$_3$)$_4$ complex. Hydrogen atoms were omitted from the original image of the crystal structure for clarity. The solid and dashed spectra in the IPCE data are those of the Cu(I)(bpyCOOCH$_3$)$_4$ and Cu(I)(bpyCOOH)$_4$ complexes respectively. Republished from [An Element of Surprise - Efficient Copper-Functionalised Dye-Sensitized Solar Cells, *Chem. Comm.*, Constable *et al*, **0**, 2008] Copyright 2008 The Royal Society of Chemistry.

Bipiridyl complexes of Cu(I) have been shown to possess light-absorption intensities of a similar magnitude to that of Ru(II) dyes such as N3 and N719,[262–265] with early recorded maximum IPCE values of 30%,[263] and later up to 50%.[264] In both cases the Cu(I) dyes showed inferior light-harvesting properties to Ru(II) dyes in most respects,[264] but it has been noted that the relative costs of Cu(I) dyes are much lower than Ru(II).[264] Furthermore, the

Cu(I) dyes showed similar or longer-wavelength IPCE onset wavelengths compared to Ru(II) dyes that would extend well into the red region of the visible spectrum (see Figure 5.6) which has been observed both experimentally[263,264] and, later, theoretically.[266] Despite its clear shortcomings in performance, the reduced scarcity of copper compared to ruthenium may make up for these shortcomings when considering industrial applications.

Overall, alternative systems to the well-established Ru-based metal-organic complexes have either shown comparable device performances with some shortcomings (in the case of rarer metals such as Pt, Os, and Re) or notably worse performance with few advantages such as reduced cost (in the case of earth-abundant elements such as Fe and Cu). In the context of metal-organic DSSC dyes, Ru-based systems are still very much the most effective, and varying their ligand systems remains the most effective means of tuning their properties.

5.1.2 Organic Dyes

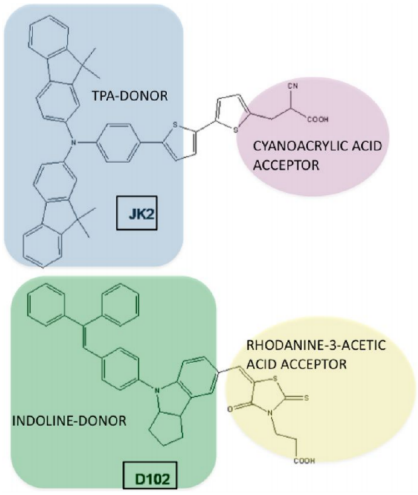

Figure 5.7: Chemical structures of two organic dyes (JK2 and D102) with annotations showing the donor and acceptor subunits (where TPA refers to triphenylamine). Reprinted with permission from [*J. Phys. Chem. C* 2013, **117**, 3685-3700]. Copyright 2013 American Chemical Society.

Although Ru-based dyes have proven to be quite effective for use in DSSCs, the low earth-abundance of Ru is a persistant issue for the production of such devices. As alternatives based on more earth-abundant metals (such as Fe and Cu) have not proven to be effective enough to rival Ru, attention has been focussed on other alternatives beyond transition-metal complexes, for instance in the field of organic dye-sensitisers. In contrast to noble metal-based dyes, organic dyes offer a number of potential advantages: Reduced production costs; reduced environmental impact from production; greater flexibility of design; and greater molecular extinction coefficients (ϵ) even compared to Ru(II) dyes.[216,217] The advantages of the first and second points are self-evident. Greater design flexibility increases the range of potential dye structures. Increased ϵ allows thin-film and solid-state DSSC systems to be produced more easily, as less dye coverage is required to achieve reasonable levels of performance. Overall, organic DSSC device performances have been shown to be steadily improving over the years, with the highest PCEs recorded at around 14%.[267] The typical architecture for an organic dye consists of two subunits, the "Donor" (D) and "Acceptor" (A), separated by a "bridge" ,[216,217,219] and can be referred to as a "push-pull" system.[219] The HOMO of the dye is localised on the D subunit, while the LUMO is localised on the A subunit along with the dye's anchoring group. The bridge then creates an orbital overlap between the two subunits by allowing each to delocalise slightly. Spatial separation of the two subunits means that, following electron transfer to the semiconductor, the positively-charged (D-subunit) end of the dye cation is spatially separated from the now more electron-rich semiconductor, which helps to slow charge recombination. D subunits are typically based on electron-rich structures, such as indoline,[268–271] and coumarin[272–275] (example structures shown in Figure 5.7 and Figure 5.8), while A subunits are based around the

carboxylic acid anchoring group.

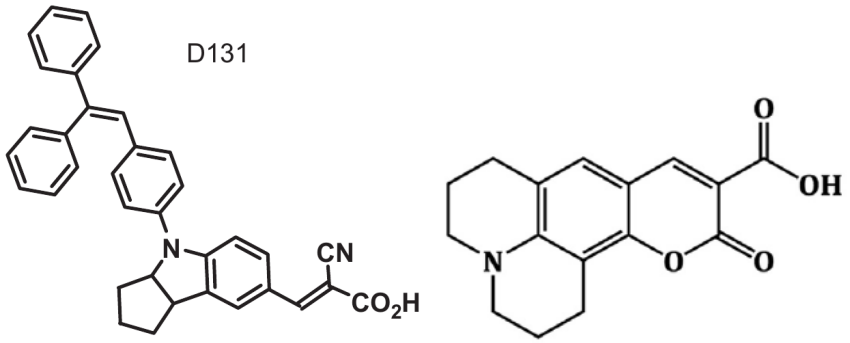

(a) (b)

Figure 5.8: Molecular structures of an indoline (a) and a coumarin (b) dye sensitiser, originally from ref[271] and ref[218] respectively. (a) reprinted from [*Solar Energy Materials and Solar Cells*, **93**, H. Tanaka *et al*, Long-term durability and degradation mechanism of dye-sensitized solar cells sensitized with indoline dyes, 1143-1148] Copyright 2009, with permission from Elsevier. (b) Reprinted from [*J. of Photochem. Photobiol. C*, **28**, A. Nattestad, P. Ishanie, and S. Leone, Developments in and prospects for photocathodic and tandem dye-sensitized solar cells, 44–71] Copyright 2016 with permission from Elsevier.

The design flexibility of organic dyes has lead to a vast array of different structures proposed in the literature, and although this leads to a large number of potential dye structures to investigate, some overall trends such as the donor-bridge-acceptor system have been found to give increased dye performance.[216,217] Calculations are, as for the case of metal-organic dyes, often the best way to determine structure-property relationships. Accurate computational insights have however been shown to be difficult to achieve, as the charge-transfer nature of the dye's HOMO-LUMO excitation results leads to inaccuracies (such as optical energy gap underestimation) in the results obtained from TDDFT simulations.[276–278] Furthermore, while results from TDDFT are quite consistent in describing trends in a series of inorganic dye complexes, it has been noted that the strong charge-transfer nature of the organic donor-bridge-acceptor system leads to a lack of consistency in describing trends in the electronic structure data produced for different organic dyes with

the same chosen functional.[279–283] Simply put, this means that there is not necessarily one "best" functional that can be reliably used for most dye systems, and it is therefore necessary to carefully evaluate the performance of the functional before using TDDFT to assess the properties of any given organic dye system. Even a simple structural change, such as changing the length of the dye's conjugated bridge, has been shown to result in a deterioration in accuracy for a variety of DFT functionals.[284] In order to improve accuracy, studies by Umari *et al*[285,286] used the GW method[287] at the so-called "G_0W_0 level"[288] to accurately and consistently calculate the HOMO and LUMO energy positions for a series of dyes, relative to equivalent DFT calculations. The GW method differs from DFT, as it derives electronic structure including the interaction of the excited state electron with its hole. The "G_0W_0 level" is a simplified, non self-consistent calculation of the GW energy.[288] This more reliably leads to increases in accuracy of electronic structure calculations for many systems. Although the results of GW method calculations are closer to experimental data and vary less unpredictably between systems, it is important to note that such calculations typically carry a high cost[219] System size must be factored into the decision of which method is the "correct" one to use, and DFT is still sufficiently accurate for use where more robust methods such as GW are impractical.

As with the case of inorganic Ru(II) dye systems, solvent has a noticeable effect on the HOMO and LUMO positions of organic dyes, computational studies often note a red-shift in calculated absorption energies for organic dyes when solvent is included,[217,219] and the excited-state geometry of some dyes can change slightly between solution- and gas-phase calculations.[289] Implicit solvation methods, such as PCM, have been shown to qualitatively reproduce the effect of solvent on various dyes.[290] However, the modelling of solvent

explicitly (i.e. including solvent molecules in the simulation itself) may be necessary in the case of protic solvents.[289,291–293] A further consideration regarding organic dyes is that the absorption spectrum of some dyes can change markedly when interacting with a surface, rather than in isolation: the addition of even a single metal atom representing the metal oxide semiconductor surface can lead to a red-shift in the absorption spectrum for organic dyes.[294] Moreover, electron transfer properties differ when either single-atom or heterogeneous interface models are used to describe the semiconductor on which the dye is adsorbed.[295]

Comparing organic to metal-organic dyes suggests, so far, that the majority Ru-based dyes are generally the most effective (based on PCEs) for DSSC work. Organic dyes however have potentially a greater scope for improvement than Ru-based dyes, as their organic framework offers greater design flexibility. The more recent examples of organic dyes have demonstrated that such dyes can have comparable or better PCEs than those of even the best Ru-based dyes. It should be stressed as well, that the other advantages of organic dyes (reduced environmental impact, reduced fabrication costs, and greater molecular extinction coefficients) also give such materials a useful edge over metal-organic dyes.

5.1.3 Dye-Semiconductor Interfaces

In addition to analysis of the dye molecules themselves, the interaction between the dye and the semiconductor surface needs to be taken into account. The stabilising effect of the surface-bonding interaction between dye and semiconductor can affect the energy alignment of the dye's MOs relative to the band energies of the semiconductor.[296] This is important to note, as changes to the dye's MO energies relative to the semiconductor could, for in-

stance, change the energy of its LUMO states relative to the CB energy of the semiconductor, thus showing that the dye will have efficient sensitisation relative to gas-phase calculations. Electronic coupling of the dye's MOs to those of the semiconductor surface must be modelled accurately, usually requiring the semiconductor system to be represented as a large cluster or periodic slab instead of simply a few atoms.[219] One of the important insights provided by calculations is the information on the possible adsorption structures, and their respective binding strengths, of a dye with the chosen semiconductor material, as it is a property which is difficult to measure experimentally. As an example of importance of adsorption configurations, experimental studies have shown that the collective orientation of the dye molecules in a DSSC device could affect the rate of competing recombination reactions (i.e. transfer of excited state to other adsorbed dyes),[297] though a clear mechanism for this observed effect has not been found so far.[219]

Computational studies into the adsorption of small carboxylic-acid-containing molecules (such as formic acid and benzoic acid) adsorbed onto TiO_2 have shown that the surface bonding interaction to rutile (110) TiO_2 (its most energetically stable and abundant surface facet) is strongest when the carboxylic acid group is de-protonated to form a carboxylate, whereupon it can form a bidentate adsorbed structure *via* both carboxylate oxygen atoms (shown on anatase (101) in Figure 5.9, structure a).[174,298,299] By contrast, for the anatase (101) surface, both the de-protonated bidentate and protonated monodentate (see structure c Figure 5.9) surface bonding interactions are found to be stable.[299,300] Further it has been found that, for the de-protonated bidentate bonding interaction, both a symmetric and an asymmetric structure is possible (having either equal or unequal O−Ti bond lengths), the symmetric arrangement is found to be more stable by around 0.26 eV than the asymmetric

arrangement.[300]

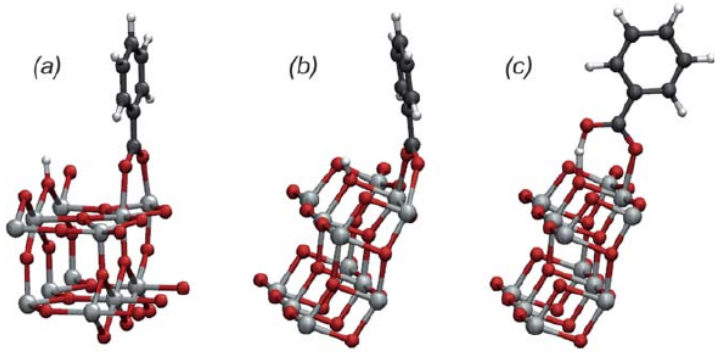

Figure 5.9: Structures of benzoic acid bonded to rutile (110) and anatase (101) surfaces, showing (a and b) the deprotonated, symmetric bidentate bonding arrangement, and (c) the protonated monodentate bonding arrangement. Republished from [Theoretical studies of dye-sensitised solar cells: from electronic structure to elementary processes, *Energy Environ. Sci.*, Martsinovich *et al*, **4**, 2011] Copyright 2011 The Royal Society of Chemistry.

Extending the analysis of adsorption structures from small molecules to organic dyes was a logical next step for studies to take, due to the fact that organic dyes typically have only one anchoring group. Studies of organic dyes adsorbed on anatase TiO_2 clusters have shown that these dyes' adsorption structures are generally similar to those found for small molecules, but the bidentate bonding interaction is preferred,[284,301,302] and there is a slight quantitative (and occasionally qualitative) difference in relative binding energy strength for each adsorption mode depending on the level of theory used in the computational model.[301] For dye molecules with multiple anchoring points, such as Ru(II) complexes, a similar preference for de-protonated bidentate bonding also was found,[303] however the rigid structure of many transition metal complexes with polydentate organic ligands often leads to non-symmetric bidentate surface bonding.[303,304] While calculations found that adsorption structures can form with up to three anchoring groups simultaneously bonded to a metal oxide surface,[304] this is generally only seen for complexes with multiple, separate,

carboxyl-containing ligands (Figure 5.10).

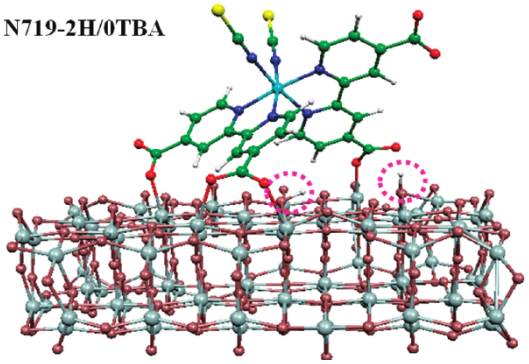

Figure 5.10: Structure of the N719 dye adsorbed on anatase (101) in a tridentate surface-anchoring arrangement, showing that carboxylic acid groups belonging to separate bipyridine ligands are involved in this arrangement. Reprinted with permission from [*J Phys. Chem. C*, 2011, **115**, 8825–8831]. Copyright 2011 American Chemical Society.

Besides information on adsorption configurations. Computational studies of the semiconductor-dye interface provides information on the alignment of electronic energy levels of the semiconductor and the dye. Accurately calculating the energy difference between the dye's LUMO and the energy of the semiconductor's CBM is necessary for determining the rate of electron injection into the semiconductor[217] The adsorption of a dye to a semiconductor surface, and the exact adsorption mode taken, has been shown in earlier studies to shift the energy of the dye's LUMO.[305–307] In a more recent study by Ronca *et al*,[308] ground-state charge transfer interactions between an organic dye and the semiconductor reportedly lead to a shift in the energy of the TiO_2 conduction band. This energy shift was also found to differ between bidentate and monodentate surface-bonded structures of the organic dye, with the former and latter yielding 0.2 eV and 0.02 eV differences respectively, thus indicating that the bidentate bonding interaction leads to stronger electronic coupling than the monodentate interaction.[308] Slight changes in the dye's HOMO energy (of around 0.2 eV) have also been noted to occur between different basis

sets,[305,306] which for some dyes could mean the difference between predicting a non-adiabatic or adiabatic charge transfer mechanism and thus change the predicted injection rate.[309] The choice of functional is important to note as well, as the "best" functional for the dye molecule might give inaccurate calculated results for the electronic structure of the semiconductor to which it is bound.[219] Even in the case of the more robust GW method,[287] which has been shown to be consistently accurate in the determination of the HOMO-LUMO energies of various dye systems,[285,286] there is still some discrepancy between the GW-derived band gap energy of anatase (101) (3.6 eV) and its experimentally-measured band gap (3.25 eV).[310]

From the discussion of dye-surface interactions, it is clear that the effect of the binding interaction on the electronic structure (in particular the MO energies of the dye) can lead to qualitative differences between solid-state and gas-phase calculations. Solvent effects are also important to consider, as these have been proven to affect the electronic structure of both metal-organic and organic dyes. While PCMs have been successfully implemented in some DFT software, this is not the case for many — in particular for some used in this work. As such, calculations of electronic structure in this work will utilise PCMs for dyes in non-periodic (gas phase) calculations, and not utilise them in periodic-cell (solid state) calculations.

5.2 Aims

In this chapter, the electronic structures of a series of cyclometallated metal-organic dyes based on Ru are investigated by ground-state DFT calculations. These dyes have been recently synthesised at the University of Northumbria,[311] with the aim to produce dyes with improved light absorption

and chemical stability compared to N3/N719. Their performance in DSSCs with a TiO_2 semiconductor has been evaluated and compared to N719, however it was found that, for the subsequent DSSCs, the new dyes produced very low photocurrents: around $4.5\,mA\,cm^{-2}$ and $12\,mA\,cm^{-2}$ for the cyclometallated dyes and N719 respectively. Furthermore, photovoltaic efficiencies were found to be reduced in the cyclometallated dyes (0.36–1.12% for each dye) compared to N719 (2.55%), and open-circuit voltages were similarly decreased ($222\,mV\,cm^{-2}$ to $350\,mV\,cm^{-2}$ for each cyclometallated dye and $450\,mV\,cm^{-2}$ for N719). In order to help explain the performances of these dyes, their MO energies have been analysed in the gas phase and when adsorbed on the anatase (101) surface . The effect of different π-conjugated substituents on the electronic structures of the cyclometallated dyes, as well as different surface-binding arrangements, have been investigated.

5.3 Methodology

5.3.1 Calculation Details

All dye molecules in the gas phase were optimised prior to calculations of the dyes adsorbed on anatase (101) using the Gaussian09 program.[312] These calculations were performed with the B3LYP[59] functional, and used 6-31G* basis sets for all elements except for Ru, which used the LANL2dz[313–315] pseudopotential basis set. The geometries of all dye molecules adsorbed on anatase (101) were done with the CRYSTAL14 program.[153] These calculations were performed using the B3LYP functional. The following basis sets were used for each element, as obtained from the CRYSTAL website: Ru, 9763-11d631G; Ti, 86-51(d3)G; S, 86-3111G(d2); Na, 8-511G; O, 6-31d1; N, 6-31d1; C, 6-31d1; H, 3-1p1. S and Na are only included in the N719 dye system, where Na is

used as the counterion to the carboxylate groups of N719 in the calculation of the adsorbed dyes and not in the gas phase. For all geometry optimisations a Monkhorst-Pack k-point sampling mesh of $2 \times 2 \times 1$ was used. For all DoS calculations a denser mesh of $12 \times 12 \times 1$ was used instead. In order to present absolute orbital energies, each density of states (DoS) spectrum shown is corrected for the energy of the electron in vacuum, which is done simply by offsetting the energies of the plots. The magnitude of the energy shift is determined using the electrostatic energy calculated at a point in the simulation box sufficiently far away in the cell's C-axis (>50 Å) from the atoms in the simulation cell.

5.3.2 Dye Structures

The following dyes are investigated in this work: PNM19, PNM46, PNM47, DPP-1, and DPP-2. Structures for these dyes are shown in Figure 5.11.

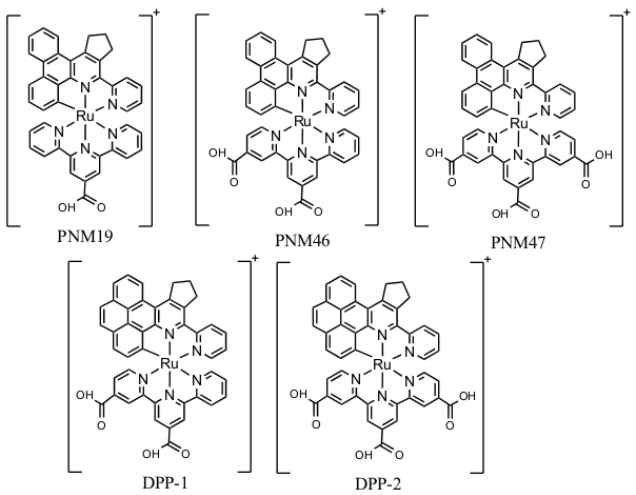

Figure 5.11: Chemical structures of the cyclometallated dyes studied in this work.

5.4 Results and Discussion

5.4.1 Adsorption Structures

The adsorption structures of each dye were investigated to assess the relative stabilities of adsorption modes which use either protonated or deprotonated anchoring groups. As the adsorption structures of DPP-1 and DPP-2 were found to be very similar to that of PNM46, only the adsorption modes of the PNM-series dyes will be shown in this section. Dye PNM19 (Figure 5.12), with a single carboxylic acid group, has a single anchoring point with the anatase (101) surface. As the dyes are postively-charged and contain an odd number of electrons in their neutral state, a carboxylic acid group on each dye was deprotonated prior to the construction and geometry optimisation of the adsorption structures to avoid the need for a charged unit cell — and therefore any interactions between charged periodic images. This was also done to keep the calculation system spin-paired and therefore to reduce calculation costs. As the dye structure is deprotonated prior to adsorbing, the pair of titanium atoms were chosen specifically as the intended adsorption sites to produce a bridging bidentate configuration, such as those modelled previously for smaller carboxylic molecules on anatase. The final geometry of the adsorbed dye molecule is slightly canted towards the anatase (101) surface, which we note to occur also with the other singly-adsorbed dye molecules in this study, as well as with smaller aromatic adsorbates studied in the literature.[300] The O−C bond lengths in the adsorbed carboxylic acid anchoring group are equal for both oxygen atoms, at 1.27 Å, both also form O−Ti bonds of similar lengths: 2.16 Å and 2.08 Å — mirroring similar results seen in other studies of dyes with single carboxylic acid anchoring points.[174,303]

It is known from past research,[299,300] that the carboxylic acid anchoring

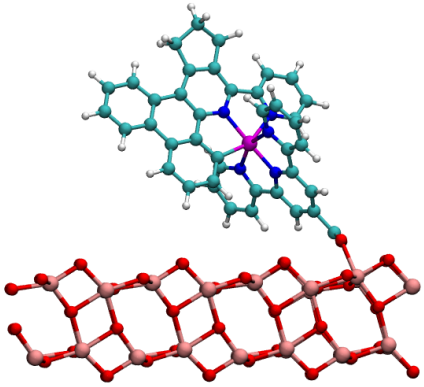

Figure 5.12: The adsorption structure of dye PNM19 on the anatase (101) surface. Colour scheme; red: oxygen, cyan: carbon, blue: nitrogen, white: hydrogen, salmon pink: titanium, magenta: ruthenium.

group can form surface bonding interactions with TiO_2 in both its protonated and deprotonated forms. For dye PNM46 this means that two different adsorption structures need to be investigated: one with only one of the two acid groups (Figure 5.13a), and another where both groups are deprotonated (Figure 5.13b). In both cases, it is found that PNM46 preferentially forms two anchoring points with anatase (101). Both structures form at least one bridging bidentate interaction with anatase (101), where a pair of carboxylate oxygen atom bonds with a pair of Ti atoms. In the case of the doubly-deprotonated system (which has two bridging bidentate anchoring points surface) we see similar bond lengths in the PNM46 anchoring groups as in the PNM19 anchoring group; the O−C bond lengths are around 1.27 Å. There is a more obvious asymmetry in surface-adsorbate bond lengths in PNM46 compared to PNM19; each PNM46 anchoring group has O−Ti bond lengths of around 2.06 Å and 2.26 Å each. The slight differences between PNM19 and PNM46 adsorption bonding lengths are likely to be due to steric hindrances caused by the fact that both anchoring groups in PNM46 interact with surface Ti atoms, but the ridgid terpyridyl backbone of the ligand is unable to completely accommodate the deformation due to its very limited torsional freedom — as shown

by the dihedral angle between the two pyridine moieties of 11.10°. This asymmetric bonding arrangement for doubly-deprotonated two-anchor dyes is also observed in other studies of similar dyes such as N3/N719,[303,304] where their two di-carboxybipyridine ligands can form a variety of different two-anchor adsorption structures. This indicates that the two carboxylate oxygen atoms in PNM46 are covalently bonded to their surface Ti atoms at different strengths.

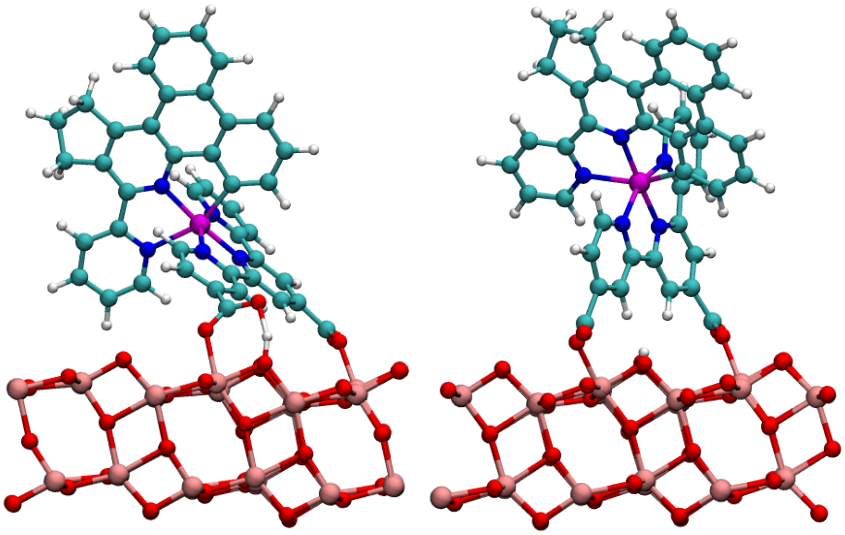

(a) (b)

Figure 5.13: Images of the PNM46 dye adsorbed on anatase (101): singly-anchored (a) and doubly-anchored (b). Colour scheme; red: oxygen, cyan: carbon, blue: nitrogen, white: hydrogen, salmon pink: titanium, magenta: ruthenium.

For the singly-anchored PNM46 adsorption structure (Figure 5.13a), the geometry optimisation was started from an upright position where the protonated carboxylic acid group was not positioned close to the anatase (101) surface. During the geometry optimisation of this PNM46 structure, the still-protonated carboxylic acid group moved to form a second bonding interaction with anatase (101) through both the carbonyl oxygen and hydroxyl oxygen in the group. The carbonyl oxygen atom forms an O−Ti bond, with a bond length of 2.08 Å, while the other oxygen remains very weakly bonded to its

hydrogen atom (at a O$\cdots$H bond length of 1.47 Å) while the hydrogen itself is more strongly bonded to a surface two-coordinated oxygen atom of anatase (101) (at a O−H bond length of 1.02 Å). The C−O bond lengths in this carboxylic acid group vary slightly more than in the carboxylate anchoring groups. For the C−O−Ti interaction , the C−O bond length is 1.29 Å, compared to 1.26 Å for the C−O bond of the C−O$\cdots$H interaction. The longer C−O bond in the carboxylic acid group is equal to that of the C−O bond measured in the benzoic acid molecule,[316] but shorter than the C−O single bond of the dye's acid group optimised in the gas phase (1.35 Å). The shorter C−O bond of the adsorbate is longer than the C=O bond length of 1.21 Å of the dye's acid group optimised in the gas phase. The length of the shorter C−O bond confirms that, although the hydrogen atom is now bound to the surface of anatase (101), there is still a weak hydrogen bonding interaction between the carboxylic acid oxygen and hydrogen atoms. This differs from the results of some other studies (for small carboxylic acids and the N719 dye), which report generally similar adsorption structures for this anchoring group, but often show the hydrogen atom being more closely bonded to the carboxyl oxygen rather than the surface oxygen.[299,300,304] Similar to the case of doubly-deprotonated PNM46 there is a very small dihedral angle between the two pyridine moieties of the terpyridine ligand, however in the case of singly-deprotonated PNM46 this is reduced to <1°.

For PNM47, with three carboxylic acid anchoring groups, two adsorption configurations were modelled. Similarly to PNM46, PNM47 can form two types of surface bonding interactions with anatase (101). For the singly-deprotonated variant (Figure 5.14a), the carboxylate group forms the same O−Ti bonds as the previous dyes, with lengths of 2.07 Å and 2.14 Å. The hydrogen atom is now bonded to the acid group, with a length of 1.03 Å, and

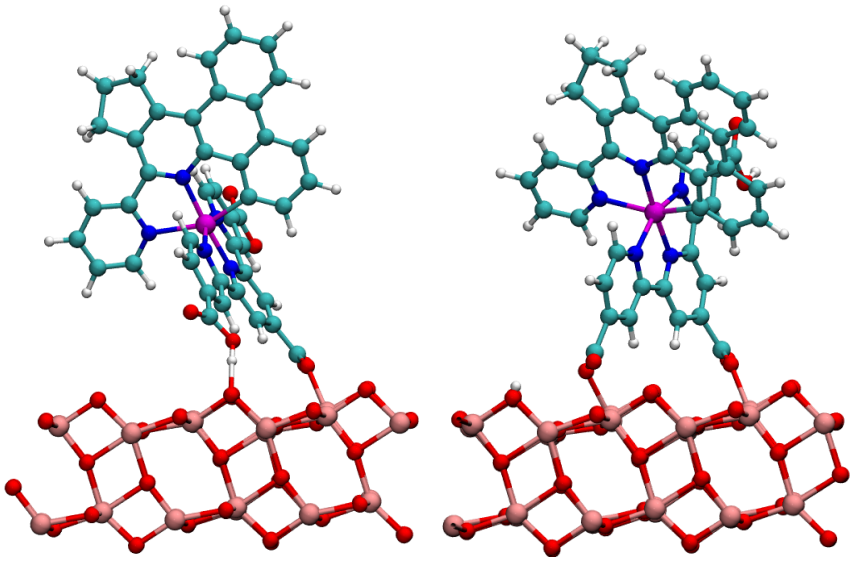

(a) (b)

Figure 5.14: Images of the PNM47 dye adsorbed on anatase (101): singly-deprotonated (a) and doubly-deprotonated (b). Colour scheme; red: oxygen, cyan: carbon, blue: nitrogen, white: hydrogen, salmon pink: titanium, magenta: ruthenium.

forms a strong hydrogen bond with the surface oxygen atom, with a length of 1.50 Å. The protonated acid group again forms a 2-centre hydrogen bond between the acid group and a surface oxygen atom, however in this instance there is no additional O−Ti bond. The C−O bond lengths in this adsorbed protonated acid group are different from each other and from those observed in PNM46, as a result of the particular adsorption configuration. The non surface-bound oxygen atom has a short C−O bond length of 1.22 Å, close to the standard carboxylic acid C=O bond length of 1.23 Å,[317] while the oxygen atom bonded to H has a longer C−O bond length of 1.32 Å, close to the C−O bond length of 1.36 Å.[317] This shows that the group has mostly retained its carboxylic acid structure, which thus indicates that there is a weaker surface interaction between this group and anatase (101) compared to singly-deprotonated PNM46. Based on our finding that the protonated acid group can form an alternative binding configuration with anatase (101) involving

both a O−H· ·O hydrogen-bonded linkage and a Ti−O bond (Figure 5.13a), this particular bonding arrangement is likely to be meta-stable. A very small dihedral angle between the two pyridine moieties of 6.66° is also present. The bonding of all their anchoring groups to anatase (101) was not found to be possible due to the inflexibility of the tripyridyl ligand. One past theoretical study of the N3/N719 dye system provides an example of a triply-anchored dye, however this structure was possible because of the presence of two separate di-carboxybipyridyl ligands affords sufficient overall flexibility to the anchoring groups[318] — as opposed to the terpyridine used in our dye systems.

The differences in total energy were calculated to determine the relative stabilities of the two binding arrangements for each dye. For all dyes except PNM47, it was found that the singly-deprotonated adsorption mode was around 0.70 eV more stable than the doubly-deprotonated one. For PNM47 instead the doubly-deprotonated adsorption mode was 0.06 eV more stable than the singly-deprotonated one. For PNM47, this indicates clearly that the adsorption structure found for the singly-deprotonated dye is metastable. Based on the total energy differences, it is likely that the singly-deprotonated adsorption mode obtained for PNM46 is the one which each of these dyes will most likely form under experimental conditions.

The adsorption structures analysed in this section are qualitatively very similar to those of other Ru-based dyes such as N3/N719,[303,304] thus allowing for comparisons to be made between both. There is, on the other hand, a clear difference between the structures of N3/N719 and the dyes presented in this work: the greater flexibility of the bis-dicarboxy bipyridine ligand system of N3/N719 allows for a wider range of adsorption structures. The limited dihedral angle range of the terpyridine ligand in the PNM dye systems thus leads to only a few different adsorption structures to analyse.

5.5 Electronic Structure Analysis

In this section, the electronic structures of the dyes in this work are analysed both in the gas-phase and in their surface-adsorbed configurations. The gas-phase calculations were performed in order to determine the energy spacing between their frontier MOs, and to assess the effect of changing the phenanthrene group on the N′C′ ligand (in the PNM series) for a pyrene group (in the DPP series). Within this analysis, the effect of the acetonitrile solvent was also investigated in a separate geometry optimisation which included a PCM for acetonitrile. The electronic structures of the surface-adsorbed dyes are then analysed in order to evaluate the dyes' likely effectiveness in a DSSC device.

5.5.1 Gas-Phase Calculations

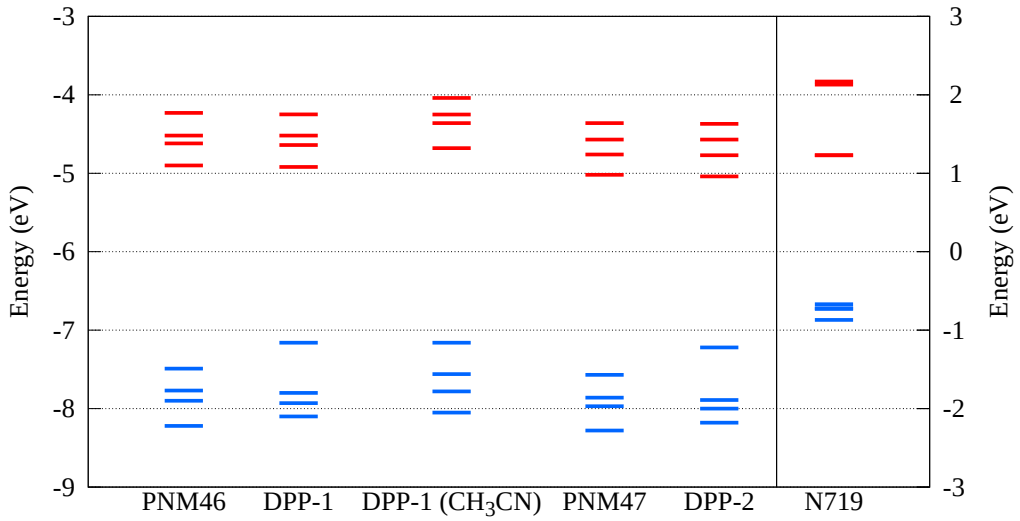

Figure 5.15: MO energies of the PNM46, PNM47, DPP-1, and DPP-2 dye molecules. The 4 highest-energy occupied MOs are shown in blue, and the 4 lowest-energy unoccupied MOs are shown in red. The data for N1719 uses the secondary (right-hand) energy axis, while all other data use the primary (left-hand) energy axis. The HOMO energy of DPP-1 with CH_3CN present has been set equal to that of DPP-1 in the gas phase in this figure.

The gas-phase optimised structures of the PNM46, PNM47, DPP-1, and

DPP-2 dye molecules were analysed to obtain their MO energies (Figure 5.15), with the N719 dye considered for comparison. The MO energies of all of the PNM and DPP dyes are quite similar to each other, differences in energy level positions between dyes within each family are around <0.2 eV for gas-phase calculations. Differences between the two cyclometalating groups (e.g. comparing PNM46 to DPP-1) shows that changing the phenanthrene group to a pyrene group has had a small effect on the HOMO energy, increasing it by 0.32 eV and 0.34 eV for PNM46/DPP-1 and PNM47/DPP-2 respectively, and does not affect the energies of the unoccupied MOs. Consequently the HOMO-LUMO gap energy decreases in each dye by 0.34 eV and 0.36 eV for PNM46/DPP-1 and PNM47/DPP-2 respectively. To investigate the effect of solvent on this dye system, DPP-1 was also optimised separately, at the same level of theory as the other dyes, in an implicit solvation model (acetonitrile, using the C-PCM model[224]). Solvent effects have been shown to have a significant effect on the HOMO-LUMO gap energy in other Ru-based dye systems.[223,225] For DPP-1 in CH_3CN, the MO energies (Figure 5.15) were found to be all shifted up in energy by around 2 eV relative to DPP-1 in the gas phase, which is noted to be a consequence of both the formal positive charge applied to the gas-phase dyes and the dielectric field of the C-PCM used. The HOMO-LUMO energy gap increases by around 0.23 eV in the solution phase dye relative to the gas-phase dye. This is consistent with the effect of polar solvent interacting with a carboxy-ter/bipyridine ligand system,[219,223] as this increases the energy of the pyridine-centered LUMO and thus leads to a blue-shift of the band gap energy. By comparison to the other dyes, the HOMO and LUMO energies of N719 are relatively close to each other in energy. The HOMO-LUMO energy of N719 calculated here (1.90 eV) is consistent with its characteristically low optical gap energy seen in experiments (around 1.38 eV,

according to its absorption onset).[216] The difference in absolute energies is, again, to be expected, as the N719 dye is assigned a formal -2 charge.

5.5.2 Adsorbed Dyes

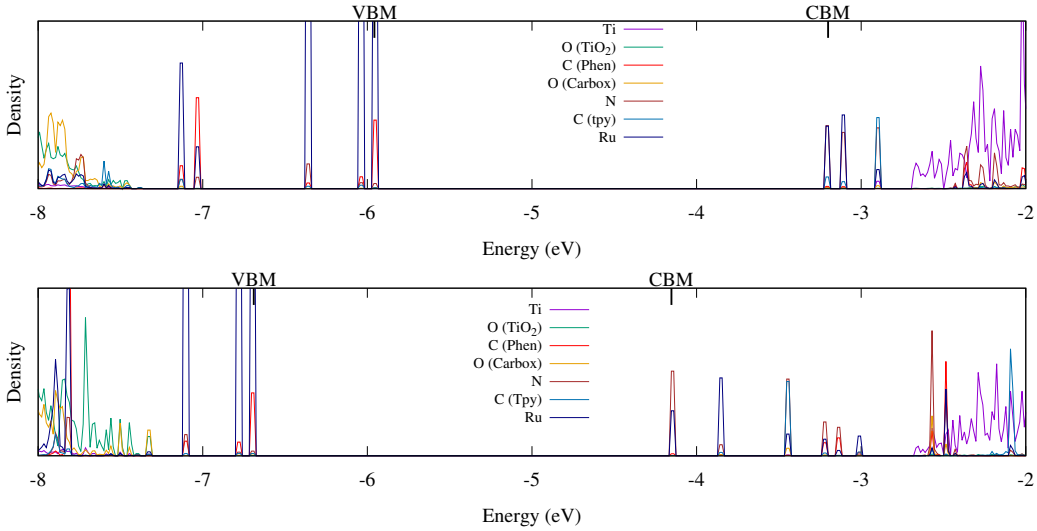

Figure 5.16: DoS plots of dye PNM46 adsorbed on anatase (101): singly-deprotonated (top) and doubly-deprotonated (bottom) adsorption structures

To compare the positions of the dyes' energy levels to the TiO_2, and therefore to assess each dye's likelihood of being able to photo-sensitise anatase (101), the electronic structures of the dyes adsorbed on anatase (101) were investigated by plotting their densities of states (DoS). In each plot the dye MOs and anatase (101) bands can be clearly distinguished; the former appear as single, sharp peaks while the latter appear as a more broad spectrum with multiple, less distinct peaks. In almost all dye systems there are clear differences in the MO energies between the singly- and doubly-deprotonated adsorption structures, with an energy shift of $-0.9\,\text{eV}$ between the equivalent dye MOs in different adsorption configurations apart from PNM47 where this difference is much smaller. The energies of the MOs relative to each other are very similar between the two adsorption modes of each dye, which indicates

that the cause of the overall shift in MO energies is related to the adsorption configurations overall rather than specific to certain MOs. The differences in total energy between the binding modes (discussed at the end of subsection 5.4.1) do not intuitively explain the observed difference in MO energies; it could be expected that, if the total energy of the system is lowered due to the change in adsorption mode, the MO energies of the dye would be lowered accordingly. Likely the decrease in MO energies indicates that the doubly-deprotonated adsorption mode increases electronic coupling between the dye and anatase (101). At the same time, the increase in total energy indicates that the energy cost of structural deformation needed for surface binding interaction makes the doubly-deprotonated adsorption mode less stable overall.

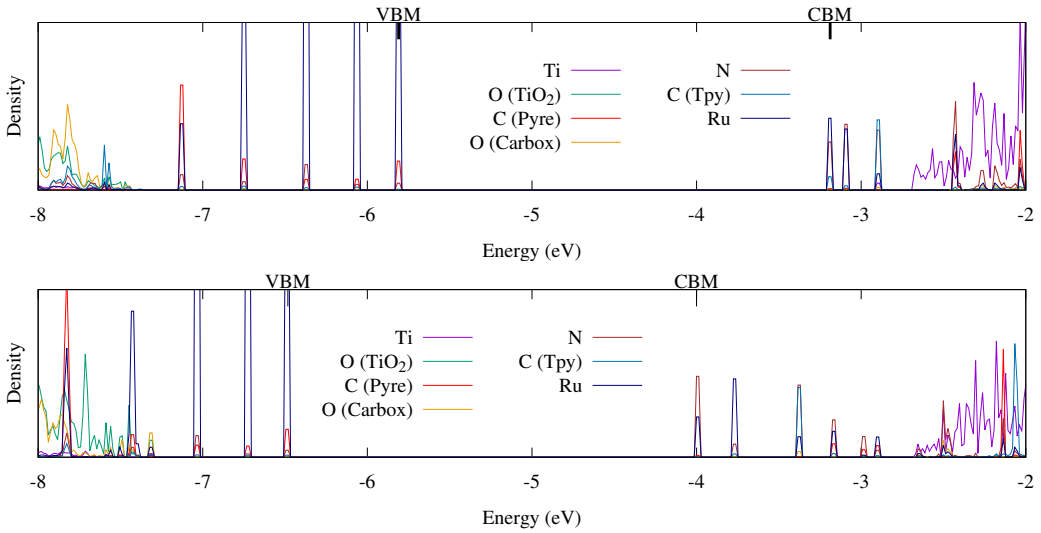

Figure 5.17: DoS plots of dye DPP-1 adsorbed on anatase (101), singly-deprotonated (top) and doubly-deprotonated (bottom)

The energy of the HOMO itself, in the DPP series dyes in both the gas phase (Figure 5.15) and the adsorbed structures (Figure 5.16–Figure 5.19), is slightly higher in energy than the equivalent HOMO in the PNM series, which directly results from changing the phenanthrene group to a pyrene group on the N′N′C′ ligand. The highest occupied MOs in each of the dyes do show some ground-

state charge-transfer character in their compositions, as each contains AO contributions from the phenanthrene/pyrene group of the N′N′C′ ligand. This is also the case for the unoccupied MOs, as there are clear AO contributions from the atoms of the terpyridine group in addition to those of ruthenium.

In each dye system displayed the first three (or more) unoccupied MOs are lower in energy than the CBM of anatase (101). This is in stark contrast to N719, where all unoccupied MOs of the dye are higher in energy than the CBM of anatase (101) (Figure 5.20). This energy alignment in the adsorbed N719 system is ideal, as it allows for spontaneous transfer of excited electrons to the semiconductor. This explains both why the photovoltaic efficiency of the N719 DSSC system (2.55%) and photocurrent (10.7 mA cm^{-2}) are greater than each of the cyclometallated dye systems in experiment (efficiencies of 0.36–1.12% and photocurrents of 1.8 mA cm^{-2} to 6.4 mA cm^{-2}).[311] For the cyclometallated dyes, the energy difference between the HOMO and the first unoccupied MO higher in energy than the CBM of anatase (101) is effectively outside of the visible range, while in the N719 system it is not. It is possible that the MOs lower in energy than the anatase (101) CBM will be able to photosensitise anatase (101) to a minor degree of effectiveness, as there may be vibronic states which are sufficienctly higher in energy for electron transfer to be thermodynamically favoured.[309] However, given the energy difference between these unoccupied MOs and the anatase (101) CBM, this is likely to result in very low DSSC performance.

The energy difference between the dyes' HOMOs and their first unoccupied MO lie higher in energy than the anatase (101) CBM, explains the poor photocurrent measurements (mentioned earlier) for these dyes.[311] Measured open-circuit voltages for N719 (450 mV) are also greater than most of the other dyes (222 mV to 350 mV). The open-circuit voltage measures the energy

difference between the semiconductor's Fermi level and the potential of the redox mediator. As this value will differ based on the electron population of the semiconductor's CB, it gives a measure of the electron population of the TiO_2 exicted state. From this we can see that N719 is more effective than the other dyes for photosensitising the exicted state of TiO_2. Furthermore, there are differences between the open-circuit voltage of the DPP dyes (around 222 mV) and PNM dyes (305 mV to 350 mV), which is a trend that is also reflected in the other performance measurements for these dyes. This indicates that, although there are slight improvements to the potential light-harvesting characteristics seen when the phenanthrene group is changed for pyrene, this also leads to a slight decrease in overall performance. However, the cause of this difference is not immediately clear from the computational data in this work. Finally, it should be noted that the calculated band gap energies are significantly higher than the known experimental band gap of anatase (101) of 3.3 eV.[174] This is a known issue with the use of the B3LYP functional, with its relatively high fraction of Hartree-Fock exchange.[59] However, PBE0,[60] with a lower fraction of Hartree-Fock exchange, is known to be less accurate in the calculation of the band gap energy of anatase (101).[174] While the range-separated HSE06 functional is known to be relatively accurate at calculating the band gap energy of anatase TiO_2,[73] it is (to the author's knowledge) not known to be accurate at the calculation of electronic structures for clusters such as the dye molecules used in this work. Further work to establish the effectiveness of HSE06 in this context is therefore recommended.

5.5.3 Conclusions

In this chapter, the adsorption modes and electronic structures of a series of recently experimentally prepared cyclometallated Ru(II) dyes adsorbed

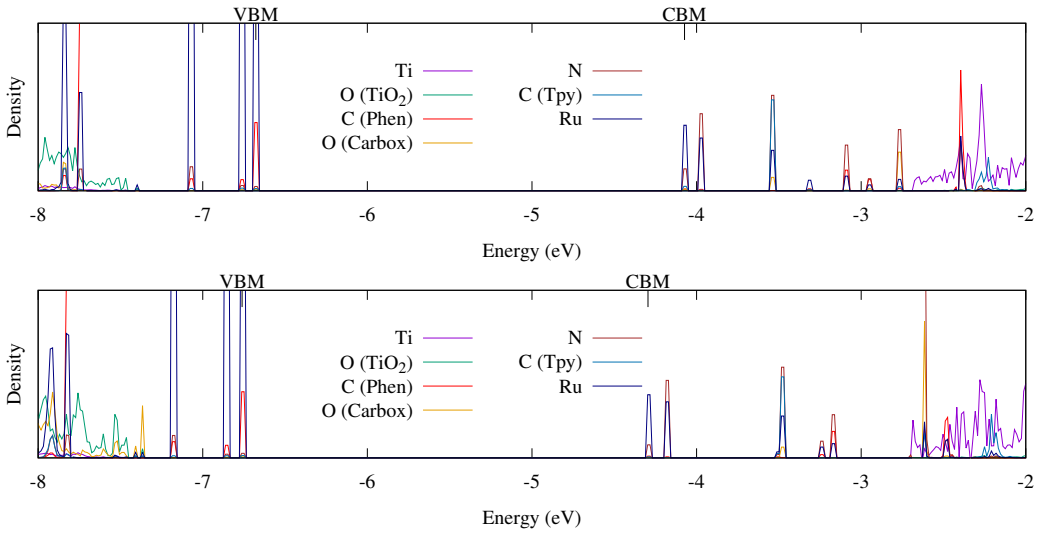

Figure 5.18: DoS plots of dye PNM47 adsorbed on anatase (101), singly deprotonated (top) and doubly-deprotonated (bottom)

on the anatase (101) surface were investigated using DFT simulations. The dye systems can adsorb to anatase (101) in one of two modes, depending upon whether one or two of its carboxylic acid anchoring groups are deprotonated. It is found that the singly-deprotonated adsorption mode, where the protonated carboxylic acid group forms both an O−Ti and an O···H−O surface bonding interaction, is the more energetically stable of the two by around 0.7 eV. From the DoS spectra of each dye system, it can be seen clearly that the cyclometallating N′N′C′ ligand is electronically coupled quite well with the ruthenium center, as HOMOs with clear ground-state charge-transfer character can be seen.

In order to interpret experimentally observed low efficiencies of these dyes in DSSC systems, DoS spectra were produced for each cyclometallated dye in each of its adsorption modes. For each system, it can be concluded that none of the adsorbed dye/TiO_2 systems will function as effective DSSC systems under visible or simulated solar light, as the position of the dyes' LUMO levels are lower in energy than that of the anatase (101) CBM, and therefore photoex-

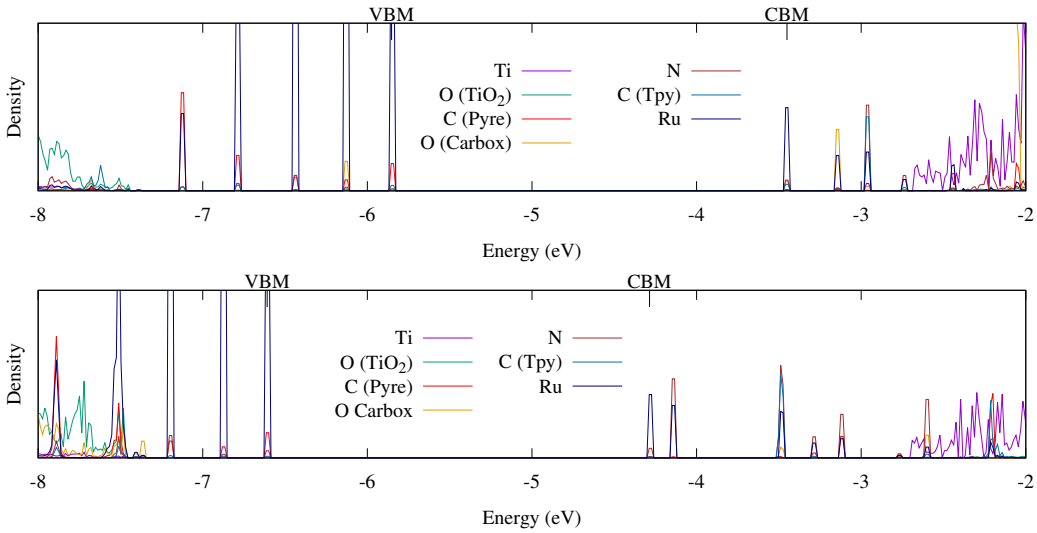

Figure 5.19: DoS plots of dye DPP-2 adsorbed on anatase (101), singly-deprotonated (top) and doubly-deprotonated (bottom)

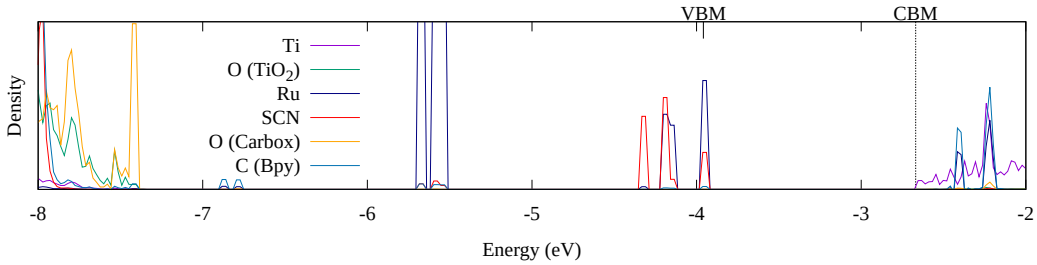

Figure 5.20: DoS spectrum of dye N719 doubly-adsorbed on anatase (101).

cited electrons in the LUMO cannot be injected into the TiO_2 CB. While some of the higher-energy unoccupied orbitals are higher in energy than the CBM of anatase (101), the calculated energy gap between them and the HOMO is, in all cases, too high in energy to absorb within the visible region of the electromagnetic spectrum. Experimental studies of the cyclometallated dye systems featured in this work[311] reported much lower efficiencies and much lower photogenerated current produced for these dye systems compared to N3/N719. From our results this can be attributed to poor electron injection from the dyes to TiO_2. The DoS results in this work also suggest that the energy alignment of the cyclometallated dyes depends strongly upon the adsorption mode.

This observed difference is likely a result of the deprotonation of both carboxylic acid groups, and a subsequent increase in interaction strength with the anatase (101) surface.

Chapter 6

Conclusions & Future Work

The work presented in this thesis was aimed at elucidating the mechanisms of photoexcitation of graphene, graphene oxide (GO), and reduced graphene oxide (RGO) interfaced with TiO_2. This analysis was also extended to explain the photosensitising properties of a series of cyclometallated Ru-based dyes for dye-sensitised solar cell (DSSC) applications. In each system the properties of the graphene material or dye molecule change when adsorbed on the surface of TiO_2, and can be very different compared to these compounds in isolation from each other. In the case of the RGO/TiO_2 composite material this change is significant, as the band gap energy changes from semimetallic (as would be the case for graphene/TiO_2) to an indirect-gap semiconductor through the chemical interaction formed between the two materials. In addition, the alignment of electronic energy levels in these systems has been shown to be crucially important for their light-harvesting properties. For graphene/TiO_2 we have demonstrated that the photosensitisation of TiO_2 is likely to proceed *via* excited state charge transfer from graphene to TiO_2, and it is within the energy range for visible-light excitations to achieve this. For the DSSC systems, however, their unfavourable energy alignment, where dye LUMOs lie below the

TiO_2 CB, explains the poor performance shown by these dyes experimental conditions.

Analysis of the graphene, graphene oxide (GO), and reduced graphene oxide (RGO) composites with TiO_2 presents us with a unified model of the interactions and electronic properties of these interfaces. For the graphene/TiO_2 system, it was demonstrated that there is ground-state charge-transfer from graphene to TiO_2 across the interface. This charge transfer shows that there is strong electronic coupling between the graphene and TiO_2 materials, which can allow the excited state electrons of graphene to transfer to the conduction band of TiO_2. Further development of the computational model to include oxygen functional groups lead to the a more complete explanation of how graphene/RGO improves the light-harvesting properties of TiO_2, as it demonstrated that the formation of Ti−O−C and Ti−O−H$\cdots$O−C bonds leads to the formation of an efficient charge-trapping electronic band. However, it must be remembered that the "real" RGO structure is amorphous and will likely have regions of both high and low concentrations of oxygen functional groups. In low concentration areas the electronic structure of RGO will closely resemble that of graphene, and therefore the excited-state electron transfer from graphene to TiO_2 observed in earlier reports[65,66,124] is likely to play a part in the overall photosensitisation mechanism of this material. The only way in which to ultimately verify that excited-state charge transfer from graphene to TiO_2 is significant in this system would be to calculate this photoexcitation directly with the robust hybrid HF/DFT methodology used in this work. While state-of-the-art computational methods such as the auxiliary density matrix method (ADMM) were able to make the ground-state calculations of this system possible on a reasonable timescale, similar techniques must be developed to do the same for excited-state calculations. Recent progress on the devel-

opment of time-dependent DFT (TDDFT) methods in the CP2K code could help to make such calculations on systems of this size possible.

The investigation of point defects within the graphene/ and RGO/TiO_2 composite systems is also important for further analysis of their electronic and photocatalytic properties. Carbon atom vacancies in graphene, have been shown in the past to result in local density of states (LDoS) with very different properties to those of pristine graphene.[319,320] Furthermore, past computational studies of oxygen atom vacancies in TiO_2 have shown that such defects will introduce electron "traps" into the system, which spatially localise the electron in the material.[321] Both of these defects are likely to exist in experimental systems, and as such the interaction of either (or both) of these with both pristine graphene and RGO, and their respective composites, will add more detail to the overall mechanism of how these carbon nanostructures interact with TiO_2.

A more general, straightforward improvement of the electronic structure analysis presented in this work would be to re-analyse the photocatalytic and photovoltaic systems in this work with a higher level of theory than the HF/DFT method used already, in order to avoid shortcomings caused by the modelling of electron correlation in the DFT and HF/DFT methods used. While electron correlation methods (such as coupled-cluster) are far too computationally demanding to employ for such large calculation tasks, methods such as the GW[287] approximation have been shown to provide quantitative improvements to the accuracy of calculated electronic structures at a moderate increase in computational cost.[73,285,286] However, the increased computational cost associated with these methods will likely mean that such analysis must wait for future improvements to computational software and hardware.

Investigating variations of the interface structures explored in this work will

help to clarify the overall mechanism of the light-harvesting properties shown by the RGO/TiO_2. In this work we have modelled the electronic structures of graphene, RGO, and GO interfaced with rutile (110), due to the ease of matching the lattice of the rutile (110) surface unit cell to that of graphene. Rutile is the most stable polymorph of TiO_2 and the (110) surface is the most energetically stable facet of rutile, however, anatase TiO_2 and P25 (containing 75% anatase to 25% rutile) are mostly used in experiments due to their better intrinsic photocatalytic properties compared to rutile.[5] Extending the analysis used in this work to interface structures featuring anatase TiO_2 instead of rutile would therefore cover a more representative range of structures. This would show whether the mechanisms for enhanced photocatalytic properties proposed in this work can be extended to all forms of TiO_2, especially considering that the band energies of TiO_2 differ between different polymorphs and surface structures. Both the inhibition of charge-recombination and enhanced visible light photocatalytic enhancement observed in the RGO/rutile (110) system originate from the formation of Ti−O−C and Ti−O−H$\cdots$O−C bonding and we expect that similar behaviour will be observed with different forms of TiO_2.

Analysis in this work of the structures of GO and RGO has brought together a variety of information from both experimental and computational works to produce what we consider to be representative models of these two amorphous materials. This "homemade" model of the GO/RGO structure meets experimental properties, such as known measurements of oxygen content and type of oxygen groups present,[198] and its construction was guided by past computational studies of the possible arrangements of oxygen functional groups,[206] but the structure itself had to be constructed by hand. This presents an issue for any researcher investigating the properties of GO/RGO as, without a well-defined crystal system, comparing the structure of GO/RGO in one

study to another in a different study becomes difficult. A possible solution to this would be to develop a more consistent means of generating structures of GO/RGO automatically rather than by hand. This can be done by the use of a Monte-Carlo algorithm. Here, firstly, information on the strengths of interactions between functional groups of GO/RGO can be compiled to give a set of rules for functional group arrangements. Then, functional groups are added sequentially to the system in randomised configurations. After numerous positions of each functional group are sampled, a lowest-energy structure is reached. An algorithmic method such as this will help create representative structures of GO/RGO, while still yielding an amorphous structure for the system, and thus reduces ambiguity in the choice of structure to represent these materials.

Bibliography

[1] United States Energy Information Administration, *International Energy Outlook 2013*, United states department of energy technical report, 2014.

[2] M. Grätzel, *J. Photochem. Photobiol. C*, 2003, **4**, 145–153.

[3] H. A. Atwater and A. Polman, *Nature Mater.*, 2010, **9**, 205–13.

[4] A. Fujishima and K. Honda, *Nature*, 1972, **238**, 37–38.

[5] M. Kapilashrami, Y. Zhang, Y.-S. Liu, A. Hagfeldt and J. Guo, *Chem. Rev.*, 2014, **114**, 9662–9707.

[6] M. Dahl, Y. Liu and Y. Yin, *Chem. Rev.*, 2014, **114**, 9853–9889.

[7] J. Highfield, *Molecules*, 2015, **20**, 6739–6793.

[8] K.-Q. Peng, X. Wang, L. Li, Y. Hu and S.-T. Lee, *Nano Today*, 2013, **8**, 75–97.

[9] Y. Bai, I. Mora-Seró, F. De Angelis, J. Bisquert and P. Wang, *Chem. Rev.*, 2014, **114**, 10095–10130.

[10] S. Shi, Y. Li, X. Li and H. Wang, *Mater. Horiz.*, 2015, **2**, 378–405.

[11] M. Grätzel, *Nature*, 2001, **414**, 338–44.

[12] A. Kudo and Y. Miseki, *Chem. Soc. Rev.*, 2009, **38**, 253–278.

[13] C. D. Windle, E. Pastor, A. Reynal, A. C. Whitwood, Y. Vaynzof, J. R. Durrant, R. N. Perutz and E. Reisner, *Chemistry - A European Journal*, 2015, **21**, 3746–3754.

[14] X. Chen, S. Shen, L. Guo and S. S. Mao, *Chem. Rev.*, 2010, **110**, 6503–6570.

[15] L. M. Pastrana-Martínez, S. Morales-Torres, V. Likodimos, J. L. Figueiredo, J. L. Faria, P. Falaras and A. M. T. Silva, *Appl. Catal. B*, 2012, **123-124**, 241–256.

[16] P. Shao, J. Tian, W. Shi, S. Gao and F. Cui, *J. Mater. Chem. A*, 2015, **3**, 19913–19919.

[17] M. Minella, F. Sordello and C. Minero, *Catal. Today*, 2017, **281**, 29–37.

[18] B. R. Cruz-Ortiz, J. W. Hamilton, C. Pablos, L. Díaz-Jiménez, D. A. Cortés-Hernández, P. K. Sharma, M. Castro-Alférez, P. Fernández-Ibañez, P. S. Dunlop and J. A. Byrne, *Chem. Eng. J*, 2017, **316**, 179–186.

[19] P. Guiglion, E. Berardo, C. Butchosa, M. C. C. Wobbe and M. A. Zwijnenburg, *J. Phys. Condens. Matter.*, 2016, **28**, 074001.

[20] M. Ni, M. K. Leung, D. Y. Leung and K. Sumathy, *Renew. Sustain. Energy Rev.*, 2007, **11**, 401–425.

[21] K. Maeda and K. Domen, *J. Phys. Chem. C*, 2007, **111**, 7851–7861.

[22] A. L. Linsebigler, G. Lu and J. T. Yates, *Chem. Rev.*, 1995, **95**, 735–758.

[23] P. V. Kamat, *J. Phys. Chem. Lett.*, 2011, **2**, 839–840.

[24] H. Kato and A. Kudo, *J. Phys. Chem. B*, 2002, **106**, 5029–5034.

[25] R. Niishiro, H. Kato and A. Kudo, *Phys. Chem. Chem. Phys.*, 2005, **7**, 2241.

[26] T. Ishii, H. Kato and A. Kudo, *J. Photochem. Photobiol. A*, 2004, **163**, 181–186.

[27] R. Konta, T. Ishii and H. Kato, *J. Phys. Chem. B*, 2004, **108**, 8992–8995.

[28] D. Hwang, H. Kim and J. Jang, *Catal. Today*, 2004, **93-5**, 845–850.

[29] S. Kim, S.-J. Hwang and W. Choi, *J. Phys. Chem. B*, 2005, **109**, 24260–7.

[30] R. Niishiro, R. Konta, H. Kato, W.-J. Chun, K. Asakura and A. Kudo, *J. Phys. Chem. C*, 2007, **111**, 17420–17426.

[31] H. Kato, Y. Sasaki, A. Iwase and A. Kudo, *Bull. Chem. Soc. Jap.*, 2007, **80**, 2457–2464.

[32] S. Buddee, S. Wongnawa and U. Sirimahachai, *Mater. Chem. Phys.*, 2011, **126**, 167–177.

[33] L. Mi, P. Xu, H. Shen, P.-N. Wang and W. Shen, *Appl. Phys. Lett.*, 2007, **90**, 171909.

[34] J. Liu, R. Han, Y. Zhao, H. Wang, W. Lu, T. Yu and Y. Zhang, *J. Phys. Chem. C*, 2011, **115**, 4507–4515.

[35] Q. Meng, T. Wang, E. Liu, X. Ma, Q. Ge and J. Gong, *Phys. Chem. Chem. Phys.*, 2013, **15**, 9549–61.

[36] C. Di Valentin, G. Pacchioni, A. Selloni, S. Livraghi and E. Giamello, *Chem. Mater.*, 2005, **109**, 11414–11419.

[37] H. Kamisaka, T. Adachi and K. Yamashita, *J. Chem. Phys.*, 2005, **123**, 084704.

[38] W. Ren, Z. Ai and F. Jia, *Appl. Catal. B*, 2007, **69**, 138–144.

[39] K. Yang, Y. Dai and B. Huang, *J. Phys. Chem. C*, 2009, **113**, 2624–2629.

[40] S. Sato and J. White, *Chem. Phys. Lett.*, 1980, **72**, 83–86.

[41] K. Yamaguti and S. Sato, *J. Chem. Soc. Faraday Trans.*, 1985, **81**, 1237.

[42] A. Iwase, H. Kato and A. Kudo, *Catal. Lett.*, 2006, **108**, 7–10.

[43] K. Domen, S. Naito and M. Soma, *J. Chem. Soc. Faraday Trans.*, 1980, 543–544.

[44] T. Kawai and T. Sakata, *Chem. Phys. Lett.*, 1980, **72**, 87–89.

[45] D. O. Scanlon, C. W. Dunnill, J. Buckeridge, S. A. Shevlin, A. J. Logsdail, S. M. Woodley, C. R. A. Catlow, M. J. Powell, R. G. Palgrave, I. P. Parkin, G. W. Watson, T. W. Keal, P. Sherwood, A. Walsh and A. A. Sokol, *Nat. Mater.*, 2013, **12**, 798–801.

[46] W. J. Hehre, R. F. Stewart and J. A. Pople, *J. Chem. Phys.*, 1969, **51**, 2657–2664.

[47] F. Jensen, *Introduction to Computational Chemistry*, John Wiley & Sons INC, The Atrium, Southern Gate, Chichester, West Sussex, PO19 8SQ, England, Odense, Denmark, Second Edi edn., 2007.

[48] S. Boys and F. Bernardi, *Mol. Phys.*, 1970, **19**, 553–566.

[49] J. G. C. M. van Duijneveldt, Frans B. van Duijneveldt-van de Rijdt and J. H. van Lenthe, *Chem. Rev.*, 1994, **94**, 1873–1885.

[50] P. Atkins and J. D. Paula, *Atkins' Physical Chemistry*, Oxford University Press, Great Clarendon Street, Oxford, UK, OX2 6DP, 9th edn., 2010.

[51] P. Pulay, *J. Comp. Chem.*, 1982, **3**, 556–560.

[52] P. Hohenberg and W. Kohn, *Physical Review*, 1964, **136**, B864–B871.

[53] W. Kohn and L. J. Sham, *Physical Review*, 1965, **140**, A1133–A1138.

[54] M. J. Gillan, D. Alfè and A. Michaelides, *J. Chem. Phys.*, 2016, **144**, 130901.

[55] A. D. Becke, *Physical Review A*, 1988, **38**, 3098–3100.

[56] C. Lee, W. Yang and R. G. Parr, *Phys. Rev. B*, 1988, **37**, 785–789.

[57] J. P. Perdew, K. Burke and M. Ernzerhof, *Phys. Rev. Lett.*, 1996, **77**, 3865–3868.

[58] J. Kohanoff, *Electronic Structure Calculations for Solids and Molecules*, Cambridge University Press, The Edinburgh Building, Cambridge CB2 8RU, UK, 1st edn., 2006.

[59] A. D. Becke, *J. Chem. Phys.*, 1993, **98**, 1372.

[60] M. Ernzerhof and G. E. Scuseria, *J. Chem. Phys.*, 1999, **110**, 5029.

[61] V. N. Staroverov, G. E. Scuseria, J. Tao and J. P. Perdew, *J. Chem. Phys.*, 2003, **119**, 12129–12137.

[62] J. Heyd, G. E. Scuseria and M. Ernzerhof, *J. Chem. Phys.*, 2003, **118**, 8207.

[63] V. I. Anisimov, J. Zaanen and O. K. Andersen, *Phys. Rev. B*, 1991, **44**, 943–954.

[64] B. Himmetoglu, A. Floris, S. de Gironcoli and M. Cococcioni, *Int. J. Quantum Chem.*, 2014, **114**, 14–49.

[65] A. Du, Y. H. Ng, N. J. Bell, Z. Zhu, R. Amal and S. C. Smith, *J. Phys. Chem. Lett.*, 2011, **2**, 894–899.

[66] R. Long, N. J. English and O. V. Prezhdo, *J. Am. Chem. Soc.*, 2012, **134**, 14238–14248.

[67] X. Li, H. Gao and G. Liu, *Comp. Theor. Chem.*, 2013, **1025**, 30–34.

[68] S. Grimme, *J. Comput. Chem.*, 2006, **27**, 1787–1799.

[69] A. R. West, *Solid State Chemistry and its Applications*, John Wiley & Sons, Ltd, The Atrium, Southern Gate, Chichester, West Sussex PO19 8SQ, UK, 2nd edn., 2014.

[70] H. J. Monkhorst and J. D. Pack, *Phys. Rev. B*, 1976, **13**, 5188–5192.

[71] P. N. O. Gillespie and N. Martsinovich, *J. Phys. Chem. C*, 2017, **121**, 4158–4171.

[72] N. Greenwood and A. Earnshaw, *Chemistry of the Elements*, Pergamon Press, Oxford, 1984, pp. 1117–1119.

[73] M. Landmann, E. Rauls and W. G. Schmidt, *J. Phys. Cond. Mat.*, 2012, **24**, 195503.

[74] J. Li and N. Wu, *Catal. Sci. Technol.*, 2015, **5**, 1360–1384.

[75] K. Maeda, *ACS Catal.*, 2013, **3**, 1486–1503.

[76] S. G. Kumar and L. G. Devi, *J. Phys. Chem. A*, 2011, **115**, 13211–13241.

[77] B. A. Pinaud, J. D. Benck, L. C. Seitz, A. J. Forman, Z. Chen, T. G. Deutsch, B. D. James, K. N. Baum, G. N. Baum, S. Ardo, H. Wang, E. Miller and T. F. Jaramillo, *Ener. & Env. Sci*, 2013, **6**, 1983.

[78] N. Serpone, E. Borgarello and M. Grtzel, *Chem. Comm.*, 1984, 342.

[79] N. Serpone, P. Maruthamuthu, P. Pichat, E. Pelizzetti and H. Hidaka, *J. Photochem. Photobiol. A: Chemistry*, 1995, **85**, 247–255.

[80] K. Vinodgopal and P. V. Kamat, *Envrionment. Sci. Tech.*, 1995, **29**, 841–845.

[81] C.-H. Wu, *Chemosphere*, 2004, **57**, 601–8.

[82] H. Wang, Z. Wu, Y. Liu and Z. Sheng, *J. Mol. Catal. A*, 2008, **287**, 176–181.

[83] P. A. Sant and P. V. Kamat, *Phys. Chem. Chem. Phys.*, 2002, **4**, 198–203.

[84] L. Wu, J. C. Yu and X. Fu, *J. Mol. Catal. A*, 2006, **244**, 25–32.

[85] J. S. Jang, W. Li, S. H. Oh and J. S. Lee, *Chem. Phys. Lett.*, 2006, **425**, 278–282.

[86] K. P. Acharya, N. N. Hewa-Kasakarage, T. R. Alabi, I. Nemitz, E. Khon, B. Ullrich, P. Anzenbacher and M. Zamkov, *J. Phys. Chem. C*, 2010, **114**, 12496–12504.

[87] Q. Kang, S. Liu, L. Yang, Q. Cai and C. A. Grimes, *ACS Appl. Mater. Inter.*, 2011, **3**, 746–749.

[88] S. B. Bubenhofer, C. M. Schumacher, F. M. Koehler, N. A. Luechinger, R. N. Grass and W. J. Stark, *J. Phys. Chem. C*, 2012, **116**, 16264–16270.

[89] Y. Wang, H. Gong, B. Fan and G. Hu, *J. Phys. Chem. C*, 2010, **114**, 3256–3259.

[90] W. Guo, Y. Shen, M. Wu and T. Ma, *Chem. Comm.*, 2012, **48**, 6133.

[91] T. Taguchi, X.-t. Zhang, I. Sutanto, K.-i. Tokuhiro, T. N. Rao, H. Watanabe, T. Nakamori, M. Uragami and A. Fujishima, *Chem. Commun.*, 2003, 2480–2481.

[92] S. Iijima, *Nature*, 1991, **354**, 56–58.

[93] M. Shiraishi and M. Ata, *Carbon*, 2001, **39**, 1913–1917.

[94] P. Vincent, A. Brioude, C. Journet, S. Rabaste, S. Purcell, J. Le Brusq and J. Plenet, *J. Non-Cryst. Solids*, 2002, **311**, 130–137.

[95] K. Hernadi, E. Ljubović, J. Seo and L. Forró, *Acta Materialia*, 2003, **51**, 1447–1452.

[96] A. Jitianu, T. Cacciaguerra, R. Benoit, S. Delpeux, F. Béguin and S. Bonnamy, *Carbon*, 2004, **42**, 1147–1151.

[97] Y. Yu, J. C. Yu, C.-Y. Chan, Y.-K. Che, J.-C. Zhao, L. Ding, W.-K. Ge and P.-K. Wong, *Appl. Catal. B*, 2005, **61**, 1–11.

[98] Y. Yao, G. Li, S. Ciston, R. M. Lueptow and K. A. Gray, *Environmental Science & Technology*, 2008, **42**, 4952–4957.

[99] B. Ahmmad, Y. Kusumoto, S. Somekawa and M. Ikeda, *Catalysis Communications*, 2008, **9**, 1410–1413.

[100] M. Cargnello, M. Grzelczak, B. Rodríguez-González, Z. Syrgiannis, K. Bakhmutsky, V. La Parola, L. M. Liz-Marzán, R. J. Gorte, M. Prato and P. Fornasiero, *J. Am. Chem. Soc.*, 2012, **134**, 11760–6.

[101] G. Khan, S. K. Choi, S. Kim, S. K. Lim, J. S. Jang and H. Park, *Appl. Catal. B*, 2013, **142-143**, 647–653.

[102] J. B. Veluru, K. K. Manippady, M. Rajendiren, K. Mya Mya, P. R. Rayavarapu, S. N. Appukuttan and R. Seeram, *Int. J. Hydro. Energy*, 2013, **38**, 4324–4333.

[103] K. Woan, G. Pyrgiotakis and W. Sigmund, *Adv. Mat.*, 2009, **21**, 2233–2239.

[104] W. Wang, P. Serp, P. Kalck and J. L. Faria, *J. Mol. Catal. A*, 2005, **235**, 194–199.

[105] K. T. Dembele, G. S. Selopal, C. Soldano, R. Nechache, J. C. Rimada, I. Concina, G. Sberveglieri, F. Rosei and A. Vomiero, *J. Phys. Chem. C*, 2013, **117**, 14510–14517.

[106] M.-Q. Yang, N. Zhang and Y.-J. Xu, *ACS Appl. Mat. & Interfaces*, 2013, **5**, 1156–1164.

[107] Y. T. Liang, B. K. Vijayan, O. Lyandres, K. A. Gray and M. C. Hersam, *J. Phys. Chem. Lett.*, 2012, **3**, 1760–1765.

[108] Y. Yu, J. C. Yu, J.-G. Yu, Y.-C. Kwok, Y.-K. Che, J.-C. Zhao, L. Ding, W.-K. Ge and P.-K. Wong, *Appl. Catal. A*, 2005, **289**, 186–196.

[109] S. Wang, Q. Gong, Y. Zhu and J. Liang, *Applied Surf. Sci.*, 2009, **255**, 8063–8066.

[110] W.-C. Oh, F.-J. Zhang and M.-L. Chen, *Journal of Industrial and Engineering Chemistry*, 2010, **16**, 321–326.

[111] F. Zhang, F. Xie, H. Xu, J. Liu and W. C. Oh, *Kinet. & Catal.*, 2013, **54**, 297–306.

[112] X. Zhang, J. Liu, S. Li, X. Tan, J. Zhang, M. Yu and M. Zhao, *J. Mater. Chem. A*, 2013, **1**, 11070.

[113] X. Lu and Z. Chen, *Chem. Rev.*, 2005, **105**, 3643–3696.

[114] K. S. Novoselov, *Science*, 2004, **306**, 666–669.

[115] B. J. Schultz, R. V. Dennis, J. P. Aldinger, C. Jaye, X. Wang, D. A. Fischer, A. N. Cartwright and S. Banerjee, *RSC Adv.*, 2014, **4**, 634–644.

[116] S. Morozov, K. Novoselov, M. Katsnelson, F. Schedin, D. Elias, J. Jaszczak and A. Geim, *Phys. Rev. Lett.*, 2008, **100**, 016602.

[117] K. Bolotin, K. Sikes, Z. Jiang, M. Klima, G. Fudenberg, J. Hone, P. Kim and H. Stormer, *Sol. State Comm.*, 2008, **146**, 351–355.

[118] J.-H. Huang, J.-H. Fang, C.-C. Liu and C.-W. Chu, *ACS nano*, 2011, **5**, 6262–71.

[119] S. M. Song, J. K. Park, O. J. Sul and B. J. Cho, *Nano lett.*, 2012, **12**, 3887–92.

[120] M. D. Stoller, S. Park, Y. Zhu, J. An and R. S. Ruoff, *Nano Lett.*, 2008, **8**, 3498–502.

[121] W. S. Hummers and R. E. Offeman, *J. Am. Chem. Soc.*, 1958, **80**, 1339–1339.

[122] J. R. Lomeda, C. D. Doyle, D. V. Kosynkin, W.-F. Hwang and J. M. Tour, *J. Am. Chem. Soc.*, 2008, **130**, 16201–16206.

[123] G. Williams, B. Seger and P. V. Kamat, *ACS Nano*, 2008, **2**, 1487–1491.

[124] K. K. Manga, Y. Zhou, Y. Yan and K. P. Loh, *Adv. Func. Mater.*, 2009, **19**, 3638–3643.

[125] C. Zhu, S. Guo, P. Wang, L. Xing, Y. Fang, Y. Zhai and S. Dong, *Chem. Comm.*, 2010, **46**, 7148.

[126] N. J. Bell, Y. H. Ng, A. Du, H. Coster, S. C. Smith and R. Amal, *J. Phys. Chem. C*, 2011, **115**, 6004–6009.

[127] L. M. Pastrana-Martínez, S. Morales-Torres, V. Likodimos, P. Falaras, J. L. Figueiredo, J. L. Faria and A. M. T. Silva, *Appl. Catal. B*, 2014, **158-159**, 329–340.

[128] A. Morais, C. Longo, J. R. Araujo, M. Barroso, J. R. Durrant, A. F. Nogueira, D. Wang, A. Manivannan, A. D. Bristow and N. Q. Wu, *Phys. Chem. Chem. Phys.*, 2016, **18**, 2608–2616.

[129] H. Zhang, X. Lv, Y. Li, Y. Wang and J. Li, *ACS Nano*, 2010, **4**, 380–386.

[130] W. Fan, Q. Lai, Q. Zhang and Y. Wang, *J. Phys. Chem. C*, 2011, **115**, 10694–10701.

[131] J. S. Lee, K. H. You and C. B. Park, *Adv. Mater.*, 2012, **24**, 1084–1088.

[132] Q. Xiang, J. Yu and M. Jaroniec, *J. Am. Chem. Soc.*, 2012, **134**, 6575–8.

[133] S. Umrao, S. Abraham, F. Theil, S. Pandey, V. Ciobota, P. K. Shukla, C. J. Rupp, S. Chakraborty, R. Ahuja, J. Popp, B. Dietzek and A. Srivastava, *RSC Adv.*, 2014, **4**, 59890–59901.

[134] S. D. Perera, R. G. Mariano, K. Vu, N. Nour, O. Seitz, Y. Chabal and K. J. Balkus, *ACS Catal.*, 2012, **2**, 949–956.

[135] V. Štengl, J. Henych, P. Vomáčka and M. Slušná, *Photochemistry and Photobiology*, 2013, **89**, 1038–1046.

[136] J. Sha, N. Zhao, E. Liu, C. Shi, C. He and J. Li, *Carbon*, 2014, **68**, 352–359.

[137] N. S. Andryushina and O. L. Stroyuk, *Appl. Catal. B*, 2014, **148-149**, 543–549.

[138] C.-T. Chien, S.-S. Li, W.-J. Lai, Y.-C. Yeh, H.-A. Chen, I.-S. Chen, L.-C. Chen, K.-H. Chen, T. Nemoto, S. Isoda, M. Chen, T. Fujita, G. Eda, H. Yamaguchi, M. Chhowalla and C.-W. Chen, *Angew. Chem. Int. Ed.*, 2012, **51**, 6662–6666.

[139] Y. Matsumoto, M. Koinuma, S. Ida, S. Hayami, T. Taniguchi, K. Hatakeyama, H. Tateishi, Y. Watanabe and S. Amano, *J. Phys. Chem. C*, 2011, **115**, 19280–19286.

[140] Q. Xiang, J. Yu and M. Jaroniec, *Nanoscale*, 2011, **3**, 3670–3678.

[141] S. Mao, H. Pu and J. Chen, *RSC Advances*, 2012, **2**, 2643.

[142] R. Long, *J. Phys. Chem. Lett.*, 2013, **4**, 1340–1346.

[143] R. Long, Y. Dai and B. Huang, *J. Phys. Chem. Lett.*, 2013, **2**, 2223–2229.

[144] Y. Masuda, G. Giorgi and K. Yamashita, *Phys. Stat. Solidi B*, 2014, **251**, 1471–1479.

[145] R. Long and O. V. Prezhdo, *Nano Lett.*, 2014, **14**, 3335–3341.

[146] Y.-C. Yang, L. Xu, W.-Q. Huang, C.-Y. Luo, G.-F. Huang and P. Peng, *J. Phys. Chem. C*, 2015, **119**, 19095–19104.

[147] B. Bukowski and N. A. Deskins, *Phys. Chem. Chem. Phys.*, 2015, **17**, 29734–29746.

[148] J. Vandevondele, M. Krack, F. Mohamed, M. Parrinello, T. Chassaing and J. Hutter, *Comput. Phys. Commun.*, 2005, **167**, 103–128.

[149] S. Goedecker, M. Teter and J. Hutter, *Phys. Rev. B*, 1996, **54**, 1703–1710.

[150] J. VandeVondele and J. Hutter, *J. Chem. Phys.*, 2007, **127**, 114105.

[151] J. Heyd, G. E. Scuseria and M. Ernzerhof, *J. Chem. Phys.*, 2006, **124**, 219906.

[152] M. Guidon, J. Hutter and J. Vandevondele, *J. Chem. Theory Comput.*, 2010, **6**, 2348–2364.

[153] R. Dovesi, R. Orlando, A. Erba, C. M. Zicovich-Wilson, B. Civalleri, S. Casassa, L. Maschio, M. Ferrabone, M. De La Pierre, P. D'Arco, Y. Noël, M. Causà, M. Rérat and B. Kirtman, *Int. J. Quantum Chem.*, 2014, **114**, 1287–1317.

[154] M. F. Peintinger, D. V. Oliveira and T. Bredow, *J. Comput. Chem.*, 2013, **34**, 451–459.

[155] D. Wolf, in *Materials interfaces: atomic-level structure and properties*, ed. D. Wolf and S. Yip, Chapman {&} Hall, London, 1st edn., 1992, ch. 1, pp. 1–57.

[156] B. J. Morgan, in *Computational Modeling of Inorganic Nanomaterials*, ed. S. T. Bromley and M. A. Zwijnenburg, CRC Press, Boca Raton, 2016, ch. 3, pp. 83–112.

[157] C. G. de Walle and R. M. Martin, *Phys. Rev. B*, 1986, **34**, 5621–5634.

[158] G. Gui, J. Li and J. Zhong, *Phys. Rev. B*, 2008, **78**, 075435.

[159] Z. H. Ni, T. Yu, Y. H. Lu, Y. Y. Wang, Y. P. Feng and Z. X. Shen, *ACS Nano*, 2008, **2**, 2301–2305.

[160] Z. H. Ni, T. Yu, Y. H. Lu, Y. Y. Wang, Y. P. Feng and Z. X. Shen, *ACS Nano*, 2009, **3**, 483–483.

[161] V. M. Pereira, A. H. Castro Neto and N. M. R. Peres, *Phys. Rev. B*, 2009, **80**, 045401.

[162] G. Cocco, E. Cadelano and L. Colombo, *Phys. Rev. B*, 2010, **81**, 241412.

[163] I. I. Naumov and A. M. Bratkovsky, *Phys. Rev. B*, 2011, **84**, 245444.

[164] N. Kerszberg and P. Suryanarayana, *RSC Adv.*, 2015, **5**, 43810–43814.

[165] E. Cadelano, P. L. Palla, S. Giordano and L. Colombo, *Phys. Rev. Lett.*, 2009, **102**, 235502.

[166] C. A. Marianetti and H. G. Yevick, *Phys. Rev. Lett.*, 2010, **105**, 245502.

[167] C. Lee, X. Wei, J. W. Kysar and J. Hone, *Science*, 2008, **321**, 385–388.

[168] L. Ferrighi, G. Fazio and C. Di Valentin, *Adv. Mat. Interfaces*, 2016, **3**, 1500624.

[169] I. V. Lebedeva, A. A. Knizhnik, A. M. Popov, Y. E. Lozovik and B. V. Potapkin, *Phys. Chem. Chem. Phys.*, 2011, **13**, 5687–95.

[170] L. X. Benedict, N. G. Chopra, M. L. Cohen, A. Zettl, S. G. Louie and V. H. Crespi, *Chem. Phys. Lett.*, 1998, **286**, 490–496.

[171] S. Bates, G. Kresse and M. Gillan, *Surf. Sci.*, 1997, **385**, 386–394.

[172] T. Bredow, L. Giordano, F. Cinquini and G. Pacchioni, *Phys. Rev. B*, 2004, **70**, 35419.

[173] F. Labat, P. Baranek and C. Adamo, *J. Chem. Theory Comput.*, 2008, **4**, 341–352.

[174] N. Martsinovich, D. R. Jones and A. Troisi, *J. Phys. Chem. C*, 2010, **114**, 22659–22670.

[175] E. Ziambaras, J. Kleis, E. Schröder and P. Hyldgaard, *Phys. Rev. B*, 2007, **76**, 155425.

[176] S. Lebègue, J. Harl, T. Gould, J. G. Ángyán, G. Kresse and J. F. Dobson, *Phys. Rev. Lett.*, 2010, **105**, 196401.

[177] A. Amtout and R. Leonelli, *Phys. Rev. B*, 1995, **51**, 6842–6851.

[178] Y. Tezuka, S. Shin, T. Ishii, T. Ejima, S. Suzuki and S. Sato, *J. Phys. Soc. Jpn.*, 1994, **63**, 347–357.

[179] E. J. H. Lee, K. Balasubramanian, R. T. Weitz, M. Burghard and K. Kern, *Nature Nanotech.*, 2008, **3**, 486–490.

[180] A. Imanishi, E. Tsuji and Y. Nakato, *J. Phys. Chem. C*, 2007, **111**, 2128–2132.

[181] Y. Nosaka and A. Y. Nosaka, *J. Phys. Chem. Lett.*, 2016, **7**, 431–434.

[182] N. Yang, Y. Liu, H. Wen, Z. Tang, H. Zhao, Y. Li and D. Wang, *ACS Nano*, 2013, **7**, 1504–1512.

[183] W. Qian, P. A. Greaney, S. Fowler, S.-K. Chiu, A. M. Goforth and J. Jiao, *ACS Sustainable Chem. Eng.*, 2014, **2**, 1802–1810.

[184] H. Gao, X. Li, J. Lv and G. Liu, *J. Phys. Chem. C*, 2013, **117**, 16022–16027.

[185] C. Zhou and X. Zhao, *Comp. Mater. Sci.*, 2013, **69**, 180–185.

[186] P. Deák, B. Aradi and T. Frauenheim, *Phys. Rev. B*, 2011, **83**, 155207.

[187] V. Barone, J. E. Peralta and G. E. Scuseria, *Nano Lett.*, 2005, **5**, 1830–1833.

[188] V. Barone, O. Hod and G. E. Scuseria, *Nano Lett.*, 2006, **6**, 2748–2754.

[189] V. Barone, J. E. Peralta, J. Uddin and G. E. Scuseria, *J. Chem. Phys.*, 2006, **124**, 114704.

[190] V. Barone, O. Hod, J. E. Peralta and G. E. Scuseria, *Acc. Chem. Res.*, 2011, **44**, 269–279.

[191] K. R. Reddy, M. Hassan and V. G. Gomes, *Appl. Catal. A*, 2015, **489**, 1–16.

[192] Q. Xiang, J. Yu and M. Jaroniec, *Chem. Soc. Rev.*, 2012, **41**, 782.

[193] F. Lakadamyali, M. Kato and E. Reisner, *Farad. Discuss.*, 2012, **155**, 191–205.

[194] P. V. Kamat, *J. Chem. Phys. Lett.*, 2010, **1**, 520–527.

[195] R. Leary and A. Westwood, *Carbon*, 2011, **49**, 741–772.

[196] N. Zhang, M.-Q. Yang, S. Liu, Y. Sun and Y.-J. Xu, *Chem. Rev.*, 2015, **115**, 1030710377.

[197] W. Geng, H. Liu and X. Yao, *Phys. Chem. Chem. Phys.*, 2013, **15**, 6025–6033.

[198] D. R. Dreyer, S. Park, C. W. Bielawski and R. S. Ruoff, *Chem. Soc. Rev.*, 2010, **39**, 228–240.

[199] S. Stankovich, D. A. Dikin, R. D. Piner, K. A. Kohlhaas, A. Kleinhammes, Y. Jia, Y. Wu, S. T. Nguyen and R. S. Ruoff, *Carbon*, 2007, **45**, 1558–1565.

[200] Z.-S. Wu, W. Ren, L. Gao, B. Liu, C. Jiang and H.-M. Cheng, *Carbon*, 2009, **47**, 493–499.

[201] H.-J. Shin, K. K. Kim, A. Benayad, S.-M. Yoon, H. K. Park, I.-S. Jung, M. H. Jin, H.-K. Jeong, J. M. Kim, J.-Y. Choi and Y. H. Lee, *Adv. Func. Mater.*, 2009, **19**, 1987–1992.

[202] M. S. Dresselhaus, A. Jorio, M. Hofmann, G. Dresselhaus and R. Saito, *Nano Lett.*, 2010, **10**, 751–758.

[203] H. He, J. Klinowski, M. Forster and A. Lerf, *Chem. Phys. Lett.*, 1998, **287**, 53–56.

[204] I. Dékány, R. Krüger-Grasser and A. Weiss, *Colloid Polym. Sci.*, 1998, **276**, 570–576.

[205] G. Wang, Z. Yang, X. Li and C. Li, *Carbon*, 2005, **43**, 2564 – 2570.

[206] D. W. Boukhvalov and M. I. Katsnelson, *J. Am. Chem. Soc.*, 2008, **130**, 10697–10701.

[207] Z. Luo, P. M. Vora, E. J. Mele, A. T. C. Johnson and J. M. Kikkawa, *Appl. Phys. Lett.*, 2009, **94**, 111909.

[208] J. Robertson and E. P. O'Reilly, *Phys. Rev. B*, 1987, **35**, 2946–2957.

[209] M. Sun, W. Li, S. Sun, J. He, Q. Zhang and Y. Shi, *Mater. Res. Bull.*, 2015, **61**, 280–286.

[210] R. Dovesi, A. Erba, R. Orlando, C. M. Zicovich-Wilson, B. Civalleri, L. Maschio, M. Rérat, S. Casassa, J. Baima, S. Salustro and B. Kirtman, *Wiley Interdiscip. Rev. Comput. Mol. Sci.*, 2017, **0**, e1360.

[211] Y. R. Luo, *Comprehensive Handbook of Chemical Bond Energies*, CRC Press, Boca Raton, FL, USA, 2007.

[212] W. Humphrey, A. Dalke and K. Schulten, *J. Mol. Graph. Model.*, 1996, **14**, 33–38.

[213] V. Barone, O. Hod and G. E. Scuseria, *American Chemical Society*, 2006, **6**, 2748–2754.

[214] C. Chen, W. Cai, M. Long, B. Zhou, Y. Wu, D. Wu and Y. Feng, *ACS Nano*, 2010, **4**, 6425–6432.

[215] B. O'Regan and M. Grätzel, *Nature*, 1991, **353**, 737–740.

[216] A. Hagfeldt, G. Boschloo, L. Sun, L. Kloo and H. Pettersson, *Chem. Rev.*, 2010, **110**, 6595–6663.

[217] N. Martsinovich and A. Troisi, *Energy & Environment. Sci.*, 2011, **4**, 4473.

[218] A. Nattestad, I. Perera and L. Spiccia, *J. Photochem. Photobiol. C*, 2016, **28**, 44–71.

[219] M. Pastore, *Computation*, 2017, **5**, 5.

[220] J. Monat, J. Rodriguez and J. McCusker, *J. Phys. Chem. A*, 2002, **106**, 7399–7406.

[221] K. Srikanth, V. Marathe and M. Mishra, *Int. J. Quantum Chem.*, 2002, **89**, 535–549.

[222] J. Guillemoles, V. Barone, L. Joubert and C. Adamo, *J. Phys. Chem. A*, 2002, **106**, 11354–11360.

[223] S. Fantacci, F. De Angelis and A. Selloni, *J. Am. Chem. Soc.*, 2003, **125**, 4381–4387.

[224] V. Barone and M. Cossi, *J. Phys. Chem. A*, 1998, **102**, 1995–2001.

[225] D. Escudero and L. Gonzlez, *J. Chem. Theor. Compu.*, 2012, **8**, 203–213.

[226] X.-Q. Gao, Q.-J. Pan, L. Li, Y.-R. Guo, H.-X. Zhang and H.-G. Fu, *Chem. Phys. Lett.*, 2011, **506**, 146–151.

[227] J. Wang, F.-Q. Bai, B.-H. Xia, L. Feng, H.-X. Zhang and Q.-J. Pan, *Phys. Chem. Chem. Phys.*, 2011, **13**, 2206–2213.

[228] X. Zhang, J.-J. Zhang and Y.-Y. Xia, *J. Photochem. Photobiol. A*, 2007, **185**, 283–288.

[229] O. Kitao and H. Sugihara, *Inorg. Chim. Acta*, 2008, **361**, 712–728.

[230] G. J. Wilson and G. D. Will, *Inorg. Chim. Acta*, 2010, **363**, 1627–1638.

[231] P. T. Nguyen, A. R. Andersen, E. M. Skou and T. Lund, *Solar Energy Mater. Solar Cells*, 2010, **94**, 1582 – 1590.

[232] P. T. Nguyen, B. X. T. Lam, A. R. Andersen, P. E. Hansen and T. Lund, *Eur. J. Inorg. Chem.*, 2011, **2011**, 2533–2539.

[233] E. C. Constable and J. M. Holmes, *J. Organomet. Chem.*, 1986, **301**, 203 – 208.

[234] E. C. Constable and C. E. Housecroft, *Polyhedron*, 1990, **9**, 1939 – 1947.

[235] Y. Chi and P.-T. Chou, *Chem. Soc. Rev.*, 2007, **36**, 1421–1431.

[236] D. Jean-Pierre, S. Jean-Baptiste, B. Laurent and P. Michel, *Eur. J. Inorg. Chem.*, 2009, **7**, 817–853.

[237] C. R. Wade and F. P. Gabbai, *Inorg. Chem.*, 2010, **49**, 714–720.

[238] S. H. Wadman, J. M. Kroon, K. Bakker, M. Lutz, A. L. Spek, G. P. M. van Klink and G. van Koten, *Chem. Commun.*, 2007, 1907–1909.

[239] T. Bessho, E. Yoneda, J.-H. Yum, M. Guglielmi, I. Tavernelli, H. Imai, U. Rothlisberger, M. K. Nazeeruddin and M. Graetzel, *J. Am. Chem. Soc.*, 2009, **131**, 5930–5934.

[240] P. G. Bomben, B. D. Koivisto and C. P. Berlinguette, *Inorg. Chem.*, 2010, **49**, 4960–4971.

[241] H. Kisserwan and T. H. Ghaddar, *Dalton Trans.*, 2011, **40**, 3877–3884.

[242] K. C. D. Robson, B. D. Koivisto, A. Yella, B. Sporinova, M. K. Nazeeruddin, T. Baumgartner, M. Graetzel and C. P. Berlinguette, *Inorg. Chem.*, 2011, **50**, 5494–5508.

[243] H. Kisserwan, A. Kamar, T. Shoker and T. H. Ghaddar, *Dalton Trans.*, 2012, **41**, 10643–10651.

[244] G. Sauve, M. Cass, G. Coia, S. Doig, I. Lauermann, K. Pomykal and N. Lewis, *J. Phys. Chem. B*, 2000, **104**, 6821–6836.

[245] G. Sauve, M. Cass, S. Doig, I. Lauermann, K. Pomykal and N. Lewis, *J. Phys. Chem. B*, 2000, **104**, 3488–3491.

[246] D. Kuciauskas, J. Monat, R. Villahermosa, H. Gray, N. Lewis and J. McCusker, *J. Phys. Chem. B*, 2002, **106**, 9347–9358.

[247] S. Altobello, R. Argazzi, S. Caramori, C. Contado, S. Da Fre, P. Rubino, C. Chone, G. Larramona and C. Bignozzi, *J. Am. Chem. Soc.*, 2005, **127**, 15342–15343.

[248] A. Govindasamy, C. Lv, H. Tsuboi, M. Koyama, A. Endou, H. Takaba, M. Kubo, C. A. Del Carpio and A. Miyamoto, *Jap. J. Appl. Phys.*, 2007, **46**, 2655–2660.

[249] H. Sugihara, L. Singh, K. Sayama, H. Arakawa, M. Nazeeruddin and M. Grätzel, *Chem. Lett.*, 1998, 1005–1006.

[250] M. Yanagida, L. Singh, K. Sayama, K. Hara, R. Katoh, A. Islam, H. Sugihara, H. Arakawa, M. Nazeeruddin and M. Grätzel, *Dalton Trans.*, 2000, 2817–2822.

[251] K. Hara, H. Sugihara, L. Singh, A. Islam, R. Katoh, M. Yanagida, K. Sayama, S. Murata and H. Arakawa, *J. Photochem. Photobiol. A*, 2001, **145**, 117–122.

[252] W.-P. Liao, S.-C. Hsu, W.-H. Lin and J.-J. Wu, *J. Phys. Chem. C*, 2012, **116**, 15938–15945.

[253] D. R. Lide, *CRC Handbook of Chemistry and Physics*, CRC Press, 2000 N. W. Corporate Blvd, Boca Raton, Fl, 33431, USA, 85th edn., 2004.

[254] S. Ferrere and B. Gregg, *J. Am. Chem. Soc.*, 1998, **120**, 843–844.

[255] S. Ferrere, *Chem. Mater.*, 2000, **12**, 1083–1089.

[256] S. Ferrere, *Inorg. Chim. Acta*, 2002, **329**, 79–92.

[257] G. Hasselmann and G. Meyer, *J. Phys. Chem. B*, 1999, **103**, 7671–7675.

[258] A. Islam, H. Sugihara, K. Hara, L. Singh, R. Katoh, M. Yanagida, Y. Takahashi, S. Murata and H. Arakawa, *Inorg. Chem.*, 2001, **40**, 5371–5380.

[259] E. Geary, N. Hirata, J. Clifford, J. Durrant, S. Parsons, A. Dawson, L. Yellowlees and N. Robertson, *Dalton Trans.*, 2003, 3757–3762.

[260] E. Geary, L. Yellowlees, L. Jack, I. Oswald, S. Parsons, N. Hirata, J. Durrant and N. Robertson, *Inorg. Chem.*, 2005, **44**, 242–250.

[261] E. A. M. Geary, K. L. McCall, A. Turner, P. R. Murray, E. J. L. McInnes, L. A. Jack, L. J. Yellowleesa and N. Robertson, *Dalton Trans.*, 2008, 3701–3708.

[262] N. Alonsovante, J. Nierengarten and J. Sauvage, *Dalton Trans.*, 1994, 1649–1654.

[263] S. Sakaki, T. Kuroki and T. Hamada, *Dalton Trans.*, 2002, 840–842.

[264] T. Bessho, E. C. Constable, M. Graetzel, A. H. Redondo, C. E. Housecroft, W. Kylberg, M. K. Nazeeruddin, M. Neuburger and S. Schaffner, *Chem. Comm.*, 2008, 3717–3719.

[265] C. L. Linfoot, P. Richardson, T. E. Hewat, O. Moudam, M. M. Forde, A. Collins, F. White and N. Robertson, *Dalton Trans.*, 2010, **39**, 8945–8956.

[266] X. Lu, S. Wei, C.-M. L. Wu, S. Li and W. Guo, *J. Phys. Chem. C*, 2011, **115**, 3753–3761.

[267] K. Kakiage, Y. Aoyama, T. Yano, K. Oya, J.-i. Fujisawa and M. Hanaya, *Chem. Commun.*, 2015, **51**, 15894–15897.

[268] T. Horiuchi, H. Miura and S. Uchida, *Chem. Comm.*, 2003, 3036–3037.

[269] T. Horiuchi, H. Miura, K. Sumioka and S. Uchida, *J. Am. Chem. Soc.*, 2004, **126**, 12218–12219.

[270] B. Liu, W. Zhu, Q. Zhang, W. Wu, M. Xu, Z. Ning, Y. Xie and H. Tian, *Chem. Comm.*, 2009, 1766–1768.

[271] H. Tanaka, A. Takeichi, K. Higuchi, T. Motohiro, M. Takata, N. Hirota, J. Nakajima and T. Toyoda, *Solar Energy Mater. Solar Cells*, 2009, **93**, 1143–1148.

[272] K. Hara, K. Sayama, Y. Ohga, A. Shinpo, S. Suga and H. Arakawa, *Chem. Comm.*, 2001, 569–570.

[273] K. Hara, K. Miyamoto, Y. Abe and M. Yanagida, *J. Phys. Chem. B*, 2005, **109**, 23776–23778.

[274] Z.-S. Wang, Y. Cui, K. Hara, Y. Dan-oh, C. Kasada and A. Shinpo, *Adv. Mater.*, 2007, **19**, 1138–1141.

[275] Z.-S. Wang, Y. Cui, Y. Dan-oh, C. Kasada, A. Shinpo and K. Hara, *J. Phys. Chem. C*, 2008, **112**, 17011–17017.

[276] A. Dreuw, J. Weisman and M. Head-Gordon, *J. Chem. Phys.*, 2003, **119**, 2943–2946.

[277] A. Dreuw and M. Head-Gordon, *J. Am. Chem. Soc.*, 2004, **126**, 4007–4016.

[278] A. Dreuw and M. Head-Gordon, *Chem. Rev.*, 2005, **105**, 4009–4037.

[279] M. Pastore, S. Fantacci and F. De Angelis, *J. Phys. Chem. C*, 2010, **114**, 22742–22750.

[280] M. Pastore, E. Mosconi and F. De Angelis, *J. Phys. Chem. C*, 2012, **116**, 5965–5973.

[281] M. Pastore, E. Mosconi, S. Fantacci and F. De Angelis, *Current Organic Synthesis*, 2012, **9**, 215–232.

[282] M. Pastore, S. Fantacci and F. De Angelis, *J. Phys. Chem. C*, 2013, **117**, 3685–3700.

[283] E. Ronca, C. Angeli, L. Belpassi, F. De Angelis, F. Tarantelli and M. Pastore, *J. Chem. Theor. Compu.*, 2014, **10**, 4014–4024.

[284] M. Pastore and F. De Angelis, *ACS Nano*, 2010, **4**, 556–562.

[285] P. Umari, G. Stenuit and S. Baroni, *Phys. Rev. B*, 2009, **79**, 201104.

[286] P. Umari, G. Stenuit and S. Baroni, *Phys. Rev. B*, 2010, **81**, 115104.

[287] L. Hedin, *Phys. Rev.*, 1965, **139**, A796–A823.

[288] M. S. Hybertsen and S. G. Louie, *Phys. Rev. B*, 1986, **34**, 5390–5413.

[289] D. Jacquemin, E. A. Perpete, G. Scalmani, M. J. Frisch, X. Assfeld, I. Ciofini and C. Adamo, *J. Chem. Phys.*, 2006, **125**, 164324.

[290] J. Tomasi, B. Mennucci and R. Cammi, *Chem. Rev.*, 2005, **105**, 2999–3094.

[291] Y. Kurashige, T. Nakajima, S. Kurashige, K. Hirao and Y. Nishikitani, *J. Phys. Chem. A*, 2007, **111**, 5544–5548.

[292] D. Jacquemin, E. A. Perpète, I. Ciofini and C. Adamo, *Theor. Chem. Acc.*, 2008, **120**, 405–410.

[293] M. Pastore, E. Mosconi, F. De Angelis and M. Grätzel, *J. Phys. Chem. C*, 2010, **114**, 7205–7212.

[294] S. Hazebroucq, F. Labat, D. Lincot and C. Adamo, *J. Phys. Chem. A*, 2008, **112**, 7264–7270.

[295] W. Duncan and O. Prezhdo, *J. Phys. Chem. B*, 2005, **109**, 17998–18002.

[296] F. De Angelis, S. Fantacci and A. Selloni, *Nanotech.*, 2008, **19**, 424002.

[297] J. Wiberg, T. Marinado, D. P. Hagberg, L. Sun, A. Hagfeldt and B. Albinsson, *J. Phys. Chem. C*, 2009, **113**, 3881–3886.

[298] A. Vittadini, A. Selloni, F. Rotzinger and M. Gratzel, *J. Phys. Chem. B*, 2000, **104**, 1300–1306.

[299] M. Nilsing, S. Lunell, P. Persson and L. Ojame, *Surf. Sci.*, 2005, **582**, 49 – 60.

[300] N. Martsinovich and A. Troisi, *Phys. Chem. Chem. Phys.*, 2012, 13392–13401.

[301] M. Pastore and F. De Angelis, *Phys. Chem. Chem. Phys.*, 2012, **14**, 920–928.

[302] C. Anselmi, E. Mosconi, M. Pastore, E. Ronca and F. De Angelis, *Phys. Chem. Chem. Phys.*, 2012, **14**, 15963–15974.

[303] F. Schiffmann, J. VandeVondele, J. Hutter, R. Wirz, A. Urakawa and A. Baiker, *J. Phys. Chem. C*, 2010, **114**, 8398–8404.

[304] F. De Angelis, S. Fantacci, A. Selloni, M. K. Nazeeruddin and M. Gratzel, *J. Phys. Chem. C*, 2010, **114**, 6054–6061.

[305] F. De Angelis, S. Fantacci, A. Selloni, M. K. Nazeeruddin and M. Gratzel, *J. Am. Chem. Soc.*, 2007, **129**, 14156+.

[306] F. De Angelis, S. Fantacci, A. Selloni, M. Graetzel and M. K. Nazeeruddin, *Nano Lett.*, 2007, **7**, 3189–3195.

[307] S. Meng and E. Kaxiras, *Nano Lett.*, 2010, **10**, 1238–1247.

[308] E. Ronca, M. Pastore, L. Belpassi, F. Tarantelli and F. De Angelis, *Energy Environ. Sci.*, 2013, **6**, 183–193.

[309] O. V. Prezhdo, W. R. Duncan and V. V. Prezhdo, *Acc. Chem. Res.*, 2008, **41**, 339–348.

[310] Y. Ping, D. Rocca and G. Galli, *Chem. Soc. Rev.*, 2013, **42**, 2437–2469.

[311] P. Nyombayire, T. Pilz, F. Black, E. A. Gibson, P. N. O. Gillespie, N. Martsinovich and V. A. Kozhevnikov, Unpublished Work.

[312] M. J. Frisch, G. W. Trucks, H. B. Schlegel, G. E. Scuseria, M. A. Robb, J. R. Cheeseman, G. Scalmani, V. Barone, B. Mennucci, G. A. Petersson, H. Nakatsuji, M. Caricato, X. Li, H. P. Hratchian, A. F. Izmaylov, J. Bloino, G. Zheng, J. L. Sonnenberg, M. Hada, M. Ehara, K. Toyota, R. Fukuda, J. Hasegawa, M. Ishida, T. Nakajima, Y. Honda, O. Kitao, H. Nakai, T. Vreven, J. A. Montgomery, Jr., J. E. Peralta, F. Ogliaro, M. Bearpark, J. J. Heyd, E. Brothers, K. N. Kudin, V. N. Staroverov, R. Kobayashi, J. Normand, K. Raghavachari, A. Rendell, J. C. Burant, S. S. Iyengar, J. Tomasi, M. Cossi, N. Rega, J. M. Millam, M. Klene, J. E. Knox, J. B. Cross, V. Bakken, C. Adamo, J. Jaramillo, R. Gomperts,

R. E. Stratmann, O. Yazyev, A. J. Austin, R. Cammi, C. Pomelli, J. W. Ochterski, R. L. Martin, K. Morokuma, V. G. Zakrzewski, G. A. Voth, P. Salvador, J. J. Dannenberg, S. Dapprich, A. D. Daniels, . Farkas, J. B. Foresman, J. V. Ortiz, J. Cioslowski and D. J. Fox, *Gaussian09 Revision E.01*, Gaussian Inc. Wallingford CT 2009.

[313] P. J. Hay and W. R. Wadt, *J. Chem. Phys.*, 1985, **82**, 270–283.

[314] W. R. Wadt and P. J. Hay, *J. Chem. Phys.*, 1985, **82**, 284–298.

[315] P. J. Hay and W. R. Wadt, *J. Chem. Phys.*, 1985, **82**, 299–310.

[316] R. Feld, M. S. Lehmann, K. Muir and J. C. Speakman, *Z. Kristallogr.*, 1981, **157**, 215–231.

[317] R. C. Weast, *Handbook of Chemistry and Physics*, CRC Press, CRC Press inc, 2000 Corporate Blvd NW, Journals Customer Service, Boca Raton, FL 33431, USA, 65th edn., 1984.

[318] F. De Angelis, S. Fantacci, E. Mosconi, M. K. Nazeeruddin and M. Gratzel, *J. Phys. Chem. C*, 2011, **115**, 8825–8831.

[319] M. M. Ugeda, I. Brihuega, F. Guinea and J. M. Gómez-Rodríguez, *Phys. Rev. Lett.*, 2010, **104**, 096804.

[320] T. Kondo, Y. Honma, J. Oh, T. Machida and J. Nakamura, *Phys. Rev. B*, 2010, **82**, 153414.

[321] E. Finazzi, C. Di Valentin, G. Pacchioni and A. Selloni, *J. Chem. Phys.*, 2008, **129**, 154113.